Generation, Acceleration and Measurement of Attosecond Electron Beams from Laser-Plasma Accelerators

by

Maria Katharina Weikum

A thesis presented for the degree of
Doctor of Philosophy in Physics

Physics Department, University of Strathclyde, Glasgow
in collaboration with DESY, Hamburg

Supervisors:
Prof. Zheng-Ming Sheng
Dr. Ralph Assmann
Prof. Dino Jaroszynski

2017

This thesis is the result of the author's original research. It has been composed by the author and has not been previously submitted for examination which has led to the award of a degree.

Signed:

Date:

Abstract

Accelerator-based light sources are extremely useful machines for investigating matter on a microscopic level, yet their capability for time-resolved research is limited by the femtosecond-scale duration of their radiation pulses. Attosecond beams could enhance these capacities enabling the measurement of most outer shell electron dynamics in molecular and atomic systems. However, one of the main challenges in this direction remains the generation of attosecond-scale electron bunches which can be used for ultrashort radiation generation or as probes themselves. The research presented in this thesis tackles this issue from two angles. First, mechanisms for ultrashort electron beam generation and acceleration in laser wakefield accelerators - as promising, compact accelerator systems - are investigated through particle-in-cell simulations. Both an optimised electron plasma injector, using upramp-assisted self-injection, and an external injection setup with the plasma stage as an energy booster to a conventionally accelerated beam are capable of providing electron bunches of few hundred attoseconds duration. The externally injected beams are found to be limited in duration, but preserve well the initial high beam quality for energies up to gigaelectronvolts, while in self-injection high beam currents and ultrashort duration can be achieved, yet at some cost to beam quality and stability. As a second research branch, longitudinal beam profile diagnostics with sub-femtosecond resolution are examined as possible means for measuring such ultrashort electron beams. A first proof-of-principle experiment of a novel streaking device is presented and compared with measurements with an X-band radiofrequency deflecting cavity. Additional computational and theoretical studies provide insights into the possibilities and challenges to apply this new diagnostic technique to sub-femtosecond electron beams from conventional and novel accelerators.

Contents

Acknowledgements

This thesis would not have been possible without the support and work of many people that made the last three years of my PhD very enjoyable and exciting. I would like to thank in particular:

- my supervisors Prof. Zheng-Ming Sheng and Dr. Ralph Assmann for giving me the opportunity to work on this collaborative project. Thanks also for the many other opportunities that they helped me find during my PhD and the guidance and advice they have always been ready to share despite both of their very busy schedules.
- Prof. Dino Jaroszynski for taking over the role as my second Strathclyde supervisor.
- Prof. Brigitte Cros and Dr. Brian McNeil for taking the time to review this thesis as my PhD examiners.
- Dr. Gerard Andonian for the very fruitful collaboration we have built. I have learned a lot through our work together.
- Dr. Fei Yu Li, Ángel Ferran Pousa, Dr. Elena Svystun, Dr. Alberto Martinez de la Ossa, Dr. Andreas Walker, Thomas Heinemann and Fahim Habib for advice and many useful discussions on plasma acceleration, simulation issues, grand radiation schemes, etc.
- the team involved in the experiments at ATF, in particular Nick Sudar, Dr. Mikhail Fedurin and Dr. Christina Swinson, who taught me about the tricks and pitfalls of experimental accelerator research.
- my colleagues at DESY for making my time in Hamburg very enjoyable; thanks especially to Ulrich for good and honest advice, to Barbara, Jun and Daniel for sharing their knowledge on RF accelerators, and to Thomas, Grygorii, Frank and Willi for discussions about diagnostics and dielectric accelerators.

- my colleagues at Strathclyde for the good working atmosphere, fun physics-filled lunch breaks, many successful SCOPE events and other aspects that have made my time in the department very successful.

- Dr. Christopher Thornton and Prof. Simon Hooker for sharing with me their results and knowledge on density profiles in gas cells.

- Dr. Jens Osterhoff and his group for successfully sharing and collaborating on my use of the simulation code OSIRIS as well as access to various supercomputing facilities in order to run the code.

- the very patient people working at DESY IT who have helped me not only to store my copious amounts of data securely, but also to make the most of the many IT-related facilities and possibilities that DESY has to offer.

- and, last but not least, my family: thank you, in particular, to my dad and sister for actually reading through my thesis (with some very useful advice!) and getting excited about chicanes, electron bunches and lasing; to my mum for her unwavering moral support; and to Michael for taking this journey, with all its back and forth travels, together with me.

Part I

Introduction

Modern short-pulse electron accelerators are essential tools for the microscopic study and observation of matter. When charged particles are accelerated in a magnetic field, they emit radiation at wavelengths dependent on their energy. Using large machines, such as synchrotron light sources and Free-Electron Lasers (FELs), electron beams with gigaelectronvolt (GeV) energies can thus generate highly intense radiation pulses with wavelengths ranging from the sub-millimetre to the X-ray regime. With pulse durations on the order of femtoseconds (fs) to picoseconds (ps), these ultrabright light flashes can help to gain insight into processes and structures relevant to biological, chemical, engineering and physical research, with both remarkable spatial and temporal resolution for techniques, such as X-ray spectroscopy and femtosecond-serial crystallography.

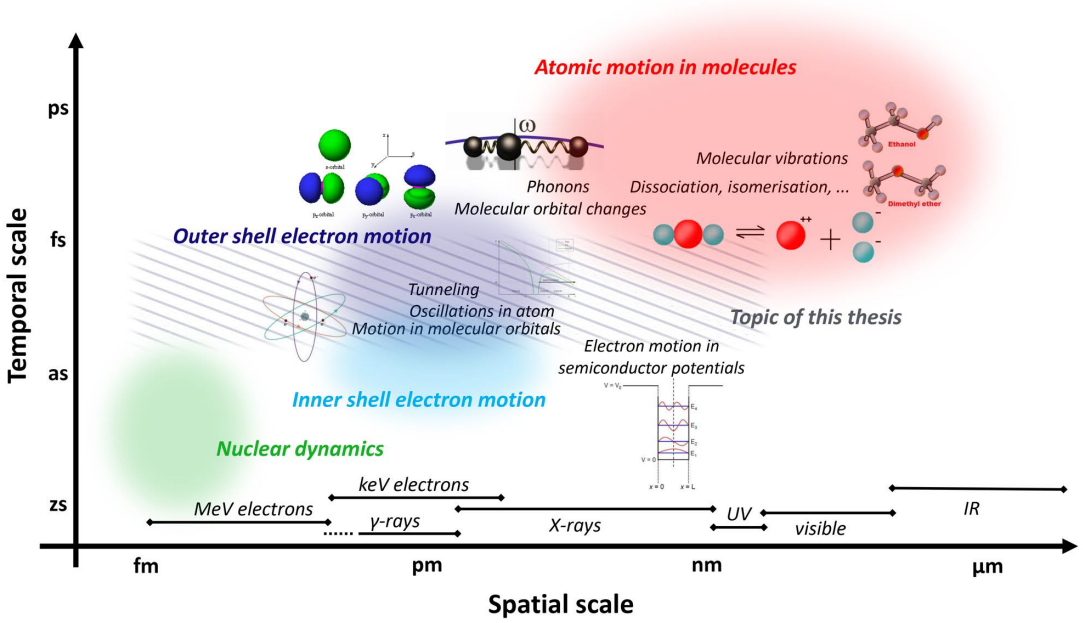

Figure 1: Spatial and temporal scales of molecular, atomic and sub-atomic processes (data based on [1–6]). The striped region describes the regime that this thesis focuses on.

While the recent rise in the number of X-ray synchrotron and FEL facilities has allowed for a tremendous advance in the understanding of intra-atom electron dynamics of many complex natural systems, the femtosecond-pulse-length limit for achievable electron beams and consequently also radiation pulses is a fundamental limitation to how accurately a system can be observed. As Fig. 1 shows, most outer shell electron processes, for example, occur on timescales of hundreds of attoseconds, while inner shell electron dynamics are dominated by single attosecond processes. Unless we can examine these events with probe pulses of equal or shorter duration, there is no possibility of understanding their dynamics in full detail. Moreover, even

for static systems, as in molecular crystallography, observations made with femtosecond beams are always adversely affected by the crystal response to the probe beam occurring on the sub-fs scale through ultrafast ionisation and decay processes. In fact, a number of interesting systems and processes to study at the attosecond scale have been proposed in the past: the AXSIS project [7], for example, aims to develop a novel electron accelerator facility for improving the understanding of photoemission dynamics by studying metal clusters and proteins involved in photosynthesis. Also many quantum phenomena and condensed matter systems could be better understood with attosecond probe pulses [8, 9]. Besides, attosecond electron and radiation pulses could also be employed to investigate radiation damage, ultrafast high intensity laser-matter interactions [10] and possibly even ways to control electron motion in materials, such as electronic circuits, in enhanced detail.

Consequently, recent years have brought forth a series of research directions aiming at the generation of attosecond beams, ranging from Free-Electron Laser related schemes (e.g. [3, 11–15]) to techniques based on newly developed high intensity laser pulses (e.g. [8, 16–18]), most of which still rely on simulation results and yet have to be tested experimentally. High harmonic generation (HHG) poses an exception to this development with a first experimental demonstration of this all-optical scheme producing few-hundred-attosecond radiation flashes in 2001 [19] and record pulse lengths down to 43 attoseconds measured in 2017 [20]. However, while extended recently to solid targets to increase the generated output power [21], HHG is currently still limited in terms of achievable brightness, especially in the hard X-ray regime and for isolated radiation pulses, where it is at least eight to ten orders of magnitude behind what Free-Electron Lasers can generate [21].

Accelerator-based radiation sources are potentially capable of surmounting this challenge to achieve high brightness at ultrashort duration and could thus be suitable alternatives, for example, for pump-probe experiments where the availability of isolated pulses at sufficient flux has been an issue to-date [19, 22]. One particularly interesting option to consider in this context is the use of novel acceleration techniques for generating attosecond beams due to their compact size and reduced costs compared to the conventional large-scale facilities. In laser wakefield accelerators (LWFA) the following advanced accelerator concept has been proposed: a short, high power laser pulse induces, while passing through and ionising a gas target, oscillations in the electron density of the generated underdense plasma which form a longitudinal wave with a strong associated electric wakefield. With gradients on the order of hundreds of gigavolt per metre or more - around three orders of magnitude stronger than in conventional radiofrequency (RF) accelerators - this generated field can accelerate, but also produce, electron beams in the

space of a few millimetres to centimetres. One consequence of the small scale of such devices is that laser wakefield acceleration produces intrinsically short electron beams with duration on the order of few femtoseconds. By optimising the accelerator physics in this process, it may thus be possible to produce and accelerate isolated attosecond electron beams. These pulses would be suitable for direct application in, for example, ultrafast electron diffraction, as well as for introduction into radiation generation schemes.

This thesis aims to study exactly such possibilities by investigating options for employing laser wakefield acceleration as a mechanism in generating and accelerating attosecond electron bunches. To this end, two different LWFA systems are explored:

- a self-injection scheme where the ultrashort beam is formed directly in the accelerating field from particles in the background plasma;
- and an external injection scheme where a sub-femtosecond electron beam is generated by an RF accelerator and propagated into a laser-driven plasma accelerator to reach higher beam energies.

Other crucial aspects in the study of attosecond electron pulses are their detection and the measurement of their longitudinal beam distribution. With most common longitudinal electron beam diagnostics designed for measuring bunch durations on the order of single femtoseconds or above, any study into the generation of attosecond beams must therefore be tied to research on developing novel detection techniques. A part of this thesis thus examines the measurement of ultrashort electron beams through the theoretical and experimental study of two different bunch length diagnostic schemes.

The thesis is organised as follows: In Part II, an introduction to the most important topics and theories regarding the generation and detection of attosecond electron beams is provided. Chapter 1 presents an overview over the research institutions involved in this work, in particular with regard to their research on photon science and novel accelerators. In Chapter 2 the main principles of particle accelerators are described and a general overview of state-of-the-art techniques for sub-femtosecond electron beam generation and measurement is given. Chapter 3 discusses more specifically the principles and theory of laser wakefield acceleration. Part III presents the detailed simulation studies conducted during this thesis on two laser wakefield accelerator systems to generate and accelerate electron beams with attosecond duration. In this respect, Chapter 4 focuses on the self-injection of ultrahigh density, few hundred attosecond duration beams using a compact plasma accelerator with a steep density upramp profile. In Chapter 5, on the other hand, an external injection setup with an RF-accelerated,

sub-femtosecond duration electron bunch, based on the design for the accelerator research & development facility SINBAD at DESY, being injected and accelerated in a low density plasma target is discussed. Chapter 6 concludes this part with a comparison of the two techniques and a discussion of possible applications and an experimental realisation. In Part IV the measurement of longitudinal bunch profiles of sub-femtosecond duration is examined. Numerical studies (Chapter 7) and a first experiment (Chapter 8) of a novel ultrahigh resolution diagnostic device are presented and compared with studies of an X-band transverse deflecting cavity as an established high resolution technique. Chapter 9 further analyses the potential of the diagnostic schemes for possible application to ultrashort electron beams. Finally, Part V concludes this thesis with a summary of the main results and an outlook to the next steps to be taken in this novel field.

Part II

Background & Theory

Chapter 1

Accelerator-Based Photon Science at DESY, the University of Strathclyde & Brookhaven National Laboratory

The work presented in this thesis has been carried out in equal parts at the German accelerator institute DESY (Deutsches Elektronensynchrotron) and the University of Strathclyde in Glasgow, UK, with additional experiments undertaken at the Brookhaven National Laboratory in Long Island, USA. This chapter introduces each of these facilities with regard to their capabilities and expertise in accelerator-based photon science, following a short overview over the main technologies.

1.1 What is Accelerator-Based Photon Science?

The working principles of most conventional accelerator-based radiation sources are similar: an electron beam is accelerated to relativistic energies before it propagates through a magnetic field in the form of a bending magnet or, more commonly, an undulator - an array of periodically poled magnets. As it passes through the magnetic field, the beam oscillates in the direction perpendicular to the field and, being accelerated radially, emits radiation along a narrow cone in the forward direction.

In Free-Electron Lasers (FELs) the process is optimised further to convert this spontaneous emission into a self-amplifying process of coherent radiation generation, hence allowing for an increase in radiated power up to tens of gigawatts [23, 24]. This effect requires a set of con-

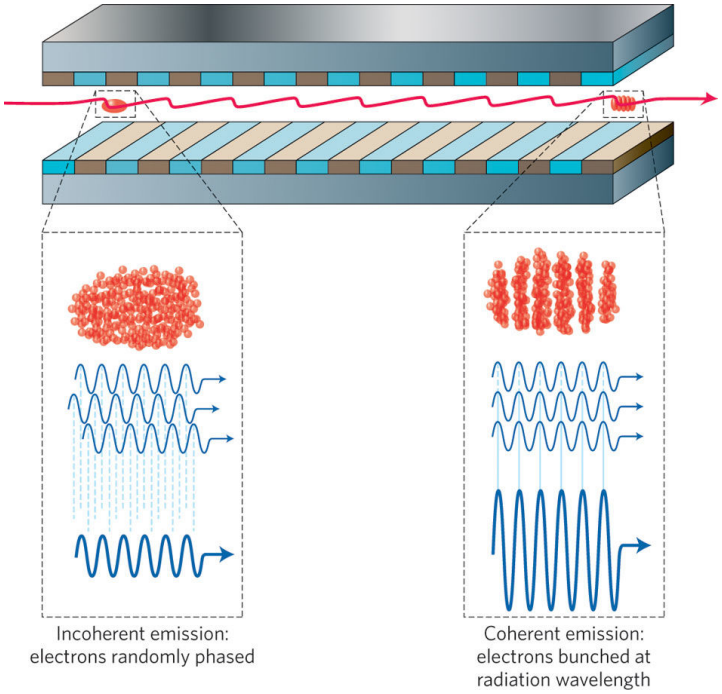

Figure 1.1: Radiation generation mechanism in a Free-Electron Laser (FEL): through the interaction between the electron beam and its emitted radiation, a self-amplifying microbunching of the electrons occurs eventually leading to the generation of a coherent radiation pulse (image reprinted by permission from Macmillan Publishers Ltd: Nature Photonics, copyright 2010 [23]).

ditions in order to achieve efficient interaction of the electron beam with its own radiation field. Specifically needed is a beam of high quality, good overlap between the bunch and its generated radiation, and a fixed slipping distance of the faster radiation field with respect to the electrons allowing for constructive interference of the radiated emission at multiple points in the undulator. As visualised in Fig. 1.1, being accelerated or decelerated in the radiation field depending on their relative position to the field, the electrons start to form a periodic modulation in energy and eventually longitudinal particle density across the beam, so-called microbunching. This, on the other hand, means that the radiation emitted by these bunched electrons adds more constructively to the already existing electromagnetic field, amplifying the radiation intensity as well as the electron microbunching. The self-amplification continues with an exponential growth in radiation intensity until the electron beam energy loss due to the radiation generation becomes significant. At this point the electron beam is significantly microbunched and individual particles radiate almost in phase at a specific wavelength depending, among others, on the electron beam energy and undulator properties.

Due to the high brightness and short duration of the radiation pulses generated in Free-

Electron Lasers, they are extremely useful as tools for probing atomic and sub-atomic processes, especially at short wavelengths in the extreme ultraviolet (XUV) and X-ray regime. As Fig. 1.2 shows, however, the number of available FELs worldwide is currently limited, especially in the X-ray wavelength range with only four machines in operation. This is to a great extent linked to the large facility size required to accelerate electron beams to the necessary energies. As a consequence, more compact accelerator-based radiation generation techniques have been developed in recent years. Often combined also with novel, small-scale accelerator concepts, these include, for example, Thomson backscattering and betatron radiation.

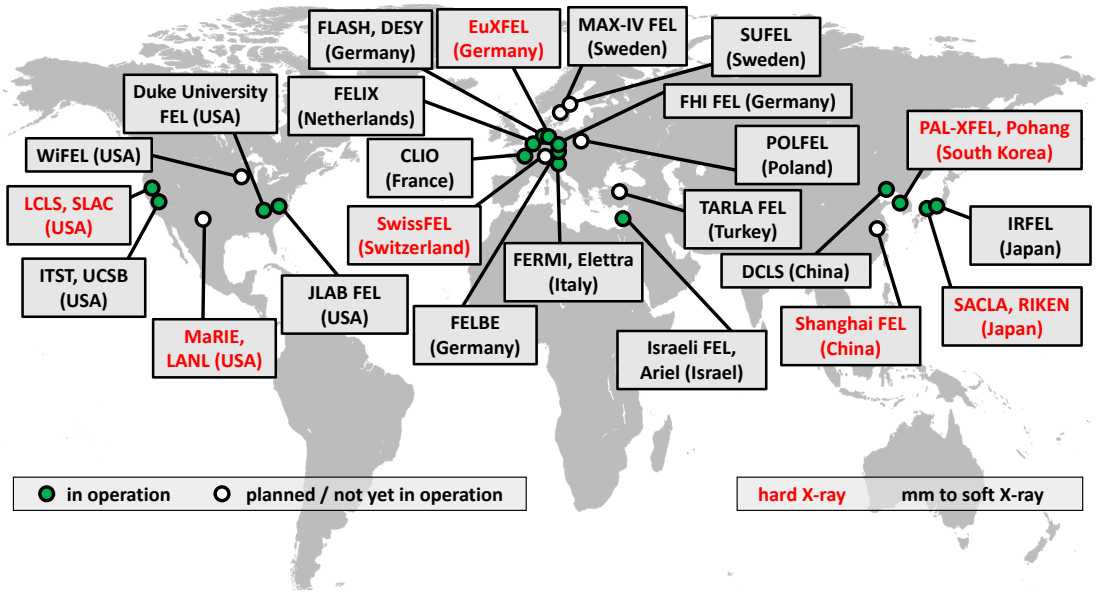

Figure 1.2: Overview over Free-Electron Laser facilities worldwide in operation and planning.

In Thomson backscattering, also called inverse Compton scattering (ICS) in its high energy limit, a short laser pulse scatters off a counter-propagating relativistic electron beam with the scattered radiation being Doppler-shifted, which allows reaching XUV and X-ray wavelengths even with modest electron energies of tens to hundreds megaelectronvolts [1]. Under the right conditions the emitted radiation pulse can also be coherent, in which case the scheme is often referred to as an "all-optical FEL".

Betatron radiation, on the other hand, is produced in plasma accelerators where the generated plasma wave driving the acceleration process can also act as an undulator. With the electron beam hence being deflected periodically in the transverse direction, it emits synchrotron radiation, the wavelength of which depends, among others, on the electron beam energy and plasma density [1]. While limited in the achievable radiation brightness, this mechanism has the

advantage that the electron beam does not need to be extracted from the plasma for radiation generation, which can be challenging due to the strong fields inside the accelerator.

Finally, in the context of photon science and throughout all of these techniques, there is one particularly important figure of merit that should be mentioned: the spectral brightness or brilliance of a radiation pulse. Measured in units of photons/s/mm^2/mrad^2/(0.1% bandwidth), it describes the photon flux in a unit source area, unit solid angle and spectral bandwidth of 0.1 % [25].

1.2 DESY and Large-Scale Accelerator-Based Photon Science

DESY (Deutsches Elektronensynchrotron) is one of the largest research centres for accelerator-based photon science in Europe, both in the context of conventional and novel technologies. Located in Hamburg, Germany, it hosts various accelerator facilities, including the synchrotron light source PETRA III as well as the world's first X-ray Free-Electron Laser FLASH. Additionally, DESY is also one of the major partners involved in the European X-ray FEL (EuXFEL) project.

PETRA III is one of the largest and most brilliant storage ring light source in the world with a circumference of 2.3 km and more than 17 different beamlines for photon science users distributed over three experimental halls. Tables 1.1 and 1.2 show the properties of the generated electron beams and synchrotron radiation pulses. The most distinguishing feature of the facility is the small horizontal electron beam emittance, a measure for transverse beam quality, which is three to four times smaller than for beams at any other high energy storage ring worldwide [26].

Parameters	**PETRA III**	**FLASH**	**EuXFEL**
Energy [MeV]	6000	0.35–1250	<17500
Energy spread [MeV]	6.0	0.2–0.5	2.5
Peak current [kA]	100×10^{-6}	1–2.5	5
Beam charge [nC]	769	0.02–1	1

Table 1.1: Electron beam parameters at PETRA III, FLASH and the European XFEL [26–28].

FLASH, the Free-Electron Laser in Hamburg, on the other hand, is a linac-driven light source with a total length of 315 m built in 2005. It consists of a superconducting linear accelerator (linac) followed by two undulator lines, FLASH1 and FLASH2, ending in two experimental halls with 11 experimental user areas. Running currently in the SASE (self-amplified spontaneous emission) mode - with research on seeding and other FEL modes ongoing - a wavelength range

Parameters	**PETRA III**	**FLASH**	**EuXFEL**
Wavelength [nm]	0.007–8.3	4–90	0.05–6.4
FWHM pulse duration [fs]	90×10^3	<10–300	<100
Peak power [GW]		1–5	22–135
Peak brilliance [photons/s/ mrad^2/mm^2/(0.1% bw.)]	$>1 \times 10^{21}$	1×10^{28}–1×10^{31}	6×10^{31}–5×10^{33}

Table 1.2: Radiation parameters at PETRA III, FLASH and the European XFEL [26–28]. Note that FWHM stands for full width at half maximum.

of approximately 4.0–90 nm can be covered with gigawatt peak power and pulse durations between 10 fs and 300 fs. The latter is achieved through compressing the accelerated electron beams from currents of around 50-80 A to 1-2 kA at energies of a few hundred MeV. For better control over the generated radiation pulses, the FLASH beamline includes a range of diagnostics, including a 3.6 m long S-band (2–4 GHz) transverse deflecting structure (TDS) and an electro-optic measurement setup (more details in Section 2.4.2) [27].

Finally, the European XFEL has a similar setup to FLASH, also employing superconducting accelerator technology, but with a length of 3.4 km and three undulator beamlines leading to eventually 10 experimental stations. Construction and commissioning of the machine has just recently been completed with a total cost of around 1.22 billion Euros. First user experiments have started in September 2017 [28].

A comparison of the different machine parameters, as seen in Tables 1.1 and 1.2, demonstrates very clearly some of the main advantages and disadvantages of these large accelerators: on the one hand extremely high peak brilliance, especially with FELs which exceed synchrotron light sources by around 10 to 12 orders of magnitude, can be achieved; yet, on the other hand, high electron energies are required to reach X-ray radiation wavelengths which in turn demands for large and costly facility footprints. The electron beam parameters between the two kinds of accelerator-based light sources can also vary quite considerably with FELs using shorter pulses and hence higher peak currents compared to synchrotrons.

1.3 Compact-Scale Accelerators at DESY and Strathclyde

Due to their reduced size and cost, research into compact-scale accelerators is distributed more strongly across different institutions and countries with the two main concepts currently pursued being plasma acceleration and acceleration with dielectric-based structures.

In this context, the University of Strathclyde in Glasgow is among the main hubs in the UK for research into plasma-accelerator-based radiation sources, both theoretically and experimentally. As part of this, the Scottish Centre for the Application of Plasma-based Accelera-

tors (SCAPA) has opened recently, providing a 1200 m^2 area with three shielded experimental bunkers and seven beamlines. As detailed in Table 1.3, two high power Ti:Sapphire laser systems have been set up and commissioned in 2017, one of them the world's highest average-power laser of its kind, to conduct experiments on

- high quality laser-driven electron plasma acceleration,
- radiation generation within plasma and through synchrotron radiation in undulators [29],
- ion and proton acceleration from solid targets,
- radiobiology and nuclear physics.

This has been complemented by theoretical and experimental work in recent years, among others as part of the ALPHA-X project. An example layout for experiments conducted as part of the project is shown in Fig. 1.3: the main laser wakefield acceleration stage with a gas jet target is followed by a beam transport section, an undulator for radiation generation and various diagnostic components, including a dipole spectrometer for energy. Additionally, the beamline now also features a setup for measuring coherent transition radiation from the electron beam in order to reconstruct its duration [30] (more details in Section 2.4.2). Highlights of the work in recent years include studies on betatron radiation from plasma wakes and its applications [31], the generation of ultrashort electron beams in laser wakefield accelerators (LWFA) [30, 32], energy spread compensation and high brightness generation schemes in plasma acceleration [33, 34] as well as proton acceleration through controlled laser-solid interactions [35].

SCAPA:	**Laser 1**	**Laser 2**
Wavelength [nm]	800	800
Energy [J]	8.75	1.4
FWHM duration [fs]	25	35
Peak power [TW]	350	40
Repetition rate [Hz]	5	10

Table 1.3: Parameters of the two high-power lasers at the SCAPA facility.

Although DESY is historically a centre for conventional accelerator research, recent years have shown increasing activity with regard to novel accelerator techniques with projects hosted in Hamburg including LUX, FLASH-Forward and SINBAD (with ARES and AXSIS).

LUX is an experiment run by a group from the University of Hamburg with the main aim to accelerate high quality electron beams from a laser-driven wakefield accelerator to be used for running a plasma-based Free-Electron Laser. The setup employs the high power laser

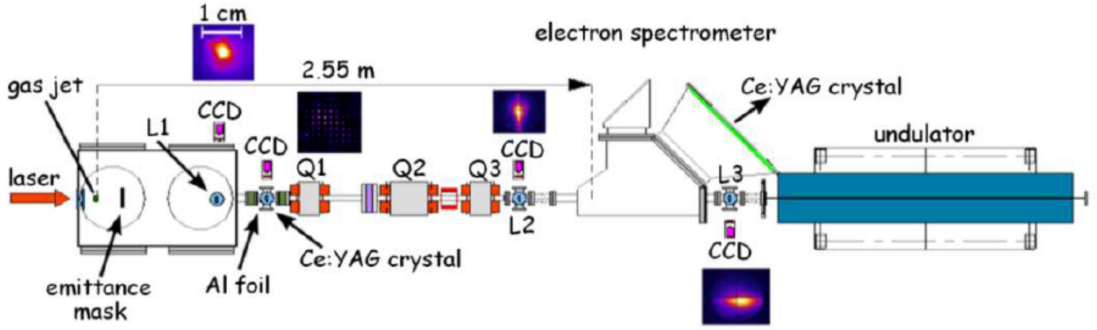

Figure 1.3: Layout for one of the experiments at the ALPHA-X beamline, now transferred to SCAPA. The components marked as Q1, Q2, Q3 represent quadrupole magnets, whereas the parts shown as L1, L2, L3 and CCD depict three LANEX screens as well as multiple CCD cameras, respectively (image reprinted from [36]).

system ANGUS, which is described in more detail in Table 1.4. First electron beam acceleration and first undulator radiation generation were reported in summer 2017 [37], with preparations currently underway for further measurements.

ANGUS Laser	
Wavelength [nm]	800
Energy [J]	5.0
FWHM duration [fs]	25
Peak power [TW]	200
Repetition rate [Hz]	5

Table 1.4: Parameters of the ANGUS high-power laser at LUX, possibly used for future plasma experiments at SINBAD.

The FLASH-Forward (Future-ORiented Wakefield Accelerator Research and Development at FLASH) project has similar aims, but plans to use beam-driven wakefield accelerator technology. Currently under construction, the experiment will employ electron beams from the FLASH accelerator beamline as wakefield drivers in the plasma target [38].

Finally, SINBAD (Short INnovative Bunches and Accelerators at DESY) is an accelerator

ARES: Electron Beam	
Energy [MeV]	100–160
Bunch charge [pC]	0.5–30
RMS bunch length [fs]	0.2–10
Norm. RMS emittance (x,y) [μm]	0.1–1
Repetition rate [Hz]	10–50

Table 1.5: Expected electron beam properties from the ARES linac [39].

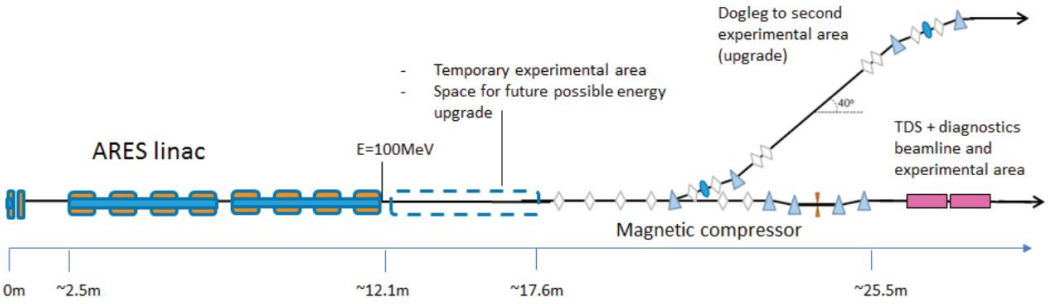

Figure 1.4: Layout of the ARES beamline (image reprinted from [39]).

research & development facility, currently under construction, which in its initial phase will include two larger experiments: ARES (Accelerator Research Experiment at SINBAD) and AXSIS (Frontiers in Attosecond X-ray Science: Imaging and Spectroscopy).

ARES [39–41] is a state-of-the-art linear RF accelerator to be used for experiments on a range of accelerator R & D topics, including dielectric laser acceleration [42–44] as well as external injection into plasma accelerators. As shown in Fig. 1.4, it consists of an S-band photocathode RF-gun which generates electron beams with 5 MeV energy, followed by two 4.2 m long normal conducting S-band accelerating cavities to increase the beam energy to around 100 MeV. This section is followed by a magnetic bunch compressor (more details in Section 2.4.1) and a focusing section, where the electron beam is shaped longitudinally and transversely for its respective applications in the experimental area. Besides the final beam capture and diagnostics section, a second experimental area is planned to split off after the focusing section via a dogleg in the future. Due to the variable photocathode laser duration, different cathode materials and bunch compression techniques, a range of electron beam charges and durations will be achievable, including sub-femtosecond electron beams with picocoulomb (pC) charges, as seen in Table 1.5. Additionally, a novel X-band (8–12 GHz) transverse deflecting structure with variable polarisation is foreseen as a diagnostic capable of measuring full 3D charge densities [45]. Together with very good timing stability with an RMS bunch arrival time jitter below 10 fs [46], this will make ARES a uniquely suited facility for compact accelerator research. The installation of the machine is planned to be finished in 2018 with experiments starting from 2019. For future plasma acceleration experiments it is planned to move the ANGUS laser from the LUX lab to SINBAD subject to funding availability.

AXSIS, also housed at SINBAD, is a collaboration between DESY, CFEL (Centre for Free-Electron Laser Science) and the University of Arizona within a European Research Council Synergy Grant [47]. The goal of the project is to employ terahertz acceleration in dielectric-

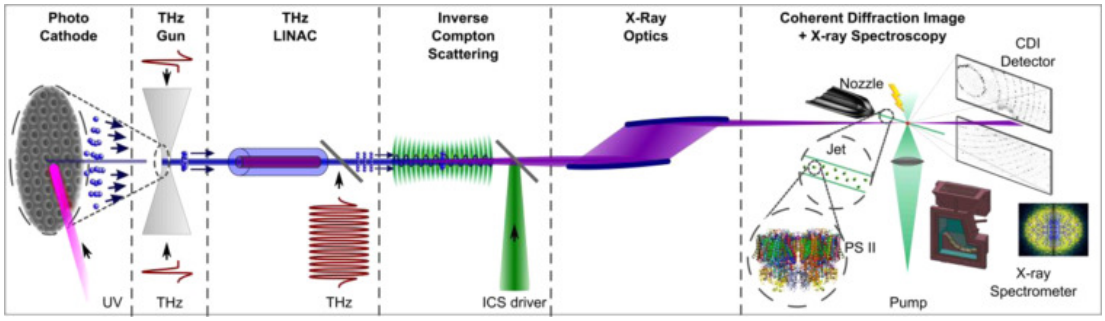

Figure 1.5: Layout of the AXSIS project (image reprinted from [7]).

AXSIS: Electron Beam	
Energy [MeV]	15–20
Bunch charge [pC]	$\leq$3.0
RMS bunch length [fs]	$\leq$1
RMS bunch width (x,y) [μm]	5.0
X-ray pulse from ICS	
Wavelength [nm]	0.103
Photons per pulse	1×10^6–1×10^9
Repetition rate [kHz]	$\leq$1

Table 1.6: Design values for electron beam properties after acceleration and compression in the THz linac as well as for the generated X-ray pulses from inverse Compton scattering (ICS) in AXSIS [7].

loaded waveguides to create a compact, coherent, attosecond X-ray source that can be used for molecular crystallography and time-resolved spectroscopy. The main mechanisms of the experiment are shown in Fig. 1.5: an ultrashort electron beam is generated and accelerated to 15–20 MeV in an electron gun and linac driven by THz instead of radiofrequency waves. Being strongly compressed in the linac to sub-femtosecond duration during acceleration, the electron beam can then generate attosecond radiation through interaction with a laser pulse via Thomson scattering. Using THz and hence higher frequency radiation to provide the electron accelerating field has the main advantage that higher accelerating gradients can be achieved compared to the conventional RF machines thanks to an increase in the field breakdown limit in the cavity. At the same time, THz wavelengths are still sufficiently long compared to the electron beam length for effects of the beam moving within the accelerating field - through phase slippage or synchronisation issues - to be manageable, hence providing a good compromise between compactness and reliability.

1.4 The Accelerator Test Facility at Brookhaven National Laboratory

The work included in this thesis was partly completed at the Accelerator Test Facility (ATF) at Brookhaven National Laboratory [48] (see Part IV). While ATF is foremost a user facility and hence not specifically focused on novel accelerators or radiation generation, the site provides a unique combination of one of the world's highest power CO_2-lasers together with a well established electron linear accelerator, making it very suitable for laser-electron interaction experiments.

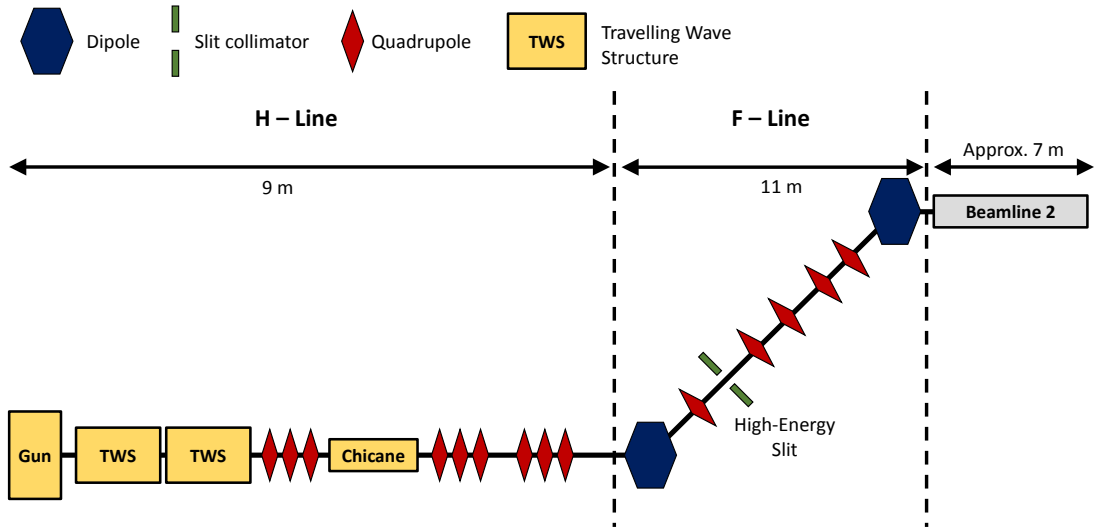

Figure 1.6: Accelerator setup at the Accelerator Test Facility (ATF).

ATF: Electron Beam	
Energy [MeV]	25–76
Bunch charge [nC]	0.05–1.0
RMS bunch length [ps]	0.05–10
CO_2-laser	
Peak power [TW]	≥1.0
Pulse duration [ps]	3.5

Table 1.7: Parameters of electron beamline 2 and the CO_2-laser at the Accelerator Test Facility (ATF).

With detailed parameters given in Table 1.7, the main laser system uses chirped pulse amplification (see Chapter 3.1 for details) through two CO_2-amplification stages to push the

initial micro-Joule, sub-picosecond seed pulse from a Ti-Sapphire pumped optical parametric oscillator to the multi-Joule, picosecond level. The electron beamline, on the other hand, as shown in Fig. 1.6, consists of an S-band photocathode gun and linac followed by a split into two user beamline sections with all experiments discussed in this thesis carried out at beamline 2.

While the accelerated electron beam has an intrinsic energy jitter on the order of 0.1 % only, a controlled energy chirp (i.e., an energy spread correlated with the longitudinal beam profile) can be applied to the bunch through shifts in the electron beam phase in the linac. This can be useful for manipulating the beam further: the bunch can, for example, be compressed to varying degrees using a magnetic compression stage in the H-line (see Fig. 1.6). It is achieved by propagating the electron beam with a chirped energy distribution through a chicane, a combination of four magnetic dipoles that over a fixed distance offset the electron beam path from the main beamline axis. As the beam gets deflected in each dipole, the electrons' path lengths vary depending on their energy in such a way that the back of the beam can catch up with the front thus shortening the whole bunch.

An additional feature of the ATF beamline is its capability for generating electron microbunches from chirped beams. As the electron bunch transverse distribution becomes correlated to energy in the dispersive F-line, a mask placed in this section removes different parts of the beam transversely due to scattering off the mask material. When the beam leaves the dispersive beamline section after the second dipole, this transverse / energy modulation is translated into a temporal microstructure in the electron bunch.

The ATF beamline includes a suite of diagnostics for characterising and controlling the beam. At the end of each user beamline, for example, a dipole spectrometer is placed, while throughout the machine multiple insertable pop-up beam profile monitors are set up, most of which use phosphor or YAG (yttrium aluminium garnet) imaging screens in combination with a CCD (charge-coupled device) camera to read out the transverse electron beam profile.

In the future, a major upgrade for the facility to ATF-II is planned, including improvements in the CO_2-laser power and electron beam energy from the linac to 100 TW and 100 MeV or more, respectively.

Chapter 2

Basic Concepts of Particle Accelerators

This chapter defines the main variables used throughout the thesis and reviews the most relevant processes in particle accelerators. Additionally, a short overview over the main alternatives to the techniques presented in this work in terms of generating and measuring sub-femtosecond electron beams is provided.

2.1 Introduction to Accelerator Systems

An electron in an accelerator can be defined by its six-dimensional (6D) phase-space with coordinates $\mathbf{r}$=[x,p_x,y,p_y,z,E]^T, where (z,E) defines the 2D longitudinal phase-space and (x,p_x,y,p_y) describes the 4D transverse phase-space. In this context, x and y are the horizontal and vertical distances from the electron reference trajectory, while z defines the distance along the latter in the main direction of acceleration and E is the electron energy. p_x, p_y, p_z are the particle momenta in the x-, y- and z-directions, respectively. The angle of the electron trajectory is defined by the horizontal and vertical divergence $\mathrm{x}' = \mathrm{p}_x/\mathrm{p}_z$ and $\mathrm{y}' = \mathrm{p}_y/\mathrm{p}_z$.

In the following, we generally consider not single electrons, but bunched particle beams which are characterised by a distinct, finite shape both in the longitudinal and transverse dimensions. In this case, the individual electron properties can be extended to the whole beam by defining RMS (root mean square) quantities:

$$\begin{aligned} \sigma_z &= \sqrt{\langle z^2 \rangle}\,, \qquad \sigma_E = \sqrt{\langle E^2 \rangle}\,, \\ \sigma_x &= \sqrt{\langle x^2 \rangle}\,, \qquad \sigma_{x'} = \sqrt{\langle x'^2 \rangle}\,, \\ \sigma_y &= \sqrt{\langle y^2 \rangle}\,, \qquad \sigma_{y'} = \sqrt{\langle y'^2 \rangle} \end{aligned} \tag{2.1}$$

with $\langle\ \rangle$ denoting the second moment of the particle distribution, with N the number of electrons in the bunch, given by

$$\langle A^2 \rangle = \frac{\sum A_i^2}{N} - (\frac{\sum A_i}{N})^2 \,. \tag{2.2}$$

Similarly, the distribution mean for these quantities can be calculated with

$$\bar{A} = \frac{\sum A_i}{N} \,. \tag{2.3}$$

In the case of the mean beam energy, $\bar{E}$ will be denoted as E for simplicity in the remainder of the thesis, unless specified otherwise. The energy spread is often described in relative terms with respect to this mean energy as $\Delta E/E$ where ΔE is the RMS energy spread σ_E, unless specified otherwise.

Another variable that is usually important for an electron beam is its current which is defined with two quantities in this thesis: the full bunch current is given by the ratio of beam charge Q to full beam duration

$$I_b = \frac{Q}{(t_{max} - t_{min})} \,, \tag{2.4}$$

whereas the peak current is defined as the maximum of the current distribution projected along the longitudinal beam coordinate.

It should be noted that this thesis in some cases quotes a 2D or 1D charge density, λ_Q and σ_Q. This is a feature of particle-in-cell simulations as the simulation technique typically used to study plasma accelerator systems: due to the calculation of the macroparticle charges in such codes (more in Section 3.5) being based on electron density rather than absolute charge, in 1D and 2D simulations only an equivalent of an actual beam charge can be calculated based on the line or slab geometry of the simulation space. These charge density values are thus defined as

$$\begin{aligned} \lambda_Q &= \sum_i q_i \ e \ n \ dA \,, \\ \sigma_Q &= \sum_i q_i \ e \ n \ dL \end{aligned} \tag{2.5}$$

with q_i the normalised charge of each macroparticle, n the density defined in the simulation and dA, dL the area, length of each cell in the simulation, respectively. The product of the last three terms represents the normalisation factor that converts the macroparticle unit into SI units.

A final concept that should be mentioned is transfer matrices. In radiofrequency (RF) accelerator systems, the dynamics of the 6D phase space of electrons and particle beams are

typically expressed through a matrix of the form

$$\mathbf{R} = \begin{bmatrix} R_{11} & R_{12} & R_{13} & R_{14} & R_{15} & R_{16} \\ R_{21} & R_{22} & R_{23} & R_{24} & R_{15} & R_{26} \\ R_{31} & R_{32} & R_{33} & R_{34} & R_{15} & R_{36} \\ R_{41} & R_{42} & R_{43} & R_{44} & R_{15} & R_{46} \\ R_{51} & R_{52} & R_{53} & R_{54} & R_{15} & R_{56} \\ R_{61} & R_{62} & R_{63} & R_{64} & R_{15} & R_{66} \end{bmatrix} . \tag{2.6}$$

The effect of a specific accelerator component on an electron can then be calculated via a matrix equation

$$\mathbf{r}_f = R\ \mathbf{r}_i\,, \tag{2.7}$$

where $\mathbf{r}_{i,f}$ are the initial and final 6D phase-space coordinates of the particle, respectively. The transfer matrix element R_{56}, for example, expresses in this case how a specific beamline element correlates the initial electron energy with its longitudinal coordinate after transport through the device.

2.2 Longitudinal Beam Dynamics

The dynamics of an electron beam in accelerator systems are generally dominated by its interaction with electric and magnetic fields $\mathbf{E}$ and $\mathbf{B}$ which can be described by the Lorentz force equation

$$\mathbf{F} = -e(\mathbf{E} + \mathbf{v} \times \mathbf{B})\,, \tag{2.8}$$

where $\mathbf{v}$ is the electron velocity and e the elementary charge of an electron. In the longitudinal direction, this is expressed as an acceleration due to an applied longitudinal electric field E_z^a where the energy of the beam changes as

$$\frac{dE}{dz} = \frac{d}{dz}(mc^2\beta^2\gamma) = -eE_z^a \tag{2.9}$$

with m the electron mass, c the speed of light in vacuum, $\beta = v/c$ the relative electron velocity and $\gamma = (1-\beta^2)^{-1/2}$ the corresponding Lorentz factor. Note that for relativistic beams β becomes very close to 1 and is thus often omitted.

In conventional accelerators, a radiofrequency wave is coupled into a metallic cavity in such a way as to generate a longitudinal electric field $E_z^a = E_m cos(\phi)$ (with ϕ the RF phase) that

co-propagates with the electron beam at a fixed phase velocity, similar to the electron velocity, and hence interacts with the beam. In plasma acceleration the longitudinal field structure can generally be described in a similar way by a sinusoidal shape, but with a much shorter wavelength. Due to these small spatial scales as well as fast and possibly more nonlinear dynamics, however, there is a number of additional effects to be taken into account, which will be discussed in more detail in Chapter 3.

Space charge effects

Another factor that can influence the longitudinal dynamics of the electron beam, in particular for short, dense bunches, is its own space-charge field, i.e., the field acting on each particle in the beam due to the presence of the other beam electrons. The longitudinal space-charge field for an electron beam with charge density $\rho(z, x, y)$ can be found from Poisson's equation: $\nabla^2\psi_{sc}(z, x, y) = -\rho(z, x, y)/\epsilon_0$. For a parabolic line charge density in the longitudinal direction, $\rho_L(z) = \rho_{L,0}(1 - z^2/b^2)$ with b half the full beam length, a linear, analytic expression for the longitudinal space-charge field is thus found [49]:

$$E_z^{sc} = \frac{mc^2\beta^2\gamma^3}{eb^3} K_{sc,L}\ z\,. \tag{2.10}$$

The longitudinal perveance $K_{sc,L}$ is a good measure for the strength of the space-charge field in this context and is defined as

$$K_{sc,L} = \frac{3gNr_c}{2\beta^2\gamma^5} \tag{2.11}$$

with $r_c = e^2/(4\pi\epsilon_0 mc^2)$ the classical electron radius, N the number of electrons in the bunch and g a geometry factor dependent on the aspect ratio of the beam. Note that the longitudinal space-charge field scales inversely with γ^2; consequently space-charge effects become less relevant for highly relativistic beams [49].

2.3 Transverse Beam Dynamics

One of the most important quantities related to the transverse phase-space of the electron beam and a good measure for the beam quality is the beam emittance. The normalised transverse RMS emittance is defined as

$$\epsilon_{n,x} = \frac{1}{mc}\sqrt{\langle x^2\rangle\langle p_x^2\rangle - \langle xp_x\rangle^2} \tag{2.12}$$

with $\langle xp_x \rangle = \left[\sum(xp_x)/N\right] - \left[(\sum x \sum p_x)/N^2\right]$ the correlation between the phase-space variables. Related to this, the geometric emittance can be defined as

$$\epsilon_x = \frac{\epsilon_{n,x}}{\bar{p_z}} \,. \tag{2.13}$$

Another way to describe the transverse beam distribution is in trace-space which relates beam divergence and position instead of momentum and position. In this coordinate space, the normalised trace-space emittance can be calculated:

$$\epsilon_{tr,n,x} = \frac{\bar{p}_z}{mc} \sqrt{\langle x^2 \rangle \langle x'^2 \rangle - \langle xx' \rangle^2} \,. \tag{2.14}$$

For monoenergetic beams trace-space and phase-space emittance are equal, as $p_z = \bar{p}_z$, but for beams with large energy spread the two can differ significantly. For this reason, although this energy spread-related effect is only observed in the studies presented in Chapter 4, in the remainder of this thesis the phase-space emittance definitions, based on Eqs. (2.12) and (2.13), are used as more meaningful measures [50].

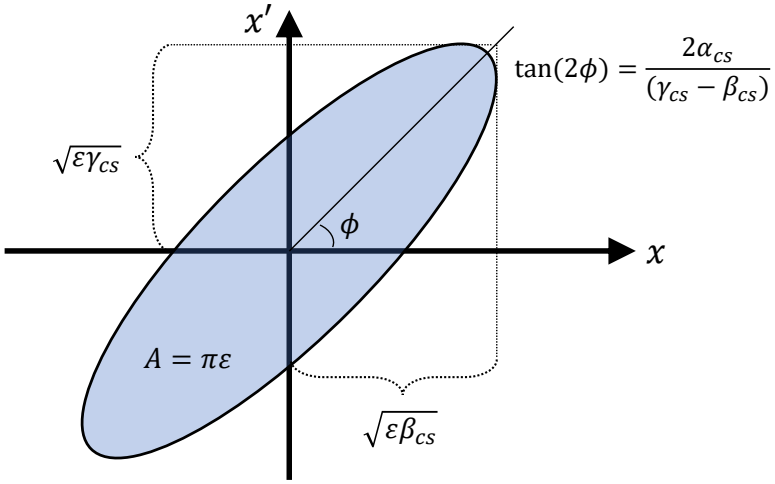

Figure 2.1: Ellipse that defines the beam emittance and Twiss parameters in phase-space and trace-space.

Based on these definitions the particle beam can be described as an ellipse in trace-space the area of which is proportional to the beam emittance, as seen in Fig. 2.1. The ellipse shape, on the other hand, can be described by the three Courant-Snyder or Twiss parameters:

$$\alpha_{cs} = -\frac{\langle xx' \rangle}{\epsilon_{tr,x}} \,, \quad \beta_{cs} = \frac{\langle x^2 \rangle}{\epsilon_{tr,x}} \,, \quad \gamma_{cs} = \frac{\langle x'^2 \rangle}{\epsilon_{tr,x}} \,, \tag{2.15}$$

where $\beta_{cs}\gamma_{cs} = 1 + \alpha_{cs}^2$ and $\epsilon_{tr,x} = \epsilon_{n,tr,x}(mc/\bar{p_z})$. The β_{cs}-function defines the beam size, the γ_{cs}-function the beam divergence and α_{cs} is correlated to the slope of the ellipse with $\alpha_{cs} = 0$ at the beam focus [49–52].

Beam propagation in a focusing channel

An important system in the context of transverse beam dynamics, both for conventional and plasma accelerators, is the propagation of an electron beam in a focusing channel, which can be described by Courant-Snyder theory [53]. Assuming an axisymmetric system with paraxial particle motion, negligible space charge as well as beam energy spread, the motion in the transverse dimension x can to first order be expressed as

$$x'' + K(z)x = 0\,, \tag{2.16}$$

where $x'' = d^2x/dz^2$ is the displacement from the beam axis along x and K(z) is the focusing strength of the channel assumed to be dependent only on the longitudinal coordinate z. For a laser wakefield accelerator, the plasma always acts as a radially symmetric focusing channel with a focusing strength that can be defined as

$$K(z) = \frac{e}{\gamma mc^2}\frac{\partial(E_r - cB_\theta)}{\partial r}\,. \tag{2.17}$$

More generally, Eq. (2.16) has solutions of the form

$$x(z) = Aw(z)cos(\phi(z) + \psi)\,, \tag{2.18}$$

where both the amplitude and phase have a component that is constant and one that is dependent on z. This is still valid, if the relation $\phi' = -w^{-2}$ is assumed (see [53]), which, together with Eq (2.18), allows to transform Eq. (2.16) into a differential equation of the amplitude function $w(z)$

$$w'' + Kw - \frac{1}{w^3} = 0\,. \tag{2.19}$$

Having a similar form to the envelope equation for a beam with emittance of elliptic shape, a connection to the previously defined Courant-Snyder parameters can be made:

$$\begin{aligned} \beta_{cs} &= w^2\,, \quad \alpha_{cs} = -ww' = -\frac{\beta'_{cs}}{2}\,, \\ \gamma_{cs} &= \frac{1}{w^2} + w'^2 = \frac{1+\alpha_{cs}^2}{\beta_{cs}}\,. \end{aligned} \tag{2.20}$$

Moreover, Eq (2.19) can be re-written in terms of β_{cs}:

$$\beta_{cs}'' - \frac{(\beta_{cs}')^2}{2\beta_{cs}} + 2K(z)\beta_{cs} - \frac{2}{\beta_{cs}} = 0\,. \tag{2.21}$$

There are a number of special cases for which Eq. (2.21) can be solved analytically. In vacuum propagation, for example, with K=0, the following solution is found

$$\alpha_{cs}(z) = \frac{z_0 - z}{\beta_{cs,0}}, \quad \beta_{cs}(z) = \beta_{cs,0} + \frac{(z-z_0)^2}{\beta_{cs,0}}, \quad \gamma_{cs}(z) = \frac{1}{\beta_{cs,0}}\,, \tag{2.22}$$

where z_0 and $\beta_{cs,0}$ are the initial position and value of the β_{cs}-function, respectively.

For a positive, constant or slowly varying value of K, the following β_{cs}-function can be derived:

$$\beta_{cs}(z) = \beta_{cs,0}\cos^2(\sqrt{K}z) + \frac{1}{\beta_{cs,0}K}\sin^2(\sqrt{K}z)\,. \tag{2.23}$$

As can be seen from this last equation, but also from Eq. (2.16), for a (close to) constant focusing channel the beam envelope oscillates in the transverse direction with the betatron frequency $\omega_\beta = c\sqrt{K}$ as the beam propagates through the channel. In phase-space this corresponds to a rotation of the beam ellipse while its area remains preserved.

It is, however, possible that the focusing strength K varies across the beam, for example for a beam with finite energy spread due to the energy dependence of K or also if, as in some plasma cases, K is a function of the longitudinal beam coordinate. In such scenarios, different parts of the beam perform betatron oscillations with different frequencies which leads to a spread of the beam ellipse, so-called betatron decoherence, as different beam slices rotate differently, like shown in Fig. 2.2. Although the area of each of these slices is preserved, the process as a whole leads to an increase in the beam trace-space area and hence a rise in projected emittance which can be very detrimental for the beam quality.

The best strategy to avoid emittance growth due to betatron decoherence, is to subdue the betatron oscillations themselves which can be achieved by *matching* the beam to the focusing channel. This means that the intrinsic defocusing of the bunch due to its emittance is exactly matched in amplitude by the focusing forces of the channel such that $\beta_{cs}'' = \beta_{cs}' = 0$. Applied to Eq. (2.21) and (2.20), this leads to a set of matched parameters

$$\alpha_{cs,m} = 0, \quad \beta_{cs,m} = \frac{1}{\sqrt{K}}, \quad \gamma_{cs,m} = \sqrt{K}\,, \tag{2.24}$$

where the matched beam size is given by $\sigma_{m,x} = \sqrt{\beta_{cs,m}\epsilon_{n,x}/(\beta\gamma)}$ [49, 51–53].

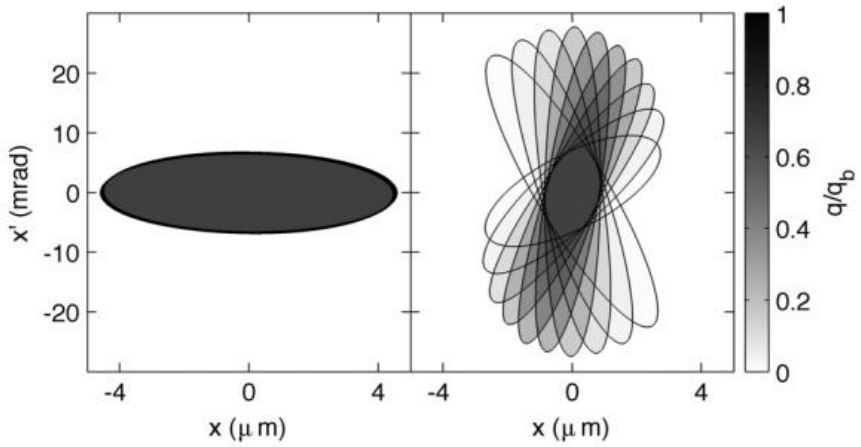

Figure 2.2: Effect of betatron decoherence on the electron beam trace-space. As different slices of the electron beam rotate in trace-space with different frequencies, the beam distribution spreads in trace-space and the projected beam emittance grows. The images show the initial (left) and final (right) trace-space distribution for an electron beam influenced by betatron decoherence with the color scale depicting relative charge (image reprinted from [54]).

Space charge effects

Finally, for ultrashort beams, as considered in this thesis, also space-charge effects in the transverse direction should be mentioned. Here the effect consists of a defocusing from the electric field of the charged beam as well as, for relativistic electrons, focusing due to the magnetic field generated from the beam current which partially compensates the electric field defocusing. Based on Gauss' and Ampere's laws and assuming a radially constant charge density $\rho(z) = I(z)/(\pi b^2 \beta c)$ (with b beam radius and I(z) beam current), a simple model of the effective transverse space-charge field, considering only transverse dynamics, can be expressed as [49]

$$(E_r^{sc} - cB_\theta^{sc}) = \frac{\beta^2 \gamma mc}{eb^2} K_{sc}\, r \tag{2.25}$$

and K_{sc} the generalised perveance

$$K_{sc} = \frac{2I(z)}{\beta^3 \gamma^3 I_0}\,, \tag{2.26}$$

where $I_0 = 4\pi\epsilon_0 mc^2/e \sim 17\,\mathrm{kA}$ is the Alfven current and ϵ_0 is the vacuum permittivity [49].

2.4 Status of Sub-Femtosecond Electron Bunch Generation and Measurement Techniques

Technological development in terms of the generation and measurement of ultrashort electron bunches is closely interconnected, as either one requires the other to advance the state-of-the-art further. With both measured bunch lengths and bunch length diagnostic resolutions at the single femtosecond to sub-femtosecond level today, it becomes difficult to prove the generation of shorter beams due to the lack of adequate measurement technology. At the same time the development of higher resolution diagnostics is challenged by generating adequately short test beams. In the following sections a number of possible techniques will thus be introduced for both of these aspects in order to give a short overview over possible alternative techniques to what is presented in the main body of this thesis.

2.4.1 Sub-Femtosecond Bunch Generation

Methods for the generation of ultrashort, accelerated electron beams can be divided into two main sub-categories: those for generating isolated sub-femtosecond beams and those to produce trains of sub-femtosecond electron microbunches. The majority of recent publications regarding the latter is based around laser-based modulation of electron beams as well as high power laser interaction with shaped underdense or overdense plasma targets, whereas isolated attosecond beams may be produced using techniques, such as bunch compression or specialised laser wakefield acceleration (LWFA) scenarios:

- **Modulation of the electron beam through laser interaction:** The idea behind laser modulation to form attosecond bunch trains is that, under the right circumstances, usually through co-propagation in an undulator, the oscillating electric field of an optical wavelength laser pulse imprints an energy modulation onto the electron beam. Through propagation in a magnetic chicane, where the path length depends on electron energy, this modulation can then be converted into a microbunching in the density of the beam. An experimental demonstration of this technique has been published in 2008 by Sears et al. [55] using an inverse Free-Electron Laser setup, as depicted in Fig. 2.3a, where a train of microbunches of 410 attoseconds full width at half maximum (FWHM) length was measured. More recent ideas include, for example, stochastic slicing of an electron beam with time-dependent gates formed from laser waves [56] as well as beam modulation in a laser wakefield accelerator through interaction of the self-injected electron bunch with the drive laser [57].

- **Interaction of intense laser pulses with shaped targets:** With regard to shaped target interaction, various different target shapes, densities and geometries have been suggested both for generating single and multiple bunches [8, 58–65]. Using the field of an ultraintense laser pulse itself to accelerate and rip electrons out of a target in microbunches spaced with the laser wavelength, in most cases the emitted bunches exhibit tens to hundreds of attoseconds duration, but at the same time large divergences and broad spectra. To the author's knowledge, the only experimental demonstration of this type of bunch train generation method was shown in 2003 by Baton et al. [66] where coherent transition radiation suggesting a sub-micrometre microbunched beam was observed after interaction of a laser pulse with a solid target.

- **Bunch compression:** Bunch compression is commonly used in conventional RF accelerator setups where bunch durations on the order of single to tens of femtoseconds can be reached (e.g. [67]) using either velocity bunching or magnetic compression. The first of these two methods relies on the beam tail catching up to the head due to velocity differences in a chirped (in other words with an energy gradient along z), non-relativistic beam, which can be generated by placing the electron beam on the slope of the RF accelerating field. Magnetic compression, on the other hand, as shown in Fig. 2.3b, uses a chicane or similar dispersive beamline section with energy dependence on the electron path length, so that also relativistic electron beams with an energy chirp can be compressed based on the beam tail travelling a shorter distance than the head. Optimised compression designs have been presented in recent years by e.g. [68], [69] and [70] where hybrid compression designs or compensation of nonlinear phase-space distortions were used to demonstrate sub-femtosecond bunch durations in simulations. Another approach has been to reach stronger velocity bunching by working with higher accelerating field frequencies that can in principle provide stronger field gradients and hence stronger chirping. This has been proposed for THz as well as optical frequencies as part of the AXSIS project and by Sell et al. [71], respectively.

- **LWFA schemes:** Plasma accelerators exhibit both in experiment and simulation the generation of naturally quite short electron beams on the order of few femtoseconds in RMS duration [30, 72–74]. Consequently, the presented ideas for pushing this into the attosecond regime, currently all simulation-based, have been quite varied. One option presented by [75] (more on this in Chapter 4) and [32, 76] is to self-inject ultrashort electron beams in the plasma in a very controlled way, such as by shaping the plasma

density or laser pulse interaction with the plasma. Contrary to that, [77] has proposed to microbunch the electron beam based on a controlled decoherence of the betatron oscillation frequencies of different longitudinal slices, whereas [78] has considered a bunch compression setup in the plasma wake similar to velocity bunching in RF accelerators.

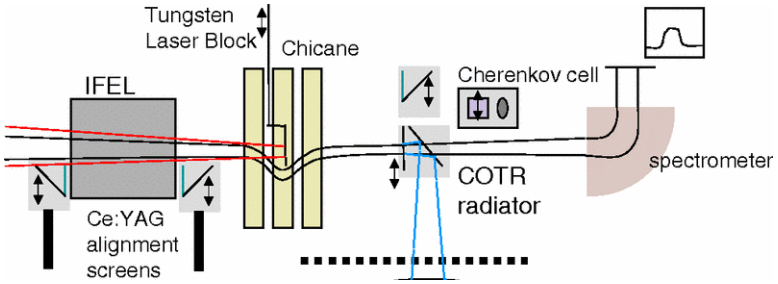

(a) Inverse Free-Electron Laser setup (image reprinted from [55]).

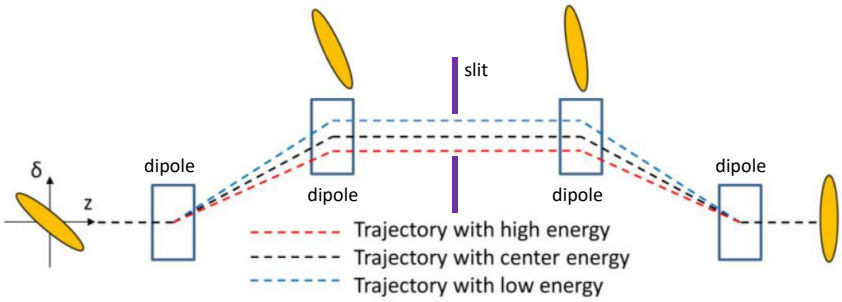

(b) Magnetic bunch compression setup (image adapted from [41]).

Figure 2.3: Schematic principle of two of the described mechanisms for generating sub-femtosecond electron bunches.

2.4.2 Sub-Femtosecond Bunch Profile Measurement

With regard to longitudinal bunch profile diagnostics, there are two different cases to consider: the measurement of sub-femtosecond beams and the measurement of beams with sub-femtosecond resolution. While the second is a requirement for the first, diagnostic devices for ultrashort electron beams have a number of additional technical challenges to handle, such as control over timing jitter (see more in Section 9). For the discussion here, the emphasis will, however, be restricted to resolution only. Whereas long beam profiles at the picosecond to nanosecond level can be measured directly using, for example, wall current monitors or single

photon counters for the radiation generated from the electron beam, most longitudinal bunch length diagnostics with femtosecond resolution or below are based on two main principles: either the fields generated by the electron beam are measured in some way or a mapping of the longitudinal profile onto another dimension of the beam phase-space is recorded [79].

The most common field-based diagnostic methods include electro-optical measurements, streaking cameras and coherent transition radiation measurements, all of which are based on the concept that the longitudinal electron beam profile is accurately represented by the profile of electromagnetic fields generated by it. Contrarily, phase-space mapping techniques, which are characterised by the longitudinal beam profile being encoded in another electron beam dimension, often the transverse or energy distribution, include transverse deflecting structures (TDS), zero-phasing and a range of novel mapping techniques.

- **Electro-optical measurement:** In electro-optical setups, such as depicted in Fig. 2.4a, the Coulomb field of the electron beam is measured by mapping it onto a probe laser pulse through interaction with an electro-optic crystal. As the electron beam passes by the crystal, its field induces a change in polarising properties in the latter which in turn lead to phase variations in the co-propagating laser pulse as it traverses the crystal. The encoded beam profile is found from analysing the probe laser either by translating the phase modulation in the pulse into a measurable intensity modulation (spectral decoding) or by cross-correlation with an equivalent laser pulse from which the beam profile can be extracted (temporal decoding). The method is non-invasive, yet only suitable for high energy beams, as resolution is affected, among others, by the electron beam Lorentz factor. Additionally, the minimal measurable beam duration also depends on the response function of the nonlinear crystal and the pulse length of the probe laser. At least the former provides a fundamental limitation which has lead to measured RMS lengths down to 60 fs with optimised resolution on the order of 28 fs [80, 81], but does not make this technique suitable for sub-femtosecond beams.

- **Streaking cameras:** Streaking describes the deflection of electrons with an angular transverse kick the strength of which depends on their longitudinal position within the beam. This effect allows the beam temporal profile to be encoded in its transverse distribution which in turn can be measured easily on a beam profile monitor. In a streak camera incoherent radiation from the electron beam, e.g. transition radiation, is employed to generate photoelectrons, with a distribution equivalent to that of the beam, which in turn can be streaked by an RF or THz radiation field, as depicted in Fig. 2.4b. The resolution of this single-shot, possibly non-invasive measurement technique is limited by

the photoelectron energy spread as well as potential effects from the optical setup up to the generation of the photoelectrons. Conventional streak cameras thus have resolution on the order of hundreds of femtoseconds, mostly due to the initial photoelectron spread [82], but this has been shown to be reducable to tens of femtoseconds [83–85] or single femtoseconds [86] through placing the whole photocathode into the streaking field.

- **Coherent transition radiation (CTR) measurements:** Coherent transition radiation is emitted by an electron beam at wavelengths longer than the beam length when hitting a material transition, such as a thin foil. As the spectrum of this radiation depends on the so called bunch form factor, related to the bunch charge distribution, its measurement, e.g. with a scanning interferometer, can be used for estimating the electron beam duration. Additionally, it is possible to reconstruct the full longitudinal beam profile from this technique, requiring, however, more complex phase retrieval algorithms and, at least for short beams, the measurement of a broad spectral range. CTR measurement is a single-shot, possibly non-destructive technique which has already demonstrated very high resolution at the single femtosecond to sub-femtosecond level (e.g. [30, 55, 72, 87, 88]). It is also, compared to some of the RF cavity-based techniques, more cost-efficient and hence suited especially for compact accelerator setups, such as plasma accelerators.

- **Transverse deflecting structures (TDS):** In transverse deflecting structures the electron beam is streaked directly instead of via its radiation field through a time-varying deflecting field. As the electrons in the beam, such as seen in Fig. 2.4c, experience an angular deflection dependent on their longitudinal bunch coordinate the longitudinal profile is mapped onto the transverse beam distribution which in turn can be easily measured. TDS setups are high cost, single-shot, destructive diagnostic devices, but they can be combined well with a spectrometer for recording the full longitudinal phase-space of an electron beam. There is no fundamental limitation of this technique to improve its resolution to the attosecond regime; factors, such as increasing beam wakefields and restrictions on beam and measurement screen sizes, however, will be challenges to tackle for ultrashort beam measurements. S-band deflecting cavities generally have demonstrated resolutions of tens of femtoseconds [89, 90], while X-band deflectors have reached single femtoseconds to sub-femtoseconds [39, 91, 92]. Moreover, there are also concepts presented for decreasing the field wavelengths further hence achieving stronger streaking fields. These include proposals for a plasma TDS [93], a THz-based TDS [94, 95] or using the electron beam's own wakefield in a dielectric lined or corrugated waveguide for streaking [96].

- **Zero-phasing:** In zero-phasing the longitudinal beam profile is mapped onto the energy distribution of the bunch. From Fig. 2.4d it can be seen that by propagating through an RF accelerating cavity at the zero-crossing, i.e., at the phase where the field changes sign, the electrons experience a change in energy the sign and amplitude of which is dependent on their position within the beam. An analysis of the energy distribution with a dipole spectrometer allows the measurement of this transformed beam profile. This concept has the advantage that it requires components often already present in conventional beamlines, thus saving costs. Yet, limitations to the achievable resolution can be caused by uncorrelated energy spread and incoming time-energy correlations, such that measured resolutions of 30 fs [97], and simulated values down to 0.3 fs [82, 98] have been reported.

- **Other techniques:** More recent papers on phase-space mapping methods have proposed employing the effect of an electron beam interacting with a high power laser pulse in an undulator: by using a specific laser mode, a strong streaking effect can be achieved, as [99] and [100] (see details in Part IV) propose. On the other hand, the laser interaction can also be used to create a time-dependent energy modulation in the electron beam which can be measured and used for longitudinal profile reconstruction either directly with a spectrometer [101] or through conversion into a spatial modulation in a chicane [102]. Whereas the last proposal has been shown experimentally to allow for 40-50 fs resolution, the other concepts remain so far untested, but with an expected resolution on the order of hundreds of attoseconds from simulations. Another proposed method by [103] and [104], specifically for LWFA-accelerated beams, uses the interaction with the drive laser pulse in the LWFA setup in the plasma to generate a measurable, time-dependent energy modulation and has demonstrated single femtosecond resolution in first experiments. Finally, a last technique is the three-phase method: here the energy spread of an electron beam is measured, e.g. via a dipole spectrometer, for at least three different phases in an accelerating cavity. This data can then be used to calculate the initial energy spread and bunch duration based on the transfer matrix equations for the system. While the required setup is very simple with most components already found in conventional accelerators, the method does not take into account space-charge effects making it possibly unsuitable for short, low-energy beams. Published simulations show the successful measurement of bunch lengths on the order of 100 fs with an S-band cavity [105] and 6 fs with a THz-driven dielectric loaded waveguide [106].

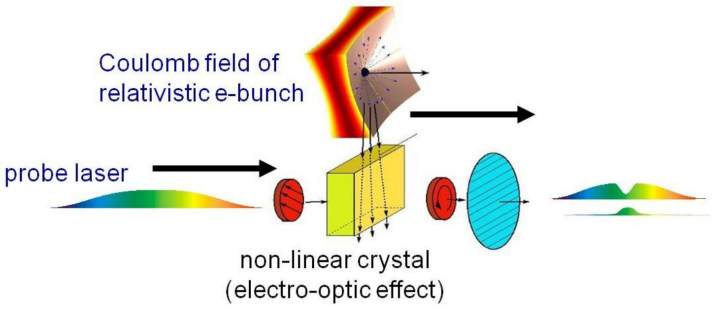

(a) Electro-optical measurement (image reprinted from [79]).

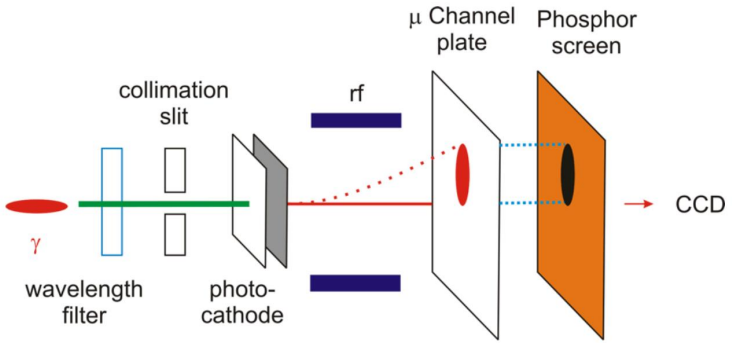

(b) Streaking camera (image reprinted from [79]).

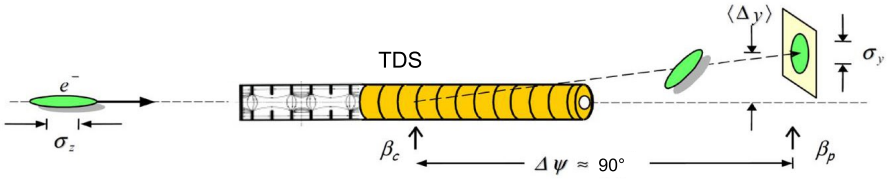

(c) Transverse deflecting structure (TDS) (image reprinted from [79]).

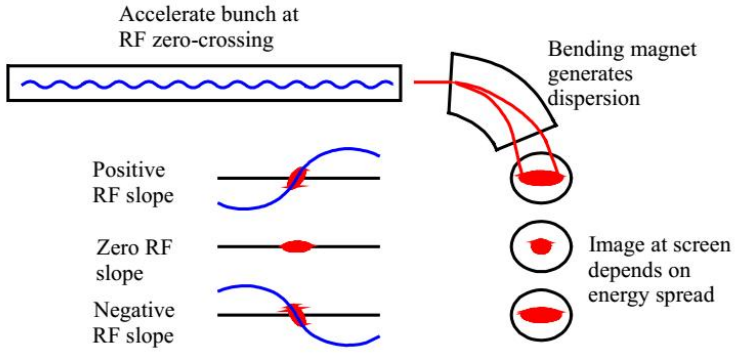

(d) Zero-phasing (image reprinted from [82] copyright 2001 IEEE).

Figure 2.4: Schematic principle of four of the described mechanisms for measuring longitudinal electron bunch profiles. The setup for CTR measurements is typically a simple interferometer or grating spectrometer to measure the radiation spectrum and is hence not depicted here.

Chapter 3

Theory of Laser Wakefield Acceleration

In this chapter the main concepts and theory of laser wakefield acceleration (LWFA) are reviewed. This includes a discussion of high power laser pulses and their role in LWFA, plasma waves in the linear, weakly nonlinear, nonlinear laser-driven and beam-driven regime, injection mechanisms, the drive laser evolution in the plasma and particle-in-cell simulation codes.

3.1 High Power Lasers and the Ponderomotive Force

An essential requirement that made laser wakefield acceleration realisable was the development of high-power, short-duration laser pulses. The technique to generate such pulses, chirped pulse amplification (CPA), was first proposed in the context of laser pulses in 1985 by Strickland and Mourou [107]. As Fig. 3.1 shows, it achieves amplification of fs- to ps-long laser pulses by first stretching the pulse, then amplifying and finally re-compressing it. A dispersive optical component, such as a set of gratings or optical fibre, stretches the beam. With the low frequency components travelling a shorter path than the high frequency parts of the pulse, it becomes chirped and increases in duration. This simultaneously leads to a decrease in pulse peak power allowing the beam to be amplified more strongly without nonlinear distortions of the beam (for example through self-focusing) or damage to the amplifying components. Having gained higher energy through amplification, the laser pulse is then compressed again by reversing the effect of the stretcher section, whereby a large pulse radius are required to avoid damage to the compression stage. Technologies based on this process have enabled the development of laser pulses with up to petawatt peak power in recent years (e.g. [108, 109]).

The pulses generated from such high power laser facilities can often be described as Gaus-

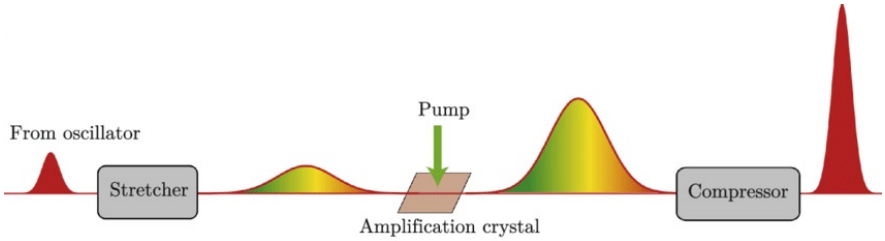

Figure 3.1: General principle of chirped pulse amplification (CPA) (image reprinted from [110]).

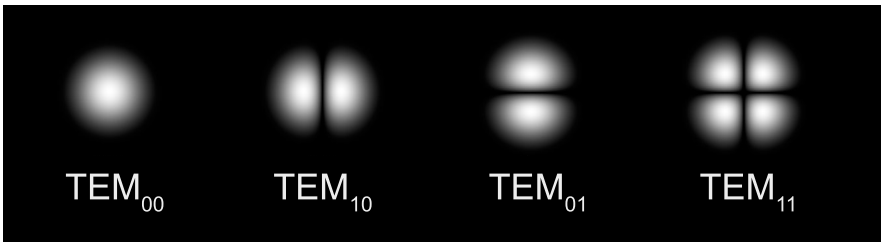

Figure 3.2: Intensity distribution of TEM-modes of different order (image adapted from [111]).

sian beams, based on their transverse intensity distribution following the TEM_{00} (transverse electromagnetic) laser mode, as shown in Fig. 3.2 [112]. The electric field for such a laser pulse can be described, assuming polarisation in the x-direction, by

$$\mathbf{E}(r,z) = E_0\ \hat{\mathbf{x}}\frac{w_0}{w(z)}\exp\left(-\frac{r^2}{w(z)^2}\right)\ \exp\left(-i(kz + k\frac{r^2}{2R(z)} - \phi(z))\right) \tag{3.1}$$

with r the radial distance from the beam axis, $k = 2\pi/\lambda$ the laser wavenumber and ϕ an extra phase term. $R(z) = z(1 + (z_R/z)^2)$ is the radius of curvature of wavefronts at z and the transverse laser spot size evolves along z as

$$w(z) = w_0\sqrt{1 + (\frac{z}{z_R})^2}\,. \tag{3.2}$$

Here w_0 is the spot radius at the laser focus point and $z_R = \pi w_0^2/\lambda$ defines the Rayleigh range which describes the distance over which the laser pulse has defocused to a value of $\sqrt{2}$ times its minimum spot size. Note that the laser transverse distribution can also take higher-order modes, as shown in the laser intensity distributions in Fig. 3.2; these are typically considered in special cases only, though (see e.g. Part IV).

For the profile of the laser field in the longitudinal direction, this work assumes either a Gaussian $\exp(-(z - z_0)^2/L_{rms}^2)$ or a $\sin^2$ shape of the form $\sin^2((z - z_0)\ \pi/L - \pi/2)$ with z_0 the position of the pulse centre. While the latter is characterised by L as the full length of the laser pulse, in the Gaussian case, the length - or, for the transverse profile, width - is defined

either by the $1/e^2$ radius or the full width at half maximum (FWHM) of the laser intensity profile given, respectively, as L_{rms} (transverse: w_0) and $L_{FWHM} = \sqrt{2\ln 2}\, L_{rms}$ (transverse: $\sqrt{2\ln 2}\, w_0$).

An important quantity with which to describe the laser intensity or strength is the normalised vector potential $\mathbf{a} = e\mathbf{A}/(mc^2)$, where $\mathbf{A}$ is related to the electric and magnetic field as $\mathbf{E} = -\partial\mathbf{A}/\partial(ct)$ and $\mathbf{B} = \nabla\times\mathbf{A}$, respectively. The amplitude of the normalised vector potential a_0 can thus be described through the laser electric field E_L and laser angular frequency ω as $a_0 = eE_L/(mc\omega)$. Assuming a linearly polarised laser pulse with a Gaussian beam profile, a_0 can also be calculated in practical units from the laser power P_L in gigawatts (GW) and peak intensity I_L in watts per square centimetre ($\mathrm{W\,cm^{-2}}$) as follows [113]:

$$\begin{aligned} P_L\ [GW] &\approx 21.5\ \left(\frac{a_0 w_0}{\lambda}\right)^2, \\ I_L\ [W/cm^2] &\approx 1.370\times 10^{18}\left(\frac{a_0}{\lambda[\mu m]}\right)^2, \end{aligned} \tag{3.3}$$

where λ is the laser wavelength in micrometres (µm).

Finally, in the context of LWFA, the interaction of short, focused high power laser pulses with charged particles needs to be considered, which generally occurs via the ponderomotive force arising due to the gradient of the laser intensity within the pulse [114, 115]. In a one-dimensional treatment, assuming a variation of the laser vector potential $\mathbf{A}$ only along z and laser polarisation along x, this can be described by analysing the Lorentz force equation in terms of $\mathbf{A}$:

$$\frac{d\mathbf{p}}{dt} = \frac{e}{c}\Big(\frac{\partial\mathbf{A}}{\partial t} - \mathbf{v}\times\nabla\times\mathbf{A}\Big), \tag{3.4}$$

which leads to a momentum change in the transverse as well as longitudinal direction:

$$\frac{dp_x}{dt} = mc\frac{d\mathbf{a}}{dt}, \tag{3.5}$$

$$\frac{dp_z}{dt} = -\frac{mc^2}{2}\frac{\partial a^2}{\partial z}. \tag{3.6}$$

The first equation describes the quiver motion of the electron as it is oscillating in the rapidly varying laser electric field, a motion that is cancelled out across the duration of the pulse, as the electron returns to its rest position. The second equation describes the effect of the ponderomotive force, which in 3D can be expressed as [115]

$$\mathbf{F}_p = -mc^2\nabla\frac{a^2}{2} \tag{3.7}$$

hence acting in all three directions due to the finite size of the laser pulse instead of just along z. This force pushes the electrons in the direction of lower laser intensity hence effectively acting as radiation pressure. The reason for this behaviour can be visualised in the following qualitative picture: as an electron is pushed outward by the laser electric field during one half cycle, it reaches a region of lower laser intensity. The force pulling the electron back, as the sign of the oscillating laser field changes, is thus not as strong as the initial outward force. This means the electron cannot be pulled back the same distance in the second half cycle of the laser field and so an overall net force is experienced.

The ponderomotive force is the main driving mechanism for a number of novel accelerator concepts, including most prominently, laser wakefield acceleration which is discussed in more detail in Sections 3.2 to 3.4.

3.2 Laser Wakefield Excitation

Plasma is defined as an ionised gas which is globally neutral, but strongly influenced in its behaviour by collective effects due to the Coulomb forces of its charged constituents [116]. It can be categorised as underdense or overdense depending on whether it lies below or above the critical plasma density

$$n_c = \frac{\omega^2 \epsilon_0 m}{e^2}\,, \tag{3.8}$$

which defines the maximum density through which an electromagnetic wave of angular frequency ω can propagate.

In laser wakefield acceleration a plasma is often created by an intense laser pulse entering a gas target and ionising the latter. With typical laser intensities on the order of 5×10^{17}–$5 \times 10^{19}\,\mathrm{W\,cm^{-2}}$, the ionisation threshold of hydrogen of approximately $1 \times 10^{14}\,\mathrm{W\,cm^{-2}}$ [117], for example, can be easily reached and a plasma is generated. As this short, high intensity laser propagates through the newly formed plasma, the plasma electrons are pushed outward both parallel and perpendicular to the laser propagation direction due to the laser ponderomotive force, while the ions remain largely stationary as a consequence of their considerably larger mass. This effect creates a localised charge separation which induces a restoring Coulomb force and, due to the electrons overshooting their rest positions, oscillations around the laser propagation axis. Hence, longitudinal plasma waves are formed which spread outward from the drive laser pulse generating a strong wakefield with components both in the laser propagation direction and perpendicular to it. Because of the collective nature of the motion of plasma particles, this oscillatory response occurs on very specific temporal and spatial scales, in particular defined by

the electron plasma frequency and plasma wavelength [116]

$$\omega_p = \sqrt{\frac{n_0 e^2}{m\epsilon_0}}\,, \tag{3.9}$$

$$\lambda_p = \frac{2\pi c}{\omega_p} = \frac{2\pi c}{e}\sqrt{\frac{m\epsilon_0}{n_0}}\,, \tag{3.10}$$

where n_0 is the electron number density, ϵ_0 the vacuum permittivity and m,e the electron mass and elementary charge, respectively. The wakefield that is formed is on the order of the cold non-relativistic wavebreaking field [113, 118]

$$E_0 = \frac{mc\omega_p}{e}\,, \tag{3.11}$$

which, for a relatively low plasma density of n_0=$1 \times 10^{23}\,\mathrm{m}^{-3}$, for example, exceeds $30\,\mathrm{GV\,m}^{-1}$. If an electron beam is placed into such a field at the correct position, it can be accelerated to very high energies over distances of millimetres to centimetres. The electron beam is typically termed the witness bunch in this case.

The exact shape and amplitude of the generated density wave and wakefield depend on the laser intensity as well as the plasma density and typically two regimes are differentiated, namely the linear and nonlinear regime. In the following, the plasma behaviour in these scenarios as well as a third intermediate regime are described in more detail. Additionally, the wakefield driven by an electron beam, instead of a laser pulse - used as an acceleration mechanism in beam-driven wakefield acceleration (PWFA) - is discussed.

3.2.1 The Linear Regime

For laser pulses with normalised amplitude of $a_0^2 \ll 1$, the plasma response to an electromagnetic pulse is described by linear plasma waves. In this regime, the plasma wakefield and density fluctuations can be expressed analytically in all three dimensions.

The derivation of the wakefield is based on the cold fluid equations, in particular the continuity equation, momentum equation, and Poisson's equation [113, 119, 120]:

$$\frac{\partial \delta n}{\partial t} + n_0 \nabla \mathbf{u} = 0\,, \tag{3.12}$$

$$\frac{1}{c^2}\frac{\partial \mathbf{u}}{\partial t} = \nabla\phi - \nabla\frac{a^2}{2}\,, \tag{3.13}$$

$$\nabla^2\phi = k_p^2 \frac{\delta n}{n_0}\,, \tag{3.14}$$

where $\delta n/n_0 = (n - n_0)/n_0$ is the normalised density of the plasma perturbation, $\mathbf{u} = \mathbf{p}/(mc)$ is the normalised plasma wave momentum and $\phi = e\Phi/(mc^2)$ is the normalised scalar potential with Φ related to the electric field by $\mathbf{E} = -\nabla\Phi$. By combining and re-arranging these three equations, differential equations for the normalised potential as well as the density perturbation are found:

$$(\frac{\partial^2}{\partial t^2} + \omega_p^2)\phi = \omega_p^2 \frac{a^2}{2}\,, \tag{3.15}$$

$$(\frac{\partial^2}{\partial t^2} + \omega_p^2)\frac{\delta n}{n_0} = c^2\nabla^2 \frac{a^2}{2}\,. \tag{3.16}$$

Eq. (3.15) can be transformed and solved to give an expression for the normalised scalar potential connected to the plasma wave:

$$\phi = \frac{k_p}{2}\int_{\xi_0}^{\xi} \sin\left(k_p(\xi - \xi')\right) a^2(\xi', r) d\xi'\,, \tag{3.17}$$

where radial symmetry is assumed with $r^2 = x^2 + y^2$ and ξ_0 is a position in front of the laser where a^2 is zero. Moreover, the coordinate system has been transformed to the co-moving frame with $\xi = z - ct$ and the quasi-static approximation has been applied. In other words, it is assumed that the propagation time of the laser is small compared to the evolution time of the laser envelope, so that temporal derivatives of $\mathbf{a}$ are neglected. The exact shape of the potential and hence the wakefield depends on the laser envelope $\mathbf{a}$; however, to simplify the integration, for positions far behind the laser pulse, it can be performed from $-\infty$ to ∞.

For a linearly polarised pulse of Gaussian shape both longitudinally and radially, centred around zero in all dimensions, for example, the laser envelope can be described by

$$a(\xi, r) = \frac{a_0}{\sqrt{2}} \exp(-\frac{\xi^2}{L_{rms}^2}) \exp(-\frac{r^2}{w^2})\,, \tag{3.18}$$

where L_{rms} is the longitudinal RMS (root mean square) size of the field and w is the transverse RMS width of the field. Eq. (3.17) may thus be simplified for a Gaussian laser driver, upon re-normalisation of the variables, to

$$\Phi = -\sqrt{\frac{\pi}{2}}\frac{mc^2}{e}\frac{k_p L_{rms}}{4} a_0^2 \exp(-\frac{k_p^2 L_{rms}^2}{8}) \exp(-\frac{2r^2}{w^2}) \sin(k_p\xi) \tag{3.19}$$

and the longitudinal electric field can then be calculated as

$$E_z(\xi, r) = \sqrt{\frac{\pi}{2}}\frac{mc^2}{e}\frac{k_p^2 L_{rms}}{4} a_0^2 \exp\left(-\frac{k_p^2 L_{rms}^2}{8}\right) \exp\left(-\frac{2r^2}{w^2}\right) \cos(k_p\xi)\,. \tag{3.20}$$

The transverse focusing field connected to the plasma wakefield can be similarly found, assuming radial symmetry:

$$(E_r - cB_\theta)(\xi, r) = -\sqrt{\frac{\pi}{2}}\frac{mc^2}{e}\frac{k_p L_{rms}}{w^2}a_0^2 \exp(-\frac{k_p^2 L_{rms}^2}{8})\exp(-\frac{2r^2}{w^2})\ r\ \sin(k_p\xi)\,. \tag{3.21}$$

Fig 3.3 visualises the fields described by Eqs. (3.20) and (3.21) which, as can be seen, are offset

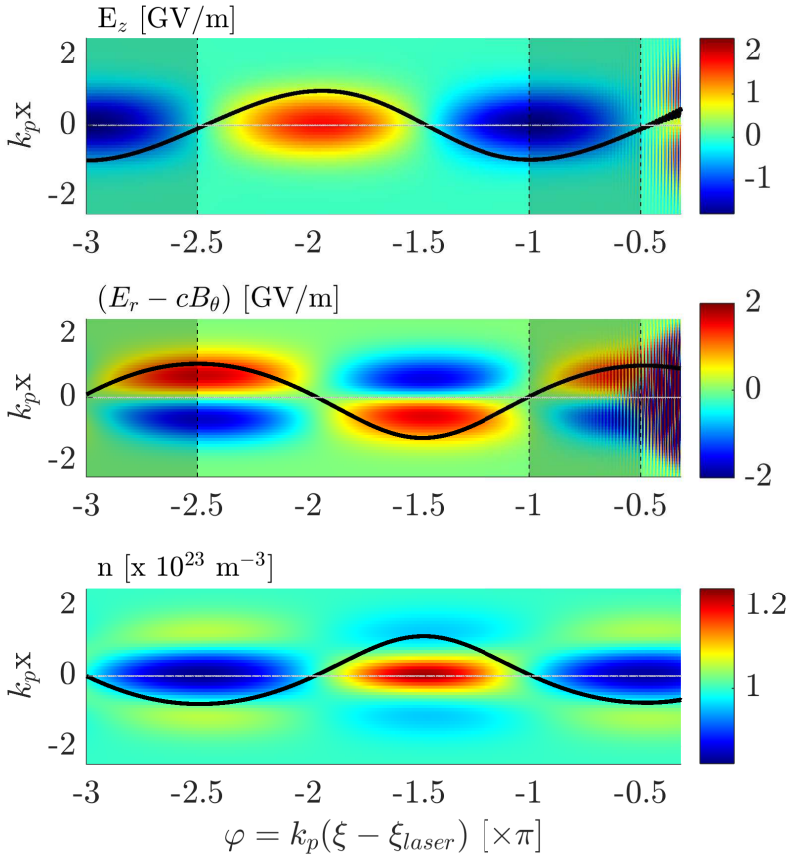

Figure 3.3: Plasma waves in the linear regime (a_0=0.5): longitudinal (top) and transverse (middle) wakefield together with the plasma density (bottom), as found from a PIC-simulation with the OSIRIS code at a plasma density of n_0=1 × 10^{23} m^{-3}. In the top and bottom plots the solid line shows the lineout along $x = 0$, while in the middle plot it represents the transverse gradient at $x = 0$ (all in arbitrary units). The shaded areas mark the accelerating and focusing region of the wakefield useful for particle acceleration.

longitudinally by a $\pi/2$ phase shift. The useful part of the wakefield is thus the region between $\varphi = -\pi$ and $\varphi = -\pi/2$ where an electron beam placed into the fields is both accelerated and focused.

3.2.2 The Nonlinear Regime

As laser strengths of $a_0^2 \gg 1$ are reached, the plasma electrons become relativistic when they are pushed away by the laser ponderomotive force and so the laser-driven plasma wave and wakefield start to change not only in amplitude, but also significantly in shape through steepening of the sinusoidal features (see Fig. 3.4). The lengthening of the effective plasma wavelength in this context can be approximated by [113, 121]

$$\lambda_{np} = \lambda_p \begin{cases} 1 + \frac{3}{16}(\frac{E_{max}}{E_0})^2, & \text{if } E_{max}/E_0 \ll 1 \\ \frac{2}{\pi}(\frac{E_{max}}{E_0} + \frac{E_0}{E_{max}}), & \text{if } E_{max}/E_0 \gg 1 \end{cases} \tag{3.22}$$

with E_{max} the maximum amplitude of the electric field.

For a more comprehensive description of the fields (see [113, 119, 120] for details), Eq. (3.12) to (3.14) are extended for a relativistic description of the momentum $\mathbf{p} = m\gamma\mathbf{v}$ and combined with the wave equation $\nabla^2\mathbf{a} - 1/c(\partial^2\mathbf{a}/\partial t^2) = k_p^2 n\mathbf{u}/\gamma$. By applying a change of coordinates to the co-moving frame, the quasi-static approximation and a change to a 1D system - assuming an infinitely wide plasma and drive laser pulse - these equations can be re-written as

$$\begin{aligned} \frac{n}{n_0} &= \frac{\beta_p}{\beta_p - \beta_z}\,, \\ \gamma(1 - \beta_p\beta_z) &= 1 + \phi\,, \\ \frac{\partial^2\phi}{\partial\xi^2} &= k_p^2(\frac{n}{n_0} - 1)\,, \end{aligned} \tag{3.23}$$

where β_z is the normalised longitudinal electron velocity, while β_p is the normalised wave phase velocity. By combining them a differential equation to describe the evolution of the scalar potential and, as $E_z = -\partial\Phi/\partial z$, also the electric wakefield can be derived as

$$\frac{\partial^2\phi}{\partial\xi^2} = k_p^2\gamma_p^2 \left[\beta_p\ (1 - \frac{\gamma_\perp^2}{\gamma_p^2(\phi+1)^2})^{-1/2} - 1\right] \tag{3.24}$$

with the plasma density given as $n = \gamma_p^2\ \beta_p\ [(1 - \frac{\gamma_\perp^2}{\gamma_p^2(\phi+1)^2})^{-1/2} - \beta_p]$. Finally, assuming that the plasma wave phase velocity is close to c, such that $\gamma_p^2 \gg 1$, Eq. (3.24) is simplified to give

$$\frac{\partial^2\phi}{\partial\xi^2} = \frac{k_p^2}{2}\left(\frac{1 + a^2}{(\phi+1)^2} - 1\right)\,. \tag{3.25}$$

Eq.(3.25) can only be solved analytically under further assumptions and for specific laser shapes in this 1D scenario. For a more realistic description, including e.g. also the evolution of the

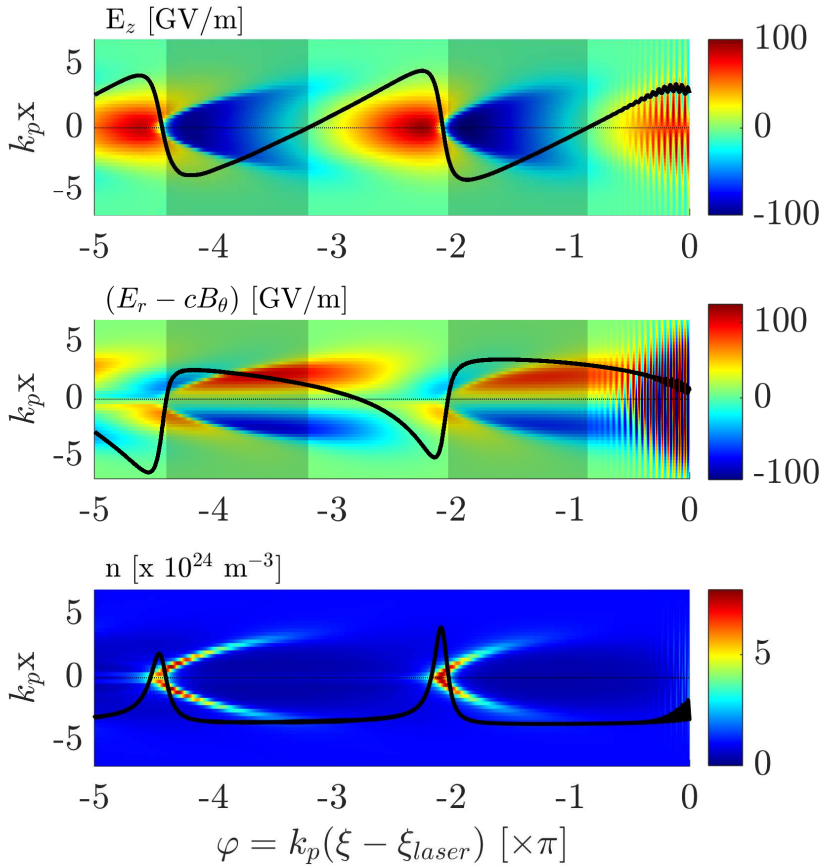

Figure 3.4: Plasma waves in the nonlinear regime (a_0=2.5): longitudinal (top) and transverse (middle) wakefield together with the plasma density (bottom), as found from a PIC-simulation with the OSIRIS code at a plasma density of n_0=1 × 10^{23} m^{-3}. In the top and bottom plots the solid line shows the lineout along $x = 0$, while in the middle plot it represents the transverse gradient at $x = 0$ (all in arbitrary units). The shaded areas mark the accelerating and focusing region of the wakefield useful for particle acceleration.

laser pulse shape in the plasma, particle-in-cell simulations need to be employed. This last approach has been followed for almost all results presented in Chapter 4.

3.2.3 The Weakly Nonlinear Regime

The weakly nonlinear laser regime with $1 \lesssim a_0 \lesssim 2$ represents an intermediate region between the two cases discussed previously where the physical behaviour of the system is still very similar to the linear regime, but the shape and amplitude of the wakefield already start to change towards the steepened peaks of the nonlinear plasma wakefield. In order to describe this regime in an analytical manner, the nonlinear differential equation Eq. (3.25), derived in Section 3.2.2, is simplified with the assumption that the scalar potential of the wakefield is small,

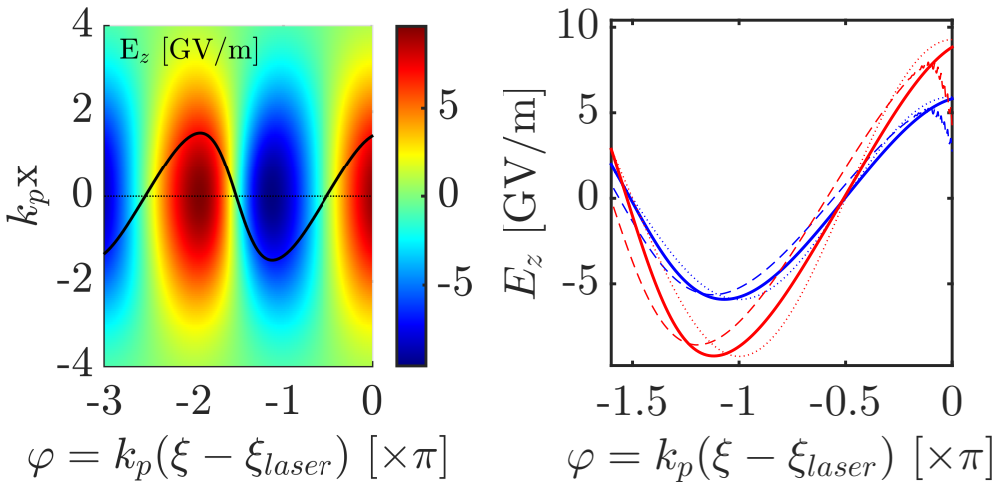

(a) Longitudinal wakefield (b) On-axis longitudinal wakefield

Figure 3.5: Plasma waves in the weakly nonlinear regime: (a) shows the longitudinal wakefield with its on-axis lineout as a function of φ and x for a laser pulse with a_0=1.65 (from the analytical model). In (b) the field calculation with the weakly nonlinear model (solid line) is compared to the on-axis longitudinal field from PIC simulations with the code OSIRIS (dashed) and estimates from the linear model (dotted). The blue lines are for a_0=1.3, while the red lines depict the cases for a_0=1.65. Note that both for the simulations and the analytical model results a homogeneous plasma of density of $1 \times 10^{23}\,\mathrm{m}^{-3}$ was assumed with a chosen laser pulse duration and width of 7.5 µm (FWHM) and 42.5 µm ($1/e^2$ radius), respectively.

i.e., $|\phi| \ll 1$, such that the latter can be expanded as $(1+\phi)^{-2} = 1 - 2\phi + 3\phi^2 - 4\phi^3 + 5\phi^4 + ...$[1]. Note that using only the zero- and first-order terms in Eq. (3.25) reduces the latter to Eq. (3.15) for the linear regime. For the weakly nonlinear case, however, the following equation can be found:

$$k_p^{-2}\frac{\partial^2\phi}{\partial\xi^2} = -\phi + \frac{3}{2}\phi^2 - 2\phi^3 + \frac{5}{2}\phi^4\,, \tag{3.26}$$

where ϕ is expanded to fourth order and only positions behind the laser pulse are considered such that a is zero. Eq. (3.26) can then be solved using the Poincaré-Lindstedt perturbation method (see Appendix A for more details) which results in the following equation describing the accelerating electric field

$$\begin{aligned}\frac{E_z}{E_0} &= b_1 a_1 \sin(\eta+\eta_0) + (\frac{13}{256}a_1^4 - \frac{1}{2}a_1^2)b_1\sin(2\eta+2\eta_0) \\ &+ \frac{21}{64}b_1 a_1^3\sin(3\eta+3\eta_0) - \frac{23}{96}a_1^4\sin(4\eta+4\eta_0)\end{aligned} \tag{3.27}$$

[1] Z.M. Sheng, private communication, 7th Feb. 2017

with $b_1 = 1 - (3/16)a_1^2$ and $\eta = b_1 k_p \xi$. a_1 is defined as the amplitude of the wakefield in the linear regime which for a Gaussian laser driver, as described in Eq. (3.18), is thus given as $a_1 = \sqrt{\frac{\pi}{2}} \frac{a_0^2 k_p L_{rms}}{4} \exp(-\frac{L_{rms}^2 k_p^2}{8}) \exp(-\frac{-2r^2}{w^2})$ with $\eta_0 = \pi/2$. As can be seen from this equation, a series of harmonics is used to express the steepening of the plasma wave which is consistent with the description of a sawtooth wave - the extreme nonlinear case - as an infinite sum of harmonics [122]. Moreover, employing the Panofsky-Wenzel theorem [123], $\partial E_z/\partial r = \partial/\partial\xi(E_r - cB_\theta)$, the focusing field in the weakly nonlinear regime is given by

$$\begin{aligned} \frac{(E_r - cB_\theta)}{E_0} &= r\Big[\frac{4a_1(1-9/16a_1^2)}{w^2 k_p b_1}\cos(\eta+\eta_0) + \frac{3a_1^2}{2w^2}\Big(\xi\cos(\eta) - \frac{\sin(\eta)}{k_p b_1}\Big) \\ &- \frac{2a_1^2(1-37/64a_1^2)}{w^2 k_p b_1}\cos(2\eta+2\eta_0) + \frac{3a_1^4}{4w^2}\Big(\xi\sin(2\eta) + \frac{\cos(2\eta)}{2k_p b_1}\Big) \\ &+ \frac{21a_1^3}{16w^2 k_p b_1}\cos(3\eta+3\eta_0) - \frac{23a_1^4}{24w^2 k_p b_1}\cos(4\eta+4\eta_0)\Big]\,, \end{aligned} \tag{3.28}$$

where $w = w(z)$ is the transverse laser spot size at position z. Figure 3.27 depicts the longitudinal wakefield based on Eq. (3.27) in a comparison with the fields calculated from particle-in-cell simulations for a_0=1.3 and 1.65. Although there are differences in the field amplitude, the shape of the wakefield can be reproduced quite well and presents a clear improvement over the linear model for this intermediate regime.

3.2.4 Beam-Driven Plasma Waves

Equations (3.12) to (3.14) are equally valid if an electron beam instead of a laser pulse is driving the plasma wave; however, the density modulation is then given by $\delta n = n - n_0 + n_b$ with n_b the beam density. In this scenario, the plasma oscillation is not induced by the ponderomotive force, but directly by the Coulomb force of the drive electron beam which pushes aside the surrounding plasma background electrons. Similarly to the laser-driven case, described in Eq. (3.25), a differential equation for the normalised electrostatic potential can thus be derived [51]:

$$\frac{\partial^2}{\partial^2\xi}\phi = k_p^2\Big[\frac{1}{2(1+\phi)^2} - \frac{1}{2} + \frac{n_b}{n_0}\Big]\,. \tag{3.29}$$

Here the local density within the plasma wave has been calculated as $n/n_0 = (1+(1+\phi)^2)/(2(1+\phi)^2)$. Assuming that the charge distribution of the drive beam is separable of the form $q_b = q_\parallel(\xi)\, q_\perp(r)$, the longitudinal wakefield due to the beam driver can be calculated from Eq. (3.29) as [124, 125]

$$E_z(r,\xi)/E_0 = Z'(\xi)R(r)\,, \tag{3.30}$$

where the longitudinal and transverse component are found separately based on the respective charge distribution. Far behind the driver beam, for example, Z' can be estimated for a Gaussian density distribution of $q_{\parallel}(\xi) = -en_b \exp(-\xi^2/(2\sigma_z^2))$ located at $\xi = 0$ as

$$Z'(\xi) = -\sqrt{2\pi}E_0 \frac{n_b}{n_0} k_p \sigma_z \exp\left(-\frac{k_p^2 \sigma_z^2}{2}\right) \cos(k_p \xi) \tag{3.31}$$

while R is typically assumed for a flat top radial density distribution with radius a for which

$$R(r) = \begin{cases} 1 - k_p a K_1(k_p a) I_0(k_p r), & \text{if } r < a \\ k_p a K_0(k_p r) I_1(k_p a), & \text{if } r > a \end{cases}. \tag{3.32}$$

$I_n(x)$ and $K_n(x)$ are modified Bessel functions of the first and second kind, respectively, in this context. Especially for small transverse beam sizes the exact density distribution is not too important for the wakefield shape, so that the flat top profile is a reasonable assumption.

While extremely relevant in electron beam-driven plasma accelerators, the beam's own wakefield, the beamloading field, can also be important in LWFA for the case of dense witness beams being accelerated in a laser-driven wake. As discussed in detail in Chapters 4 and 5 of Part III, the beamloading field can reach comparable amplitude to the laser-driven wakefield under these circumstances which affects the effective wakefield that the witness beam is experiencing and can therefore influence, for example, the energy distribution and energy spread of the accelerated electron bunch.

3.3 Wave Breaking and Self-Injection

3.3.1 General Theory

There are two ways to place an electron beam into the plasma wave for acceleration:

1. External injection where a pre-accelerated beam is sent into the plasma behind the drive laser; its relative position to the laser determines its final position in the wakefield and hence the evolution of its energy and other beam properties.

2. Self-injection where the electron beam is generated directly in the plasma by a fraction of the background electrons gaining temporarily enough energy to co-propagate with the plasma wakefield and hence, due to the strong acceleration in the wakefield, becoming trapped.

Self-injection has the advantage that the accelerator setup can be made very compact and that high-density beams can easily be generated that would otherwise be more challenging to produce and transport in conventional accelerators. Yet, self-injection is not an easy process to control as the plasma wave needs to be in the nonlinear regime where the laser pulse and plasma interact strongly and various phenomena occur simultaneously. As a consequence, several schemes, such as density downramp injection [126, 127], ionisation injection [128–130] and colliding pulse injection [72, 131], are being developed and investigated with the aim to self-inject an electron beam with good quality in a controlled manner.

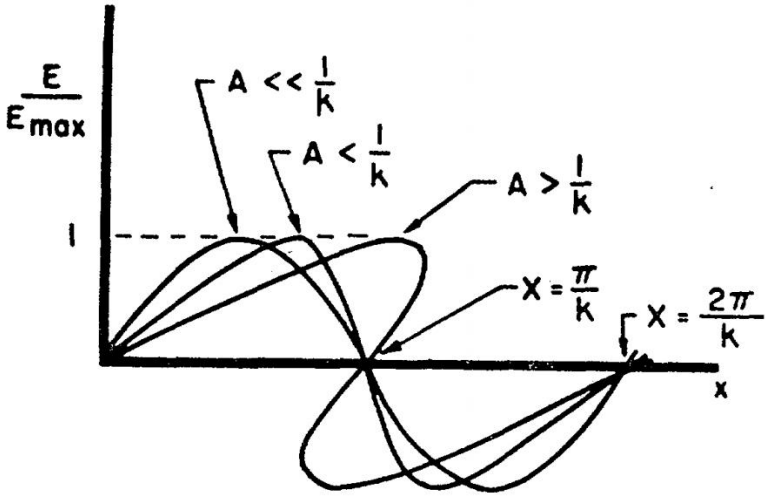

Figure 3.6: Onset of wavebreaking from a simple 1D plane wave model: as the wave amplitude A increases, the wave steepens until, for A above a certain threshold, the wave crest or spike starts to overhang marking the point of wavebreaking and breakdown of the model (image reprinted with permission from [118] copyright 1959 by the American Physical Society).

A simpler, yet less refined method of self-injection, due to its highly nonlinear nature, is through the process of wavebreaking which was used in many early LWFA experiments as an injection mechanism [132–135]. Wavebreaking occurs, similarly to the case of water waves, when the wave amplitude becomes too high, here exceeding a critical threshold of

$$E_{WB} = \sqrt{2(\gamma_p - 1)}E_0\,, \tag{3.33}$$

which is the cold relativistic wavebreaking field with γ_p the Lorentz factor associated with the plasma wave phase velocity [118]. Physically this behaviour can be explained by the plasma electron motion within the wave: as the plasma wave becomes more nonlinear, as shown in Fig. 3.6, the background plasma electrons forming the density oscillations increase in velocity

until, at the point of wavebreaking, they exceed the phase velocity of the plasma wave itself. Electron trajectories hence start to overlap within the wave exhibiting turbulent behaviour in the previously laminar electron flow and locally destroying the wave structure. A consequence is that a fraction of the plasma electrons in the local wavebreaking area gain enough energy in this process to "catch up" with the remainder of the wakefield and hence can become trapped and accelerated in it.

3.3.2 Upramp-Assisted Self-Injection

As the wavebreaking timing depends strongly on the plasma wave phase velocity relative to the plasma electron velocities, one approach to control this process better is by adjusting the latter through, for example, a variation in plasma density. Moreover, this can also lead to ultrashort duration in the electron beams injected in this way, as explained in the following.

The relative phase velocity of a plasma wave, β_{ph}, on a density ramp of length R and gradient dn/dz can be expressed as [75]

$$\beta_{ph} = \frac{\beta_{gr}}{1 - \frac{|\xi|}{2n}\frac{dn}{dz}}\,, \tag{3.34}$$

where $\beta_{gr} = v_{gr}/c$ is the relative laser group velocity and $\xi = z - \beta_{gr}ct$ is, as previously defined, the longitudinal position in the co-moving frame and hence the distance between local position z and the laser pulse. A negative density gradient slows down the wave leading to easier wavebreaking and self-injection - the main concept of density downramp injection - as the plasma electrons can become trapped at lower velocities. However, for a positive gradient the phase velocity increases and can become superluminal. With $v_{ph} > c$, however, wavebreaking is suppressed, as the electron oscillation velocities cannot reach beyond the speed of light.

A second effect on the plasma wave due to a density transition is a change in the width of the density perturbations connected to the plasma wave. Taking into account the variation of the plasma wavenumber and plasma wave phase velocity along the density transition in the nonlinear equations describing the properties of the wave (see Eq. (3.23)), the perturbation width δn along the upramp can be expressed as [136]

$$\delta n = \Big[\frac{2(\beta_{ph} - \beta_m)^3}{\beta_m(1 - \beta_m^2)^{3/2}}\Big]^{1/2} \tag{3.35}$$

with β_m the maximum electron velocity. As the phase velocity v_{ph} follows an evolution as in Fig. 3.7a for a positive density gradient, asymptotically decreasing towards β_{gr}, δn decreases

and hence the density perturbations steepen to extremely thin, dense peaks with widths on the order of hundreds of attoseconds, as seen in Fig. 3.7b.

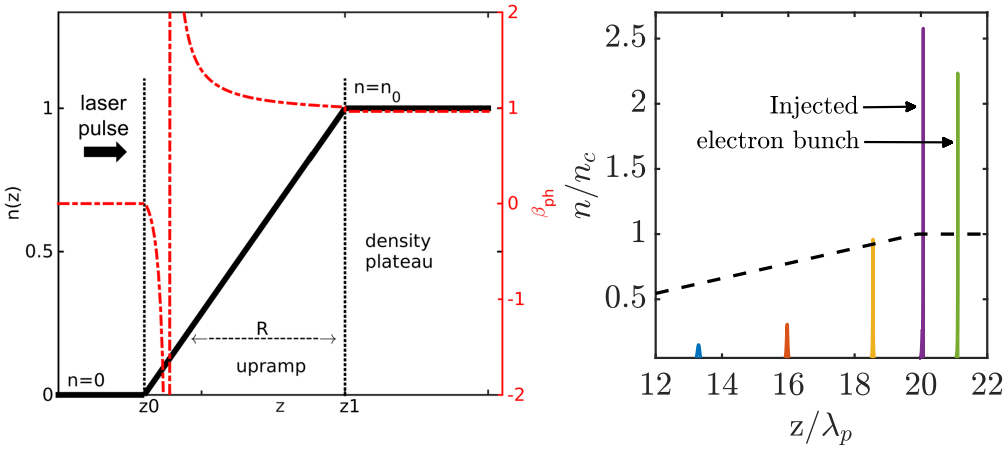

(a) Evolution of the plasma wave phase velocity.

(b) Steepening of the plasma density wave crests.

Figure 3.7: Effect of the plasma density upramp on the plasma wave shape via the variation of the plasma wave phase velocity β_{ph}. (a) Evolution of the plasma wave phase velocity along the density upramp. (b) Evolution of the first plasma density perturbation behind the drive laser at different positions on the density upramp. Following Eq. (3.35), the convergence of β_{ph} towards the laser group velocity on the upramp leads to a steepening of the plasma wave generating density perturbations with ultrashort duration and overcritical density.

At the end of the plasma ramp, as the density gradient drops to zero, the plasma wave phase velocity returns very suddenly to a subluminal value. If the wave is nonlinear enough, e.g. due to a high drive laser intensity, the previously suppressed wavebreaking process now sets in and a large fraction of the first density perturbation – the broken wave crest or spike – is injected into the wakefield. Due to the abruptness of the action and the quasi-1D nature of the wave evolution - achieved through a broad drive laser spot size -, the shape of the density structure can be well preserved during self-injection so that the witness beam to be accelerated has ultrashort duration and high charge. The use of this mechanism for attosecond electron beam generation has first been proposed by Li et al. [75]; it is also the main mechanism investigated in Chapter 4.

3.4 Effects of the Plasma on the Laser Driver

The interaction between the drive laser pulse and the plasma is a reciprocal process and consequently the laser is found to evolve during its propagation through a variety of phenomena.

This has in most cases detrimental effects on the electron beam acceleration in the plasma so that the useful acceleration length can be estimated in general based on one of the three most common interaction phenomena: defocusing, dephasing and depletion.

In linear plasma waves, defocusing of the laser pulse is usually the largest issue. As the laser evolves as a Gaussian beam in the plasma, its intensity decreases after its focal point leading to a significant reduction in the wakefield amplitude and hence accelerating gradient for distances longer than the laser Rayleigh range.

In the nonlinear regime, on the other hand, electron beam dephasing and pump laser depletion are the dominant processes that limit the acceleration distance. The former occurs because the electron beam velocity $v \sim c$ exceeds the plasma wave velocity. With the latter approximately equal to the laser group velocity in plasma $v_p \approx v_g = c\sqrt{1-\lambda^2/\lambda_p^2}$, the bunch hence catches up with the drive laser. Based on this, a dephasing length L_d can be defined as the distance during which the electron beam passes from one end of the accelerating and focusing region of the wakefield to the other [121, 137]:

$$\begin{aligned} L_d\ (1-\frac{v_p}{c}) &= \Delta_{acc} \\ \iff L_d &\approx \Delta_{acc}\frac{2\lambda_p^2}{\lambda^2}\,, \end{aligned} \tag{3.36}$$

where Δ_{acc} is the size of the accelerating and focusing region, while it is assumed that $\sqrt{1-\lambda^2/\lambda_p^2}$ $\approx 1-\lambda^2/(2\lambda_p^2)$. Approximating the accelerating and focusing region of the wakefield to span $\lambda_p/4$, as is the case in the linear regime, this can be further simplified to

$$L_d \approx \frac{\lambda_p^3}{2\lambda^2}\,. \tag{3.37}$$

Pump depletion, on the other hand, is caused by the loss of the drive laser energy to the plasma due to driving the plasma wake. Again, a pump depletion length L_{pd} can be defined, in this case as the distance over which the laser pulse loses half of its original energy [121, 137]:

$$E_z^2\ L_{pd} = E_L^2\ L_L\,, \tag{3.38}$$

where E_z is the longitudinal plasma wakefield amplitude, E_L is the laser field amplitude and L_L is the laser pulse length. Describing the laser field by $E_L = mc\omega a_0/e$, this can be simplified to

$$L_{pd} = \frac{m^2c^2\omega^2a_0^2L_L}{e^2E_z^2}\,. \tag{3.39}$$

For the linear regime a further approximation is applied by assuming the wakefield amplitude with $E_z \propto \omega_p a_0^2$ and $L_L \approx \lambda_p$, such that

$$L_{pd} \approx \frac{\lambda_p^3}{\lambda^2 a_0^2} \,. \tag{3.40}$$

3.5 Particle-In-Cell Simulation Codes

Particle-in-cell (PIC) simulation codes are one of the most common numerical tools for the study of laser-plasma interactions, as they allow the description of complex plasma processes in a detailed, yet more resource-efficient way than other techniques, such as purely kinetic plasma models. Based on tracking a number of macroparticles across time and space, while calculating their interaction with electromagnetic forces and fields on a discretised spatial grid of cells, a series of calculations is carried out per time step, as seen in Fig. 3.8. Starting with initial distributions for the particle positions $\mathbf{x}_i$ and velocities $\mathbf{v}_i$, the current and charge densities, $\mathbf{j}$ and ρ, are calculated on the spatial grid. Integrating Maxwell's equations using these now known current and charge densities, the electric and magnetic fields, $\mathbf{E}$ and $\mathbf{B}$, are found at each grid point. Employing the Lorentz equation, the force $\mathbf{F}_i$ on each particle in the system due to the electric and magnetic fields is calculated which in turn is then applied to find the particles' new position and velocity. Using this new information, the loop is repeated for the next time step.

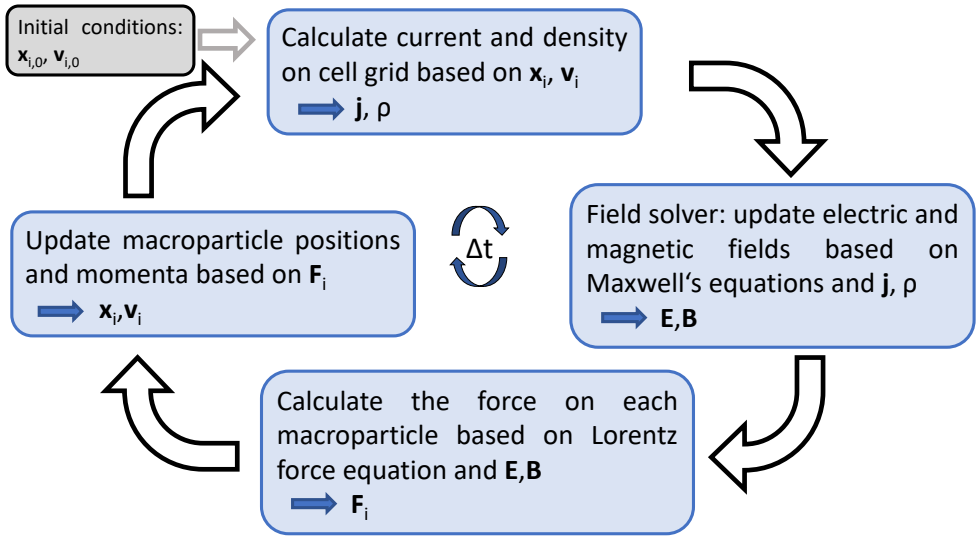

Figure 3.8: Main calculation steps involved in every time step of a particle-in-cell simulation.

It should be noted that PIC codes only work for weakly coupled plasmas where collective effects are the dominant mode of interaction between particles, as this allows the substitution of actual, point-like particles with a smaller number of finite sized macroparticles that can generate equivalent long-range collective effects [114]. In the regime of laser wakefield acceleration, especially as studied in this thesis, this condition is clearly valid.

The work presented in this thesis has been carried out using predominantly two PIC codes: initial studies in 1D have been run with the code KLAPS [138], while all of the higher dimensional simulations, both on self-injection and external injection, have been conducted with OSIRIS [139].

Part III

Numerical Study of Attosecond Electron Bunch Acceleration in Plasma

In this part two techniques for generating accelerated, attosecond-duration electron beams from laser wakefield accelerators (LWFA) are presented in detailed numerical studies. In one case, discussed in Chapter 4, a beam injector based on self-injection of electrons in a nonlinear plasma and their subsequent acceleration is investigated, while Chapter 5 explores the possibility of externally injecting a pre-accelerated attosecond beam and boosting its energy in a weakly nonlinear plasma. Chapter 4 focuses on the extension of a novel injection scheme – based on trapping assisted by a steep plasma density upramp – to a more linear parameter space. The dynamics of the injection process as well as the trapped electron beam evolution are studied with two- and three-dimensional particle-in-cell (PIC) simulations and the stability of the scheme is tested with respect to a number of factors. Chapter 5 discusses possible designs for a laser wakefield acceleration stage with an externally injected witness electron beam, in particular in the context of the SINBAD facility at DESY. Various phenomena influencing the evolution of the injected sub-femtosecond electron beam and their optimisations are introduced. Finally, start-to-end simulations are presented demonstrating a successful preservation of most of the beam parameters during plasma acceleration. The experimental realisation and applications of the two schemes are discussed in Chapter 6, where the results of Chapters 4 and 5 are also compared with each other as well as with other published techniques for attosecond electron beam acceleration.

The emphasis of both studies considered in this part lies on laser-driven wakefield acceleration (LWFA) instead of plasma acceleration with a relativistic electron beam driver (PWFA), since the former is expected to be more suitable for the kind of setups required to accelerate sub-femtosecond electron beams.

In the context of external injection, PWFA is certainly a possibility and has been studied before [140]. However, employing such a scenario for the acceleration of ultrashort witness beams would require a setup suitable to producing both longer, high energy beams for the driver as well as lower energy, sub-femtosecond bunches for the witness. As this has to result in a complex experimental stage with multiple challenges in beamline design and large space requirements, a laser-driven setup is deemed more easily realisable in this case. Moreover, possible issues related to laser-electron beam timing jitter - usually one of the main challenges in external injection with LWFA - can be mitigated by the ultrashort duration of the witness beam.

In the context of self-injection in a plasma wakefield, on the other hand, the main challenge lies in controlling the duration of the trapping process in order to ensure a short longitudinal bunch length. Figure 3.9 shows the main approaches on how this could be achieved. As a first

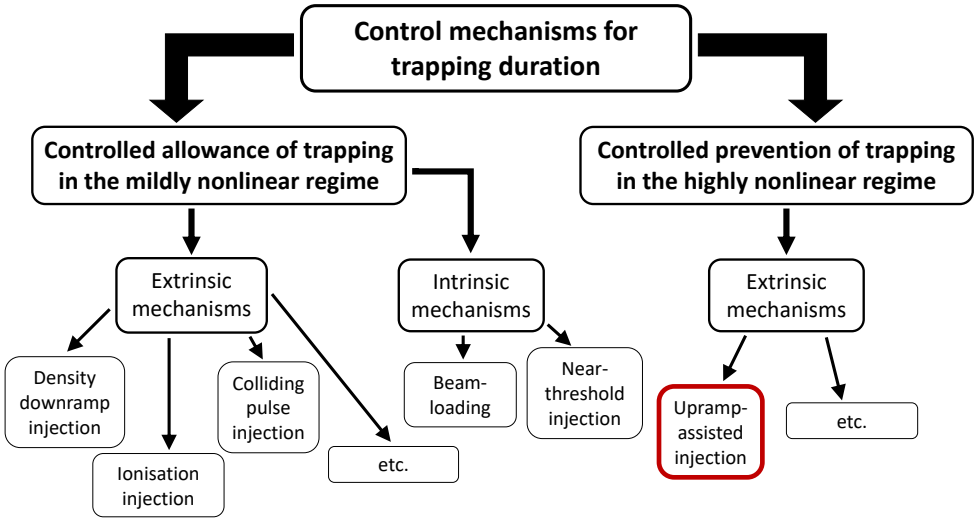

Figure 3.9: Possible self-injection mechanisms that allow control over the trapping duration and consequently the injected electron bunch length.

possibility (see left branch of Fig. 3.9), a mechanism can be introduced to the system without which self-injection is not feasible, hence allowing control over the injection duration via control of said mechanism. This technique is already employed commonly using extrinsic mechanisms to control injection, such as in the case of density downramp and ionisation injection where, e.g., a plasma density ramp or laser focal properties are used to limit possible electron trapping to a specific point and duration. While Tooley et al. [32] have shown from simulations that such a technique using micrometre-scale density fluctuations could produce electron beams of hundreds of attoseconds in duration, it remains yet to be seen how well the required precision and control of such an accelerator setup can be realised experimentally. With regard to intrinsic mechanisms, another approach to the problem was demonstrated by Islam et al. [30] in 2015 with an experiment showing self-injection very close to the trapping threshold. By providing a laser pulse barely intense enough for injection, only a small number of electrons is trapped over a short time duration before threshold conditions fade hence effectively limiting bunch durations to the femtosecond to sub-femtosecond level. Although potentially producing ultrashort beams, not much control is possible in this scenario over the exact bunch length. Fluctuations in plasma density or laser intensity will likely lead to large shot-to-shot variations in the produced witness beam.

Finally, the last proposed scenario for self-injection of attosecond electron beams, depicted as the right branch in Fig. 3.9, is based on introducing a mechanism which inhibits trapping rather than enabling it. When in the highly nonlinear regime, suddenly removing such an

inhibiting factor leads to a quick burst of electron trapping followed by a fast cut-off due to the quickly increasing beamloading fields of the bunch. Although only effective in a nonlinear and therefore, compared to the linear and weakly nonlinear regime, unstable parameter space, this technique has the advantage that the controlling mechanism does not have to be ultrashort itself and hence the beam duration should be well controllable even on the attosecond scale.

Due to its potential for a higher degree of specific control of the injected electron bunch length, this study was focused on the third presented scenario employing a nonlinear plasma wakefield with a mechanism to temporarily prevent electron trapping. Finding a suitable technique to inhibit self-injection is unproblematic with a laser driver due to the dependence of its wakefield phase velocity on a number of factors, such as plasma density (see Section 3.3.2 for more details) or the presence of an external magnetic field. However, the same is not the case for an electron beam driver for which manipulation of the wakefield structure is more difficult. Combining this consideration with the fact that, experimentally, laser-driven plasma setups are usually considerably smaller in footprint to beam-driven beamlines, the following studies are limited to investigations of LWFA.

Chapter 4

An Attosecond LWFA-Injector

In this chapter a plasma-based, high charge, attosecond electron beam injector is presented using the scheme of upramp-assisted self-injection and studied through PIC simulations. The main highlights of this work are listed in the following and have been partly published in [141]:

- First 3D simulation results of the injection scheme confirm the trapping mechanism reporting charges in the nC range and RMS durations around 200 attoseconds.
- The suitable parameter space for the setup is expanded via 1D simulation scans and 3D simulations, among others reducing the required threshold laser intensity by a factor of four.
- The injected electron beam is shown to evolve quickly over tens of µm in the plasma due to its strong space-charge forces and laser depletion; beam extraction is possible.
- The attosecond injector is proven to be functional within a range of variations in system parameters, including plasma density and upramp shape.

The studies in this chapter have been carried out through 2D- and 3D-simulations with the code OSIRIS as well as 1D-simulations with the OSIRIS and KLAPS codes. A pre-ionised, pure electron plasma has been assumed, while the positive ions and their motion have been neglected in simulation. The plasma target under investigation consists in all cases, except for those specifically described otherwise in Section 4.4, of a linear plasma density transition (upramp) from vacuum to a plateau of constant density, which in some simulations in Section 4.3 is additionally followed by a linear density transition from the plateau back to vacuum (downramp). In all, but these last cases, the properties of self-injected electron beams are only considered inside the plasma target. The PIC-simulations have been carried out at high resolution with, on average,

cell sizes of $\lambda/200$ in 1D, $\lambda/143 \times \lambda/5$ in 2D and $\lambda/63 \times \lambda/7 \times \lambda/7$ in 3D in the longitudinal and transverse directions, respectively, where λ is defined as the laser wavelength. The electron plasma is described with 30, 4 to 16, and 1 to 8 particles per cell, respectively, in the one-, two- and three-dimensional runs. Further details with regard to individual simulations are found in Appendix C. Moreover, in all cases within Chapter 4 the standard Yee solver was employed for solving the electromagnetic fields, including in most cases five-pass binomial current smoothing and quadratic interpolation between grid and particle variables. A moving window was used in the longitudinal direction in the case of the two- and three-dimensional simulations.

The subsequent sections are organised as follows: Section 4.1 introduces the full three-dimensional dynamics of the self-injection process within the original setup proposed by Li et al. [75], whereas in Section 4.2 a new parameter regime is presented and characterised through further one- and three-dimensional simulations. In Section 4.3 the propagation of the self-injected beams inside the plasma is investigated and the possibility of an extraction to vacuum assessed. Finally, Section 4.4 studies the stability of the self-injection mechanism with regard to variations in the plasma density, laser spot size, plasma temperature and plasma ramp shape.

4.1 Ultrashort Bunch Generation from a Density Upramp Profile

Laser pulse	
envelope (long./transv.)	$\sin^2$ / Gaussian
wavelength λ [µm]	1.0
peak power P_L [TW]	309.6 (a_0=6)
full pulse length L [µm]	10.0
pulse width ($1/e^2$ radius) w_0 [µm]	20.0
Plasma	
plateau density n_0 [m^{-3}]	4.4×10^{25}
ramp length R [µm]	45.0 (z =30.5 – 75.5 µm)

Table 4.1: Input parameters for the 3D OSIRIS simulation presented in Section 4.1. Note that $\sin^2$ describes a function of the form $\sin^2((\xi - \xi_0)\pi/L - \pi/2)$ (L=full beam length, ξ_0=beam centre), as defined in Section 3.1.

First proposed by Li et al. in 2013 [75], their initial studies on the scheme of upramp-assisted trapping centered on observations of the very early stages of self-injection through one- and two-dimensional PIC simulations. Since the dynamics in the plasma are highly nonlinear and complex in such a scenario, though, in this work we extend the investigation and provide a more thorough description of the injection mechanism based on first three-dimensional PIC simulations, a reference case of which is analysed and presented here. Further cases within a

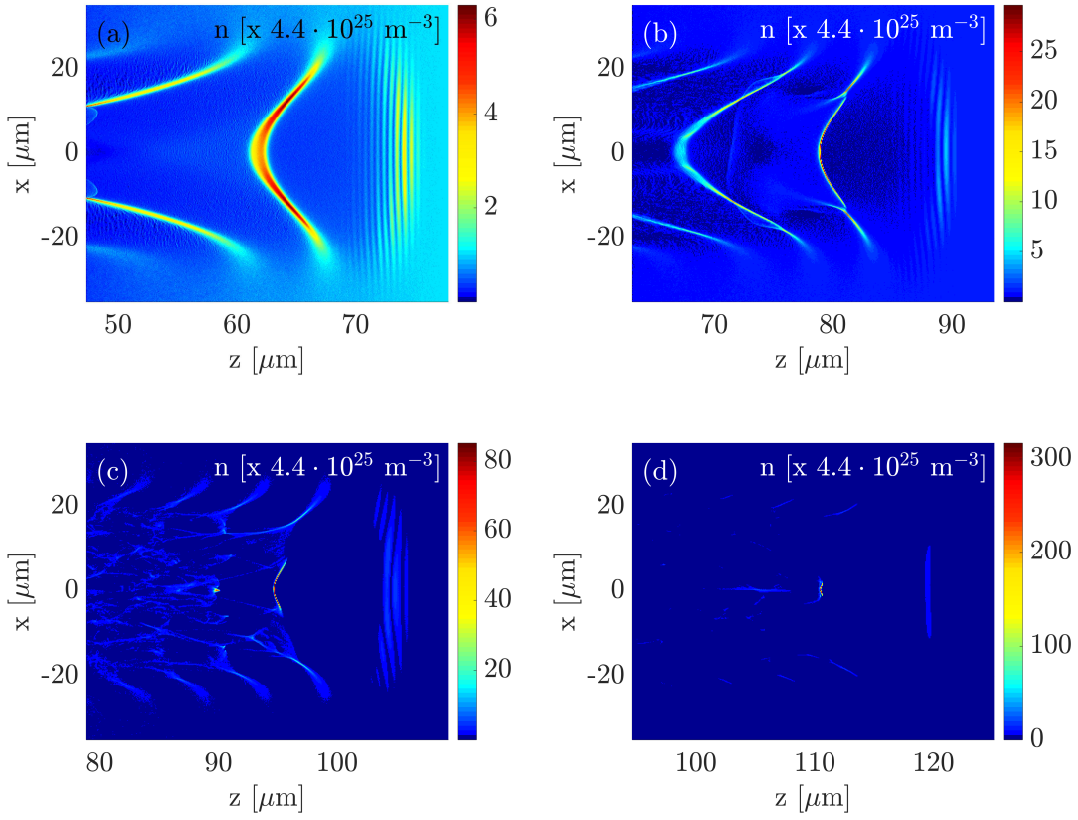

Figure 4.1: Evolution of the plasma density structure around the trapped electron bunch before (a) and during (b-d) upramp-assisted self-injection for a drive laser with strength a_0=6. The setup of this 3D simulation is described in Table 4.1.

wider parameter regime will be discussed in the following sections.

Figure 4.1 shows the evolution of the plasma density structure behind the laser pulse during the trapping of electrons at the end of a short, linear density upramp from a three-dimensional PIC simulation with the OSIRIS code and simulation parameters given in Table 4.1. The associated longitudinal wakefield of the plasma wave is depicted in Fig. 4.2 revealing further details about the complexity of this structure. As previously reported [75], the density evolution shows a breaking of the first wave crest at the end of the plasma upramp whereby a fraction of the electrons in this spike are pushed forward to become trapped in the remaining wakefield in the form of a broad, ultrashort electron sheet (Fig. 4.1b). During propagation over the following 30 µm, the disk-shaped beam focuses transversely (Fig. 4.1c) until it reaches its minimum size with a supercritical density of around $1.3 \times 10^{28}\,\mathrm{m}^{-3}$ (Fig. 4.1d).

In order to quantify the properties of the injected electron sheet, a set of criteria was

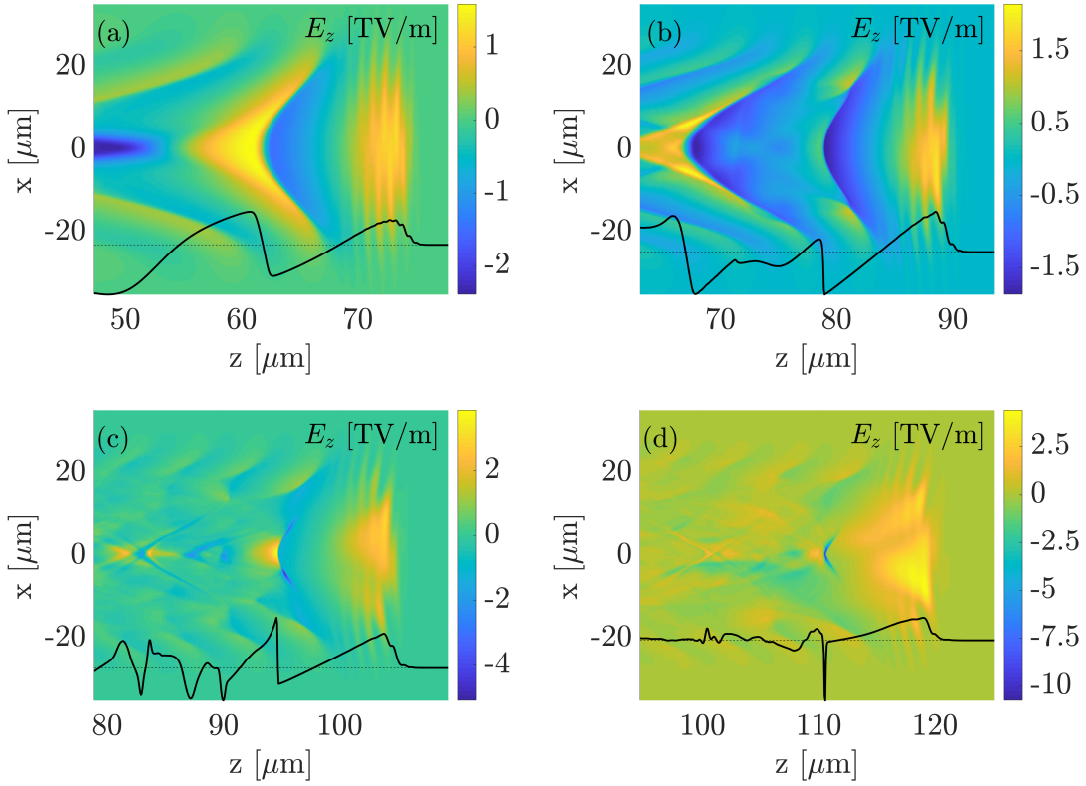

Figure 4.2: Evolution of the longitudinal plasma wakefield in the z-direction associated with the plasma wave structure shown in Fig. 4.1, around the trapped electron bunch before (a) and during (b-d) upramp-assisted self-injection for a drive laser with strength a_0=6. The black line shows a lineout of the field at x=0 in arbitrary units. The setup of this 3D simulation is described in Table 4.1.

established to distinguish trapped electrons in this beam from further spurious injection that occurs behind the main trapping point due to the nonlinearity of the plasma wakefield. It is based on separating a region in the plasma with a charge-weighted slice electron energy above a certain threshold both longitudinally and transversely. A higher limit is chosen for the back of the beam due to the majority of rogue injection occurring in this location and a radially symmetric beam is assumed. Figure 4.3 demonstrates how this selection works in practice by clearly defining the high density region of the injected beam even with low energy, low density electron structures present in the surroundings, as in Fig. 4.3b. In Fig. 4.4 the corresponding electron energy within this plasma region can be observed, clearly showing how in all cases a distinct energy spike is selected from a background of low energy electrons both from the transverse and longitudinal electron distribution. Based on this technique, the properties of the trapped electron sheet were tracked throughout the injection process with qualitative and

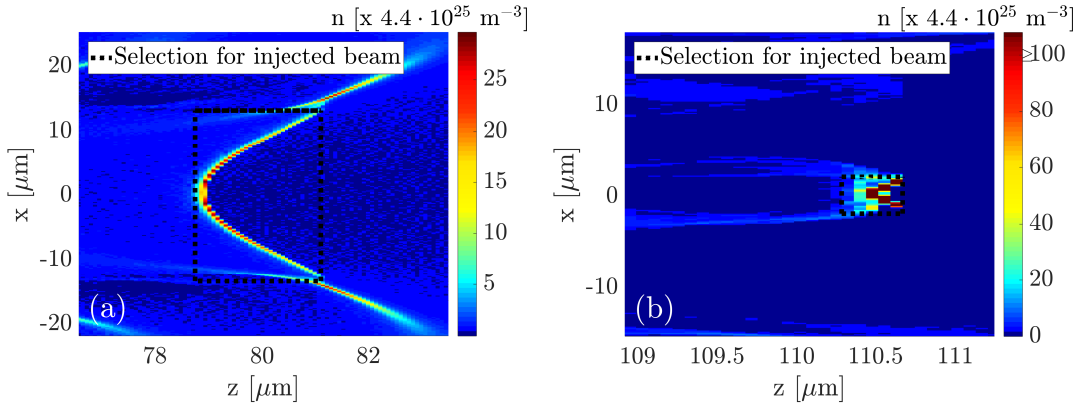

Figure 4.3: Zoom-in of the plasma density region around the injected beam of Figs. 4.1b (a) and 4.1d (b) with the space where the injected beam is defined marked by the black box. The selection is based on the charge-weighted slice energy of this area of the plasma. Within the region injected electrons are further chosen based on a minimum energy of 5 MeV with a positive longitudinal momentum.

quantitative findings presented in Figures 4.5, 4.6 and Table 4.2, respectively. After transverse focusing, the electron bunch exhibits a very large bunch current on the order of 1.25 MA with an overall charge close to 1 nC and an RMS bunch duration of 180 as. These properties make the beam very interesting for radiation generation, although space-charge effects need to be considered as a potential issue regarding beam transport, as is discussed in more detail in Section 4.3.

The energy spectrum in Fig. 4.5 depicts a clear peaked distribution, yet with large side wings, leading to a significant energy spread on the order of 40 %. Since the spectrum is taken only 30 µm behind the trapping point, the mean energy is still quite low despite the large accelerating gradient in the high density plasma.

Finally, in terms of the transverse beam properties, Fig. 4.6 shows a small RMS bunch width below 1 µm, a large divergence and, not surprising based on the initial disk-like shape, an emittance above 1 µm. The beam is radially almost symmetric with small differences between the x- and y-directions attributed to effects due to the laser pulse polarisation direction.

Comparing these 3D results with one- and two-dimensional studies (both by Li et al. [75, 142] and this author [141]), it becomes clear that the injection mechanism itself does work very similarly in all cases, but discrepancies are found in the properties of the injected beam. While some of these can be attributed to different measurement points with Li et al. studying the trapped electrons before their transverse focusing phase, another reason for the different parameters is likely the limitations of 1D and 2D PIC simulations to correctly represent some of

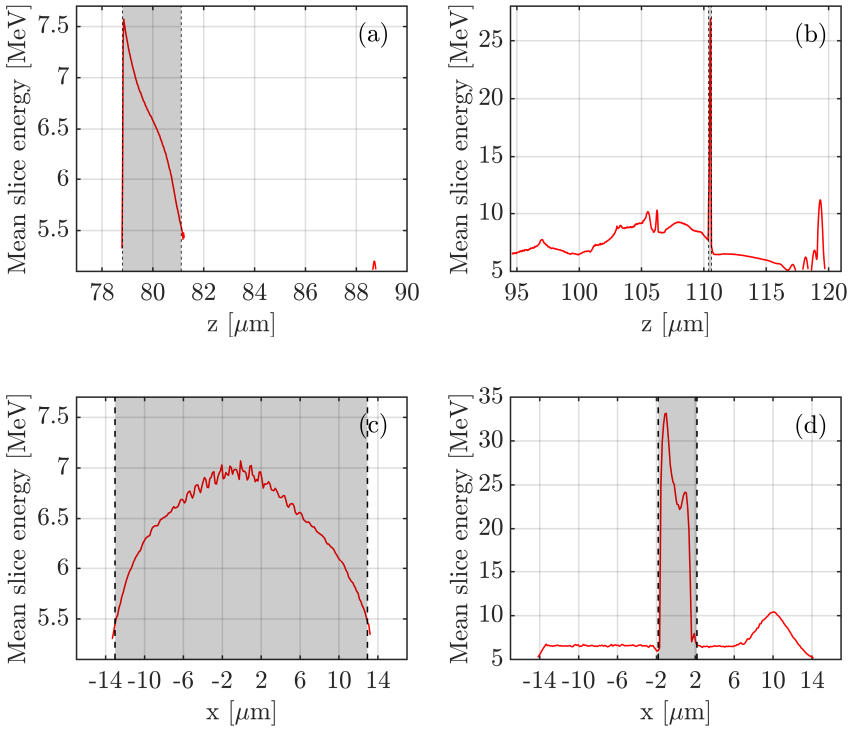

Figure 4.4: Electron energy within the simulation box based on mean values taken across slices in the transverse (a-b) and longitudinal (c-d) direction at two different times just after injection. The grey shaded areas show the region of the energy landscape defined as the injected electron beam based on the charge-weighted slice energy of this area of the plasma. Subplots (a) and (c) correspond to the plasma density plots in Fig. 4.1b, whereas (b) and (d) are taken at the same timing as Fig. 4.1d.

the physical effects relevant in this scenario, such as the laser evolution as well as wavebreaking dynamics. Consequently, a reduced strength of the simulated wavebreaking process in the 2D studies, for example, leads to the underestimation of the injected charge.

Bunch properties after injection	a_0**=6 (3D simulation)**
Charge Q [pC]	912
Mean energy E [MeV]	21.9
Relative energy spread $\Delta E/E$ [%]	43.4
RMS bunch duration σ_t [as]	180
RMS bunch width σ_x, σ_y [µm]	0.77, 0.74
Norm. emittance $\epsilon_{n,x}$, $\epsilon_{n,y}$ [µm]	1.69, 1.37
Bunch current I_b [MA]	1.25

Table 4.2: Injected electron beam parameters after compression, corresponding to the bunch shown in Figs. 4.1d, 4.5 and 4.6.

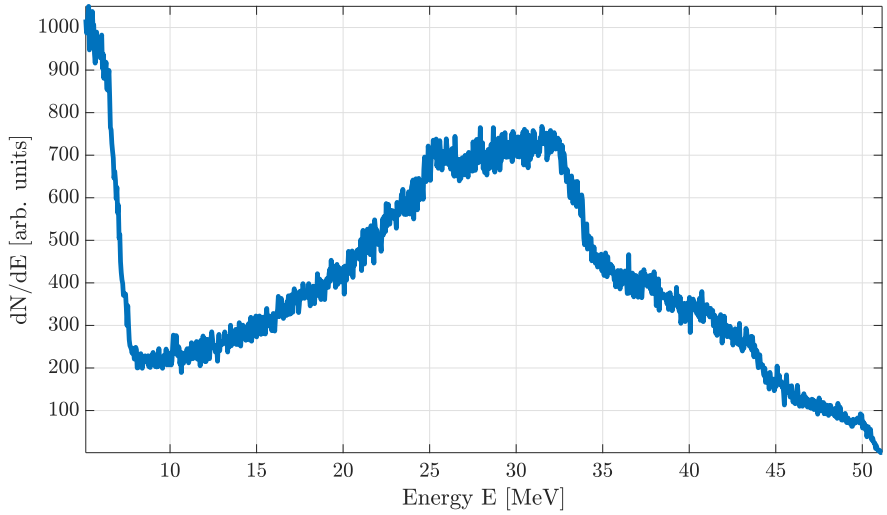

Figure 4.5: Energy spectrum of the injected beam after its compression, corresponding to the plasma density map in Fig. 4.1d.

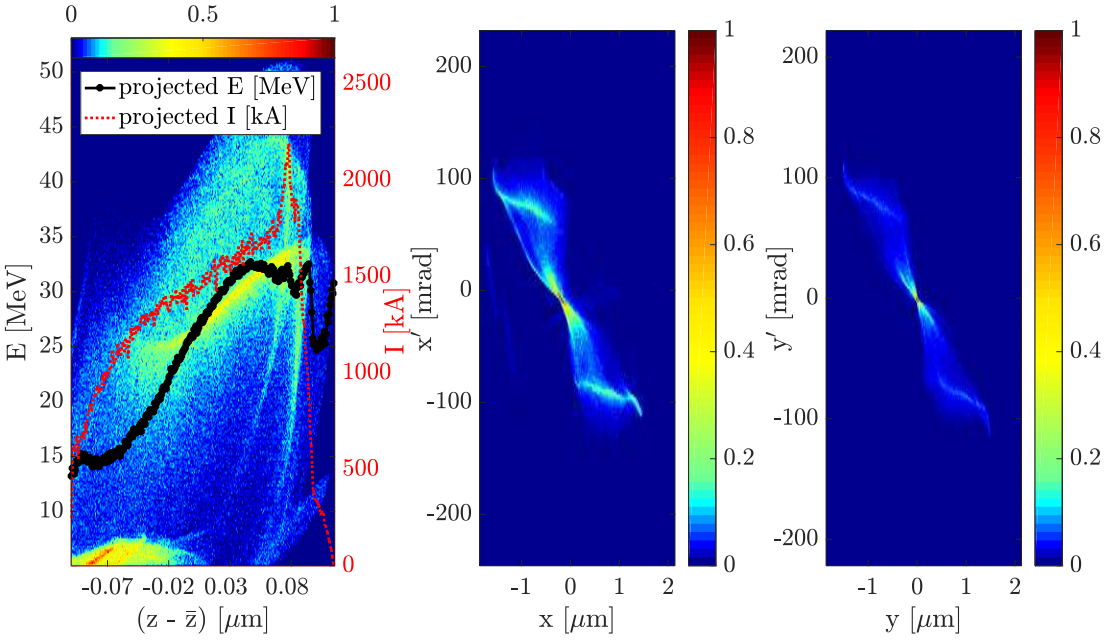

Figure 4.6: Phase-space of the injected beam after its compression, corresponding to the plasma density map in Fig. 4.1d. The colormap describes normalised charge.

4.2 Extension to a New Parameter Regime

Since the initially proposed setup described in the previous section includes a number of complex experimental requirements, such as high laser power of more than 300 TW and an ultrashort plasma density ramp of length 45 µm, an extension of the injection scheme to a wider parameter

range was explored.

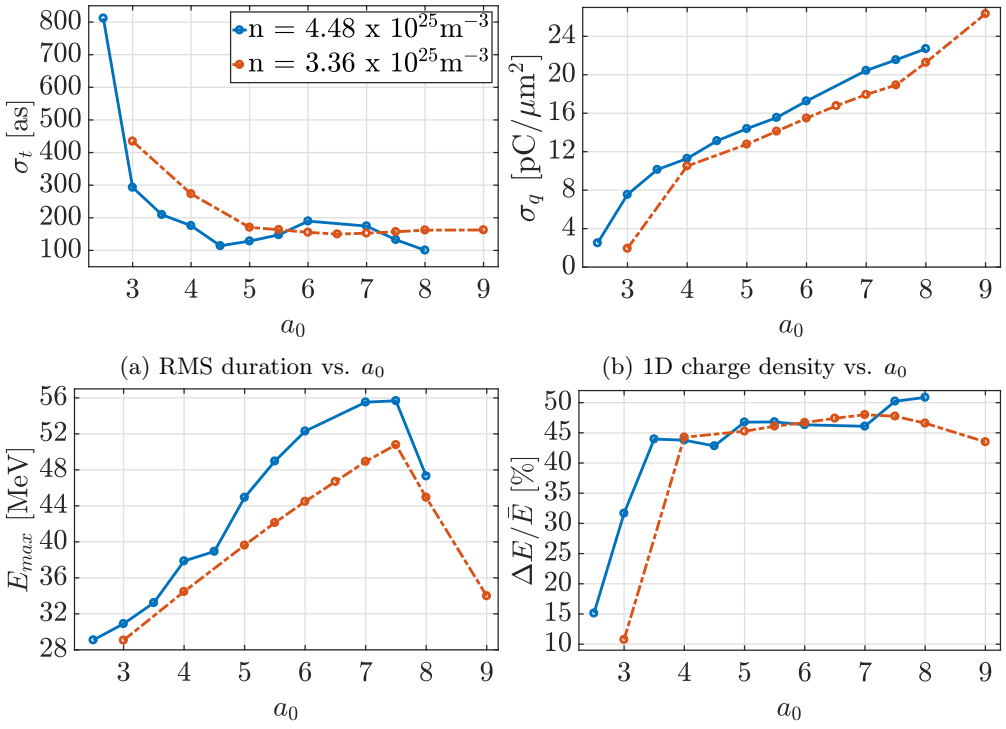

(a) RMS duration vs. a_0

(b) 1D charge density vs. a_0

(c) Maximum energy vs. a_0

(d) Relative energy spread vs. a_0

Figure 4.7: 1D parameter scan: Dependence of the injected beam parameters on laser strength a_0 for two different plasma plateau densities, $4.48 \times 10^{25}\,\mathrm{m}^{-3}$ and $3.36 \times 10^{25}\,\mathrm{m}^{-3}$. In both cases, the upramp has a length of 45 µm and a laser pulse of 6 µm duration (full length) was employed as the driver. The beam parameters are measured around 20 µm after the beginning of the injection process.

A first step towards this goal was a parameter scan based on one-dimensional PIC simulations to study variations in the trapping process and the properties of the injected beam with changes in laser intensity, plasma density, laser pulse length and plasma ramp length. Figures 4.7 to 4.10 present the results of this study with the simulation parameters given in Table 4.3. Clear trends in the dependence on the laser strength and plasma density can be observed and are explained by the following physical behaviours:

- Bunch duration (Fig. 4.7a, 4.8a): As the injected electron bunch consists of a fraction of the first broken plasma wave spike behind the laser pulse, its duration is directly related to the width of this density structure, as described by $\delta n \propto (\beta_{ph} - \beta_m)^{3/2}$ (from Eq. (3.35)). At the end of the plasma upramp, the wakefield phase velocity can be approximated by the laser group velocity $\beta_{ph} \sim \beta_{gr} \sim \left(1 - \frac{n}{2n_{cr}}\right)$; the background electron velocity β_m, on the other hand, is – with the electrons pushed by the ponderomotive force, as

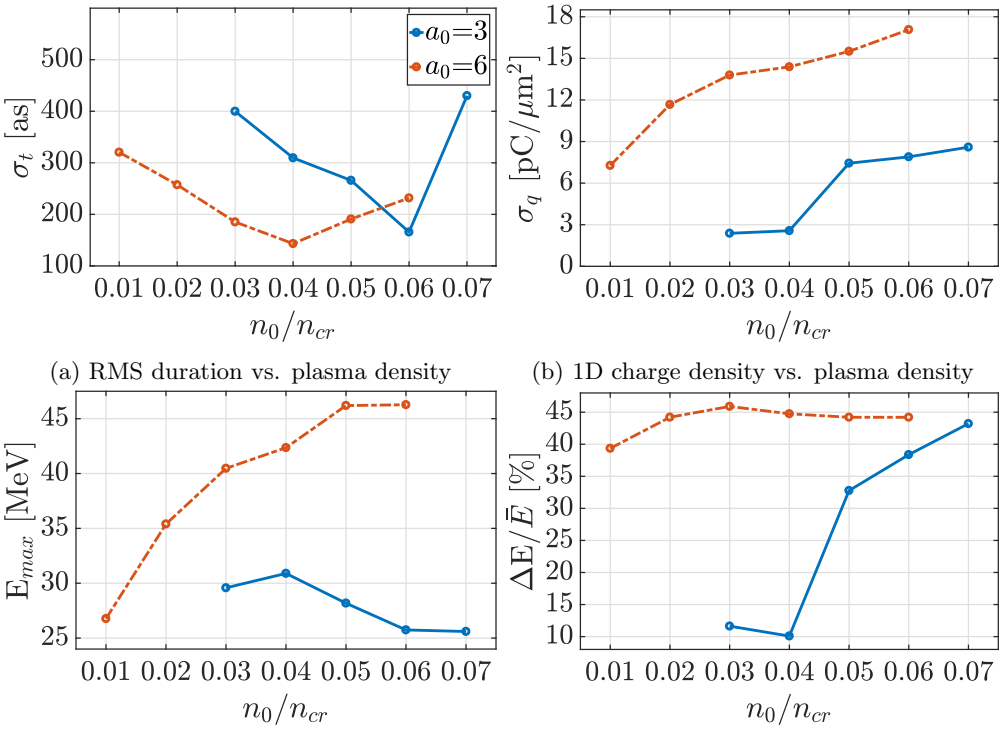

(a) RMS duration vs. plasma density

(b) 1D charge density vs. plasma density

(c) Maximum energy vs. plasma density

(d) Relative energy spread vs. plasma density

Figure 4.8: 1D parameter scan: Dependence of the injected beam parameters on the relative background plasma density n_0/n_{cr} for two different laser strength cases, a_0=3 and a_0=6. For both an upramp length of 45 µm and a full laser pulse length of 8 µm was employed. The beam parameters are measured around 20 µm after the beginning of the injection process.

described in Eqs. (3.6) and (3.7) – proportional to a_0^2 [75]. Both an increase in laser strength and plasma density therefore lead to a reduction of the bunch duration, as is also observed from the parameter scan. The increase in bunch duration for high densities in Fig. 4.8a is likely related to laser depletion, which reduces the effective a_0-value and becomes significant after propagation distances on the order of tens of micrometres for densities of a few percent of the critical plasma density.

- Charge (Fig. 4.7b, 4.8b): The charge of the trapped electron beam scales with a combination of the following factors: 1) the plasma wave spike density, 2) the wave spike width and 3) the fraction of plasma electrons with velocity above the trapping threshold. We can assume the wave spike density to be proportional to n_0, based on Eq. (3.23) from the one-dimensional nonlinear theory in Section 3.2.2, and the fraction of electrons above the trapping threshold to increase with a_0; it thus makes sense that an increase in injected charge is observed both for larger a_0 and higher plasma density. A comparison

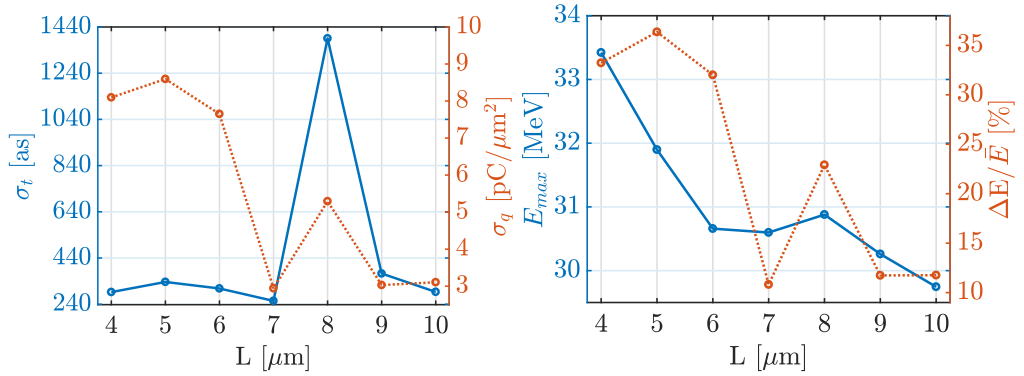

(a) RMS duration (blue), 1D charge density (orange)

(b) Maximum energy (blue), relative enery spread (orange)

Figure 4.9: 1D parameter scan: Dependence of the injected beam parameters on the drive laser pulse length L (full length). A drive laser with a_0=3 as well as plasma of density 4.48×10^{25} m^{-3} and ramp length 45 µm was used in the simulations. The beam parameters are measured around 20 µm after the beginning of the injection process.

Laser pulse	
envelope (long.)	$\sin^2$
wavelength λ [µm]	1.0
peak power P_L [TW]	14.0 – 1,130 (a_0=1 – 9)
full pulse length L [µm]	4.0 – 10.0
Plasma	
plateau density n_0 [m^{-3}]	1.12×10^{25} – 7.84×10^{25}
ramp length R [µm]	20.0 – 140.0

Table 4.3: Input parameters for the 1D OSIRIS simulations presented in the parameter scan in Section 4.2.

with electron beams at other planned or existing facilities, such as the ultrashort SINBAD beam with a surface charge density of 4.5×10^{-3} pC µm^{-2} (from the working point in Chapter 5) or the high charge FACET beam with 0.16–0.48 pC µm^{-2} [143], show that the injected charge density is multiple orders of magnitude larger here within the whole parameter space than what is usually produced in conventional accelerators.

- Maximum energy (Fig. 4.7c, 4.8c): The injected electron beam energy depends on the product of accelerating field amplitude and acceleration distance. With the field strength proportional to $a_0^2\sqrt{n_0}$, it is thus no surprise that the maximum energy increases with both a_0 and n_0. For higher plasma density, laser depletion and dephasing limit the effective acceleration distance, such that the maximum energy gain scales with $a_0^2 n_0^{-1}$ and a reduction of the beam energy is expected at high n_0. The sharp decrease in maximum energy at high values of a_0, on the other hand, is likely caused by beamloading effects

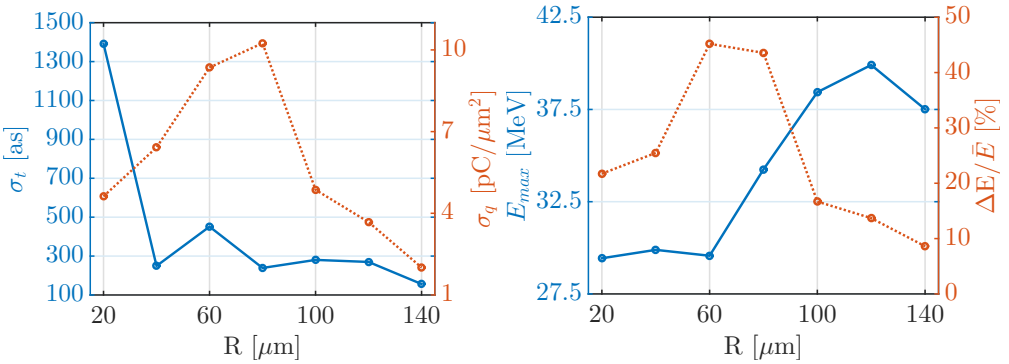

(a) RMS duration (blue) and surface charge density (orange)

(b) Maximum energy (blue) and relative enery spread (orange)

Figure 4.10: 1D parameter scan: Dependence of the injected beam parameters on the plasma upramp length R. A drive laser with a_0=3 and full pulse length of 6 µm as well as a plasma of density $4.48 \times 10^{25}\,\mathrm{m}^{-3}$ was used in the simulations. The beam parameters are measured around 20 µm after the beginning of the injection process.

due to the large injected charge which affect the wakefield experienced by the electrons and decreases the effective accelerating gradient.

- Energy spread (Fig. 4.7d, 4.8d): The behaviour of the beam energy spread can be divided into two regimes: at low a_0, the spread depends on the gradient of the accelerating field and hence increases with rising plasma density, as the wakefield steepens. In the more nonlinear regime (i.e., at high a_0 and/or n_0) the injected beam charge becomes large enough to generate its own space-charge field; this effect dominates the effective field gradient experienced by the electrons across the beam to an extent where a variation in laser or plasma parameters no longer varies the wakefield gradient strongly.

The effect of the drive laser pulse length on the injected beam properties is by far not as clear as the previously described dependences on laser and plasma properties. At a closer look, however, the behaviour in Fig. 4.9 can be divided into two parameter regions: one below L =7 µm and one above. Below this threshold, the laser pulse does not interact directly with the beam, as its full length is shorter than the nonlinear plasma wavelength ($\approx 7.8\mu$m from Eq. (3.22)); the beam properties vary smoothly. For laser pulse lengths above 7 µm, though, the laser pulse starts to overlap with the electron beam and influences its evolution. In this case, the beam properties vary erratically for different pulse lengths, as the exact position of the beam in the laser pulse becomes relevant and hence the experienced laser field amplitude changes depending on laser duration.

With regard to the dependence on the upramp length two different trends can be observed:

on the one hand, Fig. 4.10 shows an increase in the maximum energy and decrease in the bunch length for longer ramps. This is caused by the effect of a longer ramp in decreasing the ramp density gradient and hence also the plasma wave phase velocity β_{ph} (see Eq. (3.34)), as the density gradient dn/dz on the upramp can be described by n_0/R for a linear ramp and hence $\beta_{ph} \propto (1-(|\xi|n_0)/(2nR))^{-1}$. Thus, narrower and steeper wave spikes are created leading to a shorter injection and slightly stronger wakefield. If the upramp is too long, however, β_{ph} drops below 1, as the denominator in Eq. (3.34) exceeds the value of β_{gr}; in this case wavebreaking becomes possible again and, if the plasma wave is nonlinear enough, trapping occurs prematurely along the ramp in a less sudden way hence injecting less charge. This effect of premature wavebreaking starts to occur in the ramp length range between 100 µm and 140 µm, but is found to become stronger with longer ramps, such that for ramp lengths of approximately 150 µm and above many of the desirable properties of the injection scheme are expected to be lost due to a different way of wavebreaking. Similarly, for too short upramps these wave crests are not compressed as strongly and so a smaller electron fraction is trapped here, too. In both cases, the consequences are lower charge and less energy spread, due to the reduced beamloading effect, in the edge regions of Fig. 4.10.

Overall, a wide range of system parameters is hence available for the electron injection. In particular, the required minimum laser strength for the trapping process was reduced by a factor of 2 (factor of 4 in laser intensity) compared to Li et al.'s studies through optimisation of the laser and plasma properties. It should be noted, though, that below the minimum a_0 values shown in Fig. 4.7 wavebreaking does not occur at all or at a significant distance behind the end of the density ramp. Under these circumstances, the injected electrons do not exhibit the short bunch length and high charge characteristic of the upramp-assisted self-injection process.

Whereas these one-dimensional parameter scans provide a good qualitative overview over the useful parameter range, they, unfortunately, cannot offer a reliable quantitative description of the injection process, as various transverse effects, such as laser self-focusing and transverse injection, are not considered in the simulations leading to inaccurate beam features, such as an underestimation of the injected charge, as discussed earlier. Nonetheless, based on the 1D findings, a potentially interesting regime at lower laser strength of a_0=3 can be defined with $0.03 \leq n_0/n_{cr} \leq 0.04$, L $\lesssim \lambda_{Np}$ and 100 µm≤R≤120 µm in order to satisfy the following requirements:

- attosecond injection
- maximised beam energy

- minimised energy spread
- no direct interaction with the drive laser

A more detailed, 3D-simulation-based study of this regime was undertaken with the results presented in Figs. 4.11 and 4.12 as well as in Table 4.5. The simulation input parameters are listed in Table 4.4.

Laser pulse	
envelope (long./transv.)	$\sin^2$ / Gaussian
wavelength λ [µm]	1.0
peak power P_L [TW]	125.8 (a_0=3)
full pulse length L [µm]	6.0
pulse width ($1/e^2$ radius) w_0 [µm]	25.5
Plasma	
plateau density n_0 [m^{-3}]	3.36×10^{25}
ramp length R [µm]	100.0 (z = 23 – 123 µm)

Table 4.4: Input parameters for the 3D OSIRIS simulation presented in Section 4.2.

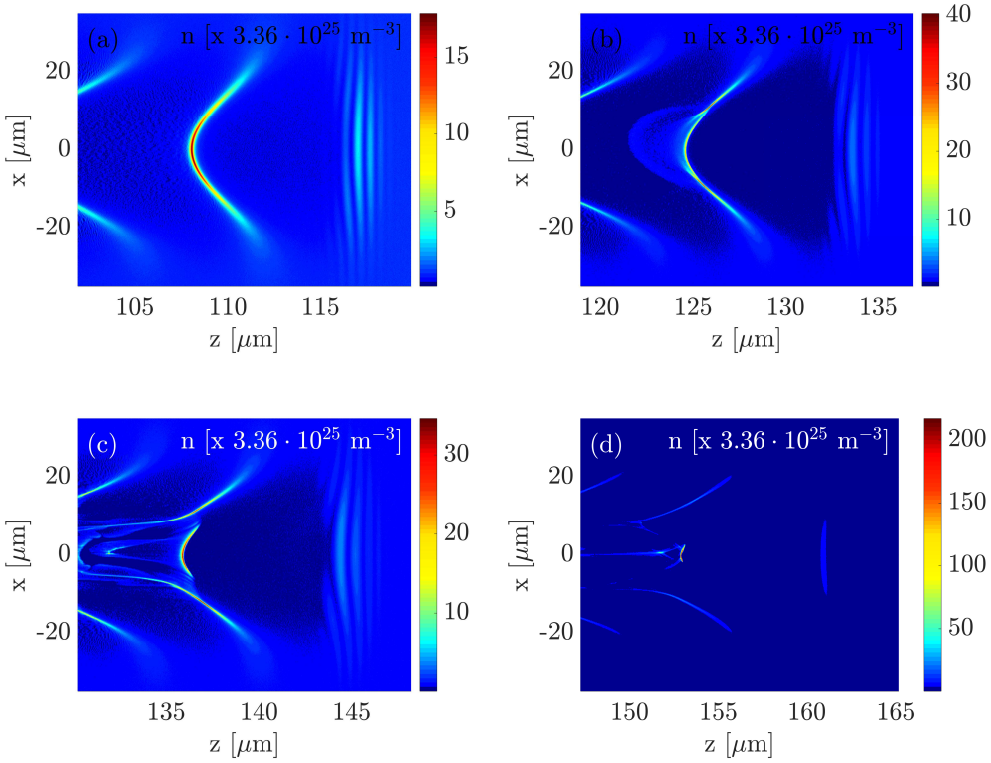

Figure 4.11: Evolution of the plasma density structure around the trapped electron bunch before (a) and during (b-d) upramp-assisted self-injection for a drive laser with strength a_0=3. The setup of this 3D simulation is described in Table 4.4.

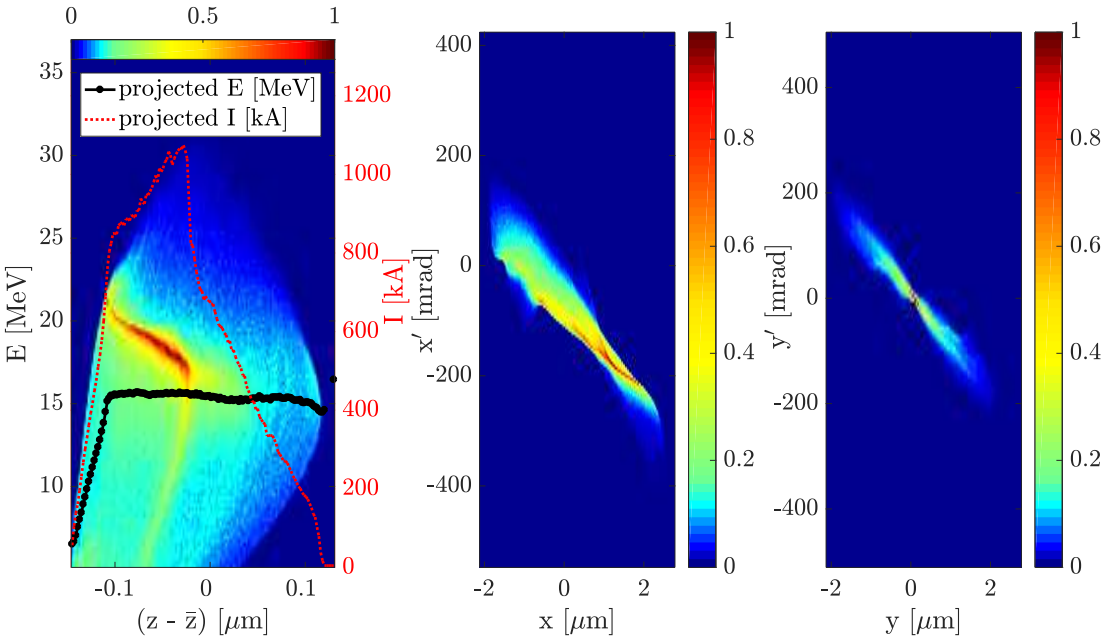

Figure 4.12: Phase-space of the injected beam after its compression, corresponding to the plasma density map in Fig. 4.11d. The colormap describes normalised charge.

Bunch properties after injection	a_0**=3 (3D simulation)**
Charge Q [pC]	519.2
Mean energy E [MeV]	15.14
Relative energy spread $\Delta E/E$ [%]	33.99
RMS bunch duration σ_t [as]	195
RMS bunch width σ_x, σ_y [μm]	1.04, 0.95
Norm. emittance $\epsilon_{n,x}$, $\epsilon_{n,y}$ [μm]	1.41, 1.09
Bunch current I_b [MA]	0.551

Table 4.5: Injected electron beam parameters after compression, corresponding to the bunch shown in Fig. 4.11d and 4.12.

From Fig. 4.11 it can be seen that the injection process behaves similar to the high-a_0 case. However, a smaller fraction of the wave spike is trapped due to the decreased nonlinearity of the system, which is also observable in the slightly less chaotic structure of the remaining wakefield behind the injected beam. Consequently, although the electron beam is still ultrashort with an RMS duration of 195 attoseconds, its charge is reduced by a factor of almost two with respect to the case in Section 4.1. With a bunch current of 551 kA, the beam is still very dense, yet promises better stability than in the previous regime. Besides this main feature, most of the properties of the electron sheet are similar at lower laser power. The reduced beam energy, energy spread and slightly larger transverse dimensions are likely related to the weaker longitudinal and transverse wakefield forces acting on the beam at a_0=3.

One can also observe, in particular, that the scalings made by the one-dimensional scans fit well with the results of the full 3D simulation in most aspects, as the predictions for lower charge, energy and energy spread at a_0=3 are all fulfilled. The only component not described correctly is the bunch length: here an important factor is the much larger absolute charge observed in 3D (3D: 519.2 pC, 1D: 18.9 pC assuming Gaussian shape and 1 µm RMS bunch width); its space-charge forces cannot be accurately described in 1D and so are not taken into account. As the three-dimensional studies show, though, these likely act as a limiting factor regarding the minimal achievable bunch duration.

4.3 Propagation of the Electron Beam within the Plasma

With the prospect of using the generated attosecond electron beam characterised in the previous section for applications, the acceleration and final extraction from the plasma of the injected bunch was investigated through further 2D and 3D simulation studies.

Acceleration

Figure 4.13 shows the evolution of the electron density around the injected beam after the initial trapping, based on the simulation parameters in Table 4.4. After reaching its transverse and longitudinal minimum size, the beam expands again and reforms to a broad disc shape similar to its initial form just after injection.

The evolution of the electron bunch itself is presented in Fig. 4.15 together with a comparison with the previously described a_0=6 reference case (Section 4.1) in Fig. 4.14. The initial injection phase is marked by a dotted, yellow line in Fig. 4.14; it is defined by the stabilisation of the beam charge after an initial ultrafast increase in charge (Fig. 4.14, marker a) followed by a quick loss of a large fraction of electrons (Fig. 4.14, marker b). Simultaneously with this evolution, the beam contracts, as can be seen in the development of the longitudinal and transverse beam sizes. The next stage of the beam evolution is defined by a rapid increase in beam energy over a few tens of micrometres up to around 50 to 60 MeV (Fig. 4.14, marker c). Afterwards, the beam starts to deteriorate in quality, as it blows up transversely, stagnates in mean beam energy and slowly increases in length during the next 100 µm (Fig. 4.14, marker d).

The stagnation in beam energy can be observed clearly from the evolution of the beam energy spectra in Fig. 4.15. A distinct peak appears early on in the beam acceleration which increases in energy until around z$\sim$192 µm. After this point the maximum energy of the beam remains constant or increases slightly, whereas the position of the energy peak moves back

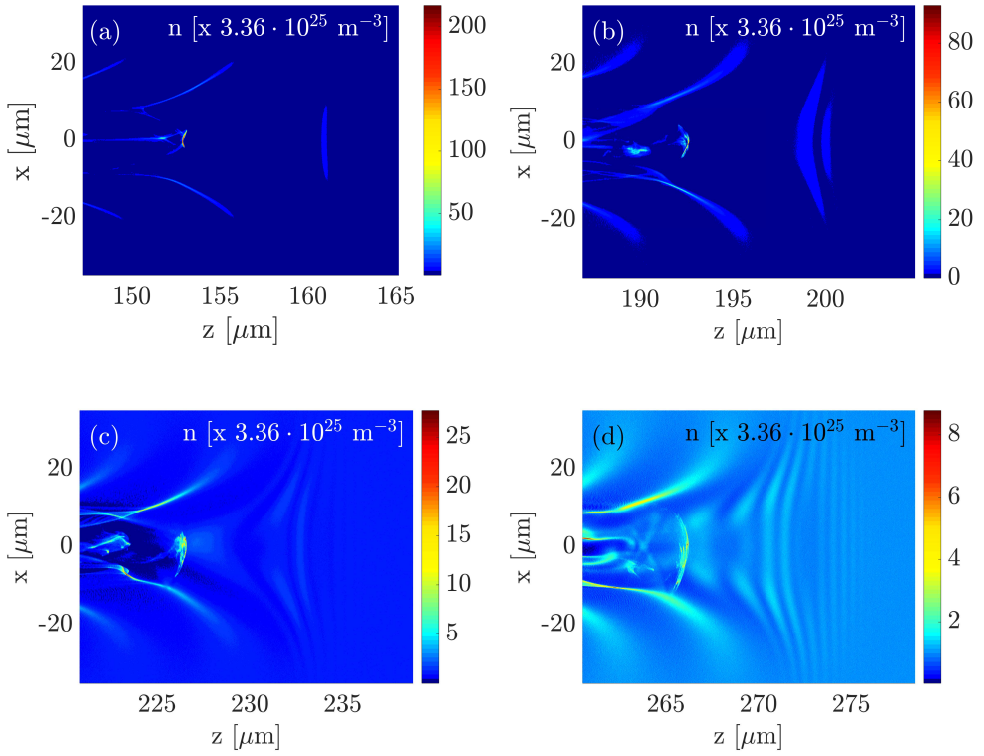

Figure 4.13: Evolution of the plasma density structure around the trapped electron bunch during its acceleration in plasma for a drive laser with strength a_0=3. The setup of this 3D simulation is described in Table 4.4.

towards lower energies indicating a deceleration of a large fraction of the beam.

	Q [pC]	γ	σ_t **[fs]**	I_b **[kA]**	K_{sc}
a_0=3 Ref. Case	519.2	29.58	0.195	551.0	2.51×10^{-3}
a_0=6 Ref. Case	912.0	42.79	0.180	1250	1.88×10^{-3}
SINBAD	0.7	195.39	0.8	0.349	5.51×10^{-9}
SPARC_LAB [144]	20	152.4	29	0.275	9.14×10^{-9}
ATF	100-500	97.69	100-500	0.398	5.00×10^{-8}
FACET [143]	1000-3000	39078	60-200	5.98-6.65	$1.18\text{-}1.31 \times 10^{-14}$
FLASH2 [27]	20-100	781.6-2344	3-50	0.798-2.66	$7.28\text{-}655 \times 10^{-12}$

Table 4.6: Comparison of the perveance K_{sc} and other beam parameters of the simulated electron beams in Sections 4.1 and 4.2 with beams from various planned and existing accelerator facilities. Note that the variation in longitudinal perveance values is expected to be even stronger due to the comparably low energies of the self-injected electron beams; they are not listed here due to its dependence on beam aspect ratio, which may vary strongly across longer beamlines.

This drastic beam evolution is observed for both the a_0=3 and a_0=6 cases with a few differences in the overall very similar behaviour. One in particular is the increased strength

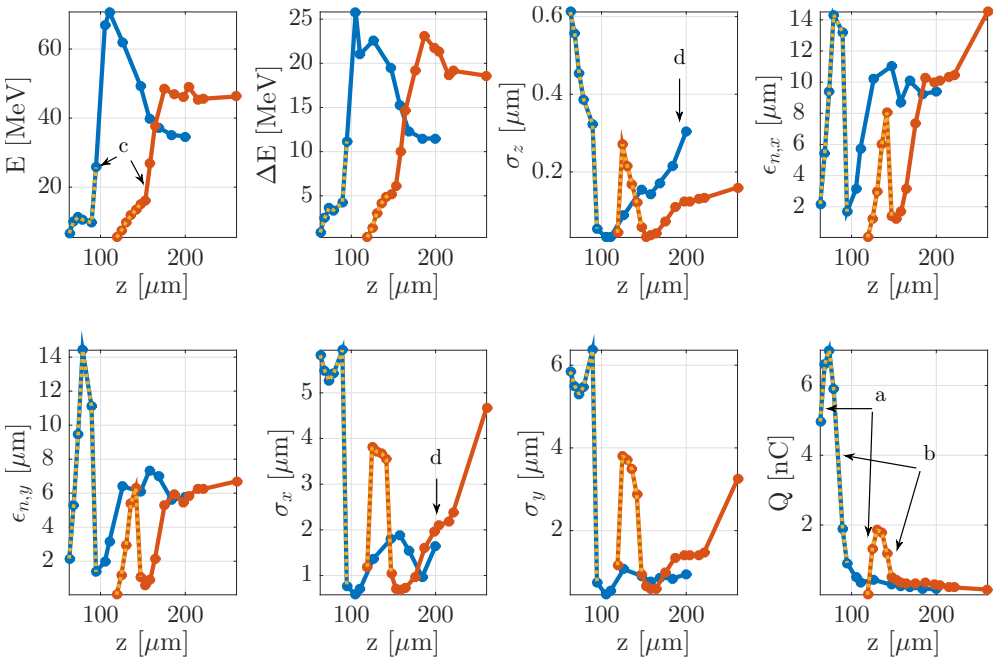

Figure 4.14: Evolution of the injected beam parameters during trapping and acceleration for the a_0=3 (red) and a_0=6 (blue) reference cases, described in Sections 4.2 and 4.1. The yellow dotted line marks the initial injection phase in each case.

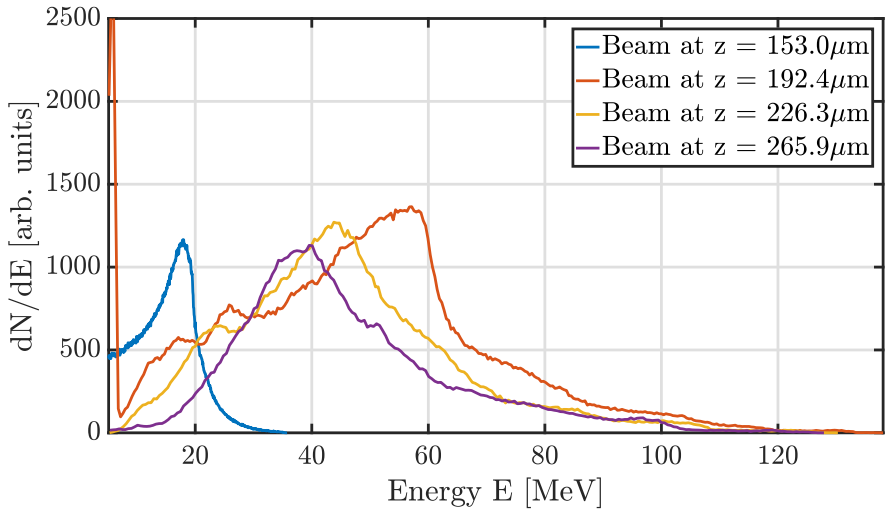

Figure 4.15: Evolution of the energy spectrum of the injected electron beam during acceleration for a drive laser with strength a_0=3. The four spectra correspond to the density maps in Fig. 4.13, respectively.

and speed of the beam development in the a_0=6 setup where the beam starts off with more than three times the charge and around double the transverse size compared to the lower laser strength scenario. As a consequence, it also deteriorates more violently with a strong decrease

in mean energy towards the later stages of propagation as well as a triplication of the beam length after 100 µm.

The strong beam development during propagation in the plasma, as observed here, can be explained by a combination of two factors:

- the effect of the electron beam wakefield caused by the very high bunch density,
- and the depletion of the drive laser pulse and the wakefield it generates.

Table 4.6 shows a comparison of the current and perveance, a measure for the strength of a beam's transverse space-charge forces (see Section 2.3 for details), for a number of example cases of electron beams used in different existing and planned accelerator facilities. The large perveance values of the beams generated through upramp-assisted injection, which are up to eleven orders of magnitude larger than other RF-accelerated beams, demonstrate that extremely strong space-charge forces and beamloading fields are expected from the bunch. These lead to the initial stop of the injection process as well as the initial loss of a large fraction of low energy electrons after the injection starts.

In a highly nonlinear plasma wave, as is present initially in the shown simulations, the bunch can, nonetheless, be contained and even accelerated due to the strong wakefield; this is observed in the stage of quick acceleration in Fig. 4.14. However, nonlinear plasma wakefields at high density have short depletion lengths, as the laser energy is quickly drained to drive the wakefield. The effect on the laser itself can be seen in Fig. 4.16: as part of the depletion process the laser pulse reshapes, elongates and loses intensity (Fig. 4.16a) [146]. On the one hand, as Fig. 4.16c shows, the total energy of the laser pulse decreases significantly due to its driving of the plasma wave. Note here that, due to limitations in the simulation code, the calculated laser field cannot be entirely separated from the plasma wakefield, so that the energy values shown include the latter as well as the plasma wakefield and electron beam self-field in the x-direction as components; the depicted laser energy is hence, particularly at longer propagation distances, slightly overestimated. Nonetheless, the observed energy loss is consistent in order of magnitude with the theoretically estimated laser depletion length demonstrating the distance at which 50 % of the laser energy is absorbed by the plasma; based on Eq. (3.39) and taking into account the FWHM laser pulse length as well as the maximum accelerating wakefield reached at the end of the plasma ramp, a value of 176 µm is found[1]. On the other hand, as Figs. 4.16a and 4.16b demonstrate, the change in laser shape also plays a relevant role in the acceleration process.

[1] Some variations between the analytical and simulation results (from Fig. 4.16c) are expected due to the plasma upramp during which the plasma wave is not driven as strongly at lower densities and the laser is thus expected to lose less energy than theoretically assumed.

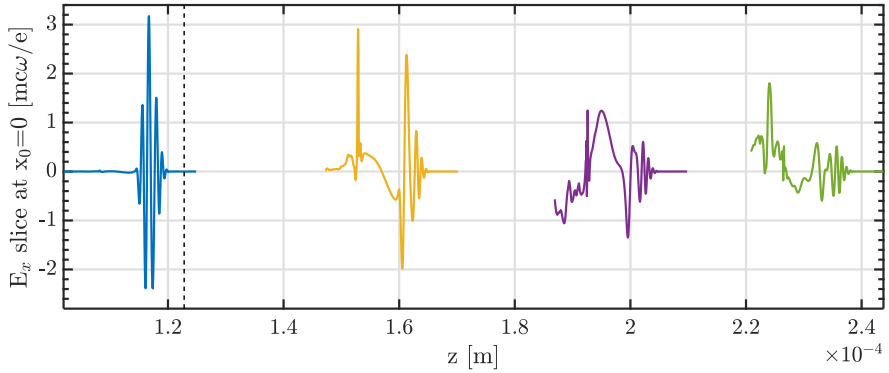

(a) Longitudinal laser profile evolution.

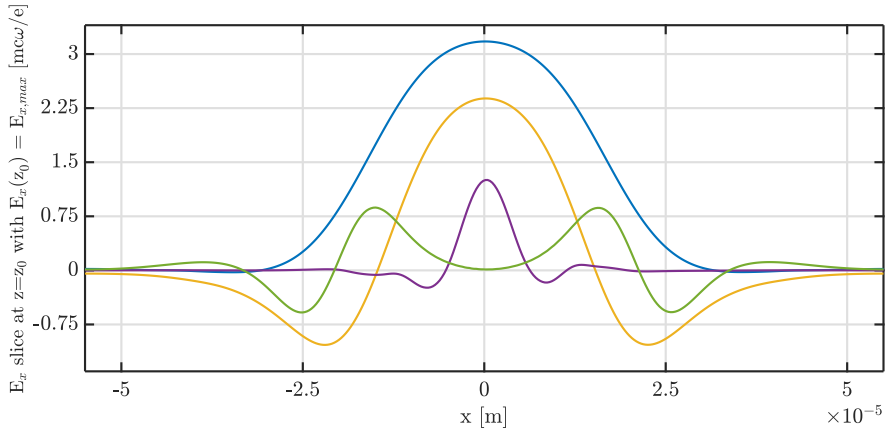

(b) Transverse laser profile evolution.

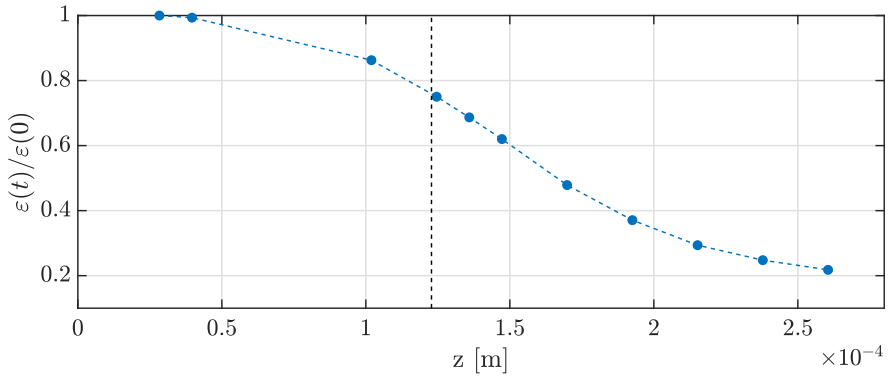

(c) Laser energy depletion.

Figure 4.16: Evolution of the drive laser energy (c) and profile both longitudinally (a) and transversely (b) after propagation through plasma with a drive laser of strength a_0=3. The colours in subfigure (b) correspond to the laser positions shown in subfigure (a). The longitudinal profiles are taken at x=0, while the transverse profiles are calculated at the position of maximum on-axis field amplitude. The dashed, black line in (a) and (c) denotes the position of the end of the plasma upramp. The relative laser energy in subplot (c) is calculated from $\varepsilon = \int_V \epsilon_0 |\mathbf{E}|^2 dV$ [145] considering the electric field in the transverse x-direction throughout the whole simulation box.

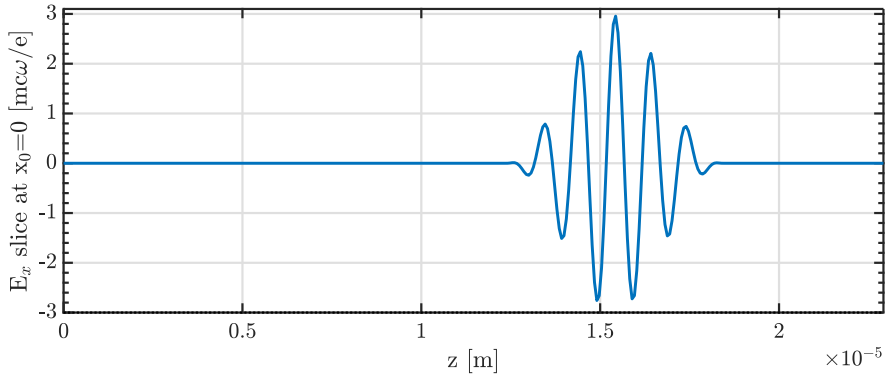

(a) At the plasma entrance

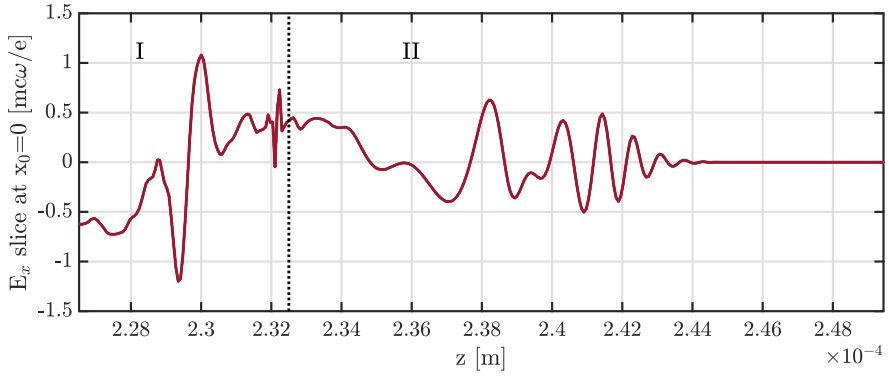

(b) After ∼220 µm propagation in the plasma

Figure 4.17: Longitudinal profile of the electric field in the direction perpendicular to the laser propagation at x_0=0 before and after entering the plasma for a drive laser with a_0=3. In (b) region II marks the field caused solely by the drive laser, while region I includes the wakefield generated by the injected electron beam positioned close to the dotted line.

With the position of the injected electron beam given by the thin, high spike in the back of the last three E_x slices, it can be seen that the laser pulse very soon starts to increase in length and overlaps with the electron beam thus completely changing the fields the beam experiences. The same phenomenon is observed when looking at the transverse laser pulse profile evolution, as in Fig. 4.16b, where the shape of the transverse slice changes as the curvature and length of the back of the laser pulse varies over time.

A main consequence of this laser evolution is that the laser wakefield experienced by the electron beam decreases to the point where, as shown in Fig. 4.17b, the self-fields of the bunch (region I) become dominant over the external fields (region II). As a result the back of the electron beam is no longer accelerated and focused leading to a lengthening of the beam by, on average, 118 nm per 100 µm as well as its deterioration in quality. The combination of these effects coming together can be observed in Fig. 4.18 depicting a lineout of the total longitudinal

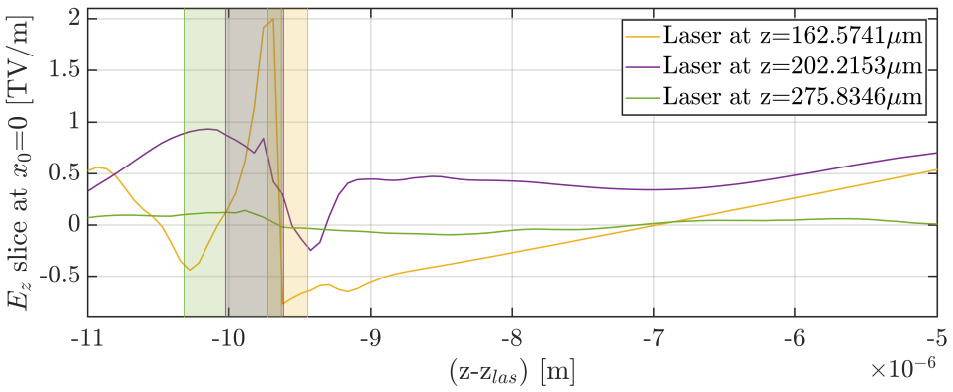

Figure 4.18: Longitudinal profile of the electric field in the direction parallel to the laser propagation at x_0=0 for three different laser positions during propagation in the plasma. In each case, the position and size of the injected witness electron beam is shown relative to the field distribution as a shaded area. The longitudinal position is provided relative to the centre of the drive laser pulse (z-z$_{las}$). Note that the laser positions correspond to those shown in some of the curves in Fig. 4.16 with the line colours being the same in both figures.

field around the witness beam. Showing the field at three different propagation distances, in each case the electron beam position and size is indicated by the shaded area in the respective colour of the field curve. On the one hand, the evolution and degradation of the laser-driven wakefield can be seen clearly, as its shape changes and the amplitude decreases at later laser positions. On the other hand, however, the beamloading field can also be observed starting within the region occupied by the witness electron beam. Initially, this field is seen to be strongly decelerating due to the high beam density, yet only affects the back of the bunch thanks to its short duration. At later laser positions, as the beam elongates, the amplitude of the beamloading effect decreases due to the decreased beam density, but a larger fraction of the bunch becomes affected, an effect that is enforced by the depletion of the accelerating laser-driven wakefield.

Extraction

Figures 4.19 and 4.20 depict the results of 2D PIC simulations studying a possible extraction of the self-injected electron beam, described in Section 4.2, from the plasma. Due to the fast evolution of the beam, discussed in the previous section, short, linear plasma density downramps were placed at the end of its acceleration phase (z=167 µm) after which deterioration of the bunch is observed. Moreover, two different downramp lengths were compared: on the one hand, a ramp with 30 µm length – in order to minimise beam deterioration in the plasma – and, on the other hand, a ramp of length 150 µm – for a slower, more stable reduction of the focusing

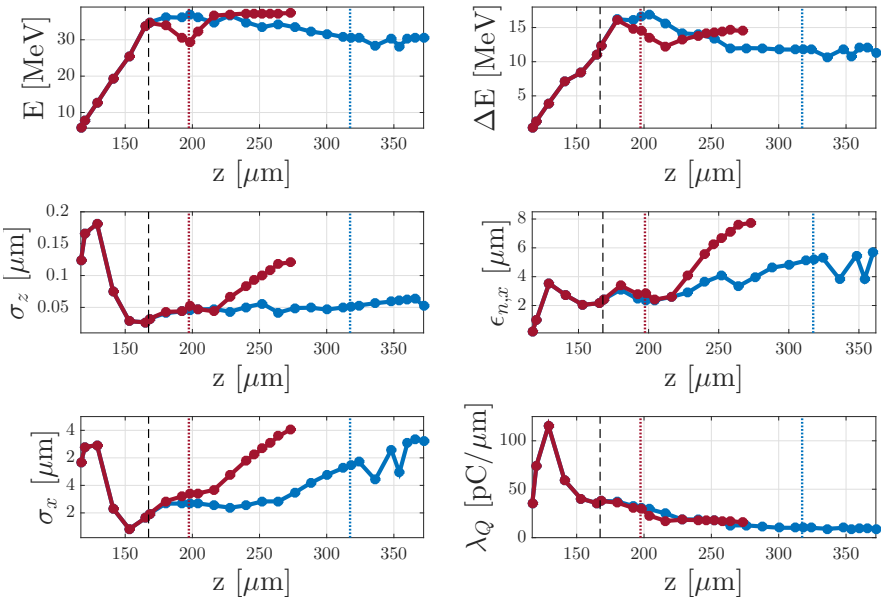

Figure 4.19: Evolution of the injected beam parameters during trapping, acceleration and extraction from 2D simulations based on the parameters in Table 4.4. Extraction from the plasma is achieved through density downramps of length 30 µm (red solid line) and 150 µm (blue solid line), respectively, with the black dashed line showing the start of the downramp and the red (blue) dotted lines the end of the short (long) ramp.

fields and hence more controlled broadening of the beam as the focusing forces are decreased.

As Fig. 4.20 demonstrates, the beam quality at the end of the plasma ramp is in both cases quite low, with the extracted electron bunch being highly non-Gaussian and exhibiting a large bunch width as well as filamentation. Moreover, for the short downramp case, depicted as the red line in Fig. 4.19, a strong blow-up of the beam dimensions is visible after it enters the vacuum with a 75 % increase in both longitudinal and transverse beam size within less than 50 µm propagation. This phenomenon is a consequence of the electron beam space-charge forces, which are still very high despite continuous charge losses along the downramp and which can now no longer be compensated by the plasma wakefield.

On the other hand, for the longer downramp, shown as the blue line in Fig. 4.19, the beam blow-up stays below 35 %; this is likely caused by the continued decrease in beam charge on the longer ramp (73.0 % instead of 21.6 % for the short ramp) as well as a slower decrease of the plasma focusing forces. In this setup, however, the beam evolves more strongly in the plasma leading to a more complex filamentation of the beam structure; the jumps in the energy spread and emittance evolution between z=324 µm and 360 µm, for example, are caused by this splitting of the beam structure, so that different parts of the bunch separate and recombine as they evolve individually in vacuum.

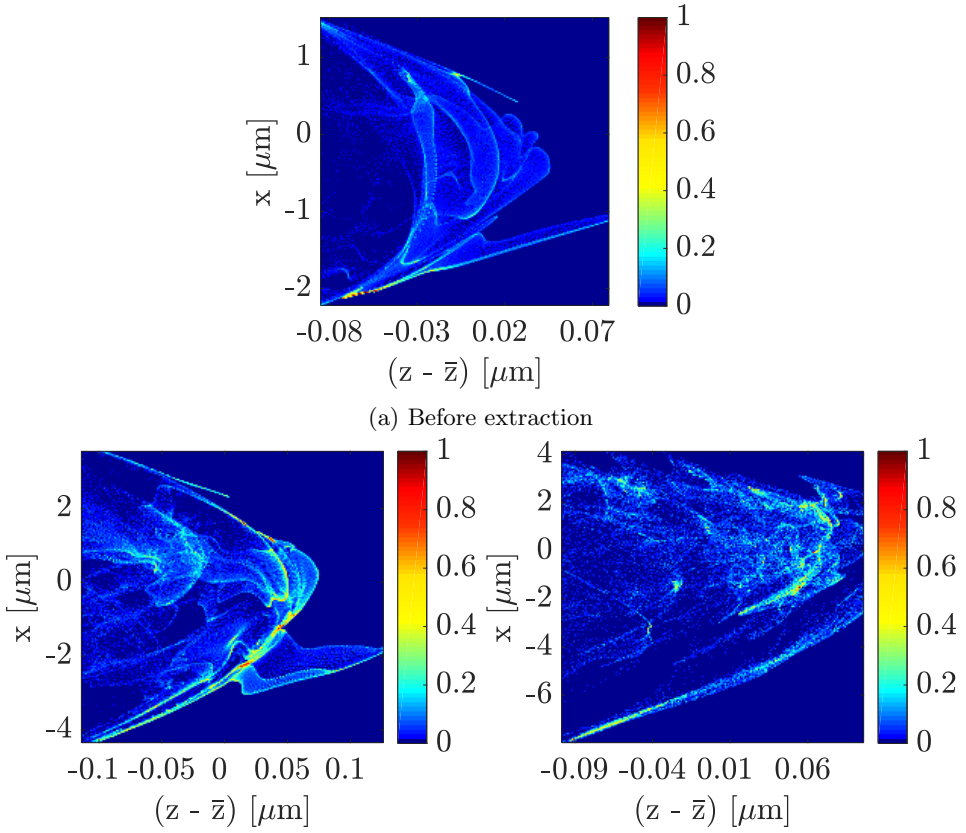

(a) Before extraction

(b) After extraction through a short ramp

(c) After extraction through a long ramp

Figure 4.20: Z-x space of the injected electron beam before (a) and after extraction from the plasma for downramps of different length (b,c). The data corresponds approximately to the positions marked by the dashed and dotted lines representing the beginning and end of the downramps in Fig. 4.19. The colormap describes normalised charge.

Overall, in both cases an electron beam with mean energy around 30 MeV, energy spread below 50 % and RMS bunch length below 180 as (full beam length below 800 as) is extracted, as shown in Table 4.7. The use of a short downramp is found to be preferable, as strong focusing placed directly behind the plasma may allow for the capture and controlled transport of the beam. With a longer plasma ramp the level of focusing at the plasma end can be decreased, but the electron beam has already deteriorated in quality irreparably at this point. In all cases, it should be noted that capturing the beam behind the plasma with focusing elements will be challenging due to the strong space-charge effects on the beam and will likely require less conventional techniques, such as plasma lenses, which go beyond the scope of this thesis. If successful, however, additional beam transport behind the plasma stage may also be able to clean up the bunch structure, for example through cutting off low charge tails with beam collimators. Variations of this parameter range could, of course, be achieved through tuning of

Bunch properties after extraction	30 µm ramp	150 µm ramp
2D charge density λ_Q [pC/μm]	29.70	10.22
Mean energy E [MeV]	29.34	30.53
Relative energy spread $\Delta E/E$ [%]	49.41	38.68
RMS bunch duration σ_t [as]	176.4	173.4
Full bunch length $\sigma_{t,full}$ [as]	796.7	646.7
RMS bunch width σ_x [μm]	1.69	2.74
Norm. emittance $\epsilon_{n,x}$ [μm]	2.83	5.26

Table 4.7: Electron beam parameters after extraction with plasma downramps of different length: Initial parameters used in the simulation included a laser length of 6 µm, width of 25.5 µm and plasma density of $3.36 \times 10^{25}\,\mathrm{m}^{-3}$ with a 100 µm ramp. Note that the beam charge is mentioned in later chapters as a full 3D charge value; this has been approximated from the calculated 2D charge density assuming a radially symmetric Gaussian beam, such that $Q \sim \lambda_Q \sqrt{2\pi}\sigma_x$.

the start and end positions of the plasma downramp as well as the general laser and plasma parameters.

A comparison of the simulated electron beams from upramp-assisted self-injection with experimental bunch length measurements of other beams from a variety of injection mechanisms is depicted in Fig. 4.21. When looking at the physical background for the electron beam lengths in the different self-injection cases, two different regimes have to be distinguished. The results by Debus et al., Buck et al. and Heigoldt et al., who generate their electron beams through self-injection in the nonlinear or bubble regime, all follow the same tendency as the simulation-based studies with higher values of a_0 leading to shorter bunch lengths. In these cases, the beam is formed from a fraction of one of the first plasma wave spikes behind the laser pulse; as the waves become denser and steeper with increasing nonlinearity, the injected electrons also form more compact bunches with trapping cut off faster due to beamloading from the typically higher charge. In the upramp-assisted injection scenario this is amplified further by the steepening effect that the density ramp has on the wave crest shape leading to a drop in bunch length by more than one order of magnitude with a doubling of a_0. The experiments by Islam et al. and Lundh et al., on the other hand, employed different trapping techniques - near-threshold and colliding pulse injection, respectively - for which the injected beam length is dominated by factors other than the wakefield nonlinearity. In these cases, a comparably short electron bunch duration can hence be achieved at lower laser strengths.

However, the nonlinearity of the plasma wave through a high laser intensity is not the only feature that makes the plasma injector setup for the proposed upramp-assisted self-injection technique different from many other injection methods. Instead the scheme also requires most prominently a high plateau plasma density, compact plasma target and few-cycle laser pulse

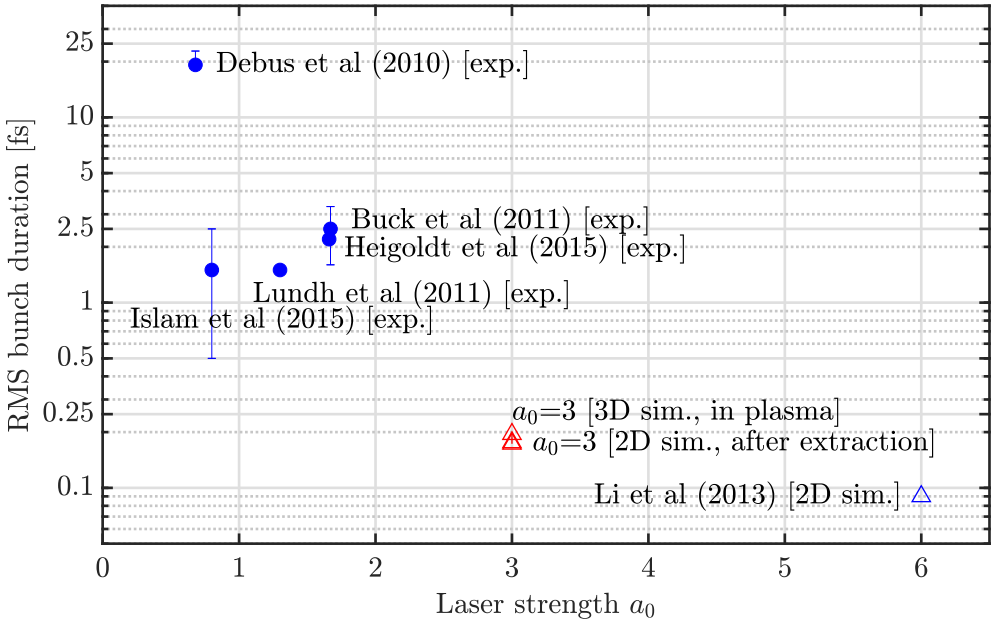

Figure 4.21: RMS bunch length as a function of laser strength a_0 for published experiments (round dots) in different setups and simulations (triangles) of the upramp-assisted self-injection technique. The red data point shows the position of the simulation results described in this chapter [141]. The experiments mentioned correspond to the following publications: Debus et al. [147], Heigoldt et al. [74], Buck et al. [73], Lundh et al. [72], Islam et al. [30] and Li et al. [75]. The simulated beam properties in and outside of the plasma are based on the results in Tables 4.5 and 4.7, respectively. Note that the bunch lengths listed were measured at different distances inside or behind the plasma target such that space-charge effects may be one cause for some of the variations in values.

duration. While the latter is an essential part for the injection process to work, as the one-dimensional parameter scans in Section 4.2 have shown, the data in Fig. 4.21, nonetheless, indicates that it is not a feature directly responsible for the short injected bunch duration. Here all experiments, besides those of Buck et al., used laser pulses of similar duration in the range between 28–45 fs, while Buck and his team employed a laser with 8.5 fs (FWHM) duration much closer to the value of approximately 7.3 fs (FWHM) assumed in the simulations in this chapter. Yet the shorter pulse duration for the latter experiment did not directly skew the injected electron beam towards comparably shorter bunch lengths, just as the consistently longer laser durations for the other setups still led to a wide range of measured bunch durations.

A more detailed analysis of the possible effects of the specific properties of the proposed upramp-assisted self-injection method can be found in Fig. 4.22 and Table 4.8, where the injected electron beam properties from simulations are compared to published results of plasma-accelerator experiments with similar setups to the one considered in this chapter. It should be noted that no experiments have been conducted yet with a qualitatively equal setup to the

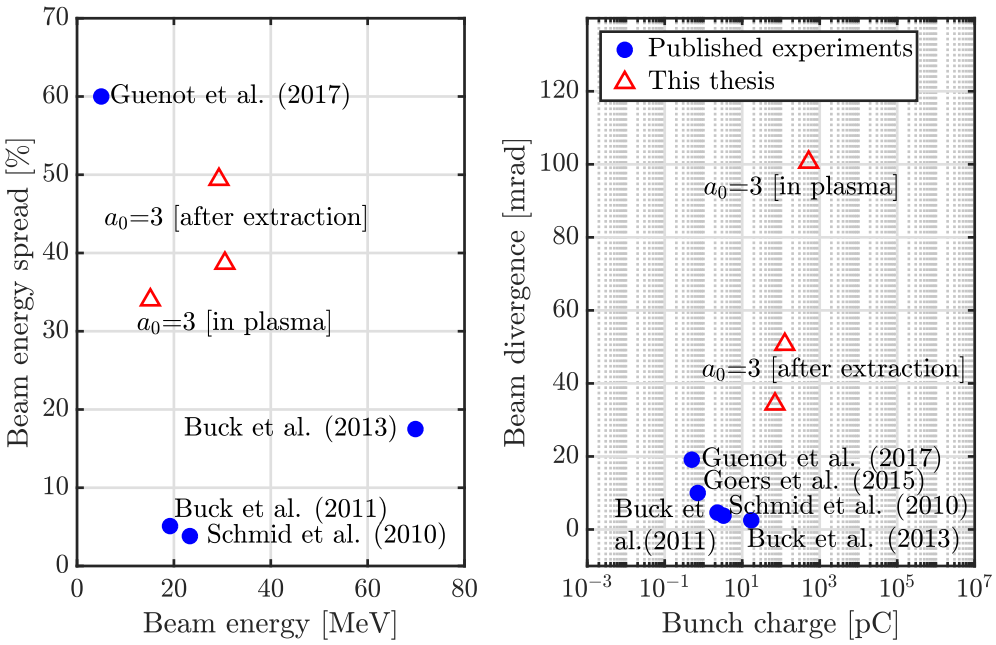

Figure 4.22: Comparison of electron beam properties from the upramp-assisted self-injection technique presented in this chapter (red triangles) and published experiments (blue dots) with simular laser and plasma setups. Table 4.8 shows the experimental conditions used in the referenced experiments, while the simulated beam properties in and outside of the plasma were taken from Tables 4.5 and 4.7, respectively. Note that to make the experimental results comparable, a Gaussian electron beam shape has been assumed to convert from FWHM to RMS values and the mean was taken, where multiple values were provided for a certain variable.

Reference	a_0	**Laser duration [fs]**	**Plasma density [$\mathbf{m^{-3}}$]**	**Plasma target length [µm]**
Buck (2011) [73]	1.67	8.5 (FWHM)	3.2×10^{25}	∼300
Buck (2013) [148]	2 – 2.5	28	3.4×10^{24} (avg.)	100 – 700
Goers (2015) [149]	≤0.8	50	1×10^{26} – 4×10^{26}	150 – 200
Guenot (2017) [150]	1.18	3.4	1×10^{26} – 2×10^{26}	∼100
Schmid (2010) [151]	1.08	8 (FWHM)	$\leq 6 \times 10^{25}$	∼200
Simulation results in Fig. 4.21 & 4.22	3.0	∼7.3 (FWHM)	3.36×10^{25}	150 – 320

Table 4.8: Details of the laser and plasma parameters of the experimental setups described in the publications compared in Fig. 4.22. Each published experiment listed here is similar to the upramp-assisted self-injection setup introduced in this chapter in at least two aspects, which are marked by the shaded grey areas in the table.

one introduced here nor with a similarly steep density upramp shown to be responsible for the self-injection process; the experiments chosen for the comparison were therefore picked based on having comparable laser and / or plasma properties in at least two aspects as the setup assumed for the attosecond plasma injector, as demonstrated in Table 4.8. Despite employing different injection mechanisms, agreement for the cases in Fig. 4.22 can be seen in their overall

low injected electron beam energy between 5 and 70 MeV as a consequence of the short plasma target lengths and hence limited acceleration distances. With regard to the other electron beam properties, however, the upramp-assisted self-injection results are in a very different regime reaching beam charges more than four times higher than in any of the experiments and a beam divergence with values 1.8 or more times the largest listed experimental result. The extreme beam charges demonstrated in this chapter are, as mentioned before, on the one hand caused by the active steepening of the plasma wave due to the plasma density upramp, but are on the other hand also as a consequence of the large focal spot size of the drive laser. With a FWHM value in intensity around 30 µm compared to spot sizes between 3.5 and 13.5 µm (FWHM) reported in the published results, the excited plasma wave is expected to be much wider leading to the injection of a larger portion of charge in the attosecond injector. Electrons being injected further away from the laser propagation axis in turn experience stronger focusing fields and hence produce a beam with stronger transverse electron momenta. This, together with the fact that the simulated results consider electron beams in or just behind the plasma target instead of after propagation in vacuum as in the experiments, can explain the larger observed beam divergence. Finally, in terms of the energy spread the electron beams from upramp-assisted self-injection are dominated by the large beam charge and associated beamloading fields, as described earlier in this section, which none of the experimental setups were expected to experience. Only Guenot et al. thus measured a relative energy spread with the same order of magnitude, yet this result has likely been caused by a combination of the steep accelerating field gradients due to the high plasma density and the short plasma target length allowing the injected bunch to only reach beam energies of around 5 MeV.

Overall, the injection mechanism studied in this chapter thus provides unusual beam properties, not only in terms of ultrashort bunch duration, but also with regard to most other important beam characteristics. As the previous comparison with recent experimental data showed, however, this behaviour is caused not as a consequence of a single feature of the plasma injector setup, but rather of a combination of setup features, including the laser intensity and duration as well as the plasma density and its profile shape. While this may make experimentally realising this injection process more challenging, the previous comparison has also shown that the proposed scheme of upramp-assisted self-injection may open up a whole new parameter range at ultrahigh currents and below the femtosecond limit which cannot easily be reproduced with other injection mechanisms or higher drive laser powers. In this respect and with regard to the currently typical, experimentally used laser strength values of a_0 around 1.0 and 2.0, the extension to a low-laser-power regime of the injection mechanism introduced in

this chapter may thus be seen as a particularly good stepping stone towards experimental realisation and a very useful compromise between ultrashort injected bunch duration and realisable laser requirements.

4.4 Stability of the Injection Process

The previous sections have presented the process of upramp-assisted self-injection assuming ideal conditions without taking into account potential variations in the injector setup that could occur during an experiment. The following series of 2D simulation studies, with general simulation parameters listed in Table 4.9, thus investigates a number of possible factors which may influence the trapping and acceleration in the attosecond injector. In particular, the dependence of the system evolution on density fluctuations, initial plasma temperature, laser spot size and plasma ramp shape is studied.

Laser pulse	
envelope (long./transv.)	$\sin^2$ / Gaussian
wavelength λ [µm]	1.0
peak power P_L [TW]	125.8 (a_0=3)
full pulse length L [µm]	6.0
pulse width ($1/e^2$ radius) w_0 [µm]	25.5–60
Plasma	
plateau density n_0 [m^{-3}]	3.13×10^{25}–4.59×10^{25}
ramp length R [µm]	100.0*

Table 4.9: Input parameters for the 2D OSIRIS simulations presented in Section 4.4.
*Note the slightly different definitions of the ramp length for varying ramp shapes in Section 4.4.

Density fluctuations

Figure 4.23 depicts how small variations in the plasma plateau density on the order of $\pm 4 \times 10^{-5}$ % (statistical fluctuations) (red and blue lines), ±1 % (violet and yellow lines) and ±10 % (green and light blue lines) affect the beam injection and evolution. The largest relative changes in this context are seen right after injection, as the trapping positions along the longitudinal direction – as shown by the z-positions of the first data point for each line in Fig. 4.23 – vary slightly by up to 13 µm. While differences in the time steps of the individual simulations likely constitute one source for this variation, another cause could also be the change in the plasma wavelength size due to the plateau fluctuation, which alters the position of the electron beam upon injection. During the propagation of the electron beam in plasma after injection, this initial parameter variation is mostly compensated, however, so that only deviations in bunch

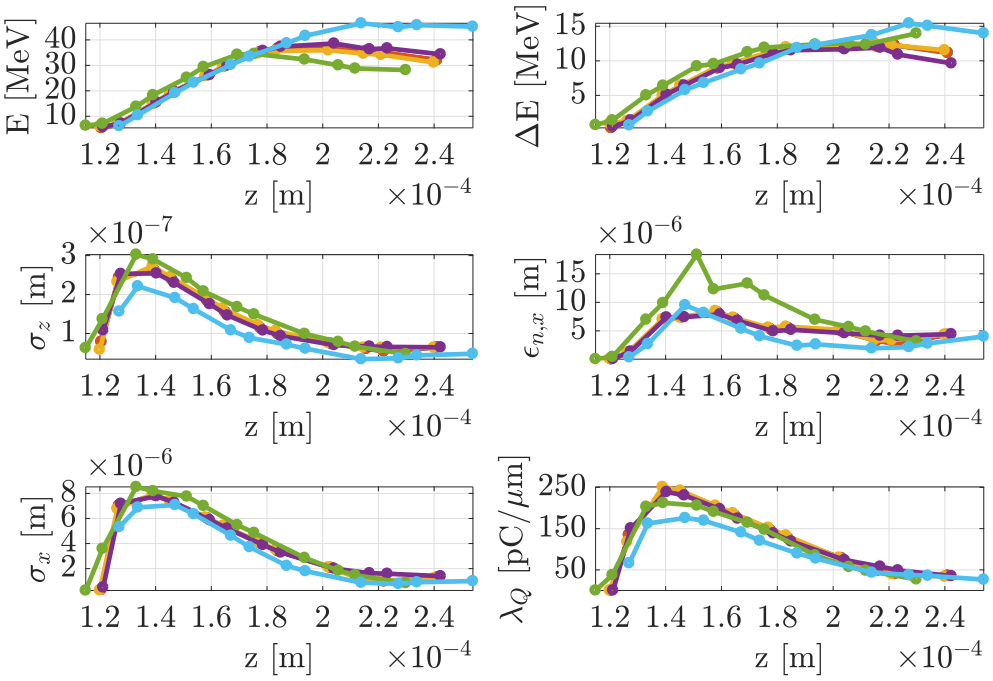

Figure 4.23: Dependence of fluctuations in the plateau plasma density by $\pm 4 \times 10^{-5}$ % (statistical fluctuations) (red and blue lines), ±1 % (violet and yellow lines) and ±10 % (green and light blue lines) on the injection and acceleration process. A drive laser with a_0=3, full length 6 µm, width 42.5 µm ($1/e^2$ radius) and a plasma of density 3.47×10^{25} m^{-3}, ramp length 100 µm (ramp end at 130.5 µm) were used. Note also that in this case the plasma upramp starts not from vacuum, but from 3.2 % of the plateau density value hence changing the gradient of the density transition and consequently also, to a small degree, the injection position relative to the ramp end.

mean energy and energy spread (by up to 17.8 MeV and 4.8 MeV, respectively) are observed due to the dependence of the wakefield amplitude on the plasma density. Overall, maximum fluctuations of around 40–80 % are found for most beam properties with the exception of the beam emittance, where a temporary variation of more than 100 % is observed with a 20 % change in plasma density. While these effects due to the plasma density appear quite strong, fluctuations in beam properties for a variation of the density by up to ±1 % are considerably less, namely up to 50 % for the beam emittance and 15 % for all other properties. Moreover, although the data shows the plateau density to be an important factor for the control of the injection mechanism, it is to a large degree only the energy properties of the electron bunch that are affected by density fluctuations, whereas most other properties are well stabilised at the later stages of acceleration.

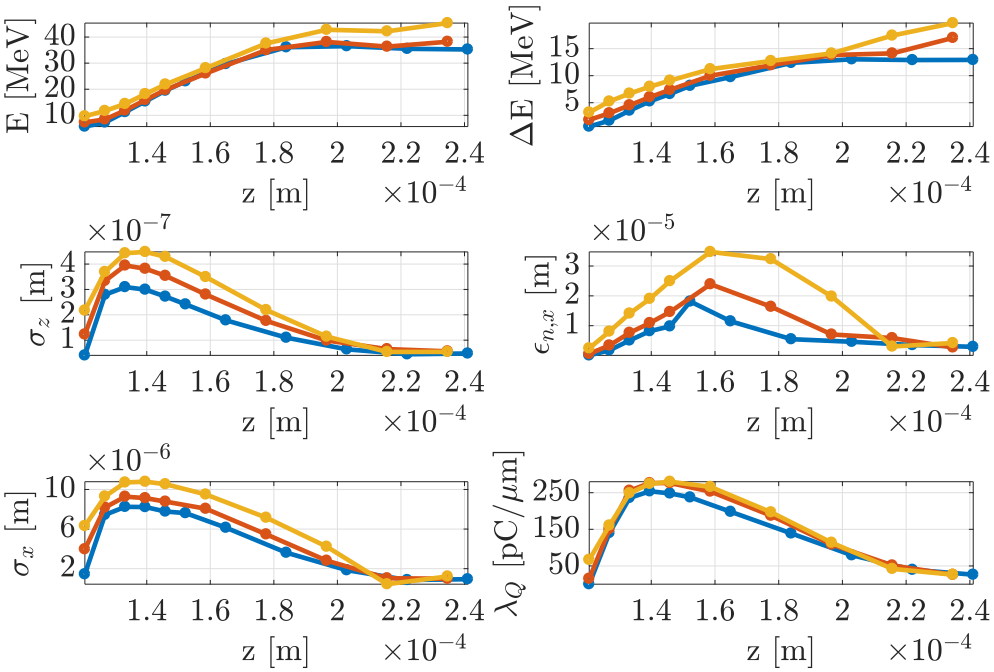

Figure 4.24: Dependence of the initial plasma electron temperature on the injection and acceleration process. Initial electron momentum increases from 1 eV (blue) to 10 eV (red) and 100 eV (yellow). A drive laser with a_0=3, full length 6 µm, width 42.5 µm ($1/e^2$ radius) and a plasma of density $3.47 \times 10^{25}\,\mathrm{m}^{-3}$, ramp length 100 µm (ramp end at 130.5 µm) were used. Note also that in this case the plasma upramp starts not from vacuum, but from 3.2 % of the plateau density value hence changing the gradient of the density transition and consequently also, to a small degree, the injection position relative to the ramp end.

Plasma temperature

Another factor that the injection process may be affected by is the initial plasma temperature T_e, i.e., the initial momentum of the electrons in the background plasma. With previous simulations assuming zero or very low initial plasma particle momentum, Fig. 4.24 presents how an initial electron temperature of 1 eV (blue), 10 eV (red) and 100 eV (yellow) influences the beam behaviour. Overall, a higher electron temperature leads to the injection of a larger beam with higher charge which eventually ends up with slightly higher energy and energy spread. As in the case of density fluctuations, all of the beam parameters, except for energy and energy spread, stabilise after longer plasma propagation to similar values; before this point, however, variations of below 80 % are observed for all beam parameters, including the beam mean energy, which varies by up to 10 MeV. In reality it is difficult to measure the initial plasma temperature with most estimates placing T_e on the order of 10 eV depending on laser and gas properties [113, 152]. As this study shows that the injection process still works well up to at least 100 eV initial electron momentum, this quantity should thus not be a main issue for

the realisation of the injection scheme in a realistic setting. Moreover, shot-to-shot fluctuations of the initial plasma temperature are expected to be caused most dominantly by variations in the laser intensity, which directly affects the momentum transferred from the laser to the plasma electrons. Assuming a variation in the laser intensity by up to 20 % shot-to-shot, these fluctuations should therefore, while non-negligible, lie well within the range under investigation in this section.

Laser spot size

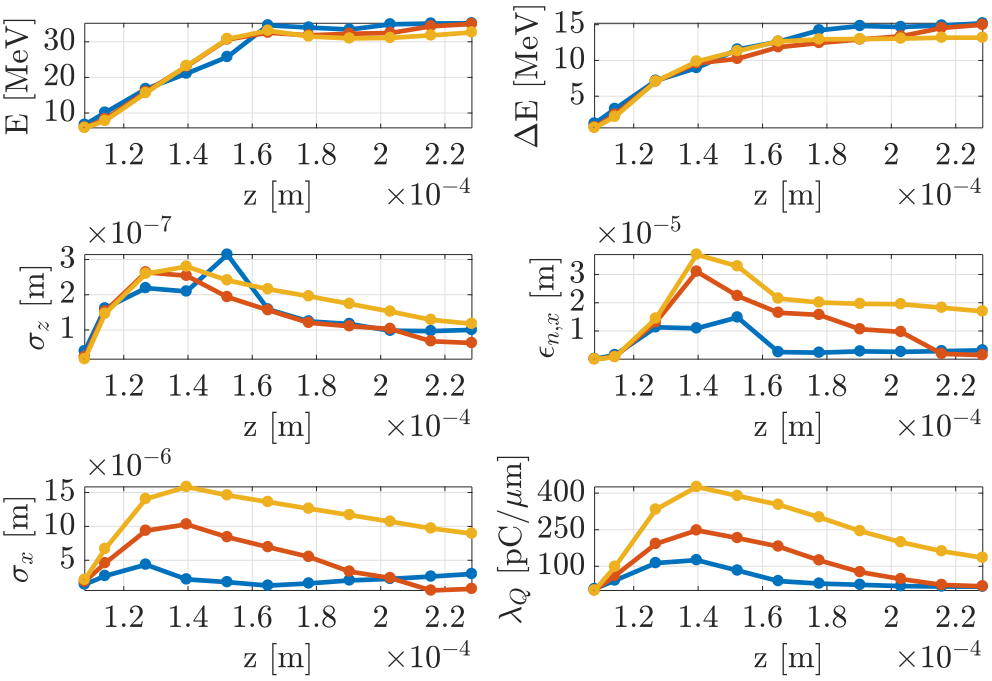

Figure 4.25: Dependence of the drive laser spot size (at focus) on the injection and acceleration process. The laser spot size varies from 26 µm (blue) to 43 µm (red) and 60 µm (yellow) ($1/e^2$ radius). A drive laser with a_0=3, full length 6 µm and a plasma of density $4.59 \times 10^{25}\,\mathrm{m}^{-3}$, ramp length 100 µm (ramp end at 132 µm) were used. Note also that in this case the plasma upramp starts not from vacuum, but from 3.2 % of the plateau density value hence changing the gradient of the density transition and consequently also, to a small degree, the injection position relative to the ramp end.

Regarding the spot size of the drive laser two different types of variations can be imagined. On the one hand, the value of the laser spot may be limited by the conditions of the setup to a certain range, while on the other hand independent of this value shot-to-shot fluctuations in the laser spot size are to be expected, such as e.g. due to thermal fluctuations along the laser beamline and hence deformations of some of the optical components. While the latter is an effect not to be neglected, this section focuses on the problem of the former and hence

aims to determine in how far the accessible range of spot sizes may affect the realisability of the upramp-assisted self-injection scheme. As shown in Fig. 4.25, an increase in laser width by a factor of 2.3 directly influences the transverse dimensions of the trapped electron sheet leading to a rise in beam width, emittance and, as the injection region widens, also charge by up to 86 %, 238 % and 795 %, respectively. The energy and energy spread, on the other hand, are much less affected by the laser spot size, so that a change of less than 20 % is observed for these properties. Finally, the bunch duration is found to increase for larger spot sizes; despite settling below 400 as almost 230 µm into the plasma target even for the widest laser width, a smaller spot size is thus preferable for fully utilizing the potential of the injection mechanism.

Upramp shape

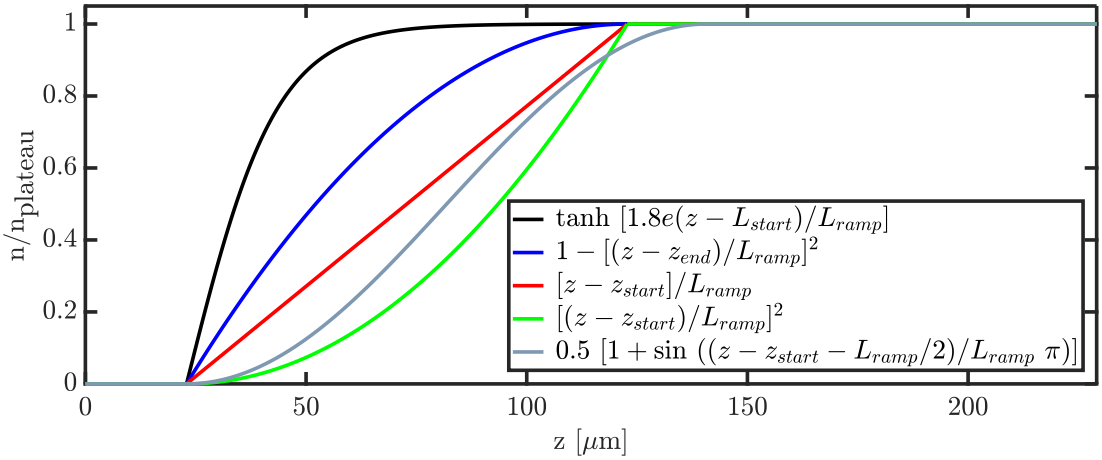

Figure 4.26: Various upramp profile shapes tested with regard to their effect on the injection and acceleration process.

The studies in the previous sections have all for simplicity assumed a linear shape for the plasma density upramp, but such a profile is not achievable experimentally. This section thus discusses the effect of the ramp profile on the injection and acceleration process with some more realistic examples. Figure 4.26 depicts the various ramp shapes that were studied using 2D PIC simulations, while the corresponding density structures for such ramps around the start of the trapping process are shown in Fig. 4.27 as well as 4.29b. When comparing these injected beams and their surrounding plasma, two features stand out particularly: first, the longitudinal injection positions in the plasma vary by up to 58 µm. This is related to the wavebreaking suppression condition (see Eq. (3.34)) valid along the upramp and its dependence on the density gradient. As a consequence, for ramp shapes with a flatter slope towards the end

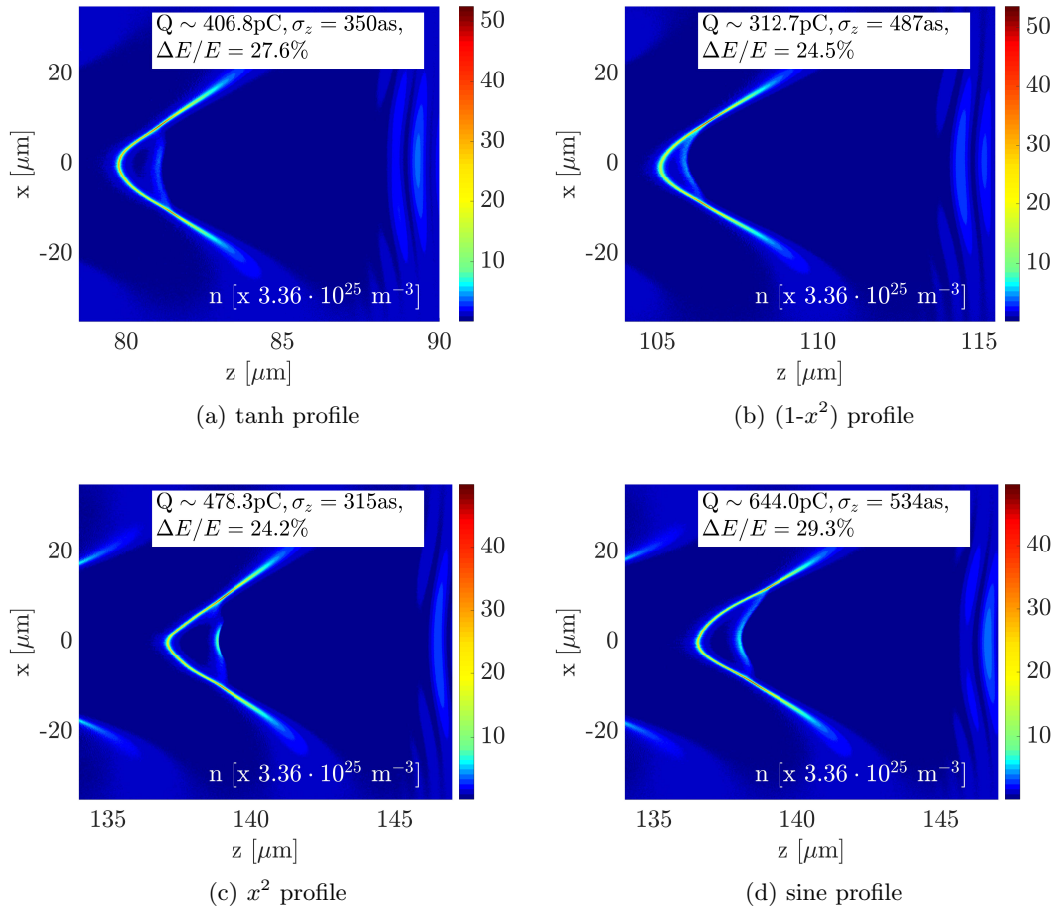

(a) tanh profile

(b) (1-x^2) profile

(c) x^2 profile

(d) sine profile

Figure 4.27: Plasma density structure just after the start of the self-injection process for the different upramp shapes shown in Fig. 4.26 based on 2D simulations of the low laser-strength reference case in Section 4.2. Note that the beam charges are approximated from the calculated 2D charge densities assuming a radially symmetric Gaussian beam, such that $Q \sim \lambda_Q \sqrt{2\pi}\sigma_x$.

of the ramp, the plasma wave phase velocity drops more easily below 1 so that wavebreaking can occur before the ramp end, such as in Fig. 4.27a and 4.27b. Because the wavebreaking process does not occur as controlled and sudden for these cases, though, the fraction of the wave crest that is trapped is smaller, creating an injected beam with generally less charge and shorter bunch duration (due to the decreased level of beam curvature).

The effect of this difference in injection for the beam dynamics during acceleration can be seen clearly in the example of a realistic upramp profile, described in Fig. 4.29 and 4.30. The shape of this density profile is based on a fluid dynamics simulation of a gas cell with OpenFOAM (by C. Thornton, Oxford University) translated to a shorter ramp length (see Appendix B for more details) and can be seen in Fig. 4.28. With a very flat density gradient

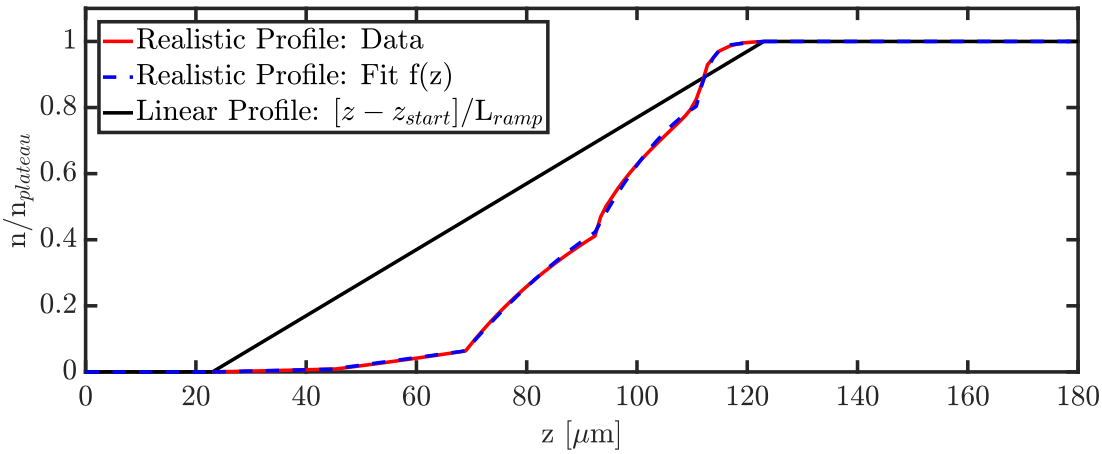

Figure 4.28: Realistic upramp profile shape and the fit used in simulations to test the ramp shape effect on injection and acceleration of the trapped electron beam (more details on fit in Appendix B).

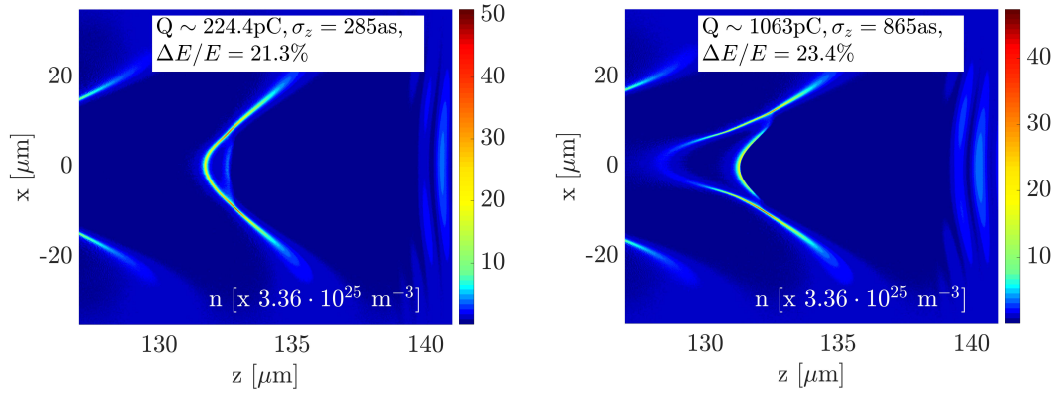

(a) realistic profile (b) linear profile

Figure 4.29: Density just after the start of the self-injection process for a realistic upramp shape, as shown in Fig. 4.28, vs. a linear ramp profile. The results are based on 2D simulations of the low laser-strength reference case in Section 4.2.

just before the ramp end, a weak breaking of the first wave crest is observed with the injection of a comparably small charge in an almost flat electron sheet. Consequently, the course of the injection phase, as defined within the beam parameter evolution in Fig. 4.14, is slower and weaker, leading to a less compressed beam with longer bunch duration, slightly less mean energy and smaller energy spread. Yet, with the bunch duration stabilising eventually to around 500 as, the ultrashort properties of the electron beam can be preserved even with such a more realistic upramp profile, while at the same time the beam's less extreme properties may allow for more stable dynamics during the propagation and extraction of the bunch.

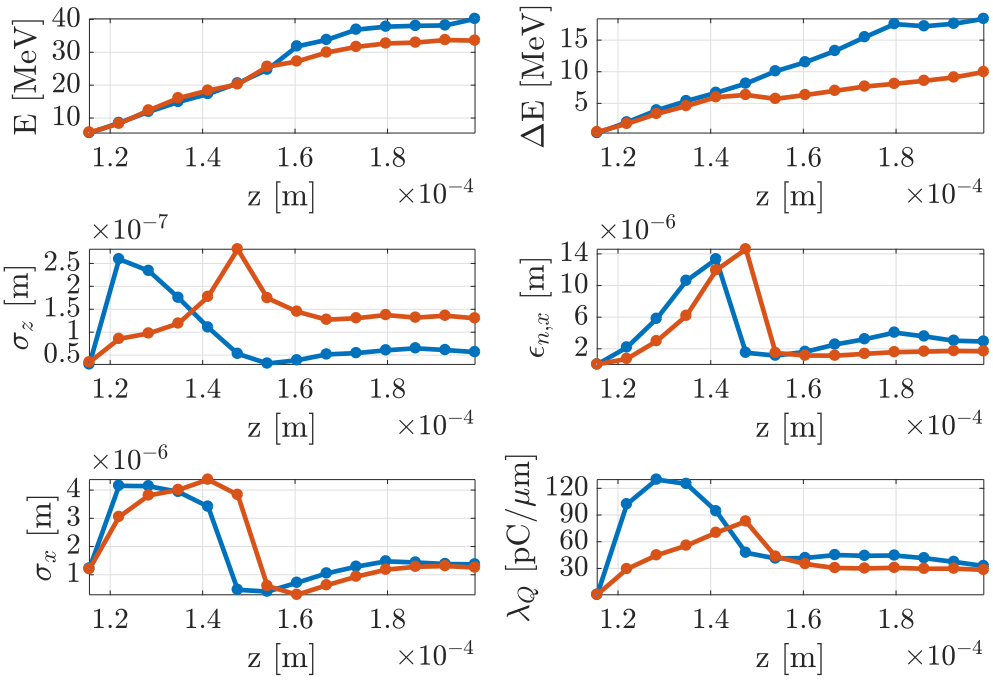

Figure 4.30: Evolution of the parameters of the injected beam during plasma propagation for a linear (blue) and a realistic (red) plasma density profile.

	Density		**Plasma temperature**	
	Min	**Max**	**Min**	**Max**
Mean energy E [MeV]	31.2	44.1	36.5	42.8
Energy spread ΔE [MeV]	11.6	13.0	13.0	14.1
RMS bunch duration σ_t [as]	167	296	213	380
Norm. emittance $\epsilon_{n,x}$ [μm]	2.5	6.3	4.6	19.8
2D charge density λ_Q [pC μm^{-1}]	67	86	79	114
	Laser spot size		**Ramp shape**	
	Min	**Max**	**Min**	**Max**
Mean energy E [MeV]	31.9	34.9	33.6	40.2
Energy spread ΔE [MeV]	13.1	14.7	9.96	18.4
RMS bunch duration σ_t [as]	327	508	189	434
Norm. emittance $\epsilon_{n,x}$ [μm]	2.6	19.5	1.7	2.9
2D charge density λ_Q [pC μm^{-1}]	19	199	28	33

Table 4.10: Maximum variations in injected beam parameters at around 70 μm behind the plasma upramp end, based on the system parameters studied in this section.

In conclusion, Table 4.10 shows an overview over the possible parameter range expected from the low-laser intensity upramp-assisted injection setup discussed in the previous sections taking into account the system variations presented in this section. By including plateau plasma density variations between $3.13 \times 10^{25}\,\mathrm{m}^{-3}$ and $3.82 \times 10^{25}\,\mathrm{m}^{-3}$, plasma temperature values from 1 eV to 100 eV, laser spot sizes (at focus) between 26 μm and 60 μm as well as various

plasma upramp profiles, it was demonstrated that the injection mechanism is possible over a wide range of system parameters. Most importantly, the RMS bunch duration of the injected beam can be limited to around 500 as or less, thus staying well within the attosecond regime.

Simulation Errors

Errors in the simulations were minimised by choosing grid cell sizes smaller than the smallest expected features within the simulation, which in this case was challenging due to the tiny size of the self-injected electron beams. Longitudinally, the smallest feature was found to be the injected beam size just after the start of the injection, corresponding to around 60–100 as, which could be resolved well in one- and two-dimensional simulations. In three-dimensional runs, compromises with regard to the required computing resources were made. However, as in this case the beam grows very quickly to the order of 400 to 500 as in full length, the beam dynamics were found not to be significantly affected. Transversely, the smallest simulation feature is the plasma wavelength on the order of 5–6 µm, depending on exact density. Again, this was resolved well in all simulation setups. The number of macroparticles representing the injected beam varies quite significantly at different stages of the beam evolution, as beam electrons are injected and lost again. A minimum of a few thousand particles was used in all simulations, with the particle number rising to more than tens of thousands particles for most beam evolution stages. This corresponds to a relative sampling error, estimated by $\Delta A/\sigma_A = 1/\sqrt{N}$ [153], of less than 1.2 % of the distribution standard deviation for all quoted beam properties.
Additionally, the effect of the grid resolution was monitored with test simulations sampling down to values of 4 nm×79 nm and hence reaching significantly below the theoretically estimated sufficient grid cell size. Small variations of the trapped electron properties were observed, but the main mechanism of injection and the order of magnitude of the beam characteristics were preserved in all cases. Especially for the 3D simulations, a reduction in grid size is not possible due to limited computing resources. However, it was found that with better resolution the injected beam generally exhibits higher mean energy, smaller bunch duration and smaller emittance, so that the results presented here can be seen as conservative estimates of the beam quality which may in reality be improved. Possible influences of the system dynamics due to numerical Cherenkov radiation were also investigated through a comparison simulation using the Lehe field solver (see Section 5.2). Again, small variations in beam parameters were observed; however, the beam dynamics, especially the beam emittance evolution, were consistent with the standard solver, so that a strong influence due to this effect can be precluded.

4.5 Summary of the Main Findings

In this chapter, the trapping and acceleration of ultrashort electron beams with the scheme of upramp-assisted self-injection was investigated. The injection mechanism was confirmed with first 3D particle-in-cell simulations. Further, one-dimensional parameter scans demonstrate that a wider parameter regime than initially predicted is usable for the scheme with laser strengths down to $a_0 \sim 2.5 - 3$ - reducing the previously predicted minimum laser intensity by a factor of four - and plasma densities of $1.12 \times 10^{25}\,\mathrm{m}^{-3}$ or higher. The laser pulse length and plasma upramp length were also found to be variables affecting the electron injection and evolution. These general trends are well reproduced in higher dimensional studies, although the bunch duration is found to be limited to around 150–200 as (RMS) by beamloading fields due to higher injected charge in 3D simulations independently of other setup parameters.

The evolution of the electron beam during its acceleration was found to be swift and non-linear. After tens of micrometres, strong laser depletion and high beam self-fields lead to the effective deceleration of a large fraction of the bunch; as a consequence a decrease in mean energy, increase in energy spread and expansion of the beam with the loss of a large fraction of charge are observed. To avoid such deterioration, the beam can be extracted after its first fast acceleration stage. The length of the plasma density downramp in this case must be kept compact on the order of tens of micrometres, as the beam continues to evolve leading to possible filamentation and quality deterioration. A disadvantage of this method is hence the large beam divergence which requires compensation through strong focusing after the plasma. Nonetheless, the short bunch duration of less than 180 as (RMS) (∼700–800 as full length) can be preserved with a mean energy of around 30 MeV, energy spread between 40 and 50 %, normalised emittance between 2.8 and 5 µm and charge up to approximately 130 pC. The scheme is reproducable even under fluctuations in the plasma plateau density, initial plasma temperature, laser pulse spot size and plasma upramp shape. Variations in beam properties are expected under these circumstances, but a bunch duration below 500 as RMS was found to be achievable in all cases.

Chapter 5

Energy Boosting of an Externally Injected Electron Bunch in LWFA

This chapter presents an energy boosting stage for an externally injected, relativistic, sub-femtosecond electron beam based on the planned setup of the SINBAD facility, currently under construction at DESY. It discusses the main challenges for external injection in the weakly nonlinear regime, as shown in Fig. 5.1, and investigates possible solutions.

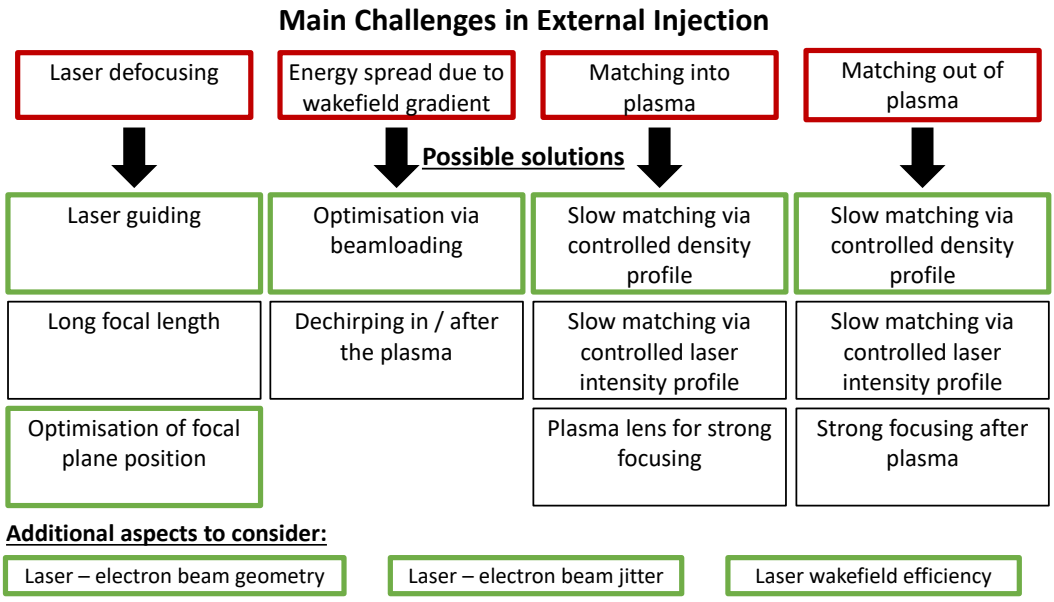

Figure 5.1: Main challenges related to external injection into an LWFA setup: The green boxes mark the respective solutions investigated in this chapter.

Published partly in [154], the chapter in particular presents the following main results:

- A first study of external injection with a high-quality, sub-femtosecond electron beam is presented.
- A clear strategy for matching the beam into and out of the plasma is proposed based on investigations of the effect of length and shape of the matching ramp in a realistic setup.
- The limits of matching theory with regard to space-charge effects are studied and defined.
- A possible optimisation of the beam energy spread through beamloading is presented and shown to be limited by the level of slice energy spread due to the transverse variation of the accelerating field.
- After target optimisation the energy booster is demonstrated to preserve beam quality to a high standard with sub-micrometre emittance and sub-half-percent energy spread up to the GeV-range.

A large fraction of the results presented in Chapter 5 are based on two-dimensional PIC-simulations with the code OSIRIS, which in Section 5.6 are complemented with 3D OSIRIS simulation results. As in Chapter 4, the simulation code assumes a pre-ionised, pure electron plasma and does not consider positive ion motion. The plasma target in all cases consists of two or three parts of varying length: a matching section in the form of a density transition from vacuum to a plateau density (upramp); an accelerating section, which is either constant in plasma density or, as described in Section 5.3, has a density profile shaped in the transverse dimensions; and, for the simulation results shown in Sections 5.5 and 5.6, a matching section out of the plasma with a density transition from the plateau density back to vacuum (downramp). With the exception of these last two sections, the electron beam properties provided are all taken inside the plasma. Details of the plasma target shape for each set of simulations can be found in Appendix C, which also lists the spatial simulation resolution and particle numbers in each case. On average, the spatial resolution values can be described as $\lambda/42 \times \lambda/1.3$ for the 2D and $\lambda/35 \times 1.75\lambda \times 1.75\lambda$ for the 3D-simulations, respectively, longitudinally and transversely. The plasma has been simulated with 1 to 8 (1) particles per cell in the two-dimensional (three-dimensional) PIC-runs, whereas the externally injected electron beam consists of, on average, 32 and, at maximum, 64 particles per cell in 2D and is described by an output file from the particle-tracking code ASTRA [155] with a total of 141,011 macroparticles in 3D. Both the standard Yee and Lehe solver have been employed for the field calculations in OSIRIS (specified in the text and Appendix C), as described in more detail in Section 5.2. Further, a moving window in

the longitudinal direction as well as five-pass binomial current smoothing are employed, which in the start-to-end simulations in Section 5.6 is complemented by additional five-pass field smoothing for the particle interpolation steps. The particle interpolation scheme was chosen to be quadratic. Different boundary conditions were tested with absorbing boundary conditions being employed in most simulations for the particle species and the fields. The properties of the drive laser pulse and witness electron beam were modelled closely to the expected parameters at the SINBAD facility and have been kept constant for all simulations in this chapter, as discussed in more detail in Section 5.1. Both the laser and electron beam profiles have been assumed to be Gaussian in the longitudinal and transverse directions with the exception of the 3D-simulation shown in Section 5.6, where a more realistic electron beam shape has been employed.

The sections of Chapter 5 are organised in the following order: Section 5.1 defines some of the properties of the plasma target based on general considerations and estimations with regard to acceleration distance and efficiency. In Section 5.2 the problem of matching the electron beam transverse properties to the plasma target in order to avoid emittance growth is investigated by studying possible influences of the length and shape of the plasma matching section as well as effects due to space-charge forces and numerical features. Sections 5.3 and 5.4 discuss the possibility to use an external plasma guiding channel and an optimised beamloading approach - controlled via a simple numerical model -, respectively, to overcome laser defocusing and an increase in energy spread during acceleration. Finally, with Section 5.5 presenting results on emittance and divergence control through the use of a tailored matching-out region, Section 5.6 summarises the overall findings of this chapter in the form of start-to-end simulations of the full plasma target. In this context, different plasma setups are investigated in 2D, while 3D-simulation results present the effects of non-Gaussian electron beam properties on the energy boosting stage.

5.1 General Considerations

The parameters considered for the electron beam and the drive laser in this study are guided by the planned setup at the SINBAD experimental facility. The witness beam properties are based on simulations of the ARES linac by Jun Zhu, while the laser characteristics are taken from the ANGUS laser currently installed at the LUX project. Whereas these parts of the accelerator setup are thus already clearly defined, as described in Table 5.1, further consideration needs to be placed on the design of the plasma target itself. For this reason, the current section discusses

some general aspects that allow narrowing down the parameter space, especially with respect to the plasma target density that will be used in the simulations in the following sections and possible future experiments.

Laser pulse	
envelope (long./transv.)	Gaussian / Gaussian
wavelength λ [µm]	0.8
peak power P_L [TW]	196.6 (a_0=1.8)
pulse length (FWHM) L_{FWHM} [µm]	7.5
pulse width ($1/e^2$ radius) w_0 [µm]	42.5
Witness beam	
charge Q [pC]	0.7
RMS duration σ_t [fs]	0.78
RMS width σ_x [µm]	5.1
mean energy E [MeV]	100
RMS energy spread $\Delta E/E$ [%]	0.37
norm. emittance in x $\epsilon_{n,x}$ [µm]	0.17

Table 5.1: Drive laser and witness beam parameters used in the simulations in Chapter 5. The parameters are equivalent to the ones described in Section 1.3 for the ANGUS laser and ARES electron beam with the latter being adapted to be radially symmetric for 2D simulations.

In order to achieve high energy, high quality electron beams from an external injection LWFA setup, two main issues need to be addressed: first, the limitations with regard to the maximum acceleration distance and, second, the requirements on timing jitter between the beam and laser pulse. As Figs. 5.2 and 5.3 show, both of these aspects depend strongly on the density of the plasma. From theoretical estimates (black and green lines) as well as PIC simulation results (blue dots) one can see that a higher density leads to a larger accelerating field gradient, yet at the same time also to a smaller size of the accelerating and focusing region of the wakefield, which is on the order of $\lambda_p/4$ for the linear and weakly nonlinear regime. For n_0=$1 \times 10^{24}\,\mathrm{m}^{-3}$, for example, the region in which the beam is accelerated and focused is only around 15 µm in length; hence, even with a control over beam synchronisation to a level of 10 fs, as is planned for the SINBAD facility, variations in beam position from shot-to-shot of about one fifth of the useful wakefield region are to be expected. By decreasing the density by an order of magnitude, on the other hand, a jitter of 10 fs only covers one thirteenth of the accelerating region making acceleration in this regime more stable and reliable from shot to shot.

A similar trend is observed when studying Fig. 5.3 depicting estimates for the dephasing and depletion length as a function of plasma density; both of these parameters are typical limitations for the length of the acceleration process (see Section 3.4 for more details) which cannot easily be overcome. Although the required acceleration distance to reach a certain

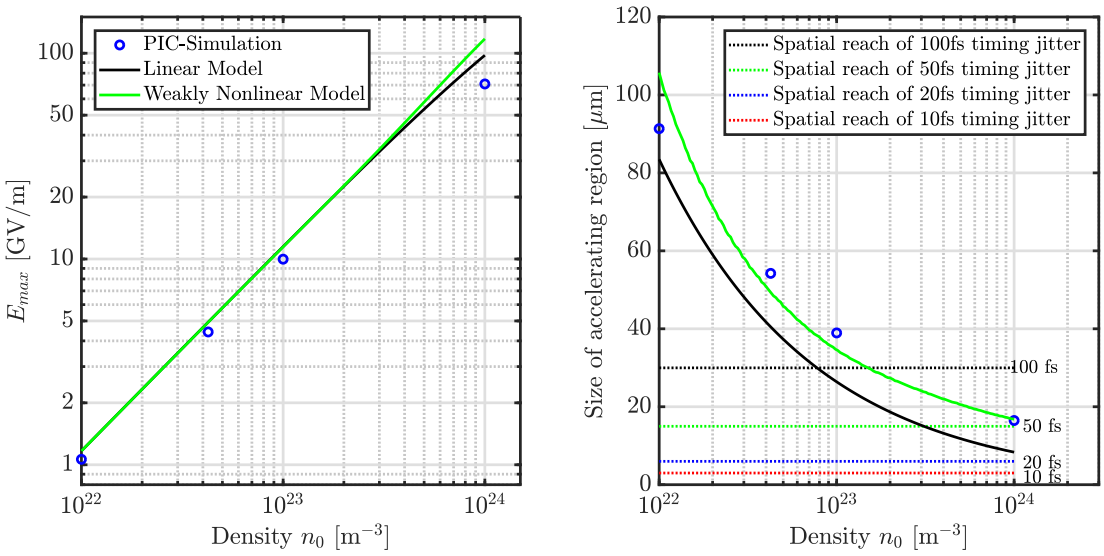

Figure 5.2: Accelerating field gradient and size of the "acceleration cavity" (accelerating and focusing region) as a function of plasma density based on linear (black line) and weakly nonlinear (green line) wakefield theory (see Sections 3.2.1 and 3.2.3) as well as PIC simulation results (blue dots). Note that for the linear model a region size of $\lambda_p/4$ has been chosen, whereas in the other two cases the distance between the zero-crossing of the accelerating field and that of the focusing field at the back of the plasma bubble has been calculated directly to define the "acceleration cavity". The PIC simulations have been carried out with the code OSIRIS and use the same laser parameters as provided in Table 5.1 with a simple, homogeneous plasma target. The plot on the right additionally shows the effective spatial region corresponding to different values of electron beam timing jitter relative to the wakefield.

energy gain (coloured bands) also decreases with higher plasma density, the rate of reduction in L_d and L_{pd} is so much higher that for n_0=1 × 10^{24} m^{-3} they are only a factor of 3.5 and 3.0, respectively, above the estimated acceleration distance to 1 GeV gain. Considering that the definition of the dephasing (depletion) length relates to the distance over which the electron beam has dephased over the whole useful wakefield region (the laser has lost half of its initial energy), the efficiency of the acceleration process already decreases considerably before reaching these points. Realistically, the required acceleration distances will thus likely be slightly larger than shown in Fig. 5.3 and hence even closer to L_d and L_{pd}.

As a conclusion, the choice of plasma density must therefore be a compromise between, on the one side, reaching high gradients to minimise the acceleration distance, and, on the other side, maximising both the possible acceleration length as well as the size of the accelerating and focusing wakefield region. The calculations show that such conditions can be reasonably obtained at densities around n_0=1 × 10^{22}–1 × 10^{23} m^{-3}.

In Fig. 5.4 the effect of the plasma density on the evolution of an externally injected wit-

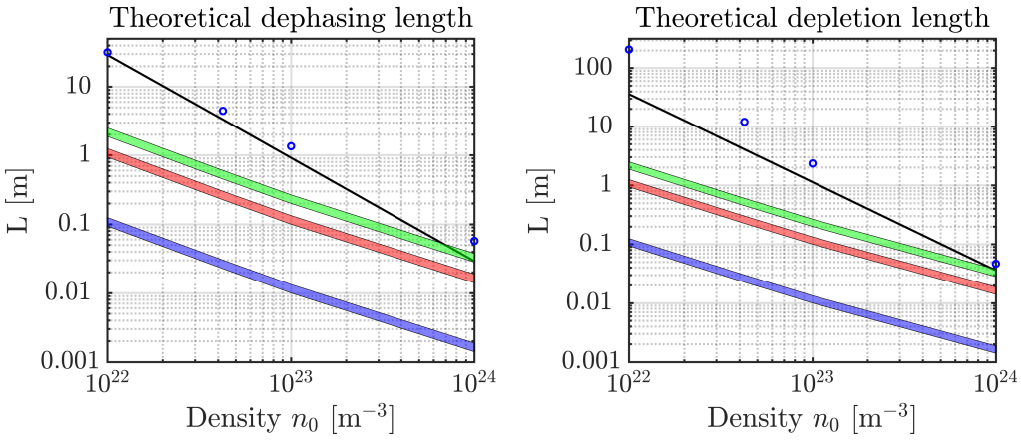

Figure 5.3: Dephasing, depletion and required acceleration lengths for different beam energy gains as a function of plasma density. The black line depicts values based on the simplified equations in Section 3.4, whereas the blue dots show calculations based on said equations, but with the accelerating region size and the accelerating wakefield determined from PIC simulations with the code OSIRIS (same setup as in Fig. 5.2). The shaded areas represent estimated acceleration lengths for an energy gain of 100 MeV (blue), 1 GeV (red) and 2 GeV (green) assuming an accelerating field between 75 % and 100 % of the maximum wakefield amplitude.

ness beam is shown. A very simple plasma target with homogeneous density after a 100 µm long plasma upramp was used. The top left plot confirms the previous theoretical estimates regarding the increased energy gain per distance with rising density. The changes in the other beam parameters, in particular the energy spread, emittance and transverse beam size, can be explained by the density-dependent influence of the laser intensity evolution and beam loading. Due to the laser defocusing and its amplitude a_0 decreasing after a certain distance, the wakefield becomes more linear changing both in amplitude and shape. This effect can be observed in Fig. 5.5, where the initially steepened wakefield curvature evolves to a more sinusoidal structure leading to a repositioning of the witness beam within the acceleration and focusing regions. As the reshaping effect is strongest at lower density, where the wakefield is closest to the linear regime, the witness beam eventually moves into the defocusing region of the plasma wave; this explains the sudden, strong increase in its transverse properties.

The energy spread, on the other hand, is to a large extent determined by the gradient of the effective longitudinal wakefield acting on the beam. Due to the comparably high density of the latter of $4.6 \times 10^{22}\,\mathrm{m}^{-3}$, it creates its own wakefield which is added as a beam loading effect to the laser wakefield. With the differences in wakefield amplitude varying with plasma density, the effective accelerating field gradient across the witness beam and thus its energy spread equally change. In this context, the compensation of the laser wakefield gradient by the beam loading is best for $1 \times 10^{23}\,\mathrm{m}^{-3}$, whereas at lower densities the energy distribution along

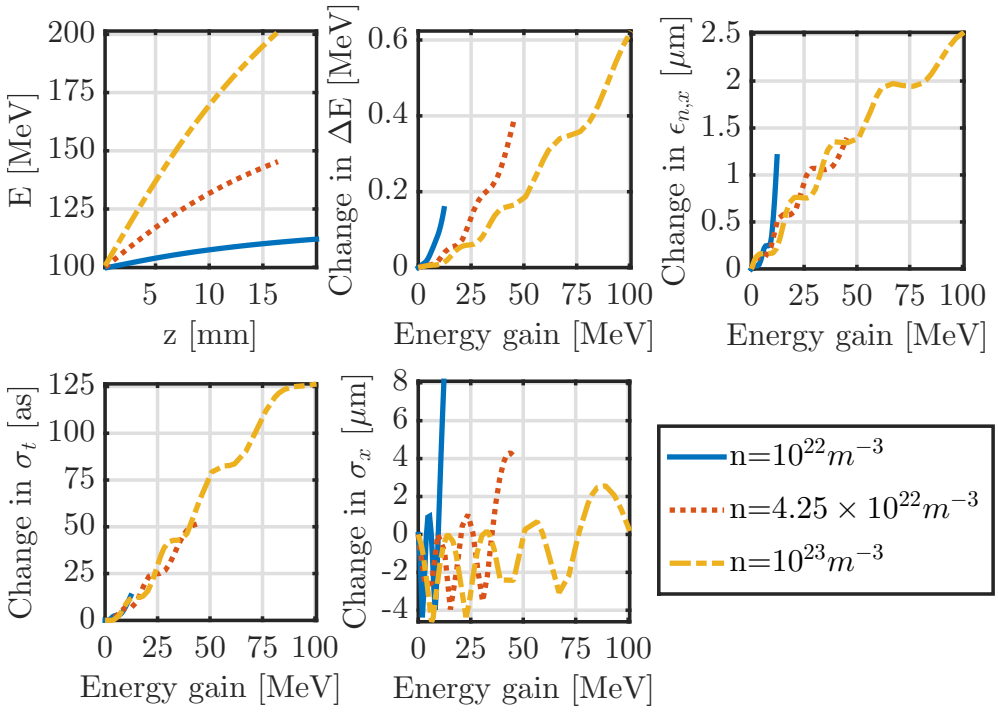

Figure 5.4: Evolution of the injected beam parameters during acceleration in plasma of different density. The OSIRIS PIC simulations assume the following setup: a homogeneous plasma target with a short 100 µm long upramp as well as a drive laser with parameters as given in Table 5.1 and laser focal position at the end of the plasma upramp.

z is dominated by the beam's own wakefield and thus has a positive chirp (see Fig 5.5).

Overall, both of these effects can be mitigated by various approaches, such as laser guiding and beam shaping, as discussed in later sections; however, the study, nonetheless, demonstrates that acceleration at lower plasma density is more vulnerable to such consequences of the laser and wakefield dynamics, not least because of the longer required acceleration distances. A plasma density on the order of n_0=$1 \times 10^{23}\,\mathrm{m}^{-3}$ is thus chosen as a suitable regime for the optimisation studies in the following sections, as it provides a more stable beam evolution, while still relaxing restrictions on acceleration distance and useful wakefield region size.

Finally, a more practical consideration to be made for the plasma target setup is the laser - electron beam geometry which is governed by the fact that both components may need to propagate over longer distances with different velocities before interacting in the plasma. The change in distance between the drive laser and witness beam, however, was found to remain well below 80 µm even after propagation over 2.5 m both in plasma and vacuum due to the relativistic energy of the electrons. Although this small dephasing will need to be taken into account during synchronisation of the beam and laser pulse, a simple geometry is thus definitely

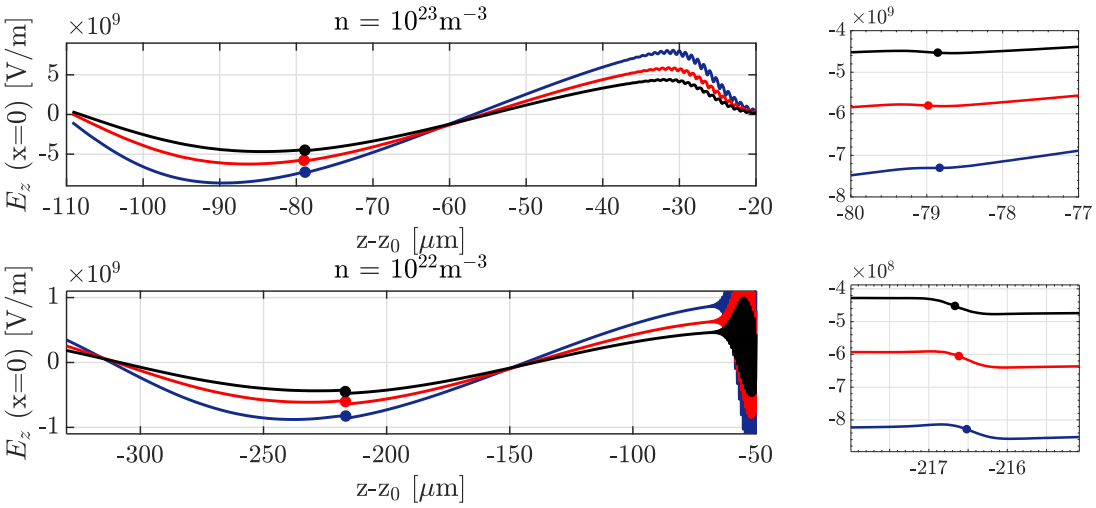

Figure 5.5: Evolution of the longitudinal wakefield shape after plasma propagation of around 5 mm (blue line), 10 mm (red line) and 15 mm (black line) for two of the cases shown in Fig. 5.4, at densities of $1 \times 10^{22}\,\mathrm{m}^{-3}$ (bottom) and $1 \times 10^{23}\,\mathrm{m}^{-3}$ (top). The plots on the right show a zoom-in of the field in the region around the witness beam, situated at the round dots. Note that the longitudinal coordinate is given relative to the front of the simulation box, so that the centre of the drive laser pulse is located at $-25.2\,\mu$m and $-53.1\,\mu$m in the top and bottom plots, respectively.

possible without having to account, for example, for the laser overtaking the electron beam, as proposed in previously investigated external injection schemes, such as at the REGAE facility [117].

5.2 Emittance Growth and Matching into the Plasma

To avoid emittance growth in the plasma due to betatron decoherence (see Section 2.3), the electron beam needs to be matched in its transverse properties to the plasma, such that the spread due to the beam emittance is fully compensated by the wakefield focusing forces [54]. Assuming a linear wakefield with a Gaussian drive laser, as derived in Eq. (3.21), the focusing strength K is given by

$$\begin{aligned} K &= \frac{e}{\gamma m c^2}\frac{\partial(E_r - cB_\theta)}{\partial r} \\ &= -\sqrt{\frac{\pi}{2}}\frac{k_p L_{rms}}{\gamma w^2} a_0^2 \exp(-\frac{k_p^2 L_{rms}^2}{8}) \sin(k_p \xi) \exp(-\frac{2r^2}{w^2})\,[1 - \frac{4r^2}{w^2}]\,. \end{aligned} \tag{5.1}$$

From Eq. (2.24), the matched β_{cs}-function (on axis) is thus

$$\beta_{cs,m,lin} = (\frac{2}{\pi})^{1/4} \sqrt{\frac{\gamma}{k_p L_{rms}}} \frac{w}{a_0} \exp(\frac{k_p^2 L_{rms}^2}{16}) \big[\sin(-k_p \xi)\big]^{-1/2} . \tag{5.2}$$

In the weakly nonlinear and the blowout regime, the focusing strength is defined similarly as

$$\begin{aligned} K_{wnl} &\approx \frac{k_p}{\gamma}\Big[\frac{4a_1(1-9/16a_1^2)}{w^2 k_p k}\cos(\eta+\eta_0) + \frac{3a_1^2}{2w^2}\Big(\xi\cos(\eta) - \frac{\sin(\eta)}{k_p k}\Big) \\ &- \frac{2a_1^2(1-37/64a_1^2)}{w^2 k_p k}\cos(2\eta+2\eta_0) + \frac{3a_1^4}{4w^2}\Big(\xi\sin(2\eta) + \frac{\cos(2\eta)}{2k_p k}\Big) \\ &+ \frac{21a_1^3}{16w^2 k_p k}\cos(3\eta+3\eta_0)\,, -\frac{23a_1^4}{24w^2 k_p k}\cos(4\eta+4\eta_0)\Big] \end{aligned} \tag{5.3}$$

$$K_{blow} = \frac{k_p^2}{2\gamma} . \tag{5.4}$$

Estimates for the matched beam spot size in the different regimes (based on Eq. (2.24), assuming ϵ_n=0.17 µm and $\gamma = 195.7$) are shown in Fig. 5.6 as a function of the plasma density. From this plot, it becomes clear that in all cases a very small beam size is required, yet low densities are preferable for matching. If the beam cannot be matched into the plasma, significant emittance growth is observed, as shown in Fig. 5.7. In this context, one of the main causes for the growth is the mixing of the transverse phase-space away from the z-axis; this is caused by the nonlinear dependence of the focusing strength on the transverse coordinate in the linear and weakly nonlinear regime. It can be observed by the strong curvature around the edges of the phase-space ellipse.

	SINBAD	Xu et al. [156]: plasma injector	Xu et al. [156]: RF injector	Dornmair et al. [157]	Tomassini et al. [158]
$\beta_{cs,m}$ [mm]	0.58 / 0.33*	0.34	0.12	0.8	0.63
$\beta_{cs,in}$ [mm]	30	0.03	5.0	40	4.7
$\beta_{cs,in}/\beta_{cs,m}$	51 / 90	0.1	42	50	7.5
ϵ_x [nm]	0.87	0.83	23	5.1	6.4

Table 5.2: Matching setups in simulations from recent publications: the parameters listed include the matched β_{cs}-function, the initial beam β_{cs}-function and the initial geometric emittance. For the SINBAD case, the matched β_{cs}-function for both the weakly nonlinear and the blowout (*) regime are listed for an assumed plasma density of $1 \times 10^{23}\,\mathrm{m}^{-3}$, laser and electron beam parameters as listed in Table 5.1 and a beam-laser pulse offset of 52.7 µm. All cases use a controlled density and / or laser intensity transition for matching.

The ultrashort duration of the beam is a further disadvantage, as beam focusing in the SINBAD setup is limited due to chromatic and space-charge effects to beta functions at the plasma entrance of around one order of magnitude larger than the matched value [41, 68]. As

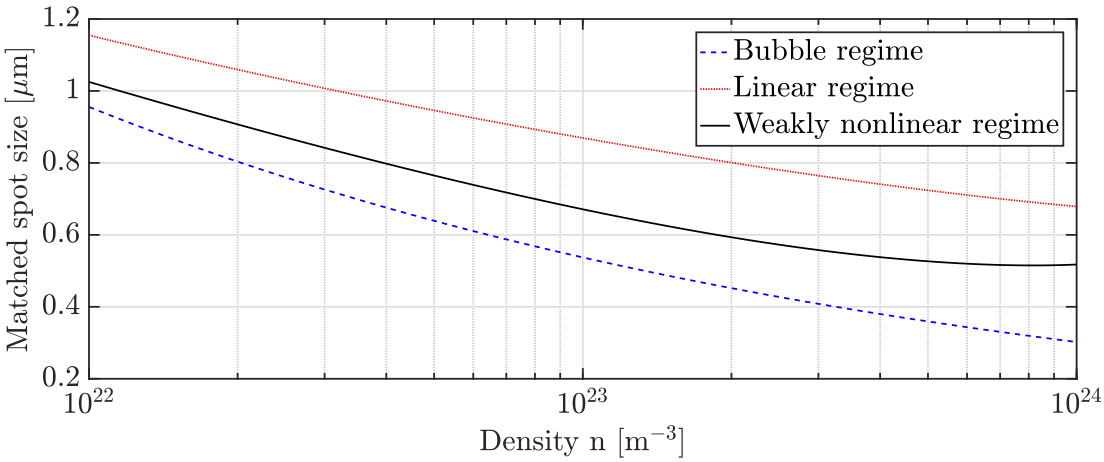

Figure 5.6: Matched electron beam spot size as a function of plasma density based on linear, weakly nonlinear and blowout wakefield theory. A relative phase of the electron beam of 0.9π within the wakefield was chosen for the linear and weakly nonlinear cases. Assuming a weakly nonlinear wakefield, the matched spot size could be increased slightly from the given values by moving further back in the plasma wake where the focusing fields are weaker.

proposed and further studied by [157, 158], however, it is possible to mitigate the expected emittance increase through the use of a plasma upramp at the start of the acceleration stage to apply additional, slowly increasing focusing from the plasma itself. If done adiabatically, i.e., slow enough for the beam size to adapt to the focusing strength changes without emittance growth, the normalised beam emittance can be preserved. Table 5.2 compares the matching requirements for the case under investigation here (assuming a plasma density of $1 \times 10^{23}\,\mathrm{m}^{-3}$) with those of such other simulation-based studies to match into plasma. In the case of Xu et al. [156], different such scenarios are studied to evaluate matching with various analytically predicted plasma upramp shapes, including for the external injection of electron beams from high density ($1 \times 10^{25}\,\mathrm{m}^{-3}$) plasma injectors and RF injectors into a low-density ($1 \times 10^{23}\,\mathrm{m}^{-3}$) plasma acceleration stage. Dornmair et al. [157] and Tomassini et al. [158], on the other hand, both investigate matching of an RF-accelerated electron beam into a plasma accelerator with a simple, linear plasma upramp, again at a low density of $1 \times 10^{23}\,\mathrm{m}^{-3}$. In the SINBAD scenario there are, in this context, two factors that make the matching particularly challenging even with the use of density ramps: on the one hand, the ratio of the initial to the required matched β_{cs}-function is among the highest studied so far, but on the other hand the emittance of the SINBAD beam is also comparably low. This leads to a very small matched beam size and particularly high requirements in terms of the focusing before and on the plasma ramp.

In the following section a practical application of this scheme for the SINBAD plasma setup is studied, in particular with regard to the effect of ramp length and shape as well as possible

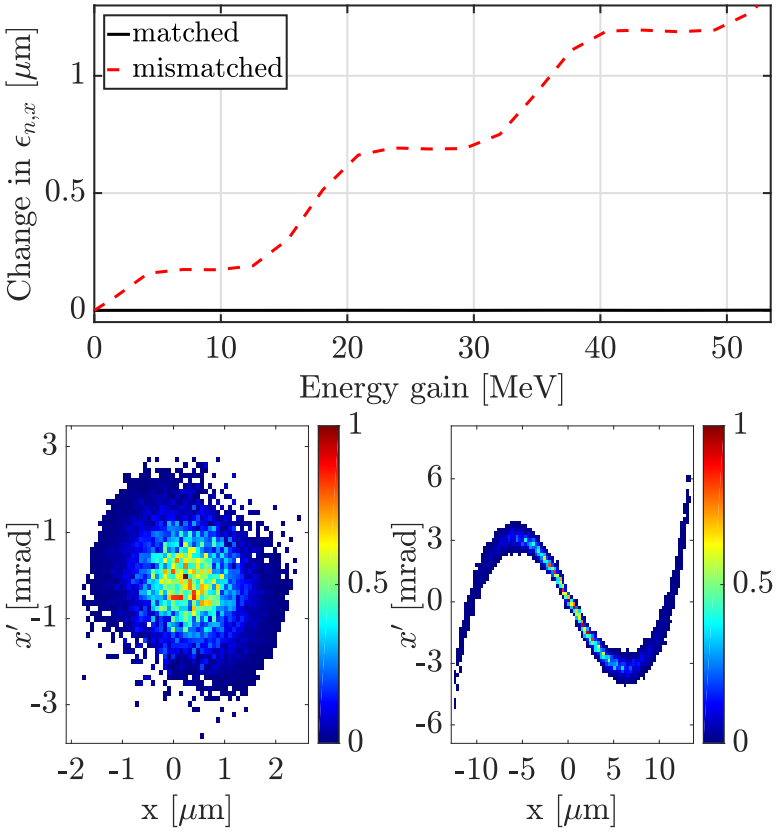

Figure 5.7: Evolution of the beam emittance and transverse phase-space for a matched (σ_x=0.7 µm, bottom left) and mismatched beam (σ_x=5.1 µm, bottom right). Phase-space plots are taken at z=6.04 mm, after around 51 MeV energy gain, with the colorbar depicting normalised charge. In both simulations a drive laser with properties given in Table 5.1 and a laser focal position of 134 µm as well as a homogeneous plasma target of density $1 \times 10^{23}\,\mathrm{m}^{-3}$ without any density ramp is assumed.

influences due to space-charge and numerical effects. A series of 2D PIC simulations with the code OSIRIS was employed for this purpose with a laser and plasma configuration, as depicted in Fig. 5.8.

Dependence on Ramp Length

Figure 5.9 depicts the evolution of the normalised emittance of an externally injected witness beam for different plasma upramp lengths. In all cases, the ramp profile is based on OpenFOAM simulations of a gas cell (work by C. Thornton, Oxford University), scaled to the desired length in order to provide a realistic plasma shape (see Appendix B for fit, Fig. 5.14 for profile shape). Unlike for a fully matched beam or with a completely adiabatic profile, the emittance in these simulations is not fully preserved; however, growth can be successfully controlled through the

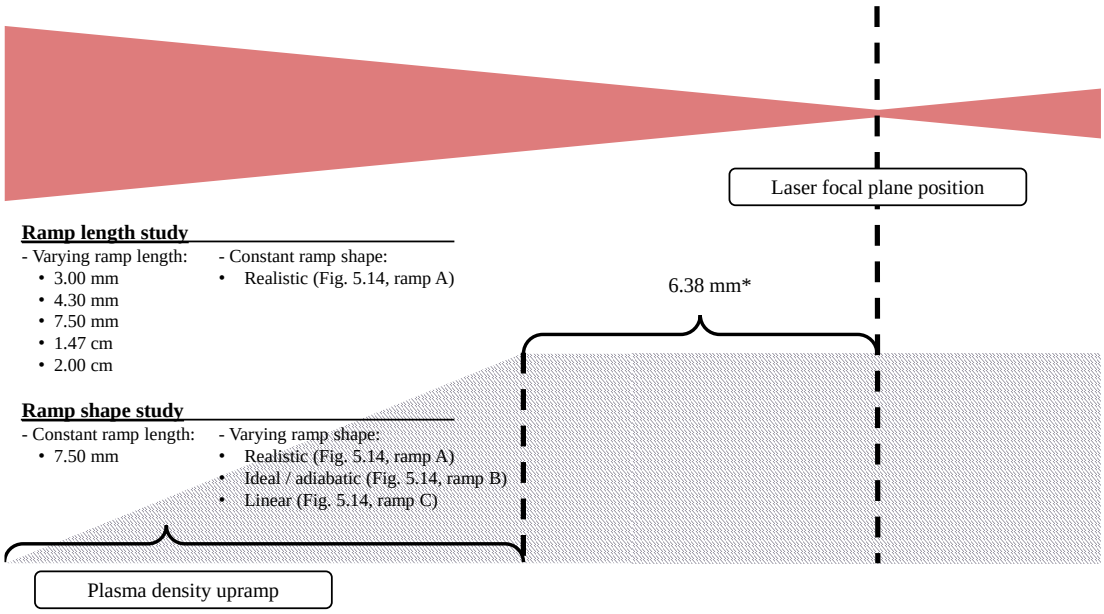

Figure 5.8: Sketch of the laser and plasma configurations employed in the simulations presented in Section 5.2, in particular for the studies on the effect of plasma upramp length and shape on the matching efficiency.
* Note that the laser focal position was placed at 6.38 mm for all cases, except for the simulation in the ramp length study with an upramp length of 1.47 cm, in which case the laser focus is positioned at the end of the upramp.

variation of the ramp length. In more detail, while a beam entering a hard-edge plasma experiences an emittance increase of approximately 2.3 µm (1353 %) over a 100 MeV energy gain, a 7.5 mm upramp can reduce this to 0.2 µm (115 %); a 2 cm ramp even ensures for the total normalised emittance to stay below 0.2 µm (11 % increase). The Twiss parameter evolution along these ramps is shown in Fig. 5.10: the longer the density transition becomes, the slower the betatron oscillations evolve along the ramp, so that phase-space mixing is reduced. At the same time, the oscillation amplitudes of $\alpha_{cs,x}$ and $\beta_{cs,x}$ are decreased and brought closer to the matched values, hence limiting the following mismatch and emittance increase in the acceleration section.

As seen in Fig. 5.11, the emittance growth roughly follows an exponential dependence on the upramp length where, at least for the conditions considered here, above 1.5 cm a further reduction in the growth rate requires considerable increase in the density ramp length. As an increasing length in the plasma target, however, brings a number of complications with it, such as the necessity to compensate for laser defocusing and beam dephasing, a compromise between minimising emittance growth and target size is a reasonable choice. The clear dependence of the emittance growth on the transition length hence provides a great tool for controlling the

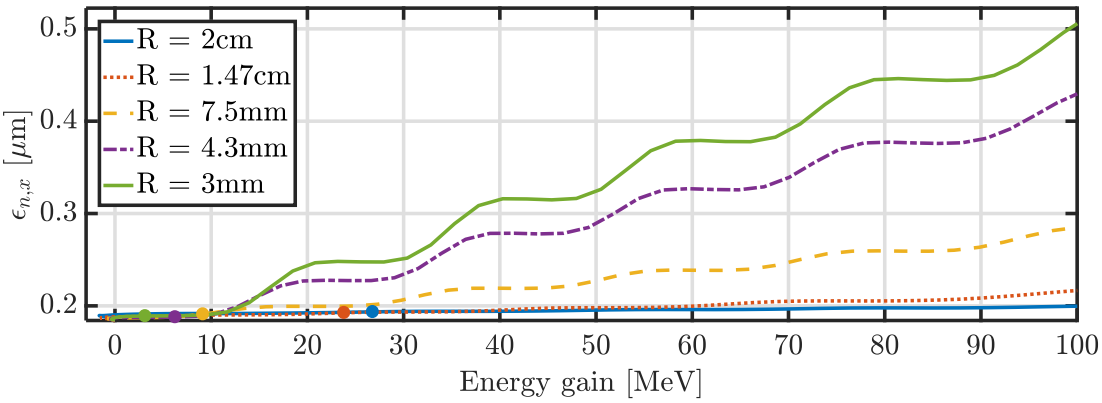

Figure 5.9: Dependence of beam matching on upramp length: Evolution of the normalised beam emittance as a function of energy gain (up to 100 MeV) for plasma targets with linear upramp of length 2 cm (blue line), 1.47 cm (red line), 7.5 mm (yellow line), 4.3 mm (violet line) and 3.0 mm (green line).

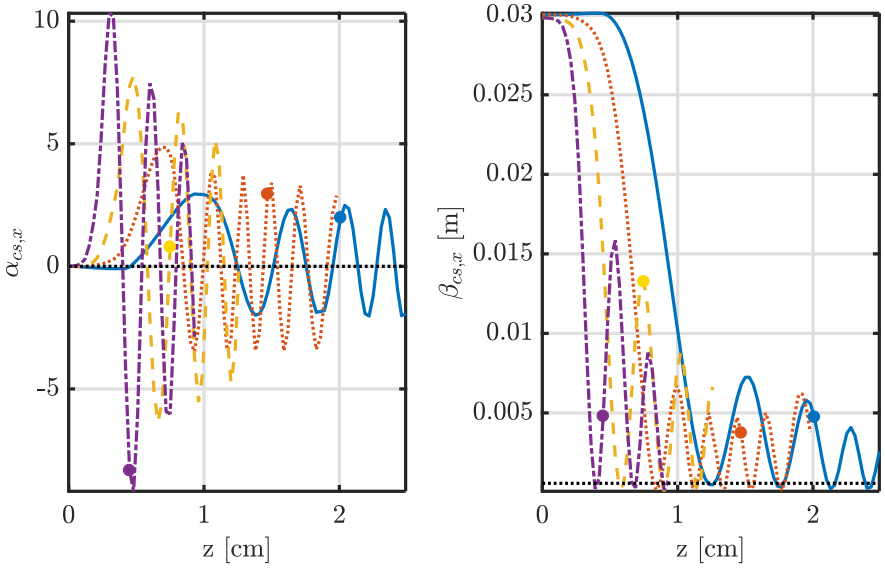

Figure 5.10: Dependence of beam matching on ramp length: Evolution of the beam $\alpha_{cs,x}$- and $\beta_{cs,x}$-functions as a function of propagation distance (up to 100 MeV energy gain) for plasma targets with linear upramp of length 2 cm (blue line), 1.47 cm (red line), 7.5 mm (yellow line) and 4.3 mm (violet line). The dots indicate in each case the position of the ramp end.

final emittance of the accelerated beam to a level that is required for planned applications.

As the emittance evolution of the beam depends, among others, on its initial transverse properties, however, the previously presented results are very specific to the witness beam investigated here. A more general solution would thus be useful to apply to different setups. On these grounds, Fig 5.12 compares the evolution of emittance and Twiss parameters with that predicted by the analytical model presented in Eq. (2.21). The latter is solved numerically

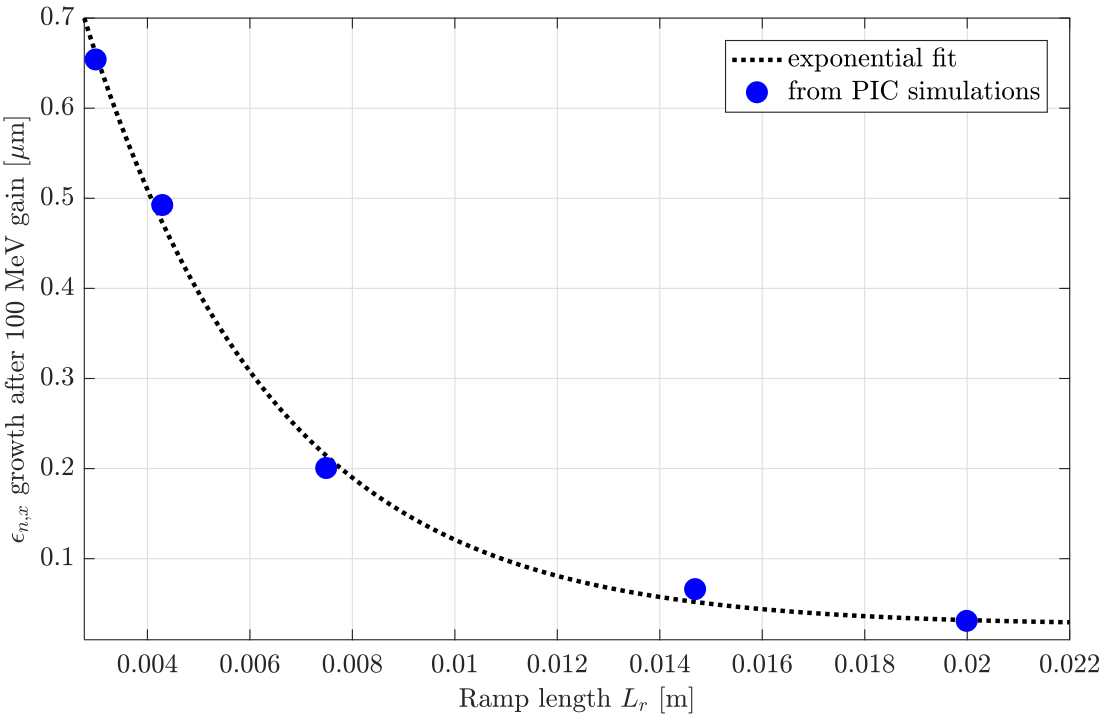

Figure 5.11: Emittance growth as a function of upramp length: The values calculated from PIC simulations up to 100 MeV energy gain (blue dots) are fit to an exponential function (black line) of the form $y = a\ \exp(bx) + c\ \exp(dx)$ with a=0.0217, b=7.286, c=1.422, d=-267.8.

assuming a weakly nonlinear plasma wakefield with a realistic plasma upramp profile of length R and Gaussian beam propagation for the drive laser following Eq. (3.2). To quantify the emittance growth, the difference between initial and final, saturated emittance is calculated where the latter is defined as [54]

$$\epsilon_{n,sat} = \frac{\epsilon_{n,i}}{2}(\gamma_{cs}\beta_{cs,m} + \frac{\beta_{cs}}{\beta_{cs,m}}) \tag{5.5}$$

with $\beta_{cs,m}$ the matched β_{cs}-function and $\epsilon_{n,i}$ the initial normalised beam emittance. $\epsilon_{n,sat}$ describes the maximum emittance caused by complete decoherence of the transverse phase-space. Assuming that the main source of phase-space mixing is the dependence of the focusing strength K on the transverse coordinate, the distance after which this final emittance is reached can be approximated by

$$L_{dc} = \frac{\pi w^2}{2\sigma_r^2\sqrt{K(r=0)}}\,, \tag{5.6}$$

where σ_r is the RMS width of the electron beam and a betatron phase difference of π has been assumed between the particles on-axis and at $r = \sigma_r$ [159].

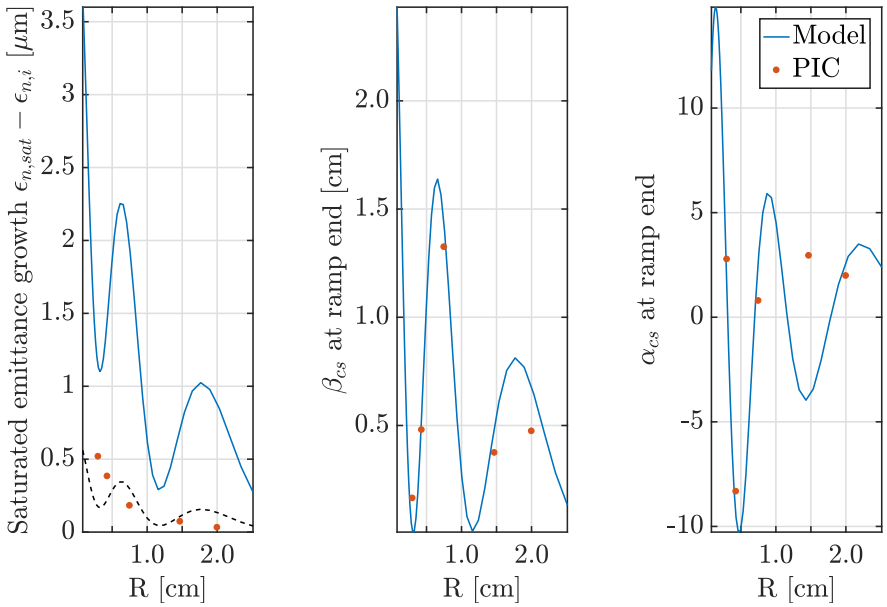

Figure 5.12: Comparison of emittance growth as well as α_{cs}- and β_{cs}-functions for model and PIC simulation results. The emittance change values from the PIC results are found at z_{acc} =1 cm plasma propagation after the ramp end with the dotted black line showing the model scaled down by a factor of L_{dc}/z_{acc}=6.55. The α_{cs}- and β_{cs}-values are taken at the end of the density ramp.

While a good agreement is found for α_{cs} and β_{cs} for small values of R, the fit quality reduces for longer ramps. This is likely caused by the increase in beam energy on the upramp not considered in this model, but could also be related to possible discrepancies of the fields in the weakly nonlinear model from the actual wakefield in the PIC simulations. The emittance growth varies strongly from the values calculated from the simulations, as the latter are taken after a propagation distance of 1.0 cm from the density ramp end and hence are not the final growth values. Scaling the model estimates down, however, by the ratio between L_{dc} and the acceleration length in the simulations (black dashed line) presents the general trend quite well. Although not sufficient to replace full simulations, the model nonetheless allows to generate rough estimates of the transverse evolution of the beam much faster than particle-in-cell codes and thus allows for a simple way to estimate required density ramp lengths under different conditions.

Finally, the length of the density upramp also influences the overall quality of the witness beam, as Fig. 5.13 shows. Due to the beam's own wakefield dominating over the initially weak laser wakefield at the beginning of the ramp profile, together with an almost constant mean energy, a large increase in relative energy spread is observed, especially for long ramps. In terms of the bunch length, on the other hand, a shorter ramp length leads to a larger growth,

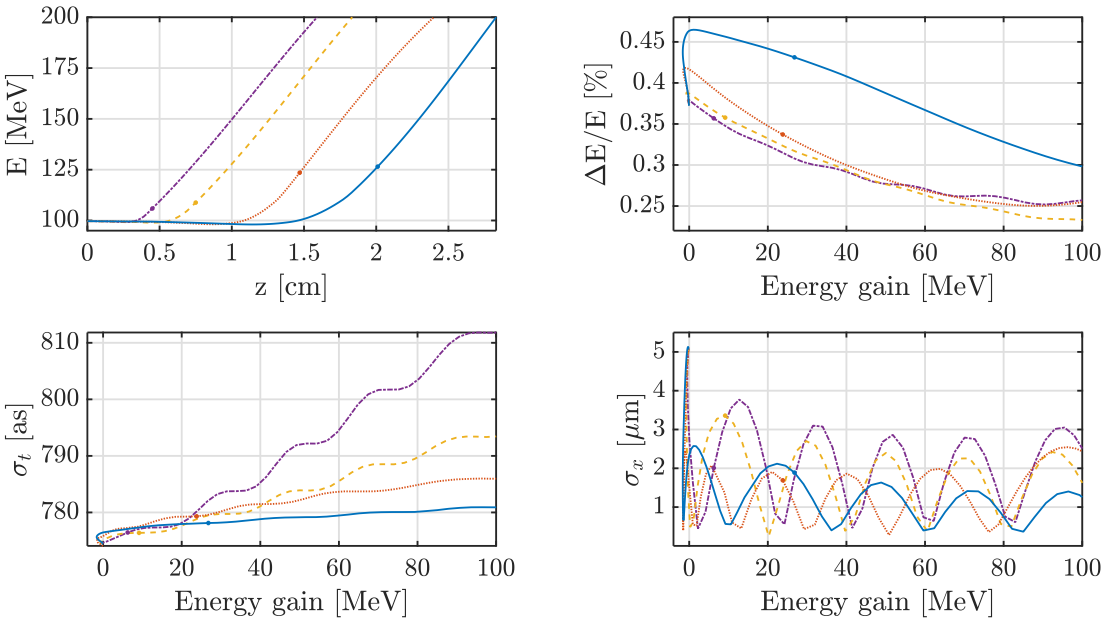

Figure 5.13: Dependence of beam matching on ramp length: Evolution of the beam parameters up to 100 MeV energy gain for plasma targets with linear upramp of length of 2 cm (blue line), 1.47 cm (red line), 7.5 mm (yellow line) and 4.3 mm (violet line). The dots indicate in each case the position of the ramp end. Note that all plots, except for the top left one, show the parameter evolution as a function of energy gain, such that an initial mean beam energy loss is indicated as an extension to negative values on the x-axis.

yet still within a margin of less than 5 % over a 100 MeV gain.

Dependence on Ramp Shape

As previous studies have put little emphasis on the shape of a matching ramp - using either an idealised adiabatic or a simple linear profile [157, 158] - the following section is dedicated to a comparison of ramp shapes. An overview over the profiles under investigation, all with overall length 7.5 mm, is depicted in Fig. 5.14: ramp A is a realistic profile based on OpenFOAM simulations, as introduced in the previous section; ramp B is an idealised profile similar to what is presented in [157]; ramp C is a simple linear profile. Each shape was simulated with (solid lines) and without (dashed lines) a pre-formed plasma channel, such that in the last case the drive laser is guided, while without the channel the pulse evolves as a Gaussian beam, as shown in Fig. 5.15. Although this laser guiding only sets in at the end of the plasma upramp where the laser focal position is located, it, nonetheless, provides a constant laser pulse spot size and a_0-value (see Section 5.3 for details) for the main accelerating region. This allows to evaluate the effect of the laser evolution on the matching process, as the transverse beam

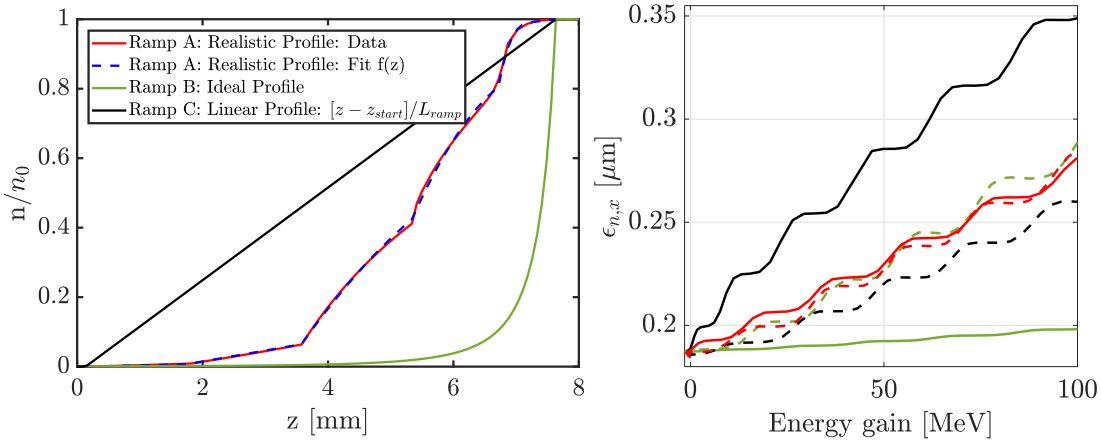

(a) Ramp shapes

(b) Emittance evolution

Figure 5.14: Dependence of beam matching on ramp shape: (a) Different ramp shapes studied and (b) evolution of the normalised beam emittance as a function of energy gain up to 100 MeV for plasma targets with 7.5 mm-long upramp profiles shown in (a) (line colours matched). Solid (dashed) lines represent simulations with a guided (unguided) laser pulse. The realistic data refers to a density profile from OpenFOAM calculations of a gas cell (C. Thornton, Oxford) (red line in (a)) with a fit to the latter used in the simulations (blue dashed line in (a)).

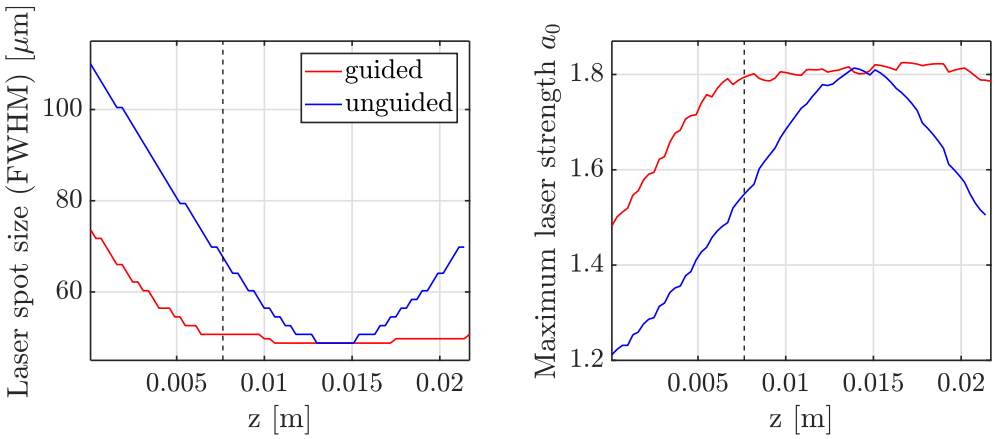

Figure 5.15: Evolution of the drive laser spot size and strength value a_0 for the simulated cases studying the dependence of beam matching on ramp shape with (red line) and without (blue line) a plasma channel for guiding. The laser focal spot is positioned at the end of the plasma density upramp at 7.635 mm, marked by the black, dashed line, for the guided scenario, while in the simulation without guiding it is placed at the centre of the plasma target at 1.388 cm. Note that the step-like features in both the spot size and laser strength curves are numerical in nature and occur due to the chosen temporal and transverse spatial simulation step sizes.

properties continue to evolve even after the plasma ramp.

In the guided scenario, as seen in Fig. 5.14, where the focal position has been placed at the end of the upramp and the start of the plasma channel, large discrepancies are seen between the different ramp shapes: while profile B minimises the total normalised emittance to below

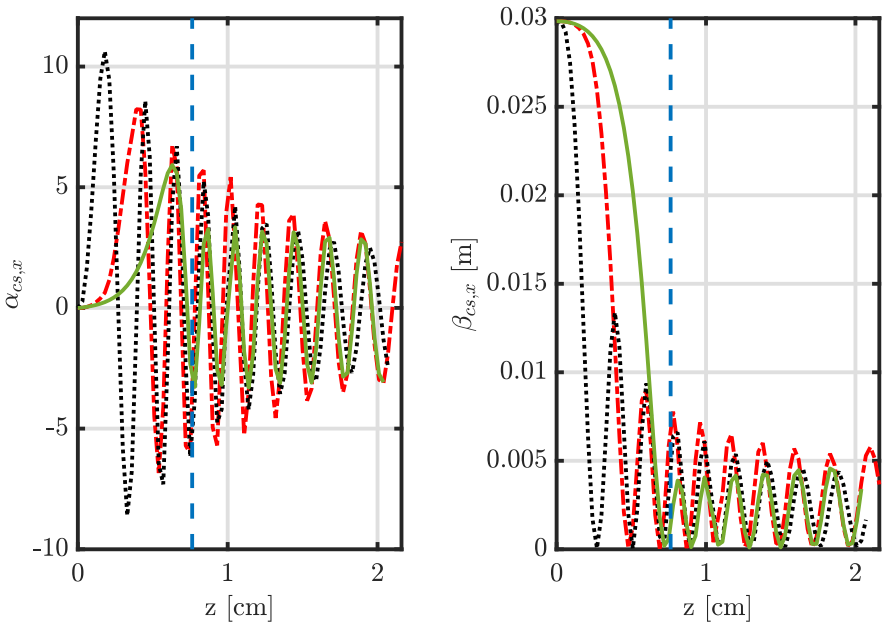

Figure 5.16: Dependence of beam matching on ramp shape: Evolution of the beam $\alpha_{cs,x}$- and $\beta_{cs,x}$-functions as a function of propagation distance (up to 100 MeV energy gain) for plasma targets with realistic (red line), linear (black line) and ideal (green line) upramp shapes of length 7.5 mm, as defined in Fig. 5.14. The blue dashed line denotes the end of the upramp in all cases.

0.2 µm (the same level as a 2 cm ramp of shape A), ramp A experiences a rise on the order of 0.19 µm (113 %), being topped by ramp C with an increase of 0.33 µm (193 %). This is consistent – also in terms of the Twiss parameter evolution in Fig. 5.16 – with the observations made with regard to the ramp length. Due to the initially small slope of profiles A and B, the beam Twiss parameters behave similarly to a comparably longer ramp length and hence the emittance growth is mitigated better.

For the unguided scenario, on the other hand, very little difference is observed in the emittance growth indicating that the effect of the laser focusing is quite dominating on the focusing fields experienced by the witness beam and hence the transverse beam evolution. It should be noted that such an effect was not seen in the previous section, as the laser focal position was adapted according to the ramp length to remove its influence as much as possible.
Overall, ramp shape A, which is naturally to be expected from the plasma profile in a gas cell, is thus quite efficient for matching. Attempts to shape the density profile further are deemed excessive considering the relatively small improvement possible and the potentially deteriorating effect that the laser evolution could have on the latter. Taking into account the strong effect of the laser profile evolution, optimising the development of the laser spot size to greater

detail is another possible route to controlling emittance growth even better. In principle such an approach for matching into the plasma should be even more effective than manipulating the density profile, as – like Eqs. (5.1) and (5.3) for the linear and nonlinear plasma regime show – the focusing strength K depends more strongly on the laser spot size than on the plasma density, hence allowing similar matching effects with considerably smaller variations in the laser spot than in plasma density. However, manipulating the range and shape of the transverse laser evolution to a detailed level is not a commonly employed technique and will likely come with considerable challenges, including, e.g., estimating the interactions between the laser shape and plasma profile; it is therefore beyond the scope of this discussion.

Dependence on Space-Charge Effects

The theory described in Section 2.3, defining the matched β_{cs}-function for a specific focusing system is valid only for an emittance-dominated electron beam and as such neglects any defocusing space-charge effects. Beams with sub-femtosecond bunch duration, however, could possibly, and more easily than longer beams, reach densities where the space-charge effects are of similar order to the emittance effect, especially when focused to small transverse sizes to be matched into a plasma structure. In order to study at what beam densities and charges such a regime is reached, the basic transverse matching theory is expanded for space-charge dominated beams and compared to PIC simulations.

To include the effect of space-charge on the transverse evolution of an electron, Eq. (2.16) is extended by a space-charge term:

$$x'' + K(z)x - \frac{K_{sc}}{a^2}x = 0\,, \tag{5.7}$$

where a is the beam radius which would be given by $\sqrt{2}\sigma_x$ for a Gaussian beam. This equation can in turn be generalised to describe the envelope evolution for an electron beam [49]:

$$\sigma_x'' + K(z)\sigma_x - \frac{K_{sc}}{\sigma_x} - \frac{\epsilon^2}{\sigma_x^3} = 0\,. \tag{5.8}$$

Similarly to the treatment with the equation for the beam β_{cs}-function (Eq. (2.21)), the matched beam size $\sigma_{x,m_{sc}}$ is defined here as the value for which $\sigma_x'' = \sigma_x' = 0$ and $\sigma_x = \sigma_{x,m_{sc}} = \text{const.}$, such that

$$\sigma_{x,m_{sc}}^2 = \frac{K_{sc} + \sqrt{K_{sc}^2 + 16K\epsilon^2}}{4K}\,. \tag{5.9}$$

It should be noted that, for the case that the factor K_{sc} is negligible, Eq. (5.9) simplifies to

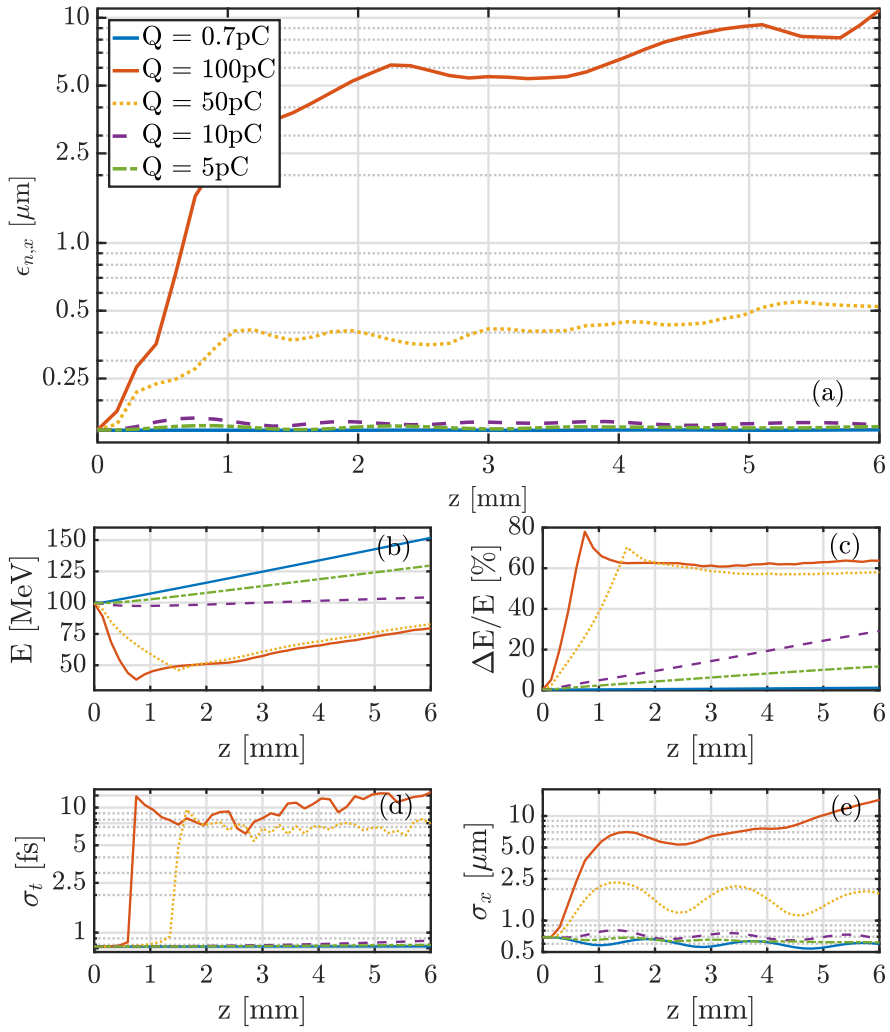

Figure 5.17: Dependence of beam matching on electron beam density: Evolution of the normalised emittance (a) and other beam parameters (b-e) as a function of propagation distance for beams with varying charge. The transverse beam size was chosen as the matched value according to Section 2.3, without taking into account space-charge effects. Note that the relative offset between laser and witness electron beam is 52.7 µm in this case, in agreement with the discussion in Section 5.4.

$\sigma^2_{x,m_{sc}} = \epsilon/\sqrt{K}$ which is equivalent to the solution derived in Section 2.3.

As Table 5.3 lists, space-charge effects in general are expected to have a very weak effect on the matching into the plasma with changes in matched spot size becoming measurable at beam currents of a few tens to hundreds of kA only, based on the theory derived above. Fig 5.17 demonstrates, on the other hand, that in PIC simulations space-charge effects become dominating to the emittance and general beam evolution at currents on the order of 5–25 kA already; this is at considerably lower currents and beam densities than expected. Interestingly,

Q [pC]	I_b [kA]	K_{sc}	$\sigma_{x,m_{sc}}$ [µm]
0.7	0.359	5.6×10^{-9}	0.71
10	5.13	8.0×10^{-8}	0.72
50	25.7	4.0×10^{-7}	0.76
100	51.3	8.0×10^{-7}	0.81
200	102.7	1.6×10^{-6}	0.92

Table 5.3: Space-charge effects and matched spot size including such effects for varying bunch charges and currents. In all cases, the bunch dimensions of the SINBAD beam have been assumed with a focusing strength of K=3.0×10^6 m^{-2}, equivalent to that expected in the SINBAD case at an electron - laser offset of 52.7 µm.

the beam expansion for the 50 pC and 100 pC cases is not limited to the transverse plane. Due to longitudinal space-charge forces the back of the beam is decelerated strongly leading to a decrease in mean energy of more than 50 MeV. Additionally, an increase in energy spread and bunch length by ≥ 70 % and 8.9 fs or more, respectively, is observed, as the beam is ripped apart. The effect on the bunches with charge less than that, in comparison, is orders of magnitude smaller with negligible or non-existent loss in mean energy.

To test the adapted matching theory further, the 50 pC simulation case was repeated with varying electron RMS widths, as seen in Fig. 5.18. With the red dotted line representing the matched case according to the adapted theory, it becomes clear that the latter is not complete, as emittance growth is still observed, although not as strongly as with the initial smaller bunch width. Considering the extreme longitudinal dynamics of the beam, a likely cause is the fast variation in energy across the bunch and in mean energy which changes the matched beam size significantly leading to a mismatch with the plasma. It thus becomes clear that these longitudinal effects cannot be neglected and a simple transverse beam theory, including space-charge, is not sufficient to describe this regime correctly.

Overall, it is found that the ultrahigh density regime above 23 pC µm^{-3} (I $\geq$ 25 kA) becomes very difficult to control leading to fast, unstable beam dynamics. Up to densities of order 5 pC µm^{-3}, where space-charge forces can be neglected in the matching strategy, the beam dynamics are more feasible. For electron beams from RF injectors, as studied in this chapter, such high beam densities are highly unlikely to achieve due to the difficulties with space-charge forces in vacuum propagation, so that the effect of space-charge on the matching process generally does not need to be taken into account. When investigating plasma injectors in more extreme regimes as potential witness beam sources, however, such as for the beams described in Chapter 4, it is a potential issue that needs to be considered in the setup design.

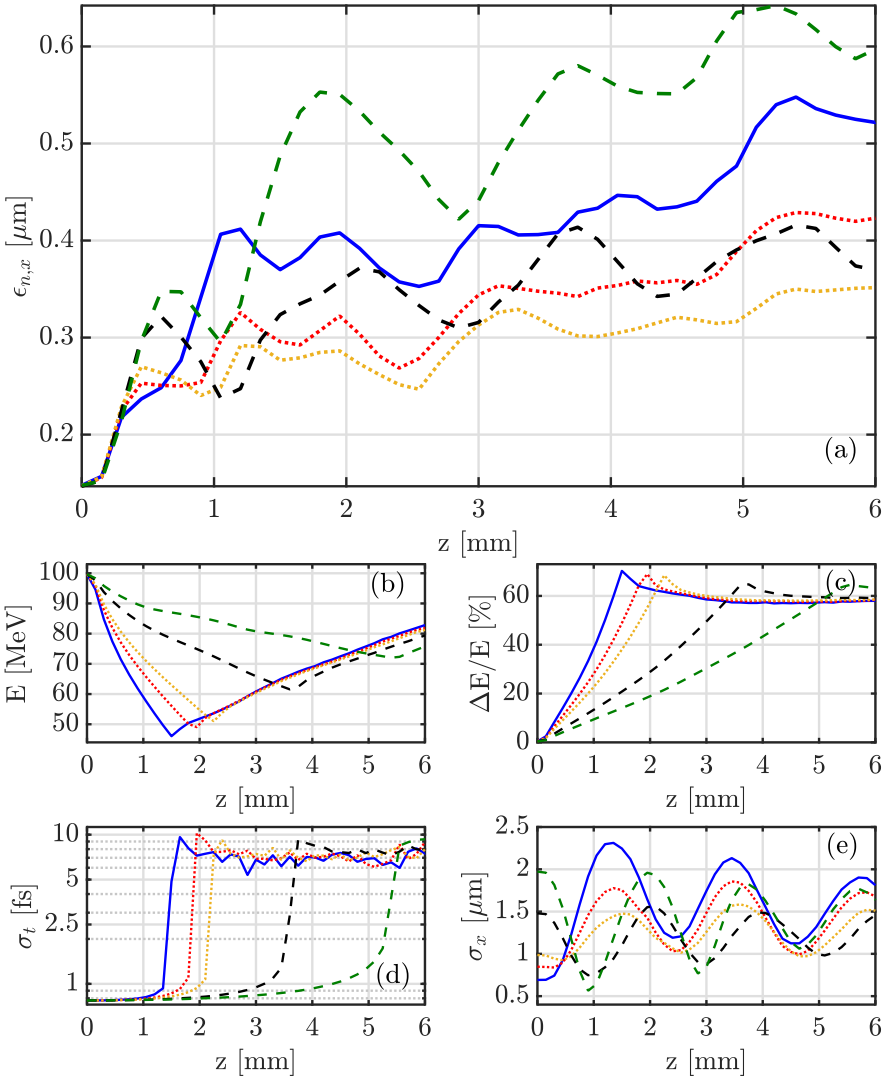

Figure 5.18: Dependence of beam matching on electron beam density: Evolution of the normalised emittance (a) and other beam parameters (b-e) as a function of propagation distance for beams with 50 pC charge and varying transverse RMS size. The latter takes values of 0.7 µm (blue line), 0.86 µm (red line), 1.0 µm (yellow line), 1.5 µm (black line) and 2.0 µm (green line).

Numerical Effects

During the studies above, it was found that numerical effects, in particular numerical heating and numerical Cherenkov radiation, can play a significant role in the emittance evolution in the plasma. Numerical Cherenkov radiation is a typical problem with the standard Yee field solver – i.e., the algorithm calculating the electromagnetic fields across the cell grid based on Maxwell's equations. This is due to the fact that the numerical velocity of electromagnetic waves is artificially reduced below the speed of light in vacuum in this scheme. Consequently,

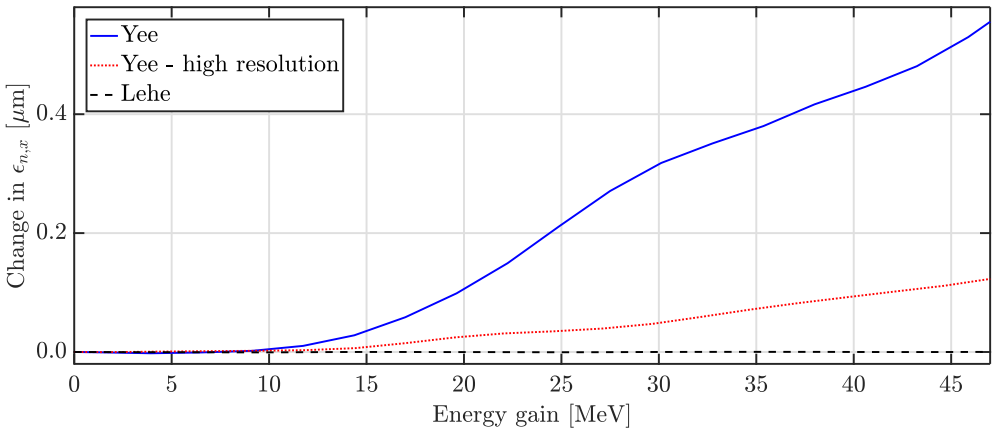

Figure 5.19: Numerical effects due to the field solver on the emittance growth in plasma: in theory no emittance growth is expected for this case, as the transverse electron beam size is matched to the plasma focusing forces. This is confirmed by the simulation with the Lehe solver. All simulations use a transverse plasma density channel for laser guiding, but no longitudinal upramp.

macroparticles can overtake these light modes and their interaction leads to the artificial generation of Cherenkov radiation. When the electron bunch in the simulation interacts with this numerical Cherenkov modes, this can lead to emittance growth [160, 161].

Numerical heating, on the other hand, is a phenomenon caused by the discretisation of the charge density into a limited number of macroparticles. If the number of these macroparticles per cell is quite low, artificial potentials are generated through variations in macroparticle numbers between cells [162]. This is especially relevant for very short electron beams, as studied here, for which the number of macroparticles and grid cells describing the beam with its fields is limited.

Figure 5.19 shows the effect of these numerical artifacts. Using the standard Yee field solver with a spatial resolution of $2.0 \times 10^{-8}\,\mathrm{m} \times 9.8 \times 10^{-7}\,\mathrm{m}$ an artificial emittance growth of more than 800 % is observed, which can be mitigated down to a growth of around 180 % by improving the resolution to $2.3 \times 10^{-8}\,\mathrm{m} \times 1.0 \times 10^{-7}\,\mathrm{m}$. In order to fully avoid this numerical noise, it was found necessary to optimise the choice of PIC field solver by employing the Lehe solver (spatial resolution: $2.3 \times 10^{-8}\,\mathrm{m} \times 5.0 \times 10^{-7}\,\mathrm{m}$) [160]. This algorithm uses a different way of discretising Maxwell's equations and is designed to avoid numerical Cherenkov radiation by increasing the electromagnetic wave velocity above c. Consequently it has been used for all of the simulations presented in this section.

5.3 Laser Guiding in a Pre-Formed Plasma Channel

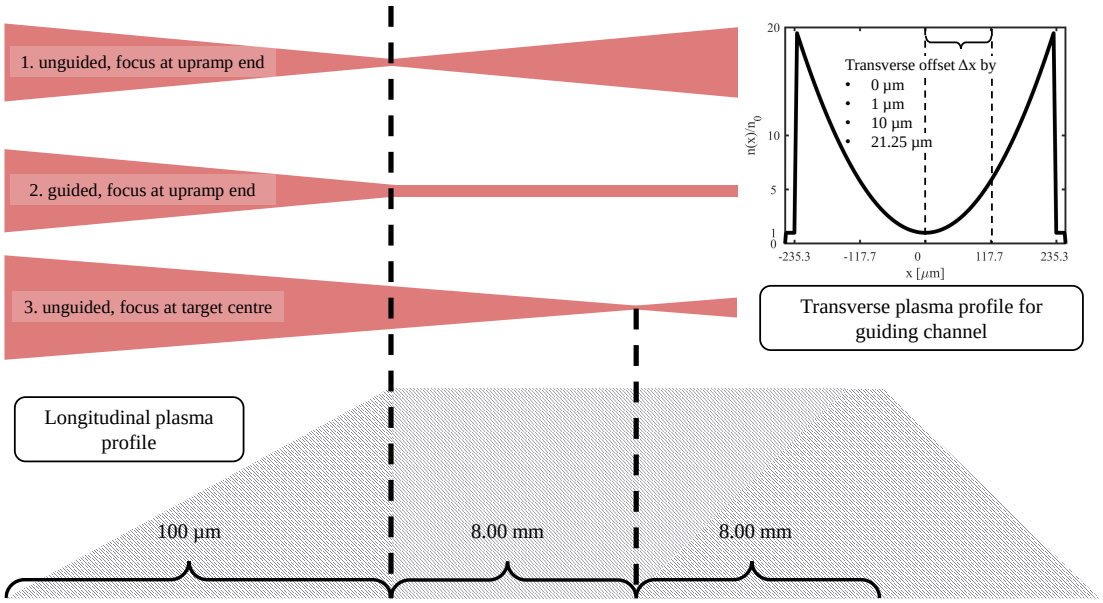

Figure 5.20: Sketch of the laser and plasma configurations employed in the simulations presented in Section 5.3, both for studying the effect of laser guiding on the witness electron beam parameters and for investigating the consequences of a transverse offset of the drive laser in the plasma guiding channel.

One of the main limitations in the linear and weakly nonlinear regime for the effective acceleration distance of the witness electron beam in the plasma, besides dephasing and depletion, is the defocusing of the drive laser pulse a few Rayleigh lengths (usually millimetres to centimetres) behind the position of its focal plane. A successful strategy to mitigate this issue is to use the plasma itself as a guiding mechanism that can keep the laser beam focused over multiple Rayleigh lengths. Both self-guiding and external guiding techniques are in principle possible for this endeavour. For relativistic self-guiding to occur, however, the laser power P_{sg} must significantly exceed the critical power for self-focusing $P_c[GW] \approx 17.4(\omega/\omega_p)^2$ [113] which for a density of $1 \times 10^{23}\,\mathrm{m}^{-3}$ lies around 303 TW. With the expected peak power of the ANGUS laser being considerably below this threshold, such an intrinsic plasma guiding mechanism is not possible. The following section hence studies the possibility and effectiveness of an external guiding mechanism, in particular the use of a parabolic plasma channel. With the laser and plasma configuration shown in Fig. 5.20, the effect of laser guiding on the witness electron beam properties as well as the consequences of a transverse offset of the laser in the guiding channel are investigated.

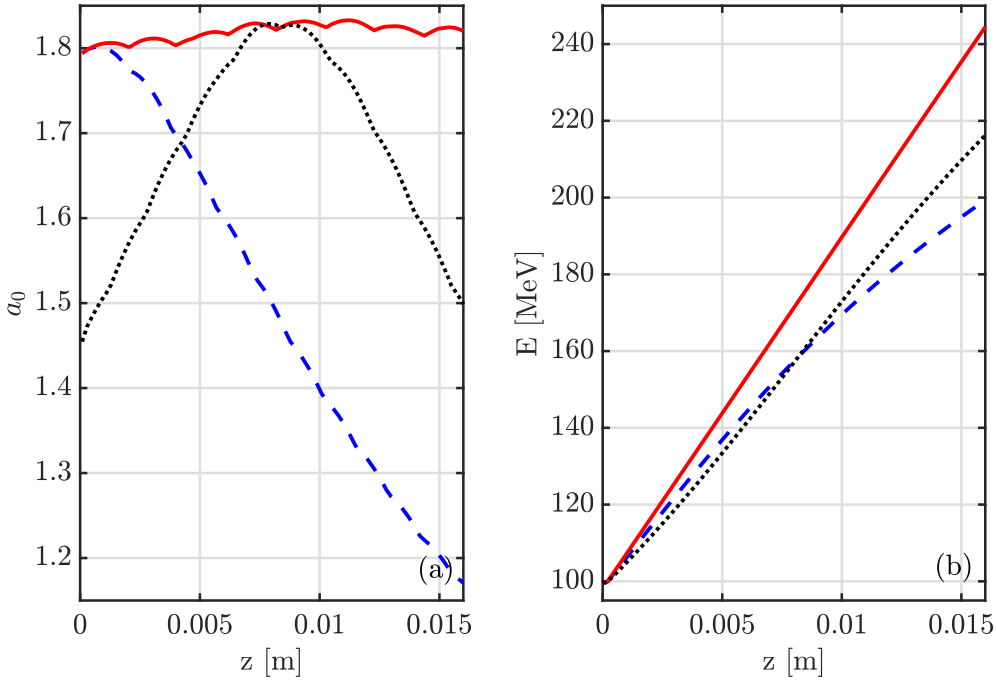

Figure 5.21: Laser strength evolution (a) and electron beam energy gain (b) for guided and unguided drive lasers in plasma with different focal positions. The blue line depicts an unguided laser with focal plane at z=209.2 µm (beginning of the plasma density plateau), the red line shows a guided laser with focal plane also at z=209.2 µm and the black line represents an unguided laser with focal plane at z=8.2 mm (centre of the plasma target).

By shaping the plasma in the direction perpendicular to the laser propagation into a channel, the refractive index η and hence also the local phase velocity of the laser pulse can be controlled as [163]

$$\eta(r) = \sqrt{1 - \frac{n(r)}{n_{cr}}}\,, \tag{5.10}$$

where n is the local plasma density. This shaping leads to a focusing effect of the laser pulse which under the right conditions fully compensates the vacuum diffraction and thus guides the laser pulse. This is the case for a matched channel of shape

$$\begin{aligned} n(r) &= n_0 \left(1 + \frac{\Delta n}{n_0}\frac{r^2}{w_0^2}\right) \\ \text{with } \Delta n &= \Delta n_c \ [\text{cm}^{-3}] \approx 1.13 \times 10^{20}/(w_0[\mu\text{m}])^2\,, \end{aligned} \tag{5.11}$$

where Δn is the channel depth, Δn_c is the critical channel depth, w_0 is the laser spot size at focus and n_0 is the density on-axis [113, 164]. It should be noted that in principle also other options can be used for guiding, such as a dielectric capillary tube [165, 166].

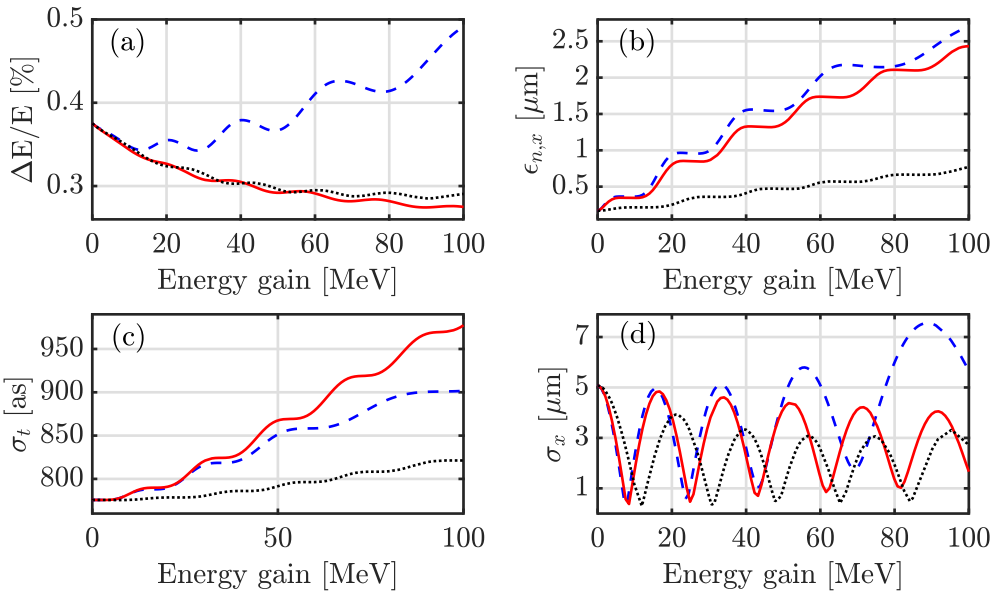

Figure 5.22: Electron beam properties for guided and unguided drive lasers in plasma with different focal positions. The line colours are defined as in Fig. 5.21 with blue representing an unguided laser with focal plane at z=209.2 µm, red a guided laser with focal plane at z=209.2 µm and black an unguided laser with focal plane at z=8.2 mm. Note that the simulations were done with the Yee solver, so the emittance evolution is affected by numerical emittance growth and should be taken only as a qualitative measure.

Figures 5.21 and 5.22 compare the evolution of an externally injected witness beam with and without the presence of a pre-formed channel up to a 100 MeV energy gain. A simple plasma target with background density of 1×10^{23} m^{-3} was used. By assuming the same position of the laser focal plane (at z=209.2 µm) with and without guiding (red and blue curves) a reduction of around 31 % in the required acceleration distance to 200 MeV is observed, as the energy gain remains linear even after more than two Rayleigh lengths (z_R =7.1 mm), while without guiding the laser strength drops by about 30 %. Similarly, the energy spread can also be decreased by around 70 % with the channel. This is caused by a continuously good match between the laser wakefield and the beamloading field, whereas without the guiding the beamloading becomes dominant as the drive laser defocuses. Interestingly, the laser pulse additionally seems to experience some small level of self-focusing in the guided case, as a_0 rises mildly above its focal spot value of 1.8. The fluctuations seen over time are likely due to interaction effects between the laser and the plasma channel which have not been taken into account in the theory for the matched channel parameters.

While this shows clearly the necessity for external laser guiding for high energy plasma stages, such as up to the GeV-level - where acceleration over multiple centimetres is required

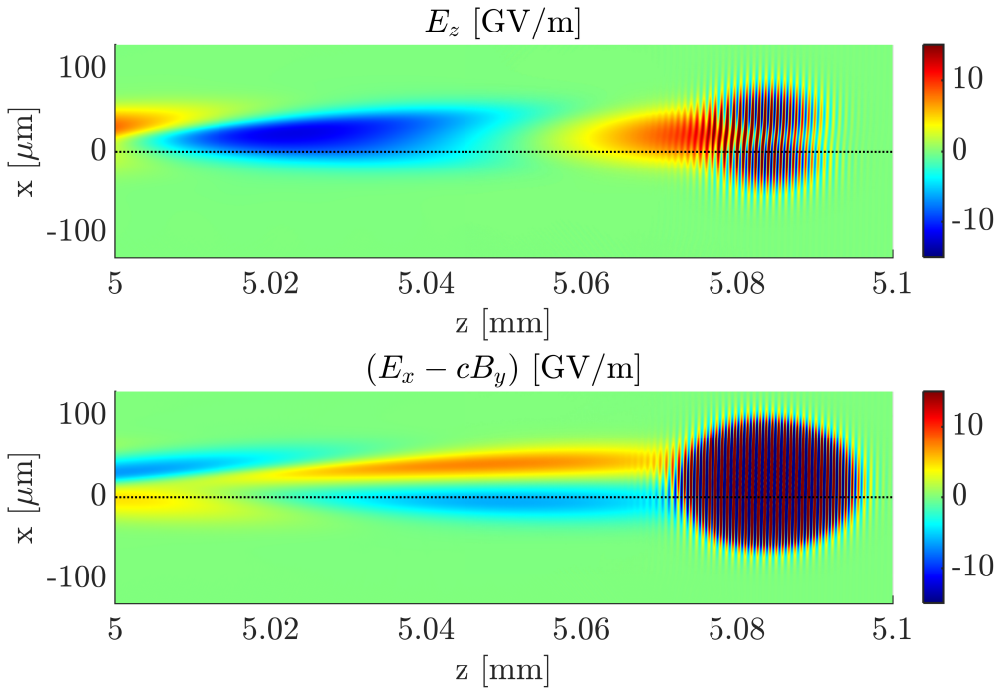

Figure 5.23: Accelerating and focusing field after 5 mm propagation for a drive laser with transverse offset of 21.25 µm from the guiding channel axis.

-, a good alternative for shorter stages was found through optimising the focal plane position in a non-guided plasma target. By placing the focal plane at the centre of the plasma cell, for example, as shown by the black curve, an increase of only 23 % in the required acceleration length with respect to the guided case is observed. Moreover, not only is the increase in energy spread variation now around 18 % only, but the beam emittance is also considerably improved. The latter is caused by the dependence of the focusing strength of the plasma on laser intensity, as was discussed in Section 5.2. It should be noted here that these simulations were completed with the Yee solver exhibiting considerable numerical Cherenkov radiation and thus the emittance evolution should be considered as a relative comparison only rather than a quantitative measure. Taking into account that the laser strength a_0 of the ANGUS laser can, assuming Gaussian beam propagation, be kept above half of its focal spot value throughout the whole stage for plasma targets shorter than 2.5 cm, a less complex setup without guiding is preferable for such low energy scenarios.

In order to get a better estimate of the laser pointing stability required for the use of a plasma channel, Figs. 5.23 and 5.24 show the effect of a transverse offset between the laser pulse and the centre of the plasma channel. The laser amplitude itself is not influenced by the

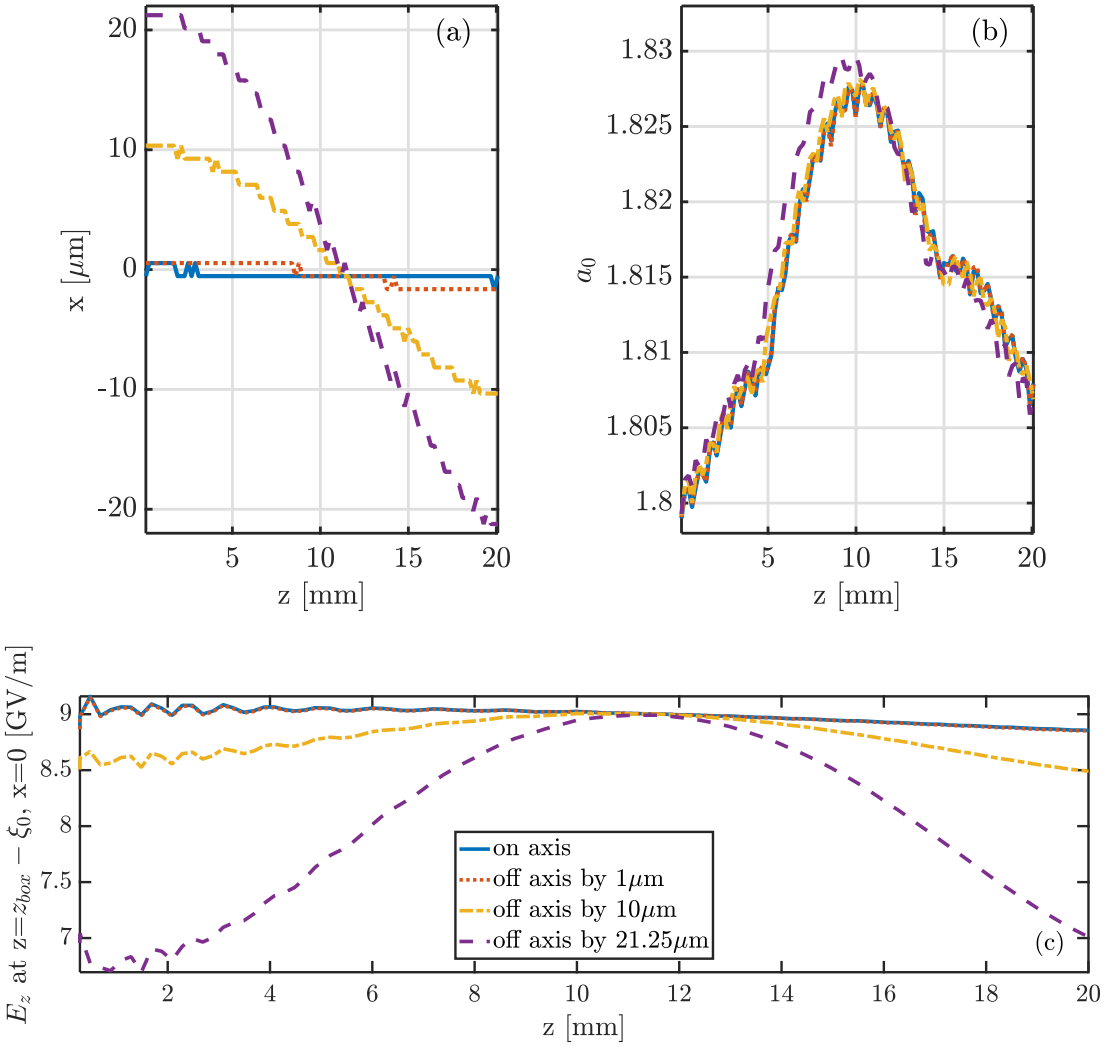

Figure 5.24: Evolution of the laser amplitude (b) and transverse central position (a) as well as the longitudinal wakefield amplitude (c) experienced by a beam ξ_0 =52.7 µm behind the laser driver for varying degrees of transverse mismatch of the laser in a guiding channel. The position in the wakefield has been measured with respect to the front of the simulation box in order to include dephasing effects and avoid fluctuations due to the laser envelope evolving.

pointing error in this case, as the variation in a_0 stays well below 1 %, even though the laser pulse oscillates transversely in the guiding channel by up to 42.5 µm depending on the initial offset. However, the wakefield experienced by a witness electron beam placed on axis in the guiding channel can be strongly affected: whereas even with a perfectly guided laser pulse a decrease of around 3 % is observed in the longitudinal field due to dephasing between laser and electron beam over 2 cm of propagation, the effect observed for a laser offset by 10 µm and 21.25 µm ($1/2 \times w_0$) is considerably larger on the order of up to 5.4 % and 26 %, respectively. Only once

the offset drops significantly below 10 µm, the oscillation of the laser pulse and consequently the amplitude variations of the accelerating field become negligible. As the wakefield amplitude has a crucial influence on both the energy and energy spread evolution of the witness beam, but also its transverse properties through the focusing fields, large shot-to-shot fluctuations on the order of tens of percent in the beam properties need to be expected if the laser pointing cannot be stabilised below a few percent of the channel radius, here 235 µm.

5.4 Beamloading Effects

As was shown in Section 5.1, the self-generated wakefield of the witness electron bunch, the beamloading field, actually plays a relevant role in the SINBAD setup, as the laser-driven wakefield is comparatively weak in the weakly nonlinear regime. It thus makes sense to utilise this beamloading effect in order to minimise the beam energy spread by flattening the effective accelerating field that the bunch is experiencing.

To this purpose, a simple semi-analytical model was developed that can predict a suitable electron beam position in a given laser wakefield based on calculating the expected bunch energy spread from the wakefield along the longitudinal axis within the beam. The effective accelerating field experienced by the electron beam is calculated as the sum of laser- and beam-driven wakefield: $E_{z,tot} = E_{z,plasma} + E_{z,beam}$. Here, the laser-driven plasma wakefield is based on the weakly nonlinear model (Eq. (3.27)), whereas the beam wakefield on-axis is found from [124]

$$E_{z,beam}(\xi, r=0)/E_0 = Z'(\xi)\,\left[1 - k_p a K_1(k_p a)\right], \tag{5.12}$$

where $Z'(\xi)$ is calculated numerically from Eq. (3.29) assuming a Gaussian beam charge distribution $q_{b,\parallel}(\xi)$. The beam radius a is given by $\sqrt{2}\sigma_x$ in this case. Note that the numerical calculation for the longitudinal field component is necessary, as the analytical description provided in Section 3.2.4 is valid behind the electron drive beam, but does not define the field within the beam correctly.

The beam energy distribution after an acceleration distance L_{acc}, given an initial beam energy ϵ_i, energy spread $\Delta\epsilon_i$ and energy chirp C_i, is then calculated as

$$\epsilon = \epsilon_i + C_i(\xi - \xi_{beam}) - E_{z,tot} L_{acc}\,, \tag{5.13}$$

$$\Delta\epsilon = \sqrt{\frac{\sum_{j=1}^{N} w_j \sum(w_j(\epsilon_j - \bar{\epsilon}))}{(\sum w_j)^2 - \sum w_j^2}} + \Delta\epsilon_i\,, \tag{5.14}$$

where w_j is used to weigh the energy spread calculation by the charge distribution of the beam, here assumed to be Gaussian [167], with N the number of cells considered for the beam. Additionally, the initial uncorrelated energy spread is added in the last step to take into account the transverse or slice energy spread across the beam. It should be noted that the model does

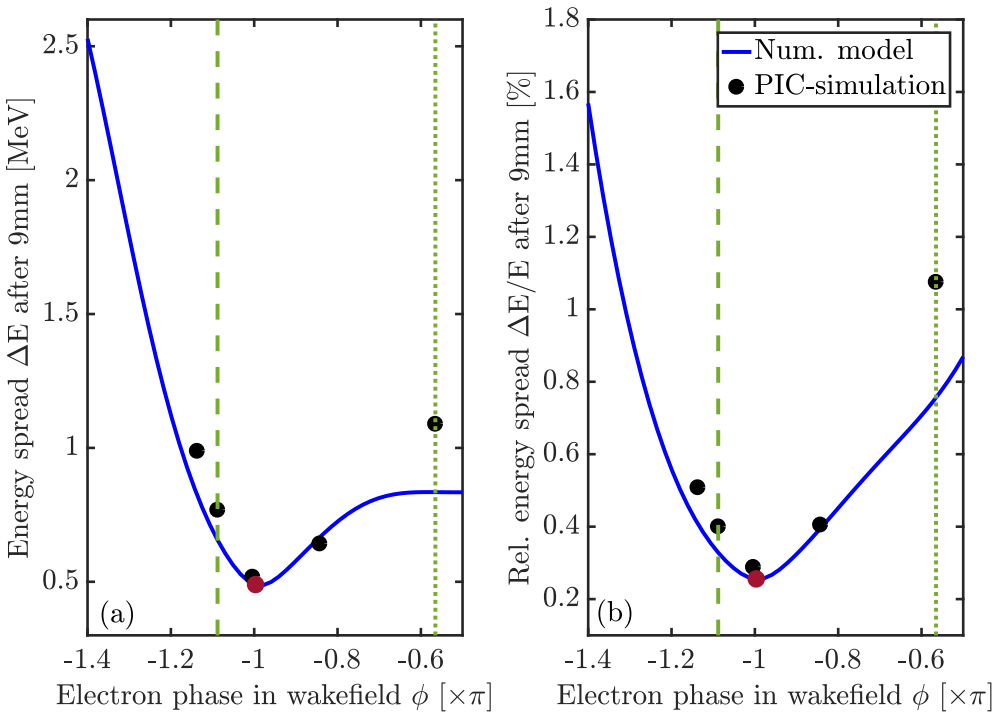

Figure 5.25: Comparison of the numerical model for energy spread minimisation (blue line) with 2D PIC simulation results (black dots). The green dashed and dotted lines show the phases for minimising the variation of the accelerating field along the z-axis and x-axis within the beam, respectively. The minimum position of the model is shown by the red dot.

not consider the influence of the off-axis accelerating field on the beam energy spread, an assumption which is valid under the conditions that the beam is narrow and the acceleration distances are small, so that the correlated transverse energy spread can be neglected. For the limited regime under investigation here, this is valid. Calculating the slice energy spread, i.e., the spread caused by the correlation of energy gain along the transverse direction, is, more generally speaking, also of limited interest in this scenario, since the relevant slice length for beam applications, such as Free-Electron Lasers, is on the same order as the beam length itself due to its short duration. Other aspects that have not been included in the model are, among others, the evolution in beam size and beam shape throughout acceleration, the evolution of the laser pulse as well as potential electron beam dephasing.

Figure 5.25 shows a comparison of model predictions (blue line) for the relative energy

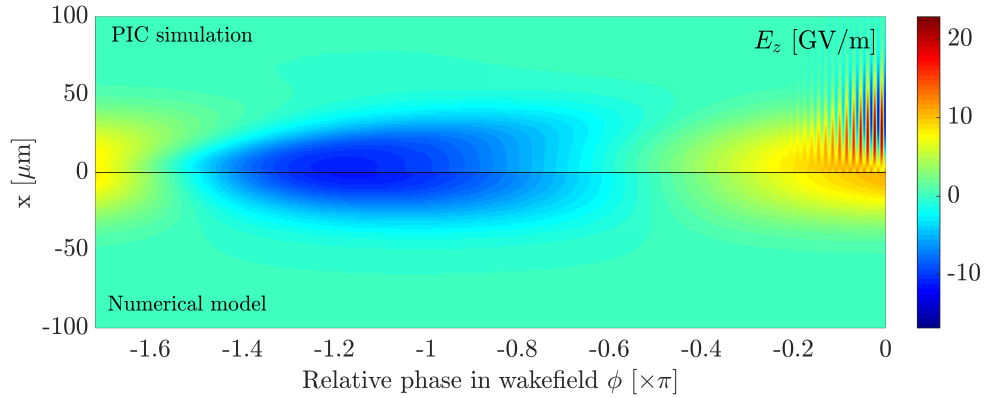

Figure 5.26: Comparison of the calculated longitudinal wakefield from the numerical model for energy spread minimisation (bottom half) with the wakefield extracted from an equivalent 2D PIC simulation (top half) after a plasma propagation distance of 9 mm in a plasma density of $1 \times 10^{23}\,\mathrm{m}^{-3}$. Consistent with the PIC simulation setup using a plasma channel for laser guiding, a constant laser spot size and strength of a_0=1.8 and w_0=42.5 µm, respectively, has been assumed in the model. The relative phase of the electron beam in the wakefield is $\phi = -\pi$ (corresponding to a laser - electron beam offset of −52.70 µm) for both calculation methods, but due to the small electron beam charge the beamloading field is visible only very weakly.

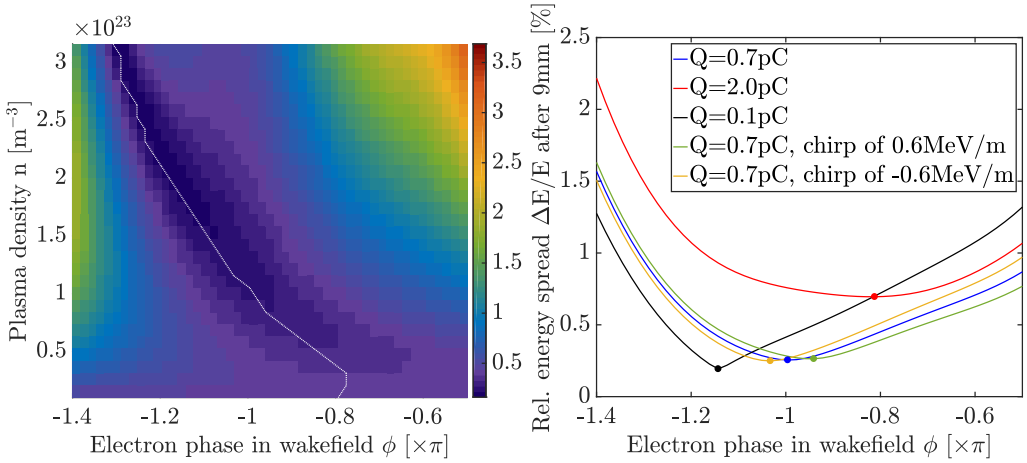

Figure 5.27: Optimum electron beam phase and plasma density to minimise the energy spread of the beam through beamloading after 9 mm acceleration. (a) shows the rel. energy spread of the SINBAD beam at different densities and beam phases with the minimum for each density plotted in white. (b) shows the relative energy spread at plasma density n=$1 \times 10^{23}\,\mathrm{m}^{-3}$ for different beam charges and degrees of chirping. The minima for each curve are shown by the dots.

spread after an acceleration distance of 9 mm in plasma in density of $1 \times 10^{23}\,\mathrm{m}^{-3}$ with results from equivalent 2D PIC simulations (black dots). The agreement close to the minimum position is very good and, most importantly, the minimum phase position is identified well. At more

negative phases, a slight discrepancy is observed which is likely related, among others, to an increase in transverse energy spread above the initial spread value, as the wakefield steepens radially faster than closer to the laser. Close to the field zero-crossing, at phase values of $\phi \gg -0.8\pi$, the fit also starts to differ from the simulation results, which could be caused by an insufficient representation of the detailed wakefield structure by the weakly nonlinear model. This last point can be seen in more detail in Fig. 5.26, where the wakefield distribution calculated from the model is compared with a 2D PIC simulation result. Although in general the shape and amplitude of the wakefield is reproduced well by the numerical model, discrepancies can be seen in particular around the zero-crossings of the field. With these ranges corresponding to the regions in Fig. 5.25 for which the energy spread prediction is not accurate, the limitations in reproducing the wakefield shape can be clearly identified as one of the sources for error in the calculation mechanism. Nonetheless, the presented model allows, in any case, to determine an estimate for the phase and plasma density for a given electron beam to generate a minimum energy spread and demonstrates particularly good agreement with PIC simulations for the main region of interest around the wakefield minimum. This is demonstrated further in Fig. 5.27 where different example cases are shown for varying plasma density (left) as well as varying beam properties (right). At higher plasma density, the beam needs to move closer to the accelerating field minimum, as the laser wakefield gradient becomes larger compared to the beamloading effect. The region close to the zero-crossing of E_z remains unsuitable in all cases, as the overall wakefield amplitude drops too far. Similarly, a reduction (increase) in the beam charge leads to a weaker (stronger) beamloading field so that the ideal beam phase moves away (closer) to the drive laser for a flatter (steeper) laser wakefield. The effect of an initial longitudinal energy chirp can also be taken into account as this changes the desired effective wakefield gradient to compensate the correlation.

Electron beam phase within wakefield [$\times\pi$]	1.09 (a)	0.565 (b)	1.00 (c)
Corresponding electron beam - laser offset [μm]	57.44	29.84	52.70
Rel. RMS energy spread [%]	0.400	1.32	0.291
Absolute RMS energy spread [MeV]	0.768	1.34	0.516
Mean slice energy spread* [MeV]	0.715	0.405	0.551

Table 5.4: Electron beam phase and energy spread corresponding to the beam images in Fig. 5.28.
*Note that slices here are defined by dividing the beam longitudinally into 50 sections.

One important aspect that the model takes into account is the shape of the electron beam. This is of particular relevance when considering a beam not optimised in shape, such as a Gaussian bunch, where the field cannot be completely flattened. In this case, the minimum

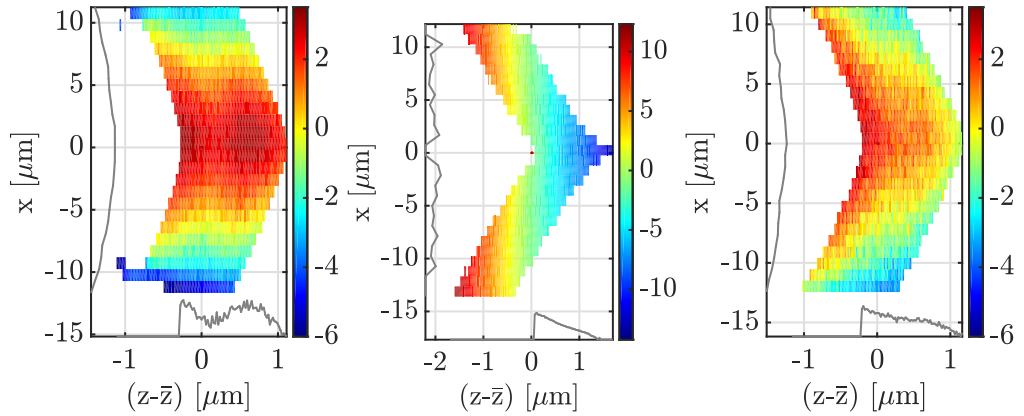

(a) Minimisation of the accelerating field along z

(b) Minimisation of the accelerating field along x

(c) Minimisation of the energy spread along z

Figure 5.28: Relative energy distribution (in MeV) across the witness beam in z and x for a beam with the phase optimised to (a) minimise the variation in E_z along z-axis across the beam (corresponding to the dashed line in Fig. 5.25), (b) minimise the variation in E_z along the x-axis across the beam and (corresponding to the dotted line in Fig. 5.25) (c) minimise the relative energy spread across the beam. The lineouts show the energy distribution along the centre of the beam in z and x, respectively, scaled to arbitrary units. The electron beam phases and energy spreads for each case are given in Table 5.4.

field gradient across the beam determines not necessarily the ideal phase conditions, as Fig. 5.28 shows: while (a) depicts the case where the on-axis longitudinal wakefield gradient is minimum, (c) shows the optimised beamloading phase based on the previously described model, where the on-axis gradient is slightly larger, but better suited to the beam charge distribution. As a comparison, (b) shows the energy distribution for a beam phase where the transverse energy spread is minimised; due to the large longitudinal energy spread and the small energy gain, this setting is not suitable. Table 5.4 quantifies the energy spread as well as slice energy spread for these cases shown: the clear reduction of the slice energy spread at a phase of 0.565π can be seen as well as the improvement in relative spread when considering the beam energy spread instead of the wakefield variation as a criterion. Moreover, in the optimised case the energy spread actually becomes limited by the value of the slice (transverse) energy spread. A more detailed optimisation procedure, especially for considering long acceleration distances, will thus require taking into account this off-axis contribution to the energy distribution. Since this, however, also requires analytically calculating the evolution of the beam shape off-axis, which can be extensive as seen from the beam shapes in Fig. 5.28, this goes beyond the scope of this work.

5.5 Extraction from the Plasma

Similarly important to matching the electron beam into the plasma is matching it out of the latter at the end of the target. In this case, the emphasis lies on controlling the beam divergence which is usually very large in plasma, but needs to be reduced in order to catch the beam using external focusing after the end of the stage. As [69, 157] proposed, this can be achieved by adiabatically decreasing the focusing strength of the plasma, either through manipulation of the laser spot size evolution or by control over the plasma density slope. Both of these options lead to a controlled increase of the beam spot size, while the divergence is reduced, without any emittance growth. Whereas [69, 157] investigated ideal cases with good matching into the plasma, the simulations presented here focus on a more imperfect scenario where the in-matching is not ideal and so the beam completes betatron oscillations in the plasma. Additionally, only the plasma density is considered as a controlling mechanism, in order to avoid having to include complex guiding mechanisms. The setup for the following simulation results is presented in Fig. 5.29.

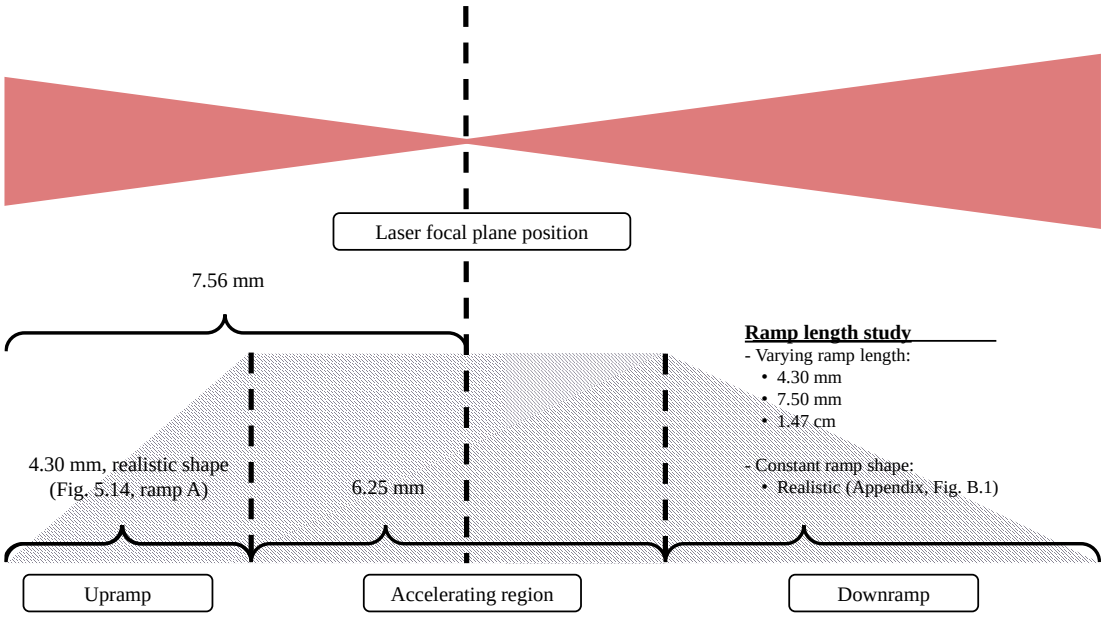

Figure 5.29: Sketch of the laser and plasma configurations employed in the simulations presented in Section 5.5.

As Fig. 5.29 shows, three different ramp lengths have been studied: 4.3 mm, 7.5 mm and 1.47 cm. Due to the large number of required computing resources on the order of few thousand core-hours per simulation, the first part of the plasma stage has been kept comparatively short with a density upramp of 4.3 mm length and a 6.25 mm acceleration section for all three cases,

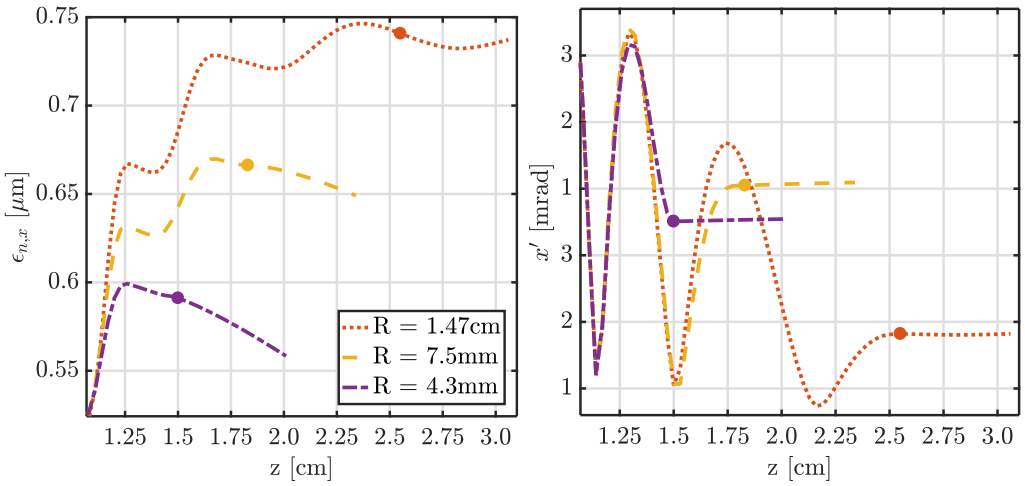

(a) Emittance evolution (b) Divergence evolution

Figure 5.30: Dependence of beam matching out of the plasma on ramp length: Evolution of the normalised emittance and divergence as a function of propagation distance for downramps of length 1.47 cm (red line), 7.5 mm (yellow line) and 4.3 mm (violet line). The plots show the parameter development starting from the beginning of the plasma downramp until approximately 5 mm after the ramp end (marked by the dots).

while the laser pulse is focused in the centre of the acceleration section. All plots show the beam evolution from the beginning of the density downramp only.

Looking at the emittance and divergence evolution in Fig. 5.30 it is found that increasing the downramp length is, in this scenario, actually not necessarily the best strategy. Whereas a stronger emittance growth on the downramp is observed for a longer ramp, the two shorter ramps exhibit some small amount of emittance compensation at the ramp end and shortly after. This unexpected behaviour can be explained when observing the trace-space evolution of the beam, as seen in Fig. 5.31. Both for a long and a short downramp the beam ellipse is slightly distorted due to betatron decoherence (see Section 2.3), as different parts of the beam evolve with different frequencies in trace-space. As this phase-space mixing is much stronger for the longer ramp, this shows that the effect occurs pre-dominantly on the downramp. With the plasma density decreasing the laser wakefield becomes weaker compared to the beamloading field which affects particularly the focusing fields that the electrons at the side of the bunch experience. These are therefore the particles that decohere and form the nonlinear tails in the trace-space ellipse of the beam. As the nonlinearity of the trace-space for the short ramp case is small, it is compensated partially towards the end of the ramp based on an effect described by [158, 168]. The phenomenon occurs as a consequence of the strong beamloading fields along the density downramp. As the laser-driven plasma wakefield becomes weaker at

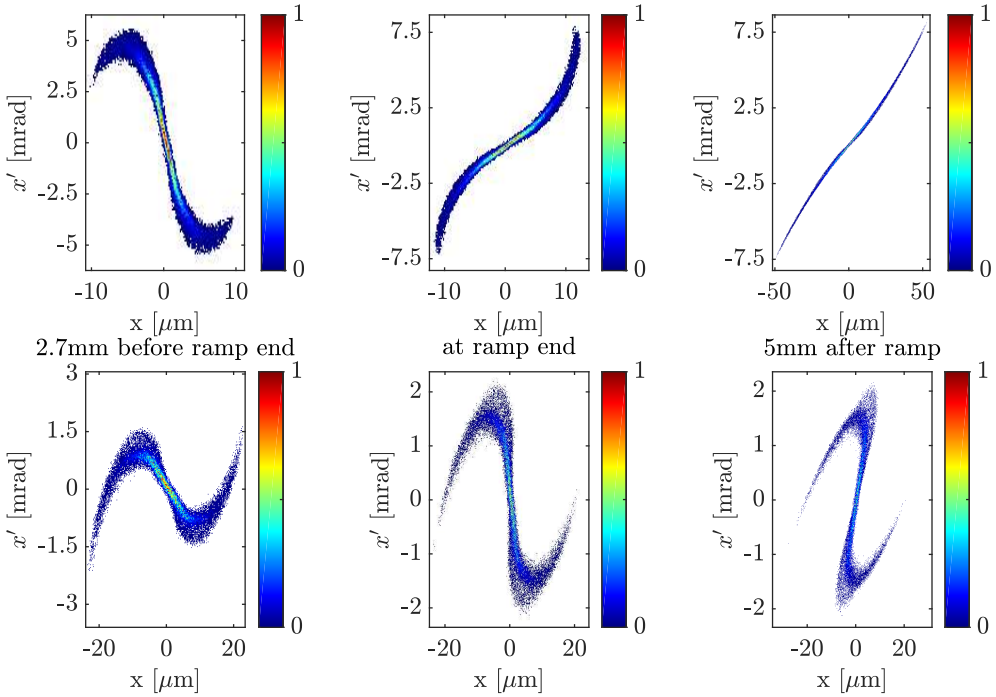

Figure 5.31: Evolution of the transverse beam phase-space during matching out of the plasma: The top row shows the development for a downramp of length 4.3 mm, while the bottom row depicts the case with a ramp of length 1.47 cm. In all cases, the colorbar depicts normalised charge.

lower density, the beamloading field largely provides the defocusing force on the beam. Due to its width being limited pre-dominantly to the beam size, however, electrons towards the sides of the beam mostly experience the very weak transverse component from the laser-driven wakefield and thus rotate much slower in phase-space. As it is mostly these electrons that form the nonlinear tails of the phase-space distribution, their and the main beam's phase-space regions can become partially re-aligned through this betatron frequency offset [158, 168], hence reducing the projected emittance. In the case of the centimetre-scale ramp, on the other hand, the trace-space is very mixed already and hence cannot be linearised anymore.

With respect to the beam divergence the behaviour is quite opposite: while the exact divergence at the ramp end depends on the angle of the beam ellipse in trace-space at this position and may hence be optimised further (see in Fig. 5.31, middle images), an increase in ramp length leads to a reduction of the oscillation amplitude of x' and hence an overall reduction of its possible values in vacuum. This therefore shows a similar development to the simulations presented in [52]. In terms of the other properties of the extracted beam, as depicted in Fig. 5.32, no significant surprises are observed. Due to the longer plasma a higher

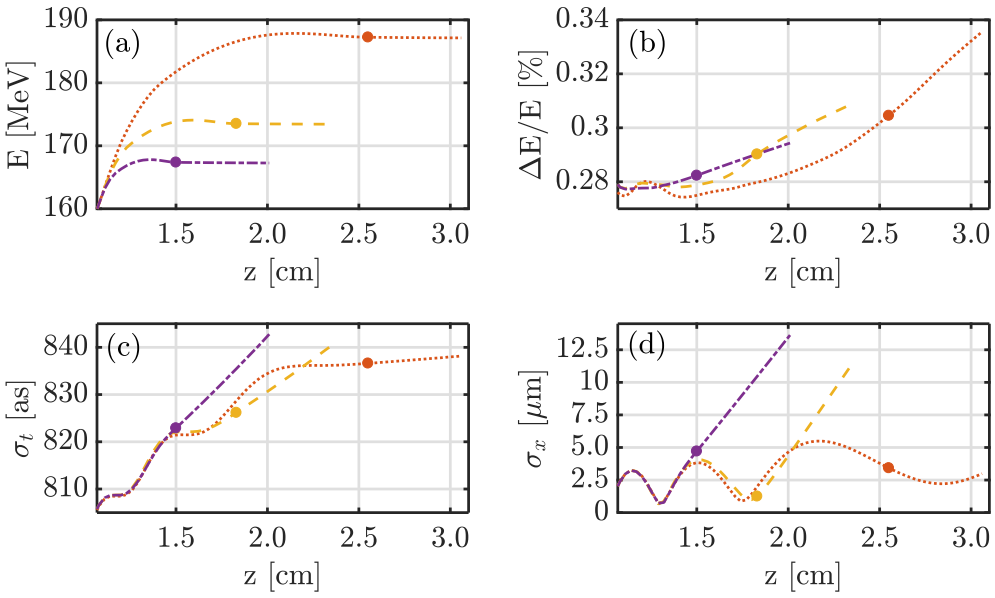

Figure 5.32: Dependence of beam matching out of the plasma on ramp length: Evolution of the main beam parameters as a function of propagation distance for downramps of length 1.47 cm (red line), 7.5 mm (yellow line) and 4.3 mm (violet line). The plots show the parameter development starting from the beginning of the plasma downramp until approximately 5 mm after the ramp end (marked by the dots).

beam energy is reached, but, as the beamloading fields become more dominant at lower density, this increases the energy spread experienced across the beam. As for dimensions, the beam expands much more quickly for millimetre-scale ramps as the divergence is almost doubled compared to the centimetre-scale case.

Overall, it is therefore found that the trace-space evolution of the beam during injection and acceleration plays a major role in the strategy to be applied when matching out of the plasma. For a beam with well preserved emittance – thanks to good matching into the plasma –, such as was observed in Section 5.2 with centimetre-length density upramps, a downramp with similar or larger length than the in-coupling upramp is recommendable in order to minimise the beam divergence as much as possible, based on the results in [52]. For a case, as shown here, on the other hand, with only partial mitigation of the beam mismatch and hence strong evolution of the beam trace-space during acceleration, a shorter downramp should be used in order to find a compromise between the emittance growth experienced during the extraction stage and the divergence reduction achievable over this distance. The exact required ramp length in this case will thus depend on the transverse beam properties as well as the capabilities of the transport line following the plasma stage to capture the electron beam.

5.6 Start-to-End Simulations

S2E Working Points	WP1	WP2	WP3
Final beam energy [MeV]	200	200	1000
Density upramp length [cm]	0.75	1.50	1.00
Acceleration region length [cm]	1.25	1.25	9.50
Density downramp length [cm]	0.75	2.00	1.00
Pre-formed guiding channel	no	yes	yes
Laser focal plane position [cm]	1.39 (stage centre)	1.51 (ramp end)	1.01 (ramp end)
Beamloading optimisation	yes	yes	yes

Table 5.5: Working points studied through start-to-end simulations.

Based on the optimisation steps for an external injection setup discussed in the previous sections, a series of start-to-end simulations is presented that demonstrates the potential of using LWFA as an energy booster for a sub-femtosecond electron beam. As shown in Table 5.5, three main working points were investigated: two with an energy gain of around 100 MeV and one with acceleration up to 1 GeV. Working point WP1 shows a very simple setup, purposefully abstaining from external laser guiding and long up- and downramps to minimise potential practical complications with the setup. Working point WP2 demonstrates a more optimised version of WP1. Finally, for WP3 a compromise was made between setup optimisation and the required computational resources to simulate the former, so that comparably short plasma ramps were employed.

The general evolution of the electron beam for all three scenarios is quite similar and is presented in Fig. 5.33, showing the phase-space evolution for working point WP1. The longitudinal phase-space of the beam is well preserved: the beam stays Gaussian with only a negligible low-charge tail developing, while a small energy modulation of $<$1 MeV occurs due to the imperfect flattening of the wakefield due to the non-optimised shape of the bunch. In the transverse phase-space, the electron beam is focused in the plasma, before slowly expanding along the final density downramp and after. The phase-space ellipse is seen to distort, especially along the beam edges, which is predominantly caused by the transverse dependence of the focusing field strength in the weakly nonlinear regime. This effect is compensated again to some extent on the downramp. The final parameters of the witness electron beam in each of the three scenarios are shown in Table 5.6 with a more detailed description of each simulated case following.

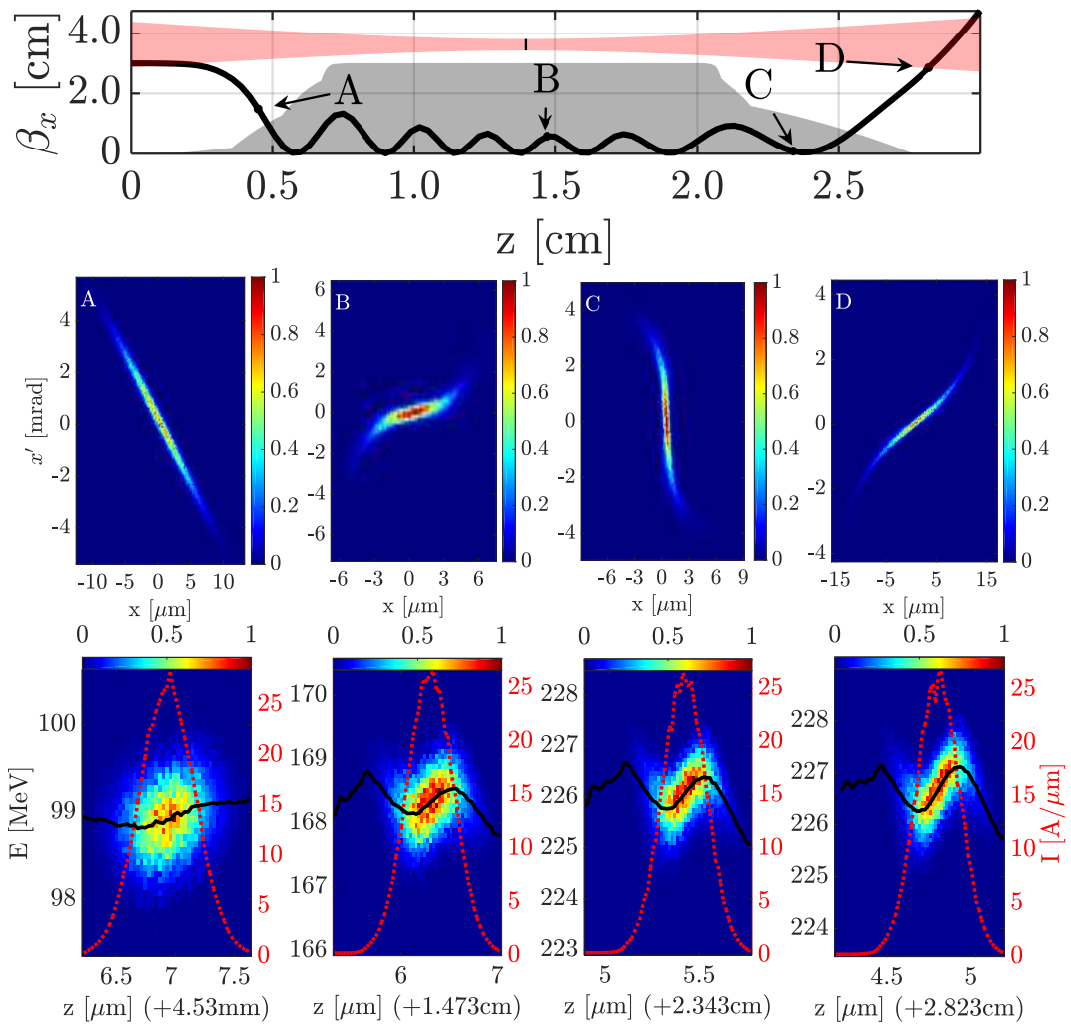

Figure 5.33: Phase-space and β_{cs}-function evolution of the witness beam during injection, acceleration and extraction in the plasma target (with the positions of the phase-space plots given by A-D in the top figure). The red lines in the longitudinal phase-space plots show the projected beam current density in A µm^{-1} and the black lines show the projected energy distribution in MeV. The colormap describes normalised charge.

Acceleration to 200 MeV

In more detail, the evolution of the electron bunch during acceleration and its final distribution for working points WP1 and WP2 is shown in Figs. 5.34 and 5.35. In both cases, even for the unguided stage in WP1 thanks to its short plasma length, the energy gain is almost linear along the density plateau. The relative energy spread decreases overall due to the beamloading and the efficient acceleration, whereas short regions of increase are only observed at the plasma ramps. The latter occur, as the beamloading fields from the electron bunch become much

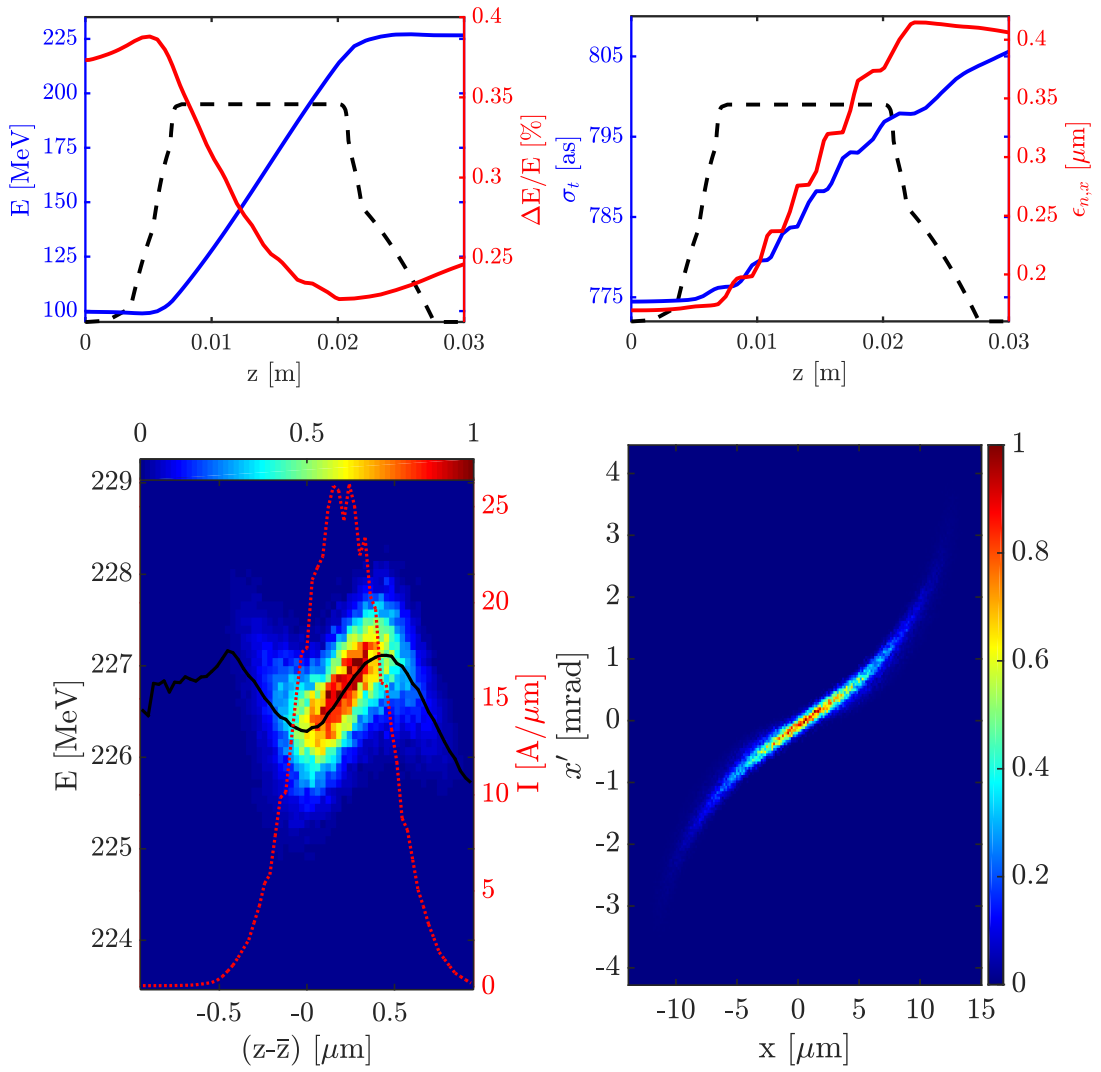

Figure 5.34: Top row: Evolution of the electron beam properties during acceleration in an external injection LWFA plasma setup for WP1. The black, dashed line represents the shape of the plasma density profile. Bottom row: Beam phase-space at the end of the plasma target. Again, the colormap shows normalised charge. The black and red lines in the bottom left plot show the projected energy and 2D current density along the longitudinal beam profile, respectively.

stronger than the laser wakefield at low density and wide laser spot size leading to a stagnation in energy gain. Additional self-fields after the plasma target lead to a further soft increase in energy spread for WP1. The RMS bunch duration increase remains small on the order of 4% or less and exhibits an oscillatory behaviour which is equivalent to the shallow betatron oscillations of the beam transversely due to its imperfect matching. The longitudinal fluctuations are a consequence of the reshaping of the beam, as observed in Section 5.4 due to the electrons off-

axis experiencing weaker wakefields and hence falling behind. Intensified through their longer path lengths during the betatron motion, it is consistent that the effect is weaker for WP2 than WP1, where the betatron oscillations are reduced in amplitude due to better beam matching. Finally, the emittance rises slightly, but remains well below 0.5 µm in both cases, exhibiting an increase with a rate of approximately 0.15 µm cm^{-1} and 0.02 µm cm^{-1}, respectively.

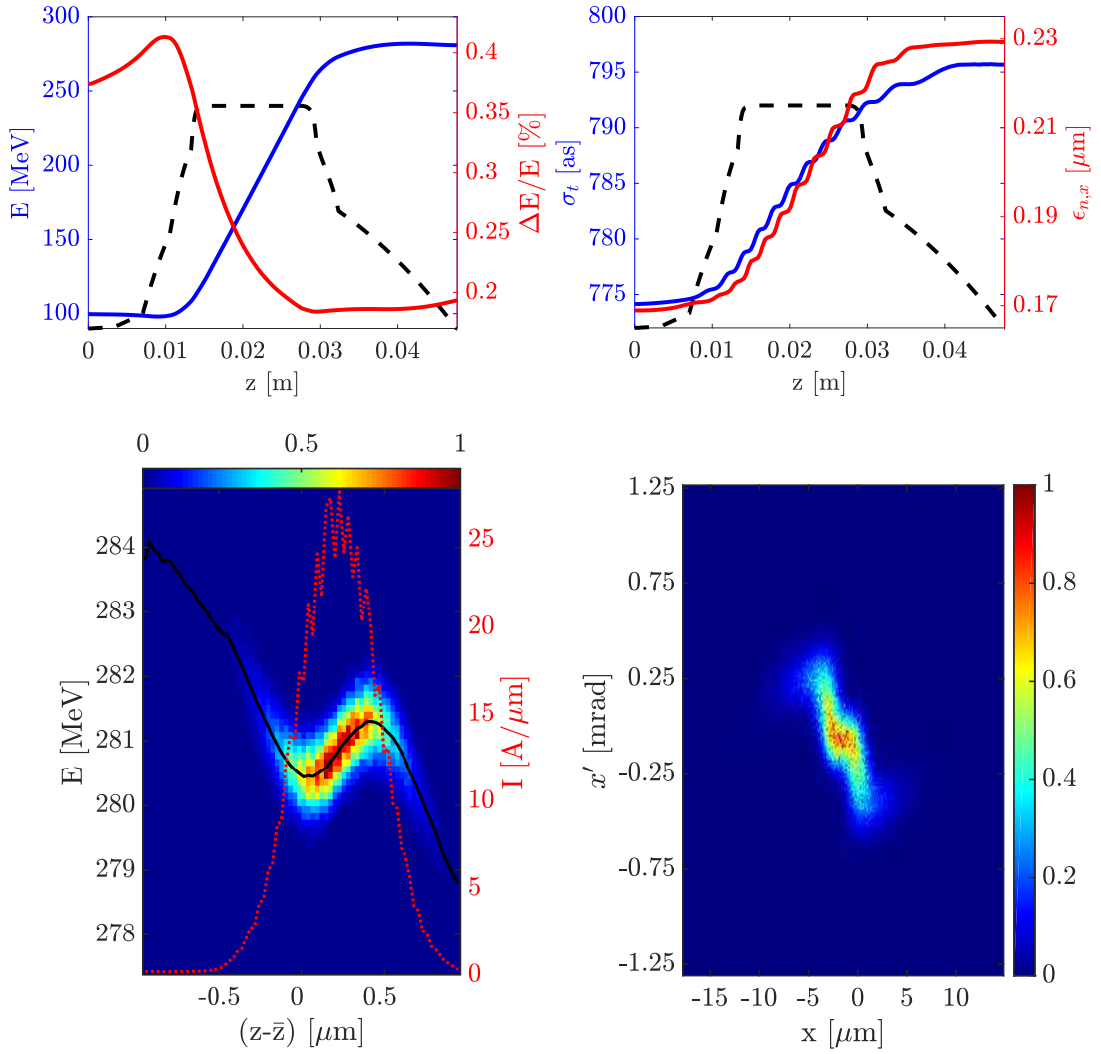

Figure 5.35: Top row: Evolution of the electron beam properties during acceleration in an external injection LWFA plasma setup for WP2. The black, dashed line represents the shape of the plasma density profile. Bottom row: Beam phase-space at the end of the plasma target. The colormap shows normalised charge. The black and red lines in the bottom left plot show the projected energy and 2D current density along the longitudinal beam profile, respectively.

Beam Properties after plasma target	WP1	WP2	WP3
Mean energy E [MeV]	227	281	943
Energy spread ΔE/E [%]	0.239	0.194	0.417
RMS bunch length σ_t [as]	804	796	867
RMS bunch width σ_x [μm]	4.67	2.53	4.47
Norm. emittance $\epsilon_{n,x}$ [μm]	0.410	0.229	1.00**
Bunch current I_b [kA]	0.11	0.11	0.09
Peak current $I_{b,peak}$ [kA]*	~ 0.33	~ 0.33	~ 0.13

Table 5.6: Beam properties for the different working points at the end of the plasma target.
*Note that the peak current in 2D needs to be scaled up to the full beam current and is thus just an approximation.
**Note that this value is estimated based on the simulation with the Lehe solver, as the emittance is spoiled by numerical Cherenkov radiation in the Yee case.

Major differences between the simple setup WP1 and the more optimised version WP2 are in the mean energy, energy spread and emittance: while the external laser guiding leads to a more efficient acceleration and hence improved energy parameters, the longer plasma ramps ensure a smaller final emittance, as shown also in Section 5.2. Note that a further improvement is likely possible if the electron beam focal position can be optimised on the ramp; this was, unfortunately, not possible within the simulation code in this case. It should be noted that there are some factors that may affect the reliability of these simulation results compared to reality. One in particular is the feature of the Lehe solver – used in the simulations to avoid numerical Cherenkov radiation – to propagate the laser pulse with superluminal group velocity which depends on the temporal and spatial resolution of the simulation [160]

$$v_{g,laser,num}/c = 1 + 2(1 - \frac{c\Delta t}{\Delta z})\,(\frac{k_{laser}\Delta z}{2})^2\,. \tag{5.15}$$

The real laser group velocity is given by [163]

$$v_{g,laser}/c \approx \sqrt{1 - \frac{n}{n_{cr}}} \tag{5.16}$$

with $\Delta t, \Delta z$ the time step and longitudinal spatial grid cell size, k_{laser} the laser pulse wavenumber and n_{cr} the critical plasma density.
Effectively this leads to an advance of 5.8 µm and 3.28 µm, respectively, of the laser pulse with respect to the simulation box for WP1 and WP2 and hence a similar artificial dephasing of the witness electron beam towards the back of the wakefield. With the advance being less than 6 % of the plasma wavelength (not considering the natural electron dephasing), however, the effects on the beam parameter evolution should be small.

Acceleration to 1 GeV

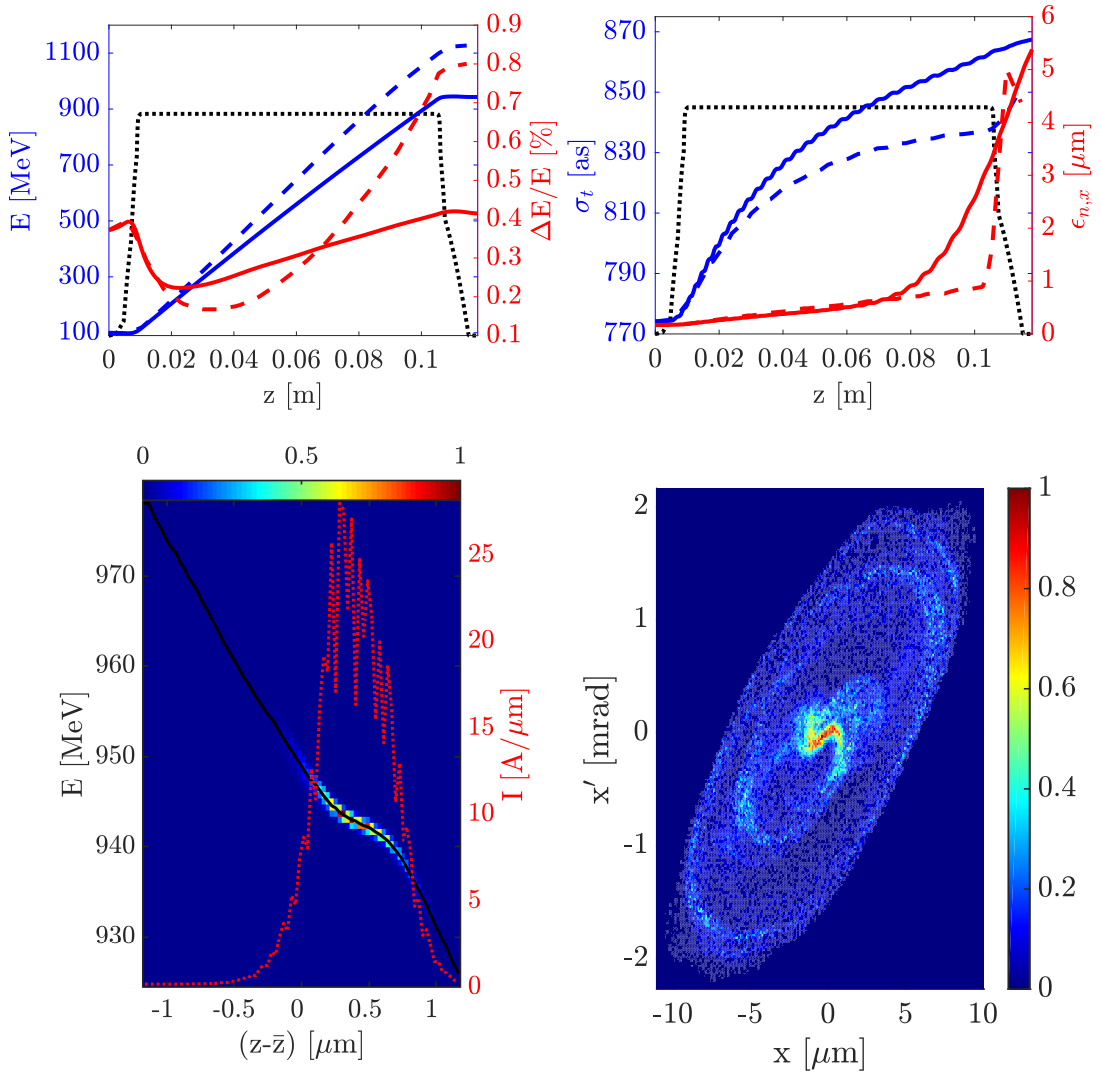

Figure 5.36: Top row: Evolution of the electron beam properties during acceleration in an external injection LWFA plasma setup for WP3. The black, dashed line represents the shape of the plasma density profile, while the solid (dashed) lines show simulation results using the Yee (Lehe) field solver. Bottom row: Beam phase-space at the end of the plasma target based on simulation with the Yee field solver. The colormap describes normalised charge. The black and red lines in the bottom left plot show the projected energy and 2D current density along the longitudinal beam profile, respectively.

For the case of working point WP3, the advance of the laser pulse in the simulation box due to the Lehe field solver plays a more considerable role, as it propagates over more than twice the distance than in working points WP1 and WP2, while at the same time a reduction

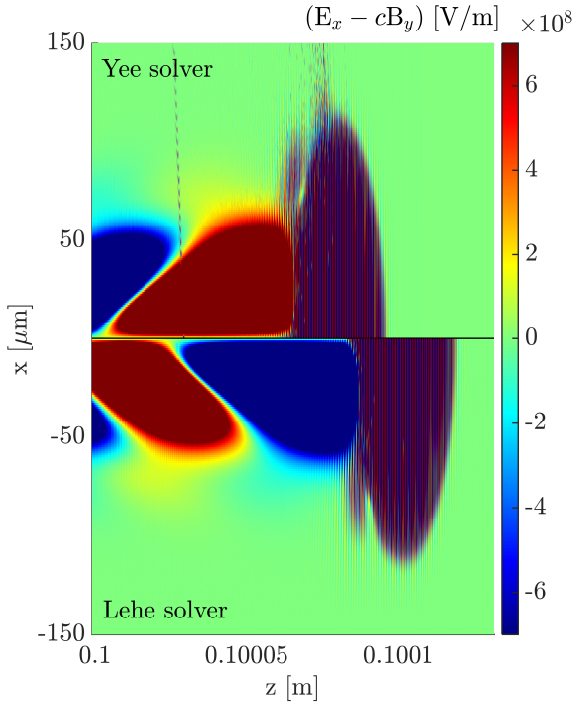

(a) Focusing field with the Yee and Lehe solver

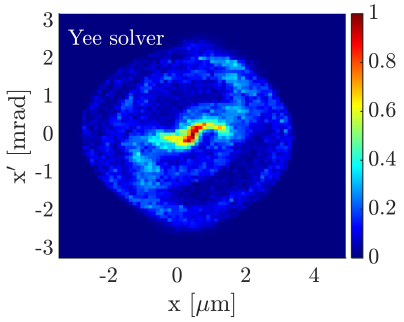

(b) Transverse phase-space: Yee solver

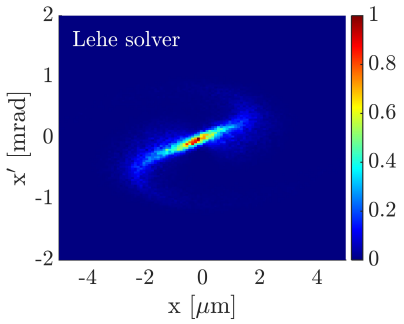

(c) Transverse phase-space: Lehe solver

Figure 5.37: Difference in focusing field (a) and electron beam phase-space ((b)-(c)) between simulations with the Yee and Lehe solver for working point WP3. The numerical effects observed in the fields for the Yee solver are the cause for the large increase in phase-space mixing compared to the Lehe solver case.

in the temporal resolution is limited by the large computational simulation requirements. Consequently, the simulation for this working point was completed using the standard Yee field solver. This was complemented by a second lower resolution run with the Lehe solver in order to get a more realistic estimate for the evolution of the beam emittance, which with the Yee solver is dominated by numerical Cherenkov radiation.

Figure 5.36 shows the beam development across the whole plasma target with both solvers. The artificial advance of the laser pulse with respect to the simulation box is 22.4 µm for the Lehe solver simulation (approx. 21 % of one plasma wavelength), whereas with the Yee solver the laser pulse propagates slower than the speed of light in vacuum and hence falls back by 4.4 µm within the box. This is comparable to what is expected in reality due to the effect of the plasma refractive index on the laser group velocity. The Yee solver simulation results thus in general represent the expected physical behaviour of the accelerator much better. More importantly, though, with the Lehe solver the laser advance leads to a relative dephasing of the electron beam with respect to the wakefield, which it consequently samples across the region from its initial

injection position to the start of the defocusing phase behind the accelerating field minimum. Upon reaching this last position, at z=10.25 cm, the beam is defocused strongly and is observed to explode in emittance, an effect which is entirely numerical. The normalised emittance for this case, as shown in Table 5.6, has thus been estimated based on the beam characteristics just before this artificial defocusing effect for the simulation with the Lehe solver.

From the phase-space plots of the beam after the plasma with the Yee solver (Fig. 5.36), it can be seen that the longitudinal shape of the bunch is well preserved, but the beamloading compensation breaks down slightly with a negative energy chirp forming. This is likely caused by the increasing influence of the transverse energy spread as well as the imperfect flattening of the field due to its Gaussian shape. In the transverse plane, the effect of the numerical Cherenkov radiation for this simulation can be seen very clearly with the phase-space having mixed strongly. This in turn explains the strong increase in emittance after 8 cm of plasma propagation (see Fig. 5.36, the solid red curve in the top right graph).

In Fig 5.37 the extent of this numerical effect can be seen in more detail, as the focusing fields and transverse phase-space distributions are compared between the Yee and Lehe solver. The extreme phase-space mixing only occurs for the Yee solver, where it is caused by the artificial radiation generated at the position of the beam, as can be seen at approximately 0.100 025 m in the field plot. As the amount of numerical Cherenkov radiation produced is smaller here than for the example shown in Section 5.2, it needs to accumulate first before an effect on the emittance is observed which sets in only after longer propagation.

Nonetheless, the Lehe-solver simulation provides a good way to also estimate the effect that the use of this field solver may have on the simulations of WP1 and WP2. As discussed earlier, the advance of the laser pulse is small for these cases, but the qualitative effect should be similar to what is observed for WP3 after an equivalent propagation distance of approximately 2 cm (i.e., the distance to the end of the acceleration stage in WP1). We can therefore estimate that the energy spread and RMS bunch length are underestimated in WP1 and WP2 by up to 10 % and 0.25 %, respectively, whereas the mean energy of the beam is overestimated by up to 8 %. The normalised beam emittance is likely also underestimated slightly, as the beam is pushed towards a weaker focusing field due to the Lehe-related laser advance; however, it is difficult to quantify the extent of this.

3D Effects

An additional assumption that was made for the start-to-end simulations of WP1 to WP3 is an initially Gaussian beam shape, as OSIRIS does not allow the read-in of full 6D beam

distributions in 2D. In order to quantify the effect of this simplification, a short 3D simulation up to around 1 cm was completed based on the parameters for working point WP1 and using a realistic electron beam distribution from an ASTRA simulation of the full ARES beamline by Jun Zhu. The beam properties after the electron beam has passed the 7.5 mm long upramp and 2.5 mm of constant density plasma are given in Table 5.7. The input electron beam parameters are in this case very similar to the previous two-dimensional start-to-end simulations (with values given in Table 5.1) in terms of their RMS-values; however, both the real space and phase-space distributions of the injected bunch in the 3D-simulation are non-Gaussian and in part considerably different from the idealised distributions assumed in the previous results, as shown in more detail in Fig. 5.38.

While a full agreement with the outcomes for the 2D-case of working point WP1 is hence not to be expected, with regard to the mean electron energy and the RMS bunch length the consistency of the results is nonetheless excellent with variations below 2.6 %. The initial transverse beam size as well as emittance are slightly different in the 2D simulation (3D: σ_x=5.0 µm, σ_y=5.3 µm, $\epsilon_{n,x}$=0.14 µm, $\epsilon_{n,y}$=0.14 µm; 2D: σ_x=5.1 µm, $\epsilon_{n,x}$=0.17 µm), as the mean of both x- and y-beam size was used, leading to some variations in the evolution of σ_x. Going beyond these small changes, however, the final normalised emittance in x as well as the relative energy spread of the beam vary strongly between the two cases with a fast increase of both from the end of the plasma upramp in 3D. A possible explanation for these observations can be provided by the phase-space distributions of the beam presented in Fig. 5.38: while the RMS values for both beams are very similar initially, the realistic beam distribution exhibits a relatively strong energy chirp with a long low-energy tail. This chirp is increased during the beam acceleration, as the bunch is placed at a phase to flatten the effective wakefield leading to a rise in $\Delta E/E$. By optimising the electron beam phase with regard to such an initial chirp, as shown in Section 5.4, a reduction of the energy spread should be achievable, even in 3D.

Beam Properties after 1 cm propagation: WP1	2D	3D
Mean energy E [MeV]	127	127
Energy spread ΔE/E [%]	0.313	0.504
RMS bunch length σ_t [as]	779	799
RMS bunch width σ_x [μm]	2.57	2.23
Norm. emittance $\epsilon_{n,x}$ [μm]	0.206	0.387
Bunch current I_b [kA]	0.13	0.18
Peak current $I_{b,peak}$* [kA]	$\sim$ 0.33	0.52

Table 5.7: Comparison of electron beam properties from 2D and 3D simulations of working point WP1 after propagation to 1.0 cm.
*Note that the peak current in 2D needs to be scaled up to the full beam current and is thus just an approximation.

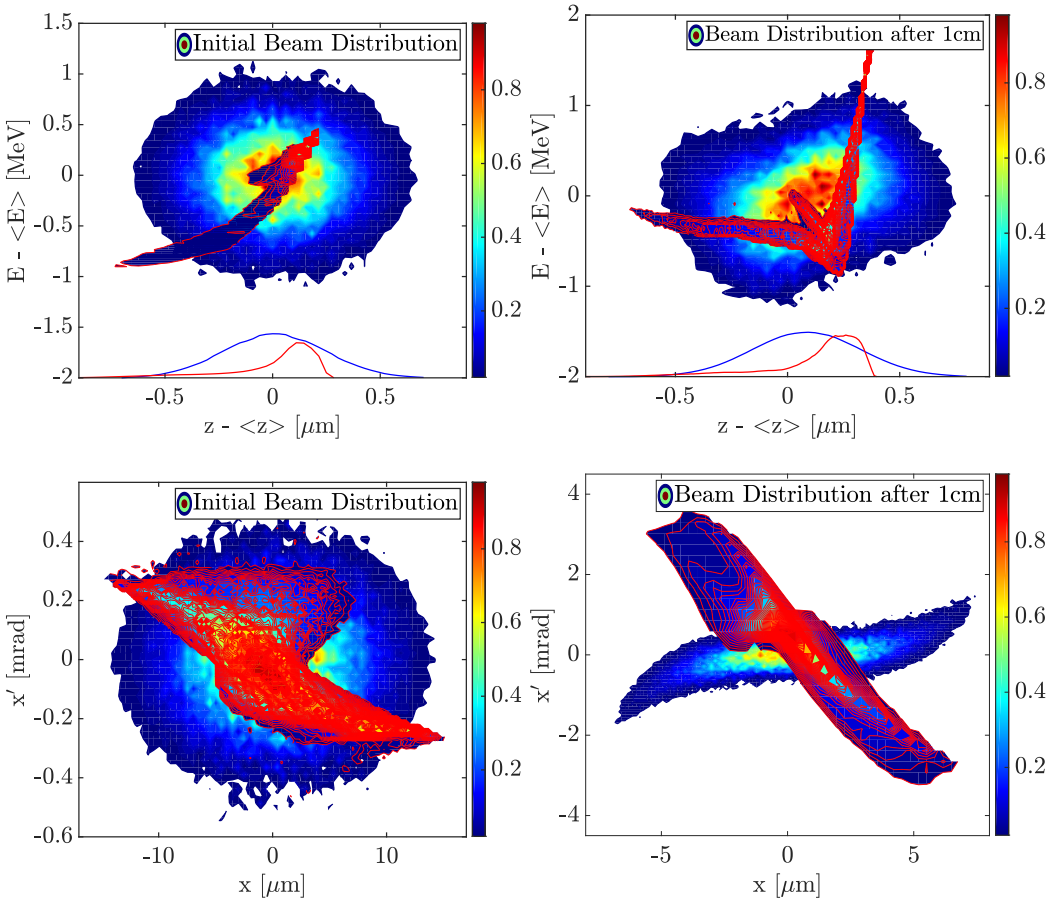

Figure 5.38: Comparison of the initial and final beam phase-space between the 2D start-to-end simulation for working point WP1 and an equivalent 3D simulation employing a realistic ASTRA beam distribution as input (based on simulations by J. Zhu). The 3D distribution and projected beam current (in arbitrary units) is given by the red-contoured feature and red line, respectively, whereas the distribution and current for the 2D simulations, assumed to be initially Gaussian, is given in blue. The colormap depicts normalised charge.

The emittance growth in the 3D simulation is likely also caused by the more complex transverse phase-space of the beam. While the nonlinearities are partially smoothed out after 1 cm of propagation, the realistic phase-space ellipse still exhibits broader features which spoil the projected emittance of the bunch. A solution to this problem may be found by increasing the matching efforts into the plasma with longer plasma ramps to minimise the betatron oscillations of the beam and hence also the transverse beam evolution.

Finally, more recent simulations of the ARES linac and the matching and focusing sections afterwards have shown that a working point with a more strongly focused beam at the plasma

entrance may be possible. The evolution of such a beam would be very similar in the plasma acceleration stage to the cases presented here, yet with two likely changes. Firstly, being closer to the matched spot size, an improvement in the emittance preservation of the beam is expected throughout the acceleration allowing for either shorter matching ramps or an improved final beam emittance. Secondly, the beamloading effect will be stronger due to the increased density of the bunch which needs to be considered in the choice of phase position in the wakefield. Depending on the exact beam density, it may still lead to some increase in the final energy spread, if the beamloading field gradient becomes too strong for the laser wakefield; a small increase in the density of the plasma stage could likely compensate for this effect, though.

Simulation Errors

As in Chapter 4, simulation errors were minimised by choosing grid cell sizes smaller than the smallest expected features within the simulation. Longitudinally, the smallest feature was found to be the injected RMS beam size at the beginning of the plasma stage, corresponding to around 700 as, which could be resolved well. Transversely, the smallest simulation feature was found to be the transverse beam size oscillating around a few micrometres for the full beam; this as well is resolved in the transverse grid. The plasma wavelength is considerably larger at these lower densities and thus provides no limitation. The number of beam macroparticles varies between simulations ranging from few thousand to few tens of thousand particles. A relative sampling error of 2.5 % or less can thus be estimated for the described beam properties [153].

Scans were completed to estimate the effect of grid cell size and particle per cell number on the beam properties found from the simulation. The effect of plasma and injected bunch particle numbers is almost negligible with variations staying well below 5 %, in most cases even below 2 %, with the beam particle numbers found to be more important. The effect of the grid resolution was tested down to values of 6.3 nm×328 nm – well below the theoretically estimated necessary cell size – and was found to be slightly larger than for the particle numbers, but still with variations below 6.5 %. The grid cell size values for most simulations in this chapter were chosen based on a compromise between required resources and expected numerical effects.

Finally, the decision to conduct almost all of the studies in this chapter through two-dimensional instead of three-dimensional PIC-simulations was based entirely on the high computing time requirements of the latter. While it is therefore possible that some of the presented results, especially in the context of transverse beam dynamics, may not represent quantitatively

the exact data anticipated from an experiment, it is, nonetheless, expected that the physical processes and particularly the relative developments of electron beam, plasma and laser pulse are well described by the presented simulations. One reason for such an assumption is the 2D – 3D comparison in Section 5.6: although the initial electron beam distributions in the two simulations considered are slightly different, very good agreement can be observed in the evolution of both the transverse size of the witness electron beam as well as the drive laser pulse development. Moreover, with the accelerator stage in the linear to weakly nonlinear regime with limited laser intensity and small witness beam charge, the laser does not experience any self-focusing or other relativistically induced behaviour, the witness beam demonstrates only weak beamloading fields and, the excited plasma structure is highly regular, evolves slowly and for the most part symmetrically. Most of the numerical effects expected to affect the simulation results due to the assumed 2D slab geometry, such as an underestimation of the effects of the electron beam charge or an underestimation of nonlinear laser effects, are thus not applicable to the parameter region under investigation.

5.7 Summary of the Main Findings

This chapter studied an LWFA energy boosting stage for a sub-femtosecond electron beam externally injected into plasma. The setup under investigation is based on the SINBAD accelerator R&D facility, currently under construction at DESY, for which various optimisation steps have been assessed via 2D and 3D particle-in-cell simulations.

A plasma target in the weakly nonlinear wakefield regime with low density of around $1 \times 10^{23}\,\mathrm{m}^{-3}$ was chosen as a suitable regime for a trade-off between maximum possible acceleration distance, accelerating field strength and required laser-electron beam synchronisation control. To avoid emittance growth, the electron beam needs to be matched into the plasma; this was found to be one of the main challenges of the setup due to limitations in the possible focusing before the plasma and was partially mitigated through the use of a plasma density ramp. A simple numerical model was employed for an estimation of the expected emittance growth dependent on the ramp length which can hence be adapted to find a suitable setup based on the required beam quality for different applications; this allows for a decrease of the required number of PIC simulations thanks to a reduction of the parameter space. The plasma ramp shape was found to also play a role in the matching strategy, but is less crucial than the influence of the laser spot size evolution. Additional factors to consider for matching were determined to be space charge - for electron beam densities above $5\,\mathrm{pC}\,\mu\mathrm{m}^{-3}$ - as well as numerical

effects in simulations causing artificial emittance growth.

External laser guiding was found to be necessary for plasma targets longer than approximately 2.5 cm ($\sim 3.5 \times z_R$); transverse pointing of the laser pulse must be controlled well in this case to within few percent of the channel radius to avoid large fluctuations in the on-axis wakefield. Furthermore, controlled beamloading can be employed to minimise the beam energy spread; the optimised beam phase and plasma density for energy spread compensation can be estimated with a numerical model. With an overall small energy spread, the limitation in this context becomes the slice energy spread caused by the variation of the accelerating field along the transverse direction. The extraction of the electron beam from the plasma also requires a density ramp. With the aim to reduce beam divergence, while preserving its emittance, a compromise in ramp length needs to be made for not perfectly matched electron beams to avoid further phase-space mixing and hence emittance growth upon extraction.

Finally, with all of these aspects implemented, start-to-end simulations up to around 200 MeV and 1 GeV are presented. They demonstrate the preservation of beam emittance and energy spread to below 1 µm and 0.45 %, respectively, both with simple and more optimised setups. The bunch length was preserved in all cases to within 11 %. For long plasma stages the main limitation was determined to be computational resources and numerical effects, so that improved results can be expected in future studies and experiments. The behaviour in 3D simulations was found to be similar to the two-dimensional studies, but a non-Gaussian shape of the electron beam needs to be taken into account in the setup optimisation and will require further studies to assess fully.

Chapter 6

Discussion

This chapter discusses the results presented previously in Part III through comparison with each other as well as with other published techniques for the generation and acceleration of ultrashort electron beams. Additionally, possible steps towards first experimental tests of the two schemes are debated and their suitability for radiation generation is assessed.

6.1 Comparison of the Two Acceleration Schemes

Chapters 4 and 5 have presented two very different generation mechanisms for attosecond electron beams based on laser wakefield acceleration. The technique of upramp-assisted self-injection (Chapter 4) excels in its compact size and simple requirements being dependent most importantly on a terawatt-scale short-pulse laser. It can produce high current, ultrashort duration beams at tens of megaelectronvolts, but is limited by sub-optimal transverse beam properties and a large energy spread. Combining a state-of-the-art RF accelerator with a plasma acceleration stage (Chapter 5), on the other hand, allows for superior control over electron beam properties, while reaching gigaelectronvolt-scale energies with a minimised machine footprint compared to conventional accelerator setups. With this strategy, high quality beams with sub-femtosecond duration can be produced, yet the size of the setup is still considerable and it relies strongly on the availability of both a high-power laser and RF accelerator.

Figures 6.1 and 6.2 compare the electron beam properties defined through simulations in the previous two chapters for upramp-assisted self-injection and external injection with other proposed mechanisms for generating attosecond and femtosecond electron beams found in the literature. The general schemes included here are 1) laser wakefield acceleration (red points), 2) bunch compression (black points), 3) inverse Free-Electron Lasers (green points), 4) interaction

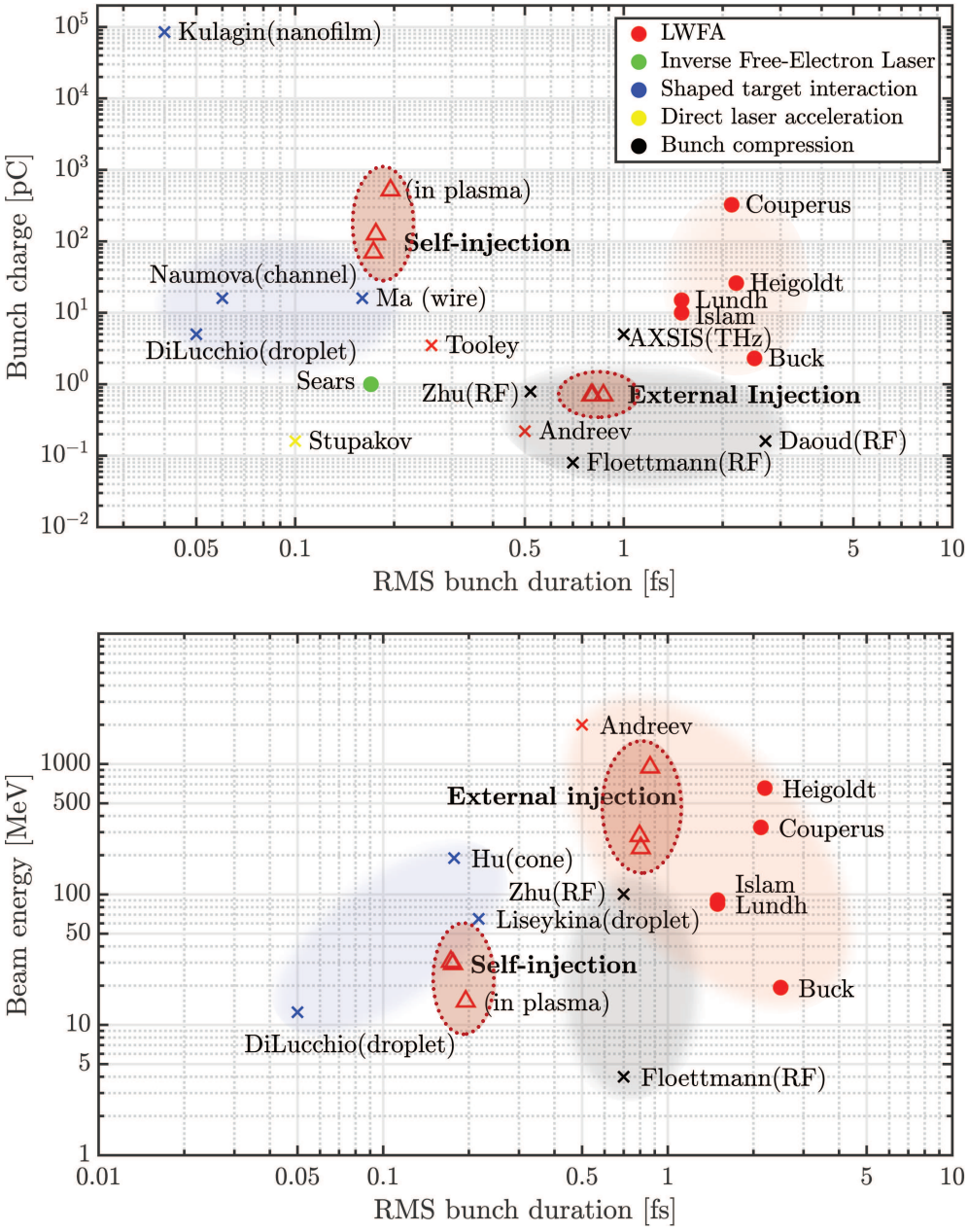

Figure 6.1: Comparison of the properties of electron beams from generation techniques discussed in Chapters 4 and 5 (marked by the red shaded regions bordered with a dotted line) with other proposed mechanisms for attosecond electron bunch production from literature (marked by the unbordered shaded regions). The symbol shape in the plots represents the status of the proposal with circles showing experimental measurements, crosses results based on simulations and triangles the simulation results of this work. The colours depict the general generation mechanism with a detailed list of references provided in Appendix D.

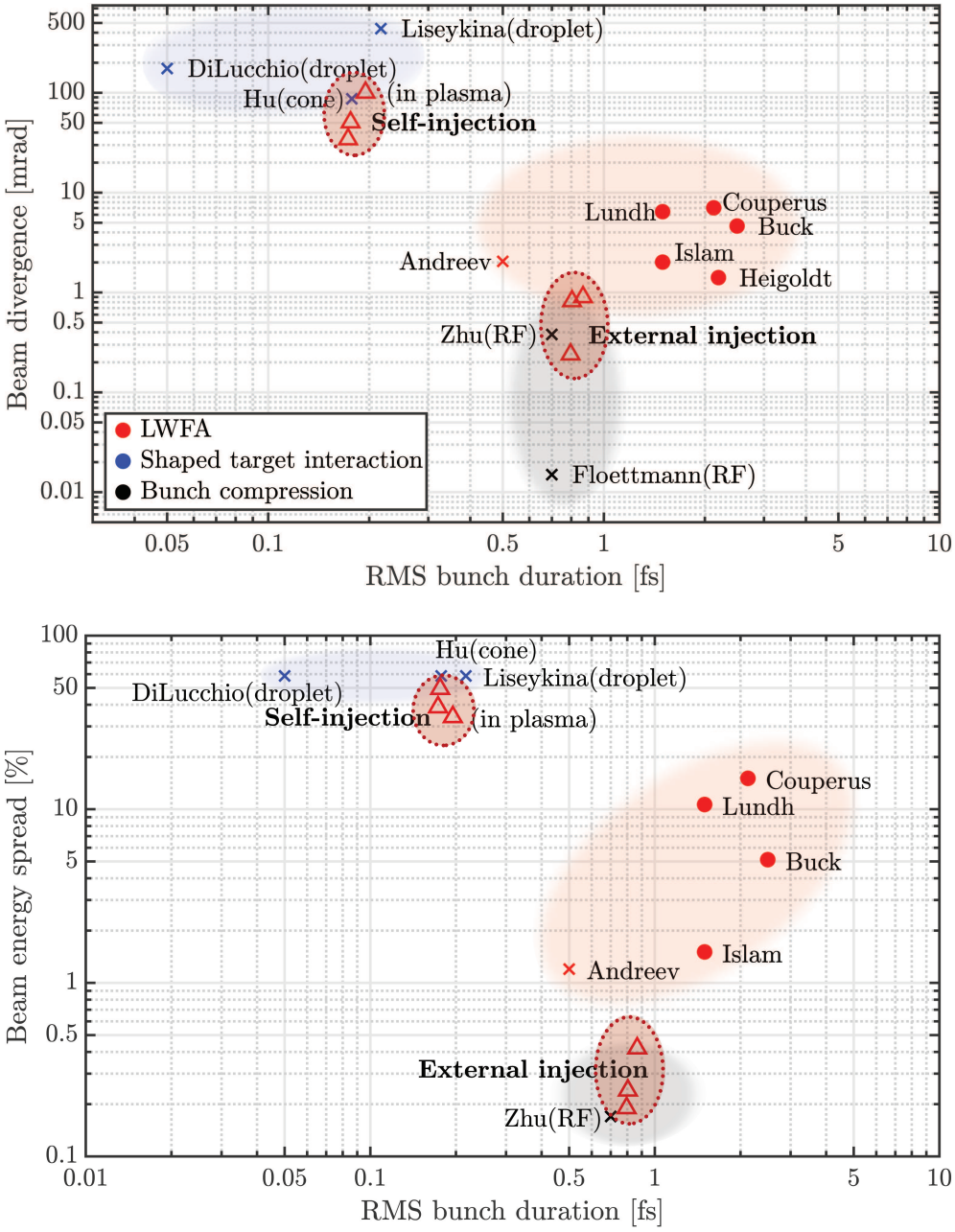

Figure 6.2: Comparison of the properties of electron beams from generation techniques discussed in Chapters 4 and 5 (marked by the red shaded regions bordered with a dotted line) with other proposed mechanisms for attosecond electron bunch production from literature (marked by the unbordered shaded regions). The symbol shape in the plots represents the status of the proposal with circles showing experimental measurements, crosses results based on simulations and triangles the simulation results of this work. The colours depict the general generation mechanism with a detailed list of references provided in Appendix D.

of ultrahigh-power lasers with shaped targets (blue points) and 5) direct laser acceleration (yellow points) (as detailed in Section 2.4.1). The results from this thesis are marked as triangles (based on Tables 4.7, 4.5 and 5.6). There are further techniques proposing attosecond electron beam generation, as introduced in Section 2.4.1, but no publications providing specific beam properties were found for these. It should be noted that comparatively many LWFA results have been included, especially experimental ones, as these provide the most direct comparison to the results presented here. Also worth mentioning is that the only experimental demonstration of sub-femtosecond electron bunches shown here has been achieved with an inverse Free-Electron Laser by Sears et al. (2008), where a train of microbunches with each approximately 400 as duration was generated.

Comparing the simulation results of Chapters 4 and 5 with these techniques, it becomes clear that very different regimes can be reached with the two schemes presented. Upramp-assisted self-injection produces electron beams that are considerably shorter than most LWFA-techniques, but at the cost of reduced beam quality. Their properties are actually more similar to what has been calculated for laser-target interaction with shaped surfaces. With the former being mostly considered for use in compact radiation sources, it is positive to see that the self-injected beams can not only match their properties, but actually demonstrate improved beam quality over the former with higher predicted charge, lower energy spread and lower divergence – all important properties in radiation generation. Taking into account that laser interaction with shaped target techniques generally have very strict, partially even currently unachievable, requirements in terms of laser power and contrast ratio, the scheme of upramp-assisted self-injection may thus provide an interesting, more realisable alternative.

External injection into LWFA, on the other hand, demonstrates longer bunch durations than many other techniques, even though it does improve slightly on what today's laser wakefield setups can achieve. Instead it is more comparable to the efforts in bunch compression techniques in RF-accelerator systems, especially also as this is its current limit with regard to achievable bunch duration. Unlike the former, however, LWFA with external injection can be pushed much more easily towards high energies, while preserving good energy spread and divergence – something which sets it apart from other techniques. With a petawatt-scale laser pulse available, for example, beam properties could be pushed even further and, due to well controlled and tunable electron beams, exceed most other laser wakefield accelerator schemes with regard to beam quality and stability. Due to its reliance on well understood, conventional accelerator technologies, it is also among the schemes with the highest probability of success and experimental realization in the near future. Finally, unlike e.g. inverse Free-Electron lasers

and shaped target-interaction schemes, both techniques presented here allow the generation of isolated attosecond electron beams instead of bunch trains, which can be advantageous, for example, for better control in pump-probe experiments.

	5D Brightness $[\mathrm{A\,m^{-2}\,rad^{-2}}]$	6D Brightness $[\mathrm{A/m^2/rad^2/(0.1\%\ \Delta E/E)}]$
Self-inj. extracted beam (Table 4.7, short ramp)	9.73×10^{16}	1.95×10^{14}
Self-inj. beam in plasma (Table 4.5)	1.43×10^{18}	4.21×10^{15}
Ext. inj. beam - low energy (Table 5.6, WP2)	1.26×10^{16}	6.49×10^{15}
Ext. inj. beam - high energy (Table 5.6, WP3)	2.60×10^{14}	6.24×10^{13}
Manahan et al. [34]	3×10^{18}	5.5×10^{17}
LCLS [169]	8.6×10^{15}	1×10^{17}
FLASH [169]	0.6×10^{15}–1.4×10^{15}	2×10^{14}–8×10^{14}
EuXFEL [169]	4.4×10^{15}	1.4×10^{16}

Table 6.1: 5D- and 6D beam brightness calculated for example beam parameters for the attosecond injector and energy booster presented in Chapters 4 and 5 (marked by the red shaded regions bordered with a dotted line) and compared with values for other machines from literature.

Finally, as an important parameter for beam quality, especially in radiation generation applications, the beam brightness has been estimated for the schemes presented in the previous chapters and is exhibited in Table 6.1 as well as Fig. 6.3. Note that in the latter case, a specific brightness criterion was defined based on the electron beam information provided in the referenced papers. The graph thus shows a brightness scaling

$$B_{beam} = \frac{Q}{\sigma_t \sigma_{x'} (\Delta E/E)} \tag{6.1}$$

with the relative energy spread in units of 0.1 %, whereas in the table the full 5D and 6D brightness definitions are used [34]

$$\begin{aligned} B_{5D} &= \frac{2I_{b,peak}}{\epsilon_{n,x}\epsilon_{n,y}}\,, \\ B_{6D} &= \frac{2I_{b,peak}}{\epsilon_{n,x}\epsilon_{n,y}(\Delta E/E)}\,. \end{aligned} \tag{6.2}$$

$I_{b,peak}$ is the peak current of the electron beam and the relative energy spread is also denoted in units of 0.1 %. It can be seen clearly that the two mechanisms presented in this thesis are quite competitive in comparison with other electron acceleration techniques in terms of

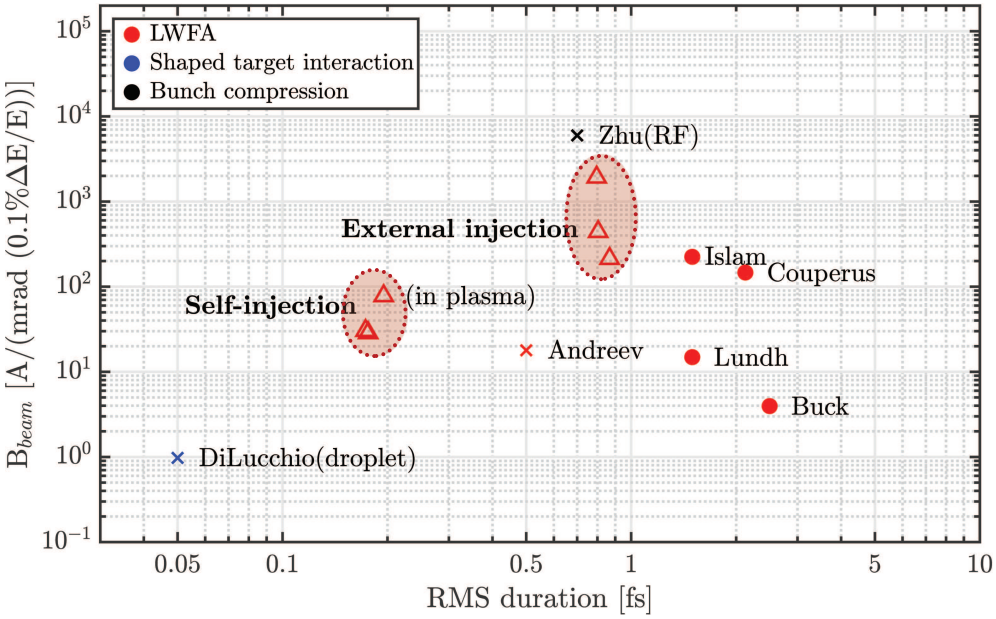

Figure 6.3: Comparison of the beam brightness parameter B_{beam} for electron bunches from the generation techniques discussed in Chapters 4 and 5 with other proposed mechanisms for attosecond electron bunch production from literature. The meaning of the symbols and colours are equivalent to that in Fig. 6.1. Note that this specific brightness parameter instead of the general beam brightness definitions was used due to a lack of detail on beam properties in some of the cited papers. A detailed list of references is provided in Appendix D.

beam brightness. As Table 6.1 shows, both the attosecond injector and the energy booster predict brightness levels on the same order as some of the largest X-ray FEL facilities with the injector excelling in particular with regard to 5D brightness. For this variable, the simulations show similar levels to specialised high brightness acceleration schemes, such as proposed by Manahan et al. [34], where the accelerator setup has been prepared specifically for maximising beam brightness. In terms of 6D brightness, all schemes lose in performance: for the self-injection mechanism this is caused by the large beam energy spread, whereas in the external injection scheme the beam charge is a significant limit. Nonetheless, in the context of sub-femtosecond electron beams, as depicted in Fig. 6.3, the techniques presented in this thesis provide a general improvement with respect to other mechanisms. Reaching values higher or on a similar magnitude as almost all other methods - with the exception of RF accelerators - they hence predict to push the boundary towards ultrashort, high brightness electron beam acceleration in a very promising direction.

6.2 Next Steps Towards Experiments

Both of the scenarios proposed in the previous chapters of Part III are experimentally realisable with current technology.

For the setup for upramp-assisted self-injection the largest challenge, and one of the most important aspects of the scheme, is the generation of a steep plasma density upramp on the scale of 100 µm. The production of such micro-scale structures within a plasma target has been shown with multiple techniques, most of which are based on the use of supersonic gas jets. The simplest possibility is to use a micro-scale DeLaval nozzle which generates a short plasma target with, depending on nozzle design, flat top profile and ramps of tens of micrometre length [170]. The whole plasma target is on the order of a few hundred micrometres in this case, limited by the size of the nozzle, but this is in good agreement with the scales used in the simulations presented earlier. Other options include the use of a larger gas nozzle, for which the gas density can be shaped using either a machining laser pulse [171, 172] or a knife edge / microwire [151, 173], as well as the design of a gas capillary with tailored gas jets, in- and outlets [174]. All of these techniques have been shown to allow control over the density profile on the order of 10 to 100 µm.

With the second main requirement, the drive laser with few-cycle duration and 100–200 TW peak power, the SCAPA facility at Strathclyde University would pose a suitable location for a first proof-of-concept test of the injection mechanism. The SCAPA laser pulse is slightly longer than the design value in the simulation, however, as the 1D parameter scans showed, this would lead to some variation in the injected beam properties, while not affecting the realisability of the injection mechanism itself. Other facilities that may be suited for experiments, based on the laser requirements, would be the Apollon facility ($\leq$10 PW peak power, 15 fs pulse duration [175]), Extreme Light Infrastructure (ELI) Beamlines facility with its L2 laser ($\sim$125 TW peak power, <15 fs pulse duration [176]) as well as the Helmholtz Institute Jena with the JETI200 laser (200 TW peak power, 17 fs pulse duration [177]).

The simulations of laser wakefield acceleration with external injection presented here have been specifically tailored towards the planned setup at the SINBAD Accelerator R&D facility at DESY. While this makes the latter a particularly suitable location for future experiments, it is also to-date the only planned or existing facility to produce sub-femtosecond electron pulses and hence fit for energy boosting of ultrashort beams. The ARES linac at SINBAD is planned to start user operation in 2019. Subject to funding availability, it may then be possible to move the high-power ANGUS laser to the SINBAD facility to be used for plasma experiments, at which point an experimental demonstration may become possible. For this scenario, one of the

main experimental points of concern is the plasma target and its shaping, in particular with regard to plasma ramps and transverse density channels required for beam matching and laser guiding, respectively. The longest capillary discharge waveguide demonstrating longitudinal and transverse density shaping until now has been reported as 9 cm in length [178], although ongoing research into creating longer channels should also make the realisation of the plasma stages considered in this work, in size up to 12 cm, experimentally achievable. An alternative option for laser guiding could be the use of a dielectric capillary tube [165, 166], which guides the pulse through the refractive index of the waveguide itself instead of shaping the plasma density distribution. A similar electron beam evolution would be expected in this case to the results presented, as the beam only experiences a small, central fraction of the plasma where the effects of both density channel and dielectric waveguide are negligible. It should be noted, additionally, that, in the simulations presented, the presence of the density channel in the plasma up- and downramps of the target has been neglected. If generated by an electric discharge, the transverse density modulation would in reality also be present in these regions, yet its effect on laser pulse and electron beam small, as effective guiding only starts with the laser pulse reaching the channel-matched spot size at its focus.

For a more detailed design study, it will be necessary as a next step to characterise the experimental setup through further 3D simulations with realistic electron beam distributions as well as through error and tolerance studies. The currently used simulation tools are unsuitable for this purpose, however, due to the high required computational resources for full PIC simulations. Instead, since the accelerator is working in a stable, almost linear regime, codes catered more strongly to resource-efficient simulations are proposed, such as quasi-static or cylindrical PIC codes, like FBPIC [179]. The latter, for example, also employs a spectral field solver, instead of the finite-difference Yee and Lehe solvers in OSIRIS, which may provide a good strategy for preventing numerical Cherenkov radiation without the side effects experienced in the current simulations.

Beyond the plasma setup itself, one important aspect for experiments with ultrashort electron beams will be the possibility to measure longitudinal bunch lengths and profiles on the attosecond scale. At SCAPA the measurement of coherent transition radiation with an interferometer is currently used for longitudinal bunch diagnostics, which has measured beam lengths on the femtosecond scale in the past [30]. At SINBAD, it is planned to use an X-band deflecting cavity [45], which as a technique has also demonstrated fs-level resolution before [91]. While these devices may be able to resolve beams on the sub-femtosecond level, if designed adequately, it will nonetheless be another essential step towards experiments where beams of tens to few

hundred of attoseconds duration become measurable. The following Part IV discusses this issue and possible solutions in further detail.

6.3 From Attosecond Electron Beams to Attosecond Light Pulses

In most radiation generation schemes, as presented in Section 1.1, an electron beam emits radiation based on wiggling through a periodic deflecting field, either in an undulator, a plasma bubble (betatron radiation) or a laser pulse (Thomson scattering). The pulse duration of the generated radiation is then determined by the difference in time of arrival at an observer of the first photon from the first electron in the beam and the last photon generated by the last electron. Mathematically this can be described as a convolution of the longitudinal radiation profile produced by a single electron, given by $N\lambda$ (with N the number of wiggling periods and λ the radiation wavelength), and the temporal electron beam distribution [1, 180]. Assuming a Gaussian distribution for both the electron beam and the radiation flash from a single electron, the convolution of the two is also a Gaussian distribution with RMS length

$$\sigma_{radiation} = \sqrt{\sigma_{e-beam}^2 + \sigma_{single-e}^2} \tag{6.3}$$

with σ_{e-beam} the electron beam RMS (root mean square) length and $\sigma_{single-e}$ the RMS length of the single electron radiation pulse [181]. Note that the assumption for the latter to be Gaussian is reasonable for, for example, Thomson scattering where a laser pulse acts as an optical undulator and hence the number of emitted photons, as a single electron passes through the pulse, depends on the local laser strength $a(z)$ varying along the longitudinal direction. $\sigma_{single-e}$ can thus be approximated by $\sigma_{single-e} \approx (\sigma_L/\lambda_L)\ \lambda$ with λ_L, σ_L the laser wavelength and RMS duration, respectively.

Considering that the single electron radiation length is typically on the order of single to hundreds of nanometres for ultraviolet (UV) and X-ray radiation, this means that the overall radiation pulse length is dominated strongly by the electron bunch length. For the electron beams considered in Chapters 4 and 5 this hence allows for the generation of radiation pulses of hundreds of attoseconds in duration. A similar treatment can be applied to undulator radiation, for example, where the single electron radiation pulse profile needs to be assumed rather by a boxcar function; again the standard deviations in the longitudinal distributions can be added in quadrature [181].

One possibility to produce radiation, especially from the self-injected beams presented in Chapter 4, is through synchrotron radiation emitted within the plasma. This phenomenon has been investigated for the initially proposed upramp-assisted self-injection scheme by Li et al. [142] and was found to generate coherent attosecond UV flashes. It is made possible on the

one hand by the large transverse momenta of the electrons in the injected beam leading to strong synchrotron emission, while on the other hand the ultrashort nature of the self-injected electron beam allows the radiation to combine coherently. Considering that the generated electron beams in the new parameter regime introduced in this thesis are equally short and similar in their transverse evolution to the ones presented by Li et al., comparable radiation pulses are expected to be generated.

A second option, as has been discussed in Chapters 4 and 5, is to extract the electron beam from the plasma in order to use it for radiation production. For the example of self-injected beams from Chapter 4, a clean up of the beam quality is useful due to, in particular, its considerable energy spread and sub-optimal transverse beam properties. This could be achieved, for example, with a simple collimator slit, where the off-axis tails of the beam are cut off. Alternatively, with a more complex energy collimation system, as used at ATF (see Section 1.4), a specific energy window within the beam with a collimator slit in a dispersive beamline could be selected. For both options, further studies, especially on the trade-off between beam quality and charge loss, will be required. Moreover, bunch decompression in a chicane, as proposed by Maier et al [182], could also be considered to improve the beam slice energy spread. While the current is large enough to allow for an elongation of the bunch without loss of its radiation capabilities, this approach would likely increase the bunch length to the femtosecond level and hence will not be discussed in further detail.

In the following, a possible application of the electron beams investigated in this thesis to Free-Electron Lasers and Thomson scattering schemes is briefly discussed based on simple scaling laws and the reference case electron properties introduced in Chapters 4 (Table 4.7, short extraction ramp) and 5 (Table 5.6, working points WP2 and WP3).

Free-Electron Laser (FEL)

While the detailed equations to describe the behaviour of an electron beam in an FEL are complex and studies are hence often undertaken using simulation codes, such as Puffin or Genesis [183, 184], a first assessment of the suitability of an electron beam to be used for lasing in an FEL can be made via a set of scaling laws. Their description and discussion in the following is based on [1, 23, 24, 185].

One important parameter in this context is the power gain length

$$L_G = L_{G0}(1 + \Lambda)\,, \tag{6.4}$$

which describes the distance over which the generated radiation power at the resonant wavelength

$$\lambda_r = \frac{\lambda_u}{2\gamma^2}(1 + \frac{K^2}{2}) \tag{6.5}$$

in the FEL has increased by a factor of e. In this context, $L_{G0} = \lambda_u/(4\pi\sqrt{3}\rho)$ is the 1D gain length for an electron beam with zero energy spread. Here, λ_u is the undulator wavelength, $K = eB\lambda_u/(2\pi mc)$ the undulator parameter and ρ the Pierce parameter

$$\rho = \Big[\frac{1}{16}\frac{I_e}{I_A}\left(\frac{K[JJ]\lambda_u}{2\pi\gamma^{3/2}\sigma_x}\right)^2\Big]^{1/3}. \tag{6.6}$$

I_e is the electron beam current, I_A the Alfven current, σ_x, γ the electron beam transverse beam size and Lorentz factor as well as $[JJ] = J_0(K^2/(4+2K^2)) - J_1(K^2/(4+2K^2))$, as defined in Section 7.1. ρ represents in this context essentially the FEL efficiency, as it determines the gain length, the reachable FEL power and other variables. The parameter Λ describes the gain length degradation due to various three-dimensional effects influencing the electron beam - laser interaction. A fitting formula has been developed by Ming Xie [185] to quantify Λ based on three main conditions that need to be fulfilled in an FEL (see e.g. [24] for details):

- First, the generation radiation pulse needs to stay focused enough over multiple gain lengths in order to avoid gain degradation due to its diffraction: $Z_R \geq 2L_{G0}$ with Z_R the Rayleigh length assuming the radiation pulse transverse size is equivalent to that of the electron beam.

- Second, only a narrow energy range around the resonant wavelength radiates efficiently, as otherwise the phase slippage between electrons and generated radiation is no longer resonant; hence, to achieve FEL gain at all, the beam energy spread must be small: $\sigma_E < \rho$.

- Third, the electron beam itself must remain transversely focused, as an angular spread can translate into a spread in the radiation wavelength again degrading the efficient beam-radiation interaction: $\epsilon < (\lambda\bar{\beta})/(4\pi L_{G0})$ with $\bar{\beta}$ the average beam β_{cs}-function.

Even under these conditions the exponential gain in power eventually stops resulting from, among others, the electron beam energy decrease due to the radiation generation. The saturated power level that is reached can be estimated by

$$P_{sat} \approx 1.6(\frac{\rho P_{beam}}{(1+\Lambda)^2}), \tag{6.7}$$

where $P_{beam} \approx E[GeV]I_e[A]$ is the electron beam power and P_{sat} directly depends on the Pierce parameter ρ. Finally, for short electron beams it is also particularly important to define the cooperation length which describes the phase slippage distance of the radiation over one gain length

$$L_c \approx \frac{\lambda_r}{4\pi\sqrt{3}\rho}\,. \tag{6.8}$$

Applying this theory to the electron beams presented in Chapters 4 to 5, it is found that, while the power output and gain length from the theory are very promising for the self-injected beam parameters, the cooperation length in this case is about a factor of eight larger than the RMS bunch length (factor of 2 with respect to full bunch length). This means that the radiation pulse will have completely overtaken the electron beam in a distance much shorter than the gain length leading effectively to insufficient radiation amplification. Another issue that could occur for this ultradense electron beam, which is not considered by the scaling laws, is that the bunch significantly changes shape, especially in the longitudinal direction, due to expansion from space-charge forces or changes in length due to its large energy spread. The latter point is a consequence of the path length dependence of the electrons on energy in the undulator, so that propagation through the latter leads to a correlation between their longitudinal position and energy (see Section 9 for further discussion).

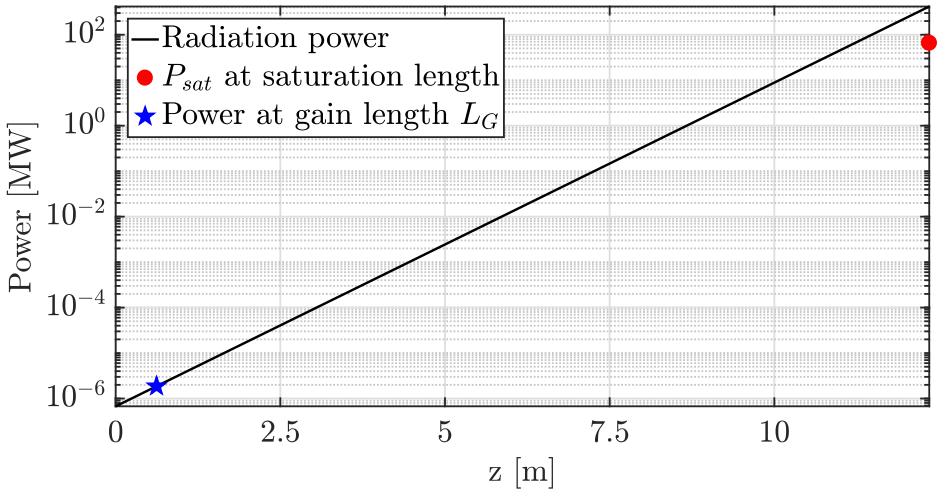

Figure 6.4: Radiation power evolution with distance for an example case using the low energy externally injected electron beam defined as WP2 in Table 5.6 (assuming an increase in transverse beam size to 90 µm) with an undulator of period 1.5 cm and peak magnetic field 2 T. The saturation power and gain length were calculated based on Eqs. (6.4) and (6.7), whereas the SASE radiation power evolution was calculated from $P_{SASE} = g_A g_S \rho\gamma mc^2\sigma_\omega/\sqrt{2\pi}\exp(z/L_G)$ with σ_ω the SASE bandwidth and the other parameters as defined in [24]. Note that the radiation power evolution does not consider the eventual saturation hence overshooting the saturation power.

Undulator peak field B [T]	2.0
Undulator period λ_u [cm]	1.5
Undulator parameter K	2.8
Radiation wavelength λ_r [nm]	117
Pierce parameter ρ	2.8×10^{-3}
3D gain length L_G [cm]	64
Cooperation length L_c [µm]	3.3

Table 6.2: Example properties for a Free-Electron Laser setup for the low-energy electron output beam (WP2) from the plasma energy booster, discussed in detail in Section 5.6. The radiation and FEL properties have been calculated using the Ming-Xie model with the electron beam parameters taken from Table 5.6 assuming an increase in transverse beam size to 90 µm. These parameters also correspond to the ones applied for calculating the results in Fig. 6.4.

The externally injected electron beams presented in Chapter 5, on the other hand, are potentially more suited for FEL application, in particular due to their considerably smaller energy spread, higher energy and better transverse properties. Nonetheless, it was found that for the high energy case (working point WP3) the emittance and beam current are still not adequate, so that even the simple Ming-Xie theory does not predict any lasing. For the lower energy beam (working point WP2) all the conditions regarding the beam quality, listed above, are fulfilled and a finite radiation output power is calculated, as shown in Fig. 6.4. The reason for this is mostly the superior beam quality - something that could also likely be improved for the high energy case. As shown together with other FEL-parameters for this assumed setup in Table 6.2, a fundamental radiation wavelength of 117 nm is found in this particular case, but the saturation power remains comparably small, on the order of 66 MW, likely due to the still quite low beam current. There may be additional aspects that are not considered in this analytical description and that may deteriorate the performance further; FEL radiation generation of these particular ultrashort beams may thus not be the most suitable application.

Thomson Scattering

Treating Thomson scattering as an interaction of an electron beam with an optical undulator, it is possible to approximately predict the generated radiation properties based on a few simple scaling laws [1]. In this frame, the undulator parameter corresponds to the laser strength $K = a_0$ and the undulator period is equivalent to half the laser wavelength $\lambda_u = \lambda_L/2$. Two regimes can be differentiated: for $a_0 < 1$ the interaction is in the undulator regime, whereas for $a_0 \gg 1$ the dynamics are more nonlinear and the laser pulse is acting like a wiggler.
Assuming a counter-propagating laser pulse with $a_0 < 1$, the generated photon energy, photon

number and radiation divergence can thus be estimated as [1]

$$\begin{aligned} E_{photon} &= \frac{4\gamma^2 hc}{\lambda_L(1+\frac{a_0^2}{2})}\,, \\ N_{photon} &= N_e N_L\ 1.53\times10^{-2}a_0^2\,, \\ \theta_{rad} &= \frac{1}{\gamma}\,, \end{aligned} \tag{6.9}$$

where N_e is the number of electrons in the beam, N_L is the number of cycles in the laser pulse as effective wiggling periods and h is the Planck constant.

In the wiggler regime, on the other hand, the maximum angle of the electron trajectory as it is deflected in the laser pulse field is considerably larger leading to a number of changes in the properties of the generated radiation. Among others, radiation is emitted at the fundamental wavelength and its harmonics up to a critical energy $E_{photon,c}$, while also the radiation opening angle in the plane of electron motion increases:

$$\begin{aligned} E_{photon,c} &= \frac{3a_0\gamma^2 hc}{\lambda_L}\,, \\ N_{photon} &= N_e N_L\ 3.31\times10^{-2}a_0\,, \\ \theta_{rad} &= \frac{a_0}{\gamma}\,. \end{aligned} \tag{6.10}$$

	Self-inj. beam	Ext. inj. beam (low E)	Ext. inj. beam (high E)
Beam energy [MeV]	29.3	281	943
Beam charge [pC]	128	0.7	0.7
Beam RMS duration [as]	176	796	867
a_0		1.5 (0.6)	
λ_L [nm]		800	
No. of laser cycles		25	
Photon energy [MeV]	0.024 (0.018)	2.11 (1.59)	23.8 (17.9)
Photon wavelength [pm]	51.6 (68.5)	0.588 (0.780)	0.052 (0.069)
Photon no. per pulse	9.92×10^8 (1.10×10^8)	5.42×10^6 (6.01×10^5)	5.42×10^6 (6.01×10^5)
Divergence [mrad]	25.6 (17.0)	2.73 (1.82)	0.813 (0.542)

Table 6.3: Example properties for radiation generated through Thomson scattering with the attosecond electron beams presented in this thesis. The values are based on Eqs. (6.9) and (6.10) with the beam properties given in Tables 4.7 (short extraction ramp) and 5.6 (WP2 and WP3). Calculations are made for a_0-values of 1.5 and 0.6 with the latter depicted as the values in brackets.

Figure 6.5 and Table 6.3 present the application of these scaling laws to the attosecond

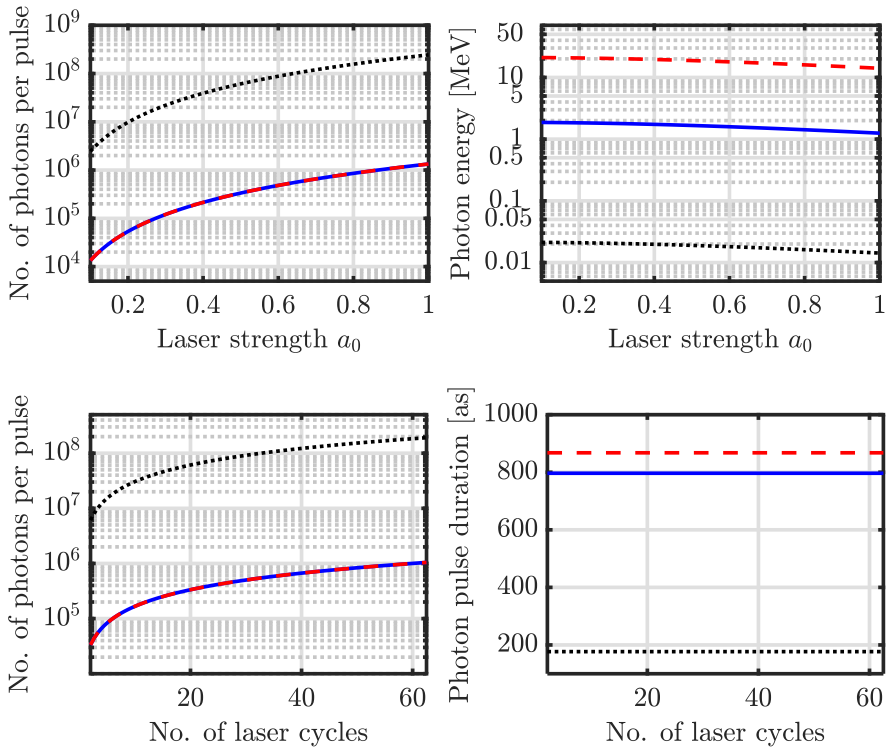

Figure 6.5: Dependence of the generated photon number, photon energy and radiation pulse length on the laser strength a_0 and number of laser cycles for the three reference cases given in Tables 4.7 (short extraction ramp, black dotted line) and 5.6 (WP2, blue solid line and WP3, red dashed line). The laser is assumed to be counter-propagating with a laser wavelength of 800 nm and, for the top and bottom rows, respectively, 20 laser cycles and a_0=0.5.

reference beams from this thesis. It can be seen that in principle Thomson scattering could be an interesting option, especially due to the generated radiation pulses having hundreds of attoseconds duration (see Fig. 6.5, bottom right-hand graph). This is more or less independent of the laser pulse length, as also shown earlier.

Using electron bunches from the upramp-assisted self-injection scheme, high intensity radiation pulses in the X-ray range with photon numbers between approximately 1×10^6 and 5×10^8 per pulse may be achieved. Due to the large electron beam energy spread the emitted radiation pulse would likely have large bandwidth, which, thanks to the high photon number, can be spectrally filtered, if necessary.

With the electron beams from external injection into LWFA, on the other hand, an entirely different radiation regime can be opened up with about an order of magnitude higher photon energy in the gamma-ray range. The photon number in this case is, unfortunately, smaller and on the order of 1×10^4 and 5×10^6 due to the reduced beam charge. The radiation pulses,

however, promise very good transverse properties with divergences at the milliradian level or less. Another advantage of employing externally injected beams is, for this purpose, that, thanks to the good control over the acceleration setup, a tunable radiation source, at least in terms of photon energy, could be provided.

Overall, the electron beam generation and acceleration schemes presented in this part thus provide interesting sources for potential radiation generation mechanisms. Although use in an FEL may be possible with the electron beams from the external injection energy boosting stage, a more compact and simpler application for both the bunches from the attosecond injector and the boosting scheme could be in a Thomson scattering setup; more detailed, simulation-based studies on this possibility are planned in the future.

Part IV

Measurement of Longitudinal Bunch Length at the Attosecond Level

This part discusses two methods for the measurement of longitudinal electron beam profiles with possible attosecond resolution:

- an X-band deflecting cavity and
- a more complex device combining such a deflector with a laser modulator providing enhanced resolution.

The latter sub-femtosecond diagnostic device is shown in Fig. 6.6 and has been originally proposed by Andonian et al. [100]. After strongly streaking the electron beam in the horizontal direction as it co-propagates with a laser pulse in the TEM_{10}-mode through an undulator, the full beam can only be resolved through additional streaking in the vertical direction with a transverse deflecting cavity (TDS). The longitudinal beam profile is finally reconstructed from the transverse beam distribution measured on an imaging screen after propagation through a drift space or beam transport line.

The two devices are investigated and compared both theoretically (Chapter 7) and based on experimental measurements (Chapter 8) carried out at the Accelerator Test Facility (ATF) at Brookhaven National Laboratory, in collaboration with researchers from Radiabeam and the University of California, Los Angeles (UCLA). In Chapter 9, the suitability for applying these techniques, in particular the combined diagnostic device, for ultrashort electron beams from novel accelerators is assessed. The following list summarizes the main highlights of this work, some of which have been published in [186]:

- A beam profile reconstruction tool for the recovery of the longitudinal bunch structure from measured images with the combined sub-fs diagnostic device under study is presented and tested.
- First measurements with the new X-band deflecting cavity at ATF demonstrate its capabilities for characterising electron beams of various shapes and durations with an experimental resolution down to around 104 fs; strategies towards improving this resolution to the single femtosecond level are proposed.
- A first proof-of-concept experiment of the sub-femtosecond diagnostic device clearly shows the streaking effect due to interaction of the electron beam with the high-power laser pulse.
- An experimental resolution of around 3 fs is measured with presented optimisation steps suggesting an improvement to around 400 as in upcoming experimental runs.
- Simulations demonstrate the successful bunch profile reconstruction of attosecond electron beams from RF and novel accelerators with the sub-femtosecond diagnostic device; major

challenges that limit the accuracy of the reconstruction are determined to be the electron beam energy spread and emittance.

Note that the experiments were carried out by the author as part of a team with other researchers from ATF, Radiabeam and the University of California (UCLA). The presented analysis was completed by the author and includes the results of discussions with Dr. Gerard Andonian, Dr. Mikhail Fedurin as well as colleagues at DESY and Strathclyde University.

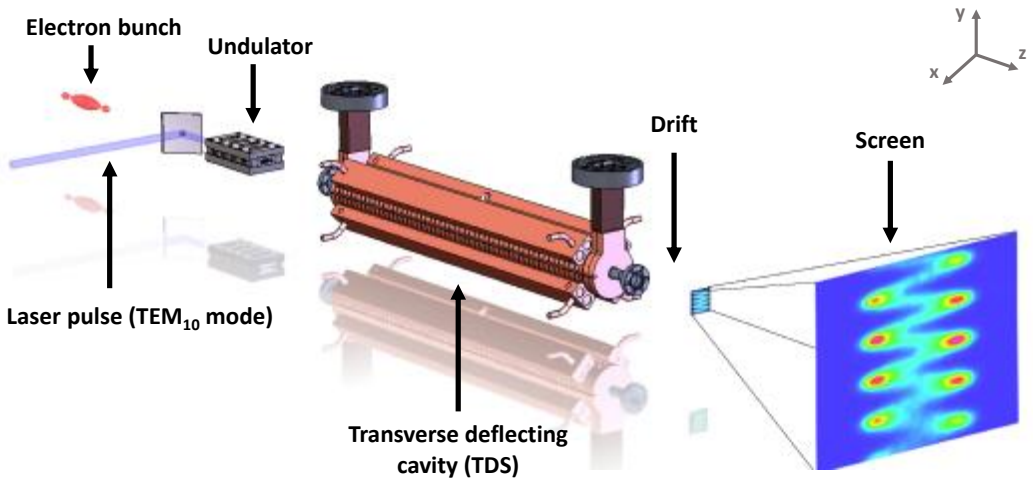

Figure 6.6: Layout of the novel sub-femtosecond bunch length diagnostic investigated in part IV. The second investigated measurement technique only uses the TDS, drift section and screen (image adapted from [187]).

Chapter 7

Theory & Simulations

This chapter derives the main theory to describe both an RF transverse deflecting structure and the novel combined diagnostic device. Moreover, a new bunch profile reconstruction tool, that can be used for experiment analysis as well as detailed simulation studies, is presented.

7.1 Theoretical Concept

Transverse Deflecting Structure

In a transverse deflecting structure (TDS), the electrons experience a transverse angular kick the strength of which depends on the longitudinal position s of the electrons within the bunch [188, 189]:

$$\begin{aligned} \Delta y'(s) &= \frac{eV_{rf}}{p_z c}\sin(k_{rf}s+\phi) \\ &\approx \frac{eV_{rf}}{p_z c}\left[k_{rf}s\cos(\phi)+\sin(\phi)\right], \end{aligned} \tag{7.1}$$

where p_z is the electron longitudinal momentum, $k_{rf}=2\pi/\lambda_{rf}$ is the RF wave number, ϕ the RF phase and V_{rf} the RF voltage in the cavity. The simplification in the second line of Eq. (7.1) is made assuming that the bunch coordinate s is small compared to the RF wavelength, i.e., $k_{rf}s \ll 1$.

The applied voltage V_{rf} can be found based on the peak input power P_{rf} into the deflecting cavity [190]

$$V_{rf} \approx A_{cav}L_{cav}\sqrt{P_{rf}} \tag{7.2}$$

with A_{cav} denoting a factor quantifying the efficiency of the cavity and L_{cav} the cavity length.

Further beam transport after the deflector, described, when neglecting space-charge, by the transport matrix element R_{34}, converts this kick angle, shown in Fig. 7.1a, into a final transverse offset

$$\Delta y_f(s) = R_{34}\Delta y'(s)\,, \tag{7.3}$$

which can be measured, for example, on an imaging screen.

Taking into account a full ensemble of particles, the beam signal on the screen has a transverse centroid offset $\langle \Delta y_f \rangle$ and an RMS size $\sigma_{y,f}$ of

$$\begin{aligned} \langle \Delta y_f \rangle &= R_{34} S_{rf} \frac{\sin(\phi)}{\cos(\phi)}\,, \\ \sigma_{y,f} &= \sqrt{\sigma_{y,D}^2 + (\sigma_z R_{34} k_{rf} S_{rf})^2}\,, \end{aligned} \tag{7.4}$$

where $S_{rf} = eV_{rf}/(p_z c)\cos(\phi)$ is the streaking amplitude and σ_{yD}, σ_z are the RMS beam width at the screen and beam length at the deflector, respectively. The longitudinal profile and bunch length of the electron beam can thus be recovered from the measured profile and beam size in y.

However, in order to resolve a longitudinal feature Δs, the beam needs to be streaked more strongly than the effect of the intrinsic beam divergence $\sigma_{y'}$ such that

$$\Delta y'(\Delta s) \approx S_{rf} k_{rf} \Delta s \geq \sigma_{y'}\,, \tag{7.5}$$

assuming the beam to be placed at a zero-crossing ($\phi = 0$). This can be used to define the resolution of the TDS

$$\Delta s \geq \frac{\sigma_{y'}}{S_{rf} k_{rf}} = \frac{\epsilon_{n,y}\, mc^2}{\sigma_y e V_{rf} k_{rf}} \tag{7.6}$$

with $p_z = \beta\gamma mc$ and σ_y, $\epsilon_{n,y}$ denoting the beam size and emittance at the deflector.

Laser Modulator

A laser modulator, consisting of a laser pulse co-propagating with the electron beam in an undulator, has been proposed to be used to streak the electron bunch, similarly to a TDS [100]. In this setup, the electrons exchange energy with the laser field E_x based on

$$\frac{d\gamma}{dt} = \frac{e}{mc} E_x \beta_x\,, \tag{7.7}$$

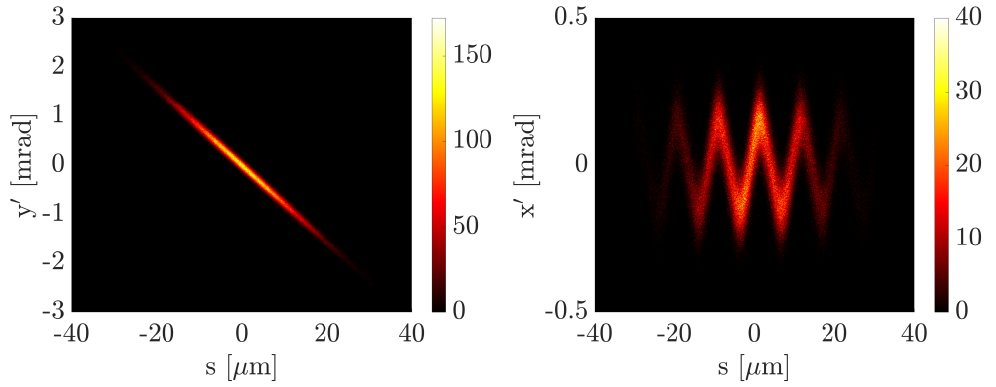

(a) Transverse deflecting cavity (b) Laser modulator

Figure 7.1: Angular kick due to the RF deflector (left) and the laser modulator (right), both right after each device. For the TDS a deflecting voltage of 15 MV has been assumed, while the laser power in the laser modulator is taken to be 5 GW in *elegant*-simulations.

where β_x is the transverse electron velocity due to the wiggling motion in the undulator

$$\beta_x = -\frac{K}{\gamma}\sin(k_u z)\,. \tag{7.8}$$

Here $K = eB\lambda_u/(2\pi mc)$ is the undulator parameter, while λ_u is the undulator period with $k_u = 2\pi/\lambda_u$ and B is the undulator magnetic field. The transverse motion due to the laser field itself has been neglected assuming it is much weaker than the effect of the undulator field.
The laser electric field is in the TEM_{10} mode (see Section 3.1 for details) and can, close to its axis, be described as

$$E_x(z,x,t) = \frac{2\sqrt{2}E_0 x}{w_0(1+(z/z_R)^2)}\sin(k(z-ct)+\Phi)\,. \tag{7.9}$$

By applying Eqs. (7.8) and (7.9) to Eq. (7.7) and defining $x = x_0 + K/(k_u\gamma)\cos(k_u z)$ (based on Eq. (7.8)), the accumulated change in energy in the undulator for a particle with initial position (s,x) co-propagating with the laser pulse is calculated to be [13]

$$\begin{aligned} \frac{\Delta\gamma}{\gamma} &= S_{LM}\,kx\cos(ks) \\ \text{with}\quad S_{LM} &= \frac{2K}{\gamma^2}\sqrt{\frac{P_L}{P_0}}[JJ]f(\lambda, w_0, \sigma_\tau, \lambda_u, L_u, K, \gamma, s)\,, \end{aligned} \tag{7.10}$$

where P_L is the laser peak power, $P_0 = I_0 mc^2/e$ with $I_0 = 4\pi\epsilon_0 mc^3/e \sim 17\,\mathrm{kA}$ the Alfven current and $[JJ] = J_0(K^2/(4+2K^2)) - J_1(K^2/(4+2K^2))$ (for planar undulators) with J_n

denoting the nth-order Bessel function of the first kind. The function f is given by [13]

$$f = \frac{2c}{kw_0^2}\int_{-0.5L_u/c}^{0.5L_u/c} \frac{\cos\left(\frac{4\pi c\delta\gamma}{\lambda_u\gamma_r}t - 2\tan^{-1}(\frac{2c}{kw_0^2}t)\right)}{1+(\frac{2ct}{kw_0^2})^2} \exp\Big(-(\frac{\pi}{k\lambda_u\sigma_\tau}t - \frac{s}{2c\sigma_\tau})^2\Big)dt \tag{7.11}$$

with L_u the undulator length, σ_τ the laser duration and s the relative position of the electron in the bunch.

By employing the Panofsky-Wenzel theorem $\partial\Delta x'/\partial s = \partial/\partial x(\Delta\gamma/\gamma)$ [123], the angular horizontal kick $\Delta x'$ that the electron experiences in the laser modulator due to the energy exchange, shown in Fig. 7.1b, can be expressed as

$$\Delta x' = S_{LM}\sin(ks+\Phi)\,. \tag{7.12}$$

The laser modulator can therefore be used for mapping the longitudinal bunch profile onto the x-coordinate of the beam, only in this case with a resolution of

$$\Delta s \geq \frac{\sigma_{x'}}{S_{LM}k} = \frac{\epsilon_{n,x}}{\beta\gamma\sigma_x S_{LM}k}\,, \tag{7.13}$$

where $\sigma_{x'}, \sigma_x$ are the horizontal beam divergence and width, respectively, at the laser modulator. It should be noted, however, that this streaking effect is only possible due to the dependence on the transverse coordinate of the laser field in the TEM_{10}-mode; while employing the TEM_{00}-mode also has the effect to generate an energy modulation in the beam, this is not translated into a transverse kick in this case, as Fig. 7.2 shows.

Combined Sub-Fs Diagnostic Device

In the proposed sub-femtosecond bunch length diagnostic investigated here, laser modulator and transverse deflecting cavity are combined together as a device [100]. Due to $k \gg k_{rf}$ typically, the laser modulator can streak the beam with resolution on the order of sub-femtoseconds to hundreds of attoseconds providing a considerable improvement to a measurement with the RF deflecting cavity alone. However, if the electron beam is longer than half a laser wavelength, the streaked images of different parts of the beam overlap on the screen due to the sinusoidal dependence of the kicking angle on the bunch coordinate. The role of the TDS in the setup is therefore to resolve these different sections by spreading them in the y-direction on the screen. As a consequence, the device not only provides high resolution, but also, by using the screen

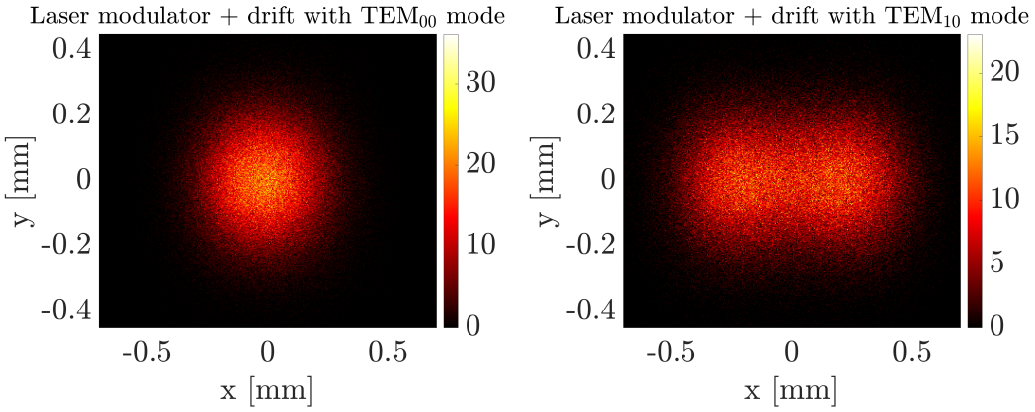

Figure 7.2: Effect of the laser-electron beam interaction in the laser modulator for the TEM_{00}- and TEM_{10}-mode, respectively, on the measured transverse beam distribution after a drift section of 2 m using 5 GW laser power. It is only the TEM_{10}-mode, due to its linear field dependence on the transverse coordinate, that can generate the angular kick required for streaking. Note that these graphs are based on *elegant*-simulations.

area very efficiently, a good dynamic range.

In more detail, the effect of the diagnostic setup on a single electron can be derived by a simple analytical model taking into account drift lengths of distance L_1 and L_2 between and after the laser modulator and TDS, respectively. After propagation through all stages, the coordinates of an electron being initially described by $(x_0,x_0',y_0,y_0',s_0,\eta_0)$ (with η_0 the initial relative energy spread compared to mean beam energy γ) can be defined by its coordinates on the screen

$$
\begin{aligned}
x_f &= x_0 + (L_1+L_2)x_0' + S_{LM}(L_1+L_2)\sin(ks_0)\,, \qquad (7.14)\\
x_f' &= x_0' + S_{LM}\sin(ks_0)\,,\\
y_f &= y_0 + (L_1+L_2)y_0' + S_{rf}k_{rf}L_2 s_0 + S_{rf}k_{rf}L_1L_2\Big(\frac{\eta_0}{\gamma^2} + \frac{S_{LM}kx_0}{\gamma^2}\cos(ks_0)\Big)\,,\\
y_f' &= y_0' + S_{rf}k_{rf}s_0 + S_{rf}k_{rf}L_1\Big(\frac{\eta_0}{\gamma^2} + \frac{S_{LM}kx_0}{\gamma^2}\cos(ks_0)\Big)\,,\\
s_f &= s_0 + (L_1+L_2)\Big(\frac{\eta_0}{\gamma^2} + \frac{S_{LM}kx_0}{\gamma^2}\cos(ks_0)\Big) + L_2\frac{S_{rf}k_{rf}}{\gamma^2}(y_0 + L_1y_0')\,,\\
\eta_f &= \eta_0 + S_{LM}kx_0\cos(ks_0) + S_{rf}k_{rf}(y_0 + L_1y_0')\,.
\end{aligned}
$$

Here, the following effects of each component, as derived previously, have been assumed [100]:

- laser modulator: $\Delta x' = S_{LM}\sin(ks)$, $\Delta\eta = S_{LM}kx\cos(ks)$
- RF deflector: $\Delta y' = S_{rf}k_{rf}s$, $\Delta\eta = S_{rf}k_{rf}y$

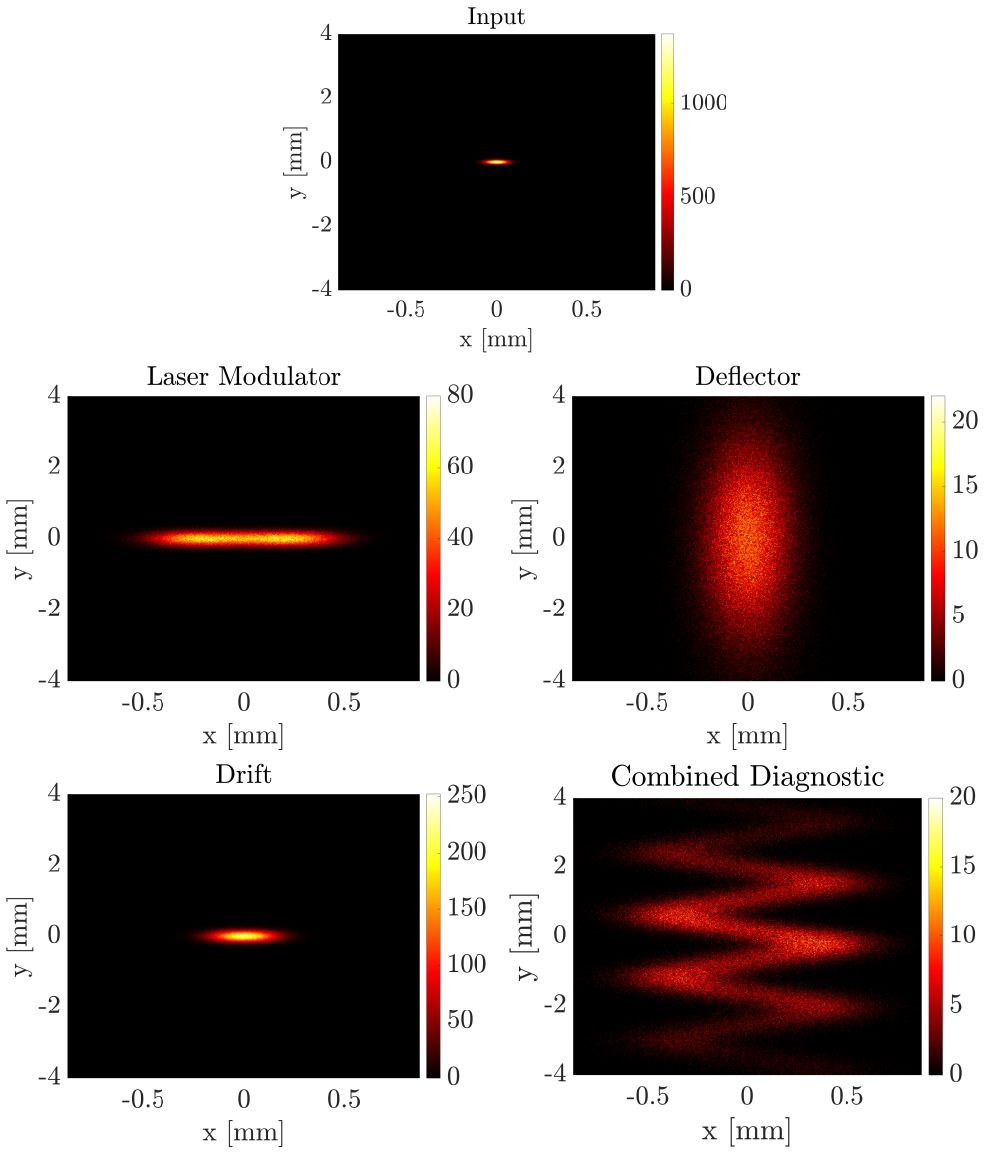

Figure 7.3: Screen image with different components of the diagnostic setup present. Note that the axis scaling is equal for all cases and the initial beam distribution is symmetric in x and y. The laser power in the laser modulator is taken to be 5 GW, the deflecting voltage in the RF TDS is 15 MV and a drift length of 2 m has been assumed in *elegant*-simulations.

- drift space L: $\Delta x = Lx'$, $\Delta y = Ly'$, $\Delta s = L\eta/\gamma^2$

Under the assumption that the relative energy variation is small, $\eta_0 + S_{LM} k x_0 \cos(k s_0) \ll \gamma^2$, or L_1 is short, the horizontal and vertical RMS sizes of a full electron beam can be estimated

to be

$$\begin{aligned} \sigma_{xf}^2 &= \sigma_{xD}^2 + \frac{S_{LM}^2(L_1+L_2)^2}{2}\Big(1-\exp(-2k^2\sigma_s^2)\Big)\,, \\ \sigma_{yf}^2 &= \sigma_{yD}^2 + S_{rf}^2 k_{rf}^2 L_2^2 \sigma_s^2 \end{aligned} \tag{7.15}$$

with $\sigma_{xD}^2 = \sigma_x^2 + (L_1+L_2)^2\sigma_{x'}^2$ the horizontal beam size at the measurement screen without the diagnostic and σ_{yD} the equivalent in the vertical direction.

This can be used to define some boundary constraints for the diagnostic device, as the bunch length dependent streaking effect must be dominant over the effect of initial beam size and divergence, yet allow the beam image to fit on the diagnostic screen of size (X_{sc},Y_{sc}):

$$\sqrt{\frac{Y_{sc}^2}{\sigma_{yD}^2}-1} \gg \frac{S_{rf}k_{rf}(L_1+L_2)\sigma_s}{\sigma_{yD}} \gg 1\,, \tag{7.16}$$

$$\sqrt{\frac{X_{sc}^2}{\sigma_{xD}^2}-1} \gg \frac{S_{LM}(L_1+L_2)}{\sqrt{2}\sigma_{xD}} \gg 1\,. \tag{7.17}$$

The image that is observed on the screen is that of a sinusoidal pattern with amplitude $S_{LM}(L_1+L_2)$ and wavelength $\lambda_y = \lambda S_{rf}k_{rf}L_2$, where the trace of the pattern corresponds to the longitudinal beam profile. Figure 7.3 depicts the expected screen image with the sub-fs diagnostic compared to the effect of each component individually on the beam.

7.2 Design and Testing of a Beam Profile Reconstruction Tool

In order to recover the information on the longitudinal bunch profile from a screen image measured behind the diagnostic setup a reconstruction tool was developed. With its front end shown in Fig. 7.4, the tool works for both a simple TDS and the more complex sub-fs diagnostic device. Figure 7.5 depicts the algorithm behind the tool, while the full program code is available on github (`https://github.com/mweikum/Attoscope_ReconTool`). It works based on three major steps: first the vertical streaking effect due to the deflecting cavity is scaled back using the streaking amplitude S_{rf} obtained from a calibration of the deflector. If the measurement is done with the inclusion of a laser modulator, as a next step a sinusoidal curve is fit to the screen signal, based either on the data itself or a theoretical estimate of the strength amplitude S_{LM}. Finally, the screen data is integrated along the sinusoidal fit, hence recovering the relative intensity along the longitudinal beam profile. The resolution described in Eq. (7.13) is, due to the sinusoidal dependence of the streaking effect, only valid for the linear

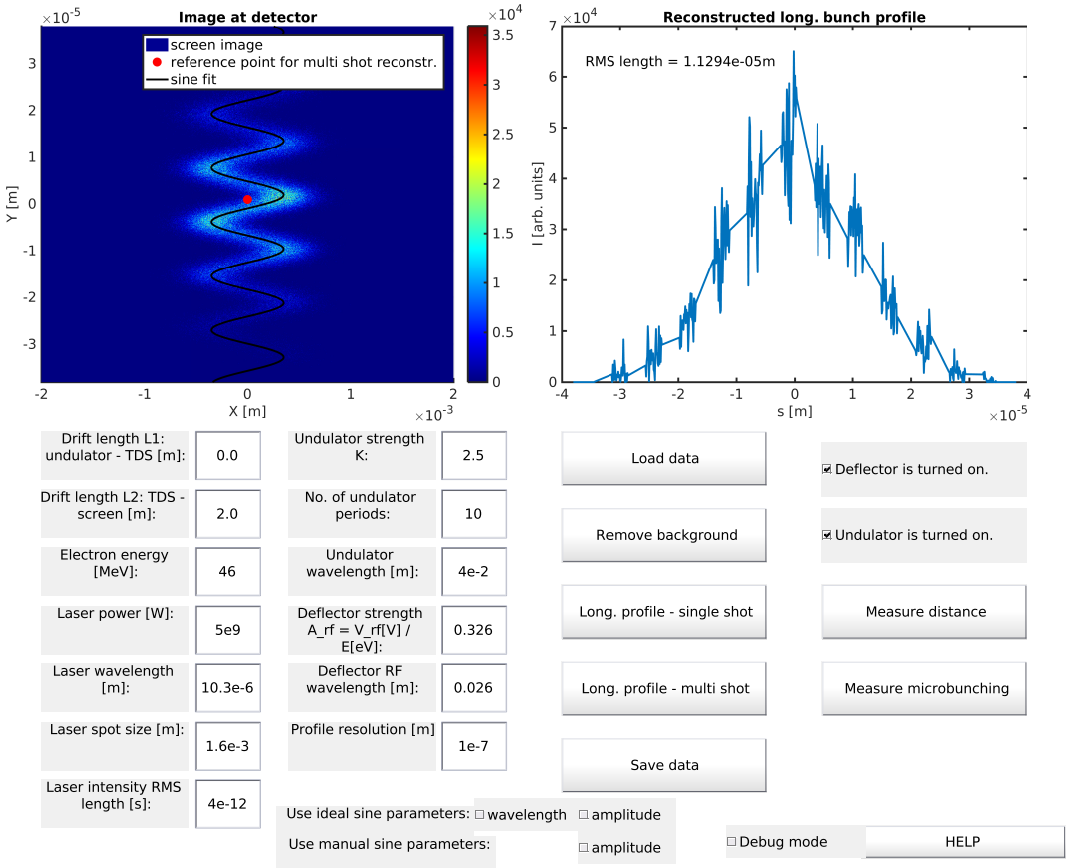

Figure 7.4: Attoscope Reconstruction GUI.

sections of the signal, while it is reduced to that of the RF deflector at the turning points making them significantly harder to reconstruct. As a consequence, the algorithm treats these regions differently calculating the signal there based on the surrounding non-turning point regions in order to avoid distortions in the reconstructed profile.

Additionally to the main algorithm, the tool includes a number of extra features, such as the calculation of the reconstructed bunch length as well as possible microbunching features, and, most importantly, the option to combine multiple screen images for the reconstruction. The latter allows, if using images of the electron beam at different phases in the laser modulator - as would naturally occur in an experiment due to jitter -, to compensate very well for the diminished resolution along the turning points of the screen signal. This is the case because the variation in phase leads to the position of the beam along the sinusoidal screen pattern to change slightly, so that different parts of the beam can be resolved in the high resolution regions with each shot. These can then be stitched together to form an overall high quality

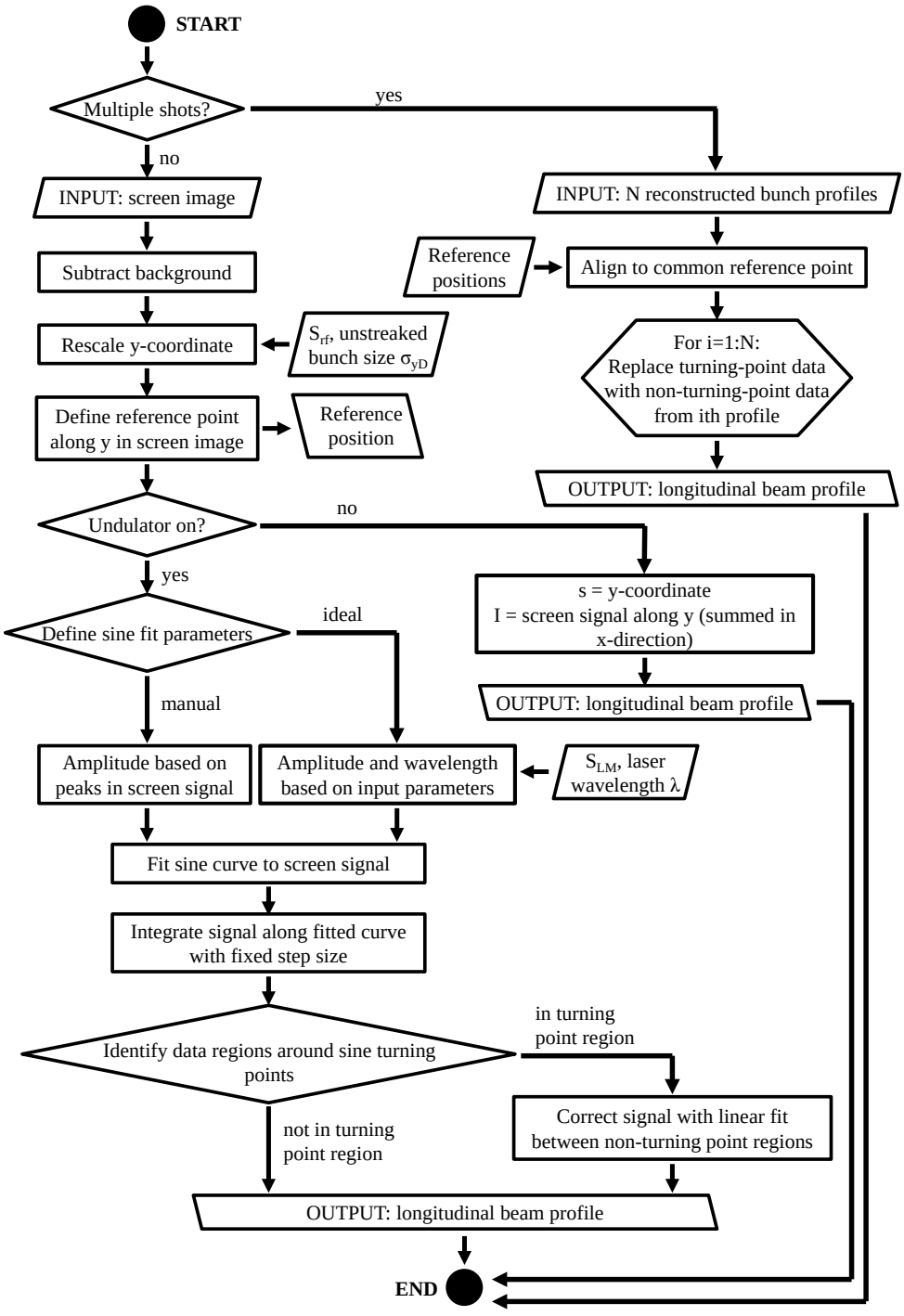

Figure 7.5: Algorithm applied in the reconstruction tool presented in Fig. 7.4.

beam profile.

Two examples to test the capabilities of the reconstruction tool are shown in Fig. 7.6 and 7.7.

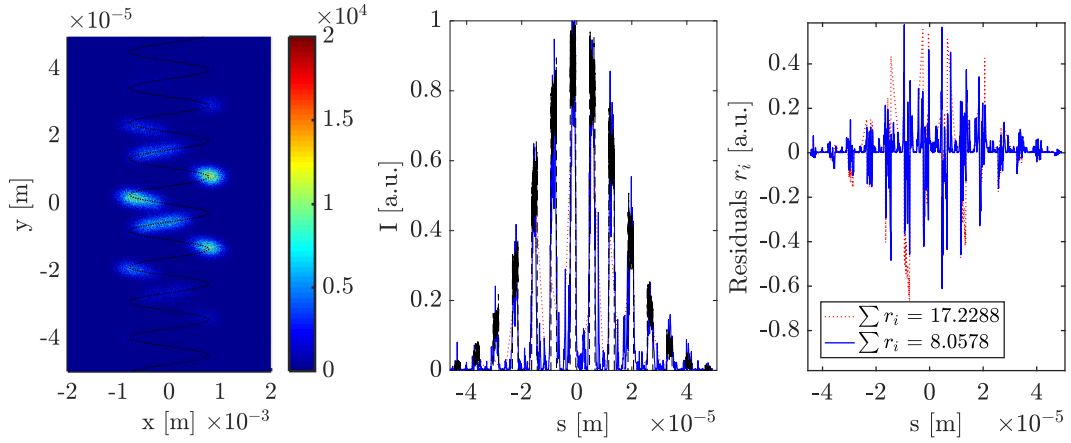

(a) Screen image

(b) Reconstructed longitudinal profile

(c) Residuals with respect to original profile

Figure 7.6: Reconstruction of an electron beam of 15 µm RMS length consisting of 2 µm long microbunches, each at 5 µm distance. The reconstructed values are 15.55 µm for the full rms beam length, 1.94 µm for the microbunch length and 5.00 µm for the average microbunch distance. a): transverse beam distribution at the imaging screen with a sinusoidal fit overlaid; b): original beam distribution (black) and recovered profiles based on a single sub-fs diagnostic measurement (dotted red) and five measurements with slightly varying laser phase (solid blue), c): residuals between original and reconstructed profiles as a measurement of the reconstruction error.

In the first case, an electron beam with 15 µm RMS length consisting of 2 µm long microbunches at 5 µm distance is tracked through the full diagnostic setup, using the analytical model in Section 7.1. It is then analysed with the reconstruction tool, based on a single screen image (red dotted line) as well as on multiple phase-shifted images (blue solid line). For both inputs, the internal features of the beam can be recovered very well with an error of 3 % or less in the length and distance of the microbunches. Moreover, a clear improvement can be seen by the use of multiple screen images.

The second example in Fig. 7.7 uses a simple Gaussian electron beam of 10 µm RMS length, yet here the effect of the diagnostic device is modelled with the tracking code *elegant* [191]. Again the shape of the longitudinal profile is recovered well with a reduction in the error to the original profile by using multiple screen images. However, the reconstructed RMS length is overestimated in this scenario which can be attributed to the widened sides of the final beam profile. As closer analysis of the *elegant* beam output shows, this lengthening of the beam is a physical effect expected to occur, when the beam passes through the undulator (see Chapter 9 for a more detailed discussion), and hence cannot be compensated in the reconstruction tool.

Nonetheless, the usefulness of the developed reconstruction tool for observing the actual longitudinal electron beam profile - which cannot be deducted easily through other means or

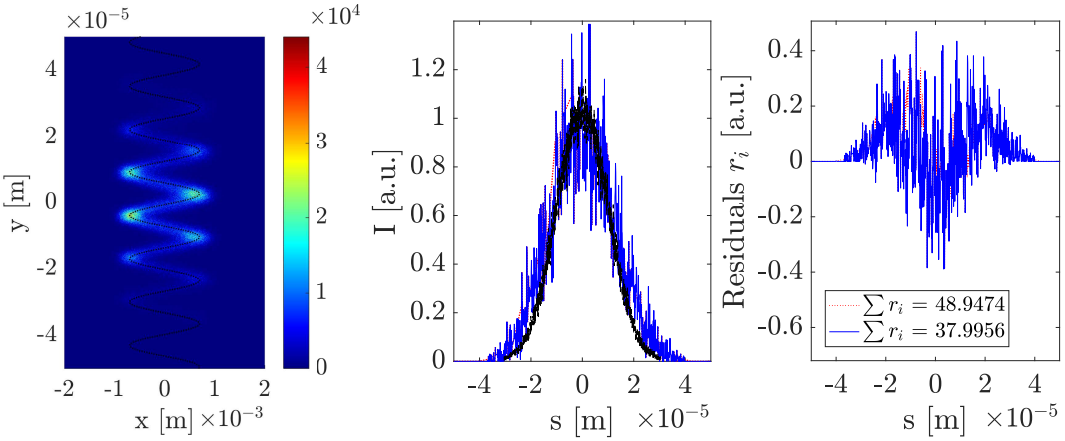

(a) Screen image

(b) Reconstructed longitudinal profile

(c) Residuals with respect to original profile

Figure 7.7: Reconstruction of a Gaussian electron beam of 10 µm RMS length. The reconstructed value for the RMS beam length is 12.33 µm. a): transverse beam distribution at the imaging screen with a sinusoidal fit overlaid; b): original beam distribution (black) and recovered profiles based on a single sub-fs diagnostic measurement (dotted red) and three measurements with slightly varying laser phase (solid blue), c): residuals between original and reconstructed profiles as a measurement for the reconstruction error.

from the measured screen distribution directly - is demonstrated. The sufficient reconstruction quality is shown well, allowing its use in the experimental analysis in the following chapters.

Chapter 8

Experiment

In this chapter, the experimental setup and experimental results of measurements with an X-band deflecting cavity as well as the novel sub-femtosecond diagnostic device are presented. Both were carried out at the Accelerator Test Facility (ATF) at Brookhaven National Laboratory.

8.1 Experimental Setup

8.1.1 X-band Deflector Measurement

First test measurements of the new X-band deflecting cavity at ATF as a longitudinal bunch length diagnostic were taken based on the setup of beamline 2 shown in Fig. 8.1 with parameters in Table 8.1. The electron beam was propagated and monitored through a set of transport optics and diagnostics before being streaked by the TDS. Measurements were observed at the screen with flag IPOP8 around 30 cm downstream of the deflecting cavity.

Besides employing the capabilities for bunch compression and generating microbunches in the H- and F-lines of ATF, for some measurements a dielectric wakefield structure and a mini-chicane (more in Section 1.4) were built into the beamline. The purpose of these last two components is to reshape the longitudinal beam profile, as the electron beam generates a wakefield in the dielectric waveguide which leads to a relative energy modulation across the beam [192]

$$\delta(z) = \frac{eQW(z)L_d}{E_0} \tag{8.1}$$

with Q the beam charge, L_d the waveguide length, E_0 the initial beam energy and $W(z)$ the convolution of the beam distribution and a structure-dependent wake function. In the following

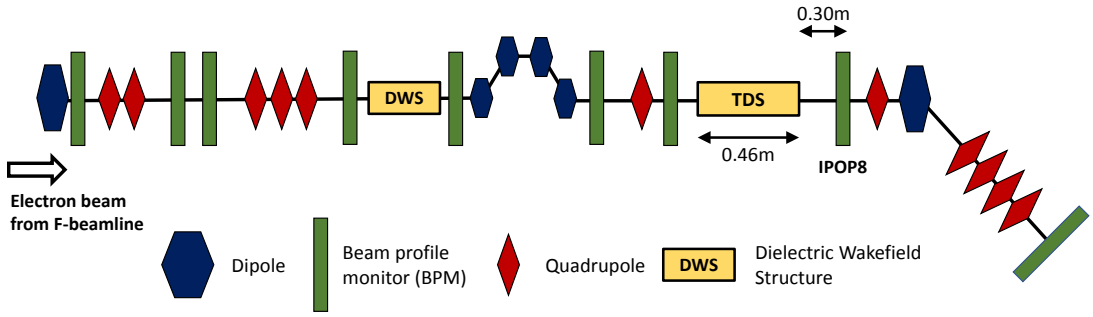

Figure 8.1: ATF beamline 2 setup for the X-band deflecting cavity experiment.

chicane, this energy modulation is converted into a position modulation along z which can lead to a ramping of the longitudinal beam profile, a good feature to test the deflecting cavity with.

Deflector wavelength [m]	0.026 (X-band)
Deflector length [m]	0.46
Max. deflector input power [MW]	16
Deflector A_{cav} [kV/(mW$^{1/2}$)] [193]	8.48
Electron beam energy [MeV]	50

Table 8.1: Setup parameters for the X-band deflector measurement.

8.1.2 Combined Sub-Femtosecond Diagnostic Measurement

For the proof-of-concept experiment of the full sub-femtosecond diagnostic device, beamline 2 was re-arranged and an undulator was added about 1.6 m downstream of the first dipole. The CO_2-laser enters the beamline at the beginning of this section to run in parallel with the electron beam direction being focused at the centre of the undulator to maximise interaction there. Additionally, the dipole spectrometer at the end of the beamline was also used in this experiment with the beam measured at screen IPOP8.5 in this case. A list of setup parameters is provided in Table 8.2.

As the actual measurement requires a TEM_{10} mode, a mode converter was installed just before the laser entrance to the beamline. With a Michelson interferometer-style setup, the

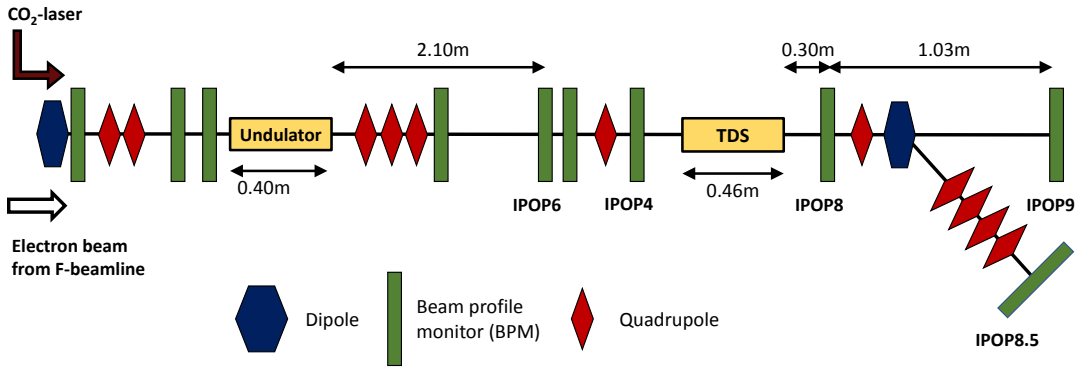

Figure 8.2: ATF beamline 2 setup for the full sub-fs diagnostic experiment.

incoming TEM_{00} mode is split whereby controlling the amplitude and delay between the two arms achieves an interference pattern of two off-axis TEM_{00}-modes very closely resembling the field distribution of the TEM_{10}-mode [187].

The timing between laser pulse and electron beam was adjusted with a two-step procedure: first, a rough timing scan was performed using a Germanium wafer placed in the beam path [194]. While usually transparent to the laser, the wafer starts to block the latter, if it is hit first with the electron beam due to the generation of a plasma at the wafer surface. By scanning through the delay between laser and electron beam and measuring the laser transmission, taking into account the plasma decay time, the timing between the two components can thus be found to picosecond level. A second finer timing scan was completed by measuring and optimising, using the spectrometer, the energy modulation caused by the electron beam - laser interaction. Both of these timing scans were performed with the laser in the TEM_{00} mode, as the usable power for the TEM_{10} mode was limited by the damage threshold of the mode converter components hence making the observation of the interaction easier with the initial laser mode.

Thereafter, measurements of the laser-electron interaction with the TEM_{10} mode were taken at the beam monitor with flag IPOP6, while full diagnostic shots with the RF deflector were measured at the two screens at the end of the beamline, IPOP8 and IPOP9.

Undulator length [m]	0.40
Undulator period [cm]	4.0
Undulator magnetic field [T]	0.67 (K=2.5)
Laser wavelength [µm]	10.3
Laser power (in TEM_{00} mode) [GW]	5.7–143
Electron beam energy [MeV]	46

Table 8.2: Setup parameters for the sub-femtosecond bunch length diagnostic measurement. Note that it is estimated that approximately 50 % of the laser power is lost during the mode conversion, such that the remaining power available in the experiment in the TEM_{10} mode can be assumed to lie between 2.8 and 72 GW.

8.2 Experimental Results

8.2.1 X-band Deflector Measurement

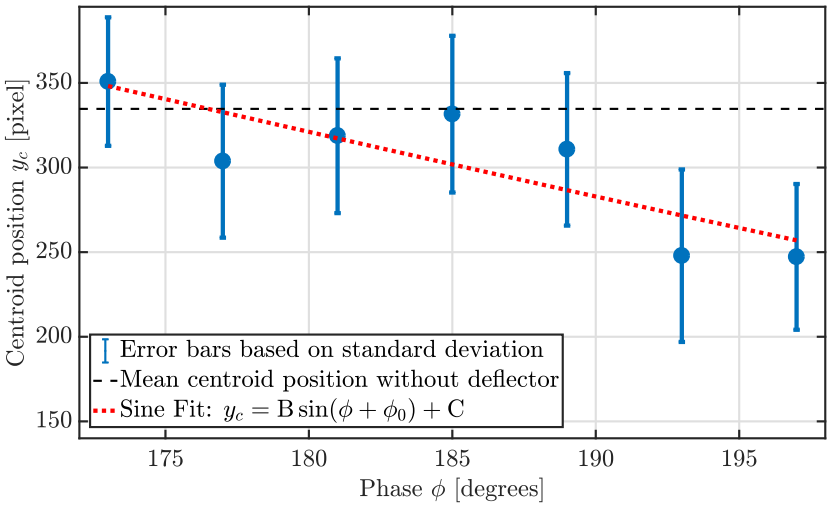

Figure 8.3: Phase calibration of the deflecting cavity: Fit parameters are B=221.8 ± 117.2 pixels (corresponding to (1.4870 ± 0.7858) cm), ϕ_0=$-356.5°$, C=334.7 pixels (corresponding to 2.245 cm).

The first step to use the recently commissioned X-band deflecting cavity in a quantified way was to perform a phase calibration, the results of which are presented in Fig. 8.3. The transverse beam profile was measured at screen IPOP8 for different deflector phases and the centroid position in the y-direction determined in each case. Each data point in the graph is based on 20 consecutive measurements with the error bars showing the standard deviation of the sample. A fit of the form $y_c = B\sin(\phi + \phi_0) + C$ was made which allows the estimation of the deflecting strength as [190]

$$V_{rf} = \frac{\gamma mc^2}{eR_{34}} B\,, \tag{8.2}$$

where γ is the electron beam Lorentz factor and the R_{34}-value is given by the drift length between the deflector and measurement screen of 0.3 m. The scan showed that the measurement was accidentally taken 180° out of phase of the zero-crossing that is usually employed for phase calibration. While not problematic, this was a consequence of the large deflector jitter which is visible in the significantly sized error bars in centroid positions and which made it difficult to judge the beam offset by eye. The calibration scan also provided an estimate of V_{rf}=(2.48 ± 1.31) MV for the deflecting voltage. Note that the uncertainty in V_{rf} has been calculated based on the error in the slope of the fit with $\delta B = \sqrt{\frac{\sum(1/e_i^2)}{\sum(x_i^2/e_i^2)\sum(1/e_i^2) - (\sum(x_i/e_i^2))^2}}$ where e_i is the standard deviation at phase data point x_i [195]; its effect on the error in a measurement of the electron beam duration with the deflecting cavity is discussed at a later point in this chapter.

An alternative estimate of the deflecting voltage can be given based on a power measurement at the klystron feeding the deflector of P_{rf}=2.4 MW. Applying Eq. (7.2) with A_{cav}=8.48 kV m^{-1} W$^{-1/2}$ (see Table 8.1), the deflecting voltage is calculated to be around 6.04 MV. This estimate is higher by a factor of more than 2 compared to the phase calibration result, but at least proves the deflecting voltage to be within the same order of magnitude. Overall, since only a single power measurement was taken and losses likely occur between the klystron and the deflector itself, the phase calibration was found to be the more reliable estimate.

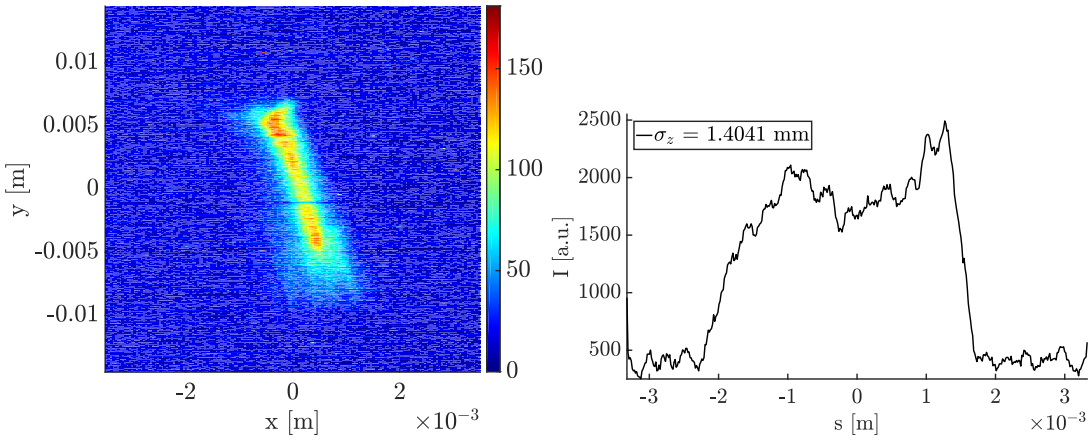

(a) Measured transverse beam distribution (b) Reconstructed longitudinal beam profile

Figure 8.4: Example of a bunch reconstruction with the previously presented tool based on a non-chirped beam image streaked with the X-band deflector.

Figure 8.4 shows a first application of the newly calibrated deflecting cavity as well as the reconstruction of the longitudinal beam profile from a measured screen image with the

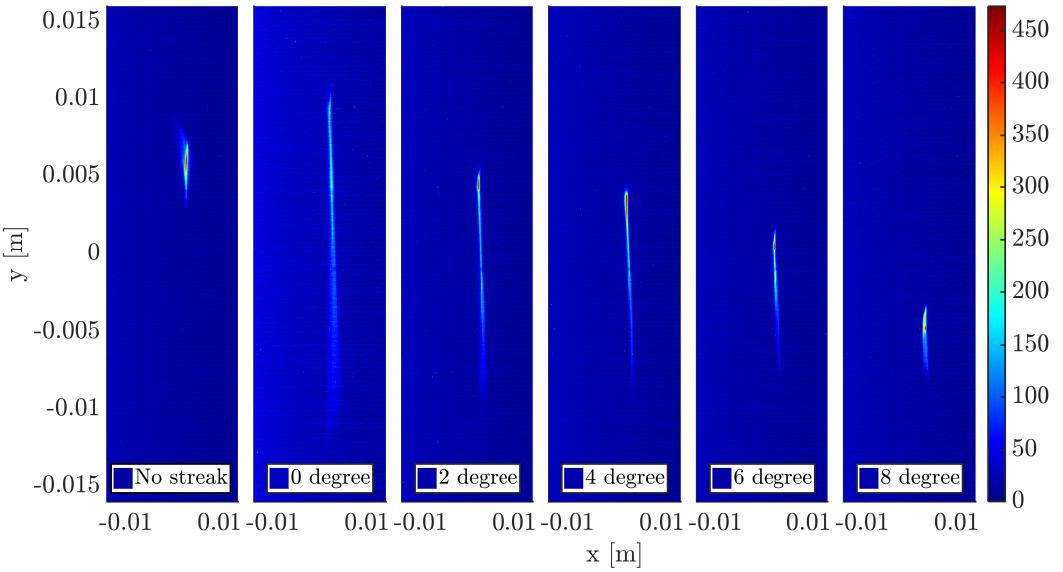

Figure 8.5: Screen images showing the transverse distribution of an unstreaked beam together with streaked beams of different lengths. The length variation is achieved by compressing the beam with a controlled energy chirp in a chicane.

reconstruction tool presented in Section 7.2. The image is part of a set of measurements of electron beams with varying degrees of compression, as shown in Fig. 8.5. By changing the degree of energy chirp in the beam, the bunch length after compression in the chicane in the H-line can be controlled. This can be observed also by the varying length of the beam in the y-direction after streaking.

For the example given in Fig. 8.4 the RMS bunch length was calculated with two methods: firstly, as shown here, by use of the reconstruction tool. The error calculation was then based on combining the contributions from the following variables: 1) the estimate of the deflecting voltage, 2) the unstreaked RMS size in the y-direction and 3) the standard deviation of the recovered RMS lengths the variation of which is a consequence of the fluctuation in the streaked RMS size in the y-direction.

The second technique is based on the calculation of the bunch length from Eq. (7.5), as described in [190]. The vertical RMS beam size is measured for varying deflecting voltages the results of which can be fitted to a parabola of the form $\sigma_y^2 = A(V_{rf} - V_{rf,0,min})^2 + \sigma_{yD}^2$. As a full amplitude scan was not possible at the time of the experiment due to still limited control over the deflector phase and amplitude, the method was simplified to the calculation of the fitting factor A from just two data points (deflector on and off) assuming $V_{rf0min} = 0$. The latter is true if the bunch does not have an initial transverse-longitudinal correlation [91]. The

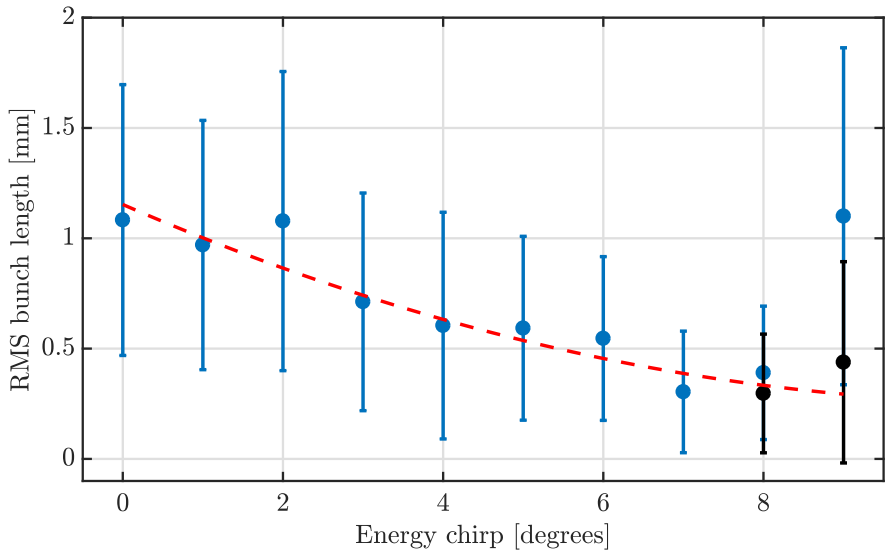

Figure 8.6: Dependence of the reconstructed bunch length on the applied beam energy chirp after compression in the chicane. For a strong chirp the beam is split into two components with each listed separately in the plot. The fit is of the form $y = a + bx + cx^2$ with a=1.153 mm, b=−0.158 mm/degree and c=6.9×10^{-3} mm/degree^2.

RMS bunch length is then reconstructed from

$$\sigma_z = A^{1/2} \frac{\gamma mc^2}{eR_{34}k_{rf}} \tag{8.3}$$

with the error calculated, based on the propagation of uncertainties, from the contributions of σ_y, σ_{yD} and V_{rf} on A:

$$\delta\sigma_z = \sigma_z \sqrt{\left[\sigma_y/(\sigma_y^2 - \sigma_{yD}^2)\ \delta\sigma_y\right]^2 + \left[\sigma_{yD}/(\sigma_y^2 - \sigma_{yD}^2)\ \delta\sigma_{yD}\right]^2 + \left[\delta V_{rf}/V_{rf}\right]^2}.$$

The reconstructed RMS beam lengths are thus (assuming V_{rf}=(2.48 ± 1.31) MV)

- σ_z=(1.450 ± 0.781) mm using the reconstruction tool
- σ_z=(1.080 ± 0.614) mm using the parabola method

Based on a charge measurement which can be used due to a charge-duration correlation for a rough beam length estimation, an RMS bunch length of around 0.45 mm was expected for the measurement. This means that not only do both techniques agree in their results - providing a good validation for the reconstruction algorithm -, but also they estimate the correct order of magnitude for the bunch length, although just within the limits of the large uncertainties of the measurement.

In Fig. 8.6 the same procedure using the parabola method has been applied to all measured compression stages so that the reconstructed RMS bunch lengths can be related directly to the

applied energy chirp. It should be noted that for strong compression the beam split into two parts due to coherent synchrotron radiation in the chicane [196]; in this case both beamlets are plotted. In accordance with the theoretical bunch compression effect of the chicane, given by [197]

$$\Delta L = R_{56}(\frac{\Delta E}{E}) + T_{566}(\frac{\Delta E}{E})^2\,, \tag{8.4}$$

a parabolic fit of the form $y = a{+}bx{+}cx^2$ was made to the data with a=1.153 mm, b=−0.158 mm/degree and c=6.9×10^{-3} mm/degree^2. ΔL is in this case the change in bunch length, whereas R_{56} and T_{566} are both transport matrix elements used to describe the first and second order variation in the longitudinal beam coordinate dependent on beam energy.

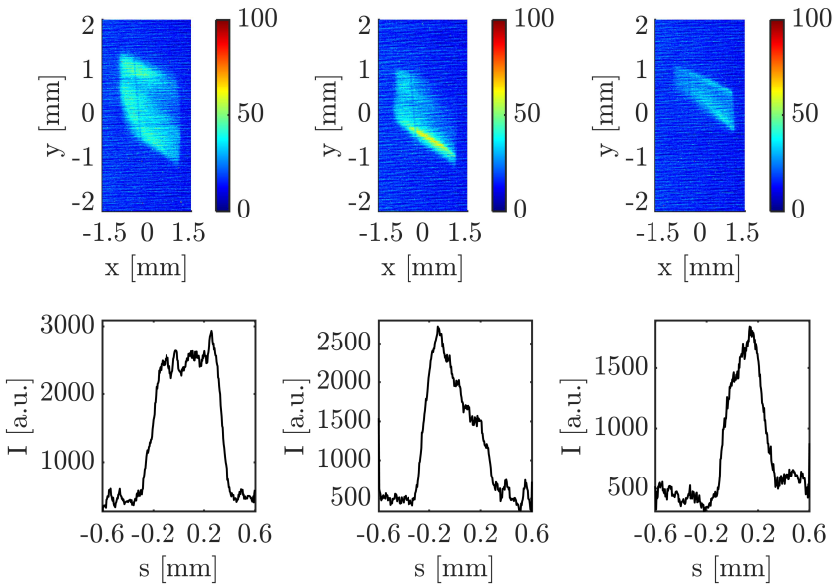

Figure 8.7: Analysis of the ramped beam profile for electron bunches propagating through a dielectric wakefield structure and a chicane for reshaping. Left column: no wakefield structure, so no ramping (100pC); middle column: with wakefield structure, ramped, 100pC; right column: with wakefield structure, ramped, 50pC, due to different charge ramping is different. The top row shows the directly measured screen image, while the bottom row depicts the reconstructed longitudinal bunch profile in each case.

A final measurement set was run with the TDS to demonstrate reshaping of the longitudinal beam profile during propagation through a dielectric wakefield structure and a chicane (see Section 8.1 for details). Figure 8.7 depicts the streaked images and their reconstructed longitudinal profiles with and without the inclusion of the dielectric waveguide. Note that the broad horizontal shape of the beam is induced during propagation through the chicane, where the electron

Sample	Ratio
no wakefield structure (100 pC)	(1.21 ± 0.10)
wakefield structure (100 pC)	(1.67 ± 0.14)
wakefield structure (50 pC)	(0.55 ± 0.06)

Table 8.3: Ratio between the front half and the back half of the measured beams. Each half is defined as the distance between the beam peak to the respective end of the beam.

beam may be entering off-axis or with an angle. As the reconstructed profiles show very clearly, when the beam passes through the dielectric waveguide and the mini-chicane, its longitudinal shape changes whereby the exact shape and direction of the ramping depends on the initial beam charge and bunch length in agreement with Eq. (8.1). As Table 8.3 proves, the effect can also be quantified by analysing the ratio of the two sections before and after the peak of the beam profile. This is an effect where not only the bunch length, but also the exact longitudinal beam shape needs to be observed thus proving the reconstruction of the profile to be very useful.

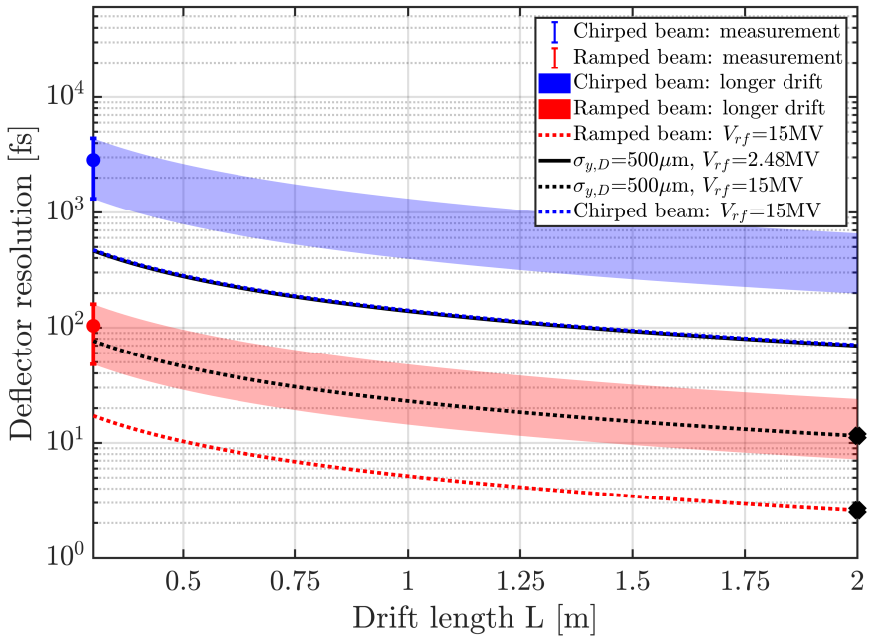

Figure 8.8: Expected deflector resolution for different deflecting voltages, transverse beam sizes at the deflector and drift lengths. The resolution estimates from two of the measurements are depicted with error bars as blue and red dots. The extrapolated optimised resolution values employed for reference in Fig. 8.14 are depicted as black crosses.

The temporal resolution of the TDS, as defined in Eq (7.6), can be translated into an

experimental estimate of the resolution at the imaging screen of

$$\Delta t_{exp,rf} = \frac{\sigma_{y,D}}{S_{rf} c k_{rf} R_{34}} , \tag{8.5}$$

where the factor $S_{rf} R_{34}$ corresponds to the gradient of the phase calibration curve in Fig. 8.3. In this first experimental run a variety of settings and beam sizes were investigated, so the measurements were taken with a range of resolutions. For the chirped and ramped beam measurements, discussed above, values of (2.85 ± 1.54) ps and (103.9 ± 55.9) fs were found, respectively, with the main difference between the two cases being the better focusing and collimation of the beam during propagation through the dielectric waveguide for the latter. While this is still very far from the desired sub-femtosecond regime, among others due to the short drift space and the large unstreaked beam size for the chirped beam case, Fig. 8.8 demonstrates that a significant improvement in resolution is, nonetheless, possible to the single femtosecond level, even with the ATF setup that is clearly not designed for ultrashort bunch length measurements. Increasing the deflecting voltage to its maximum of around 15 MV (based on 16 MW maximum input power), for example, improves the resolution by a factor of six, whereas better focusing of the beam and a longer drift length can further improve the deflector capabilities down to 2.6 fs. Finally, a more complex transport line to control the beam phase advance instead of a simple drift section, as assumed here, can lead to additional improvements, so that overall, the femtosecond limit may be reached after optimisation.

An additional limitation for the measurement of ultrashort bunches found in the experiment is the large deflector jitter estimated to vary between 547 fs to 2.77 ps, depending on the measurement settings. The cause of this fluctuation, measured through the variation of the beam centroid on-screen for different shots, is likely related to the deflecting cavity, although further tests will be necessary to determine whether the dominant jitter is in the RF amplitude or phase. The jitter from the linac and the electron gun, on the other hand, are believed to be comparably small, among others also as the collimation of the beam at the high-energy slit mitigates possible linac jitter effects. If the large deflector jitter cannot be stabilised in the future through technical improvements in the cavity power supply, any higher resolution measurements will require a large number of statistics to overcome this uncertainty. Especially for beams produced with novel, and usually less stable, accelerator techniques, this could prove to become a problem, if the shot-to-shot variation in the electron beam properties is large.

8.2.2 Combined Sub-Fs Diagnostic Measurement

Before starting full measurements with the sub-femtosecond diagnostic device, as shown in Fig. 8.2, the experimental setup was calibrated. Figure 8.9 depicts the calibration of the high

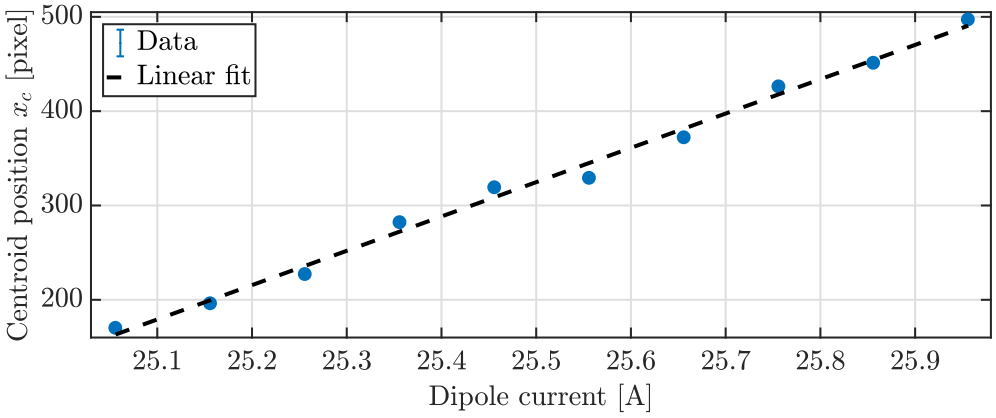

Figure 8.9: Energy calibration of the screen at the high energy slit in Beamline F. This measurement can be used to also calibrate the spectrometer screen, as a constant beam energy spread is assumed along the beamline without the laser modulator and RF deflector. An error of 0.5 pixel is assumed in the centroid position measurements.

energy slit and dipole spectrometer through a scan of the beam centroid position at the screen behind the slit for varying current of the dipole upstream (in beamline F, see Fig. 1.6). With a bending strength of 1.8 MeV A^{-1} of the dipole, the gradient of the linear fit can be translated into an energy resolution of (4.95 ± 0.01) keV/pixel and (0.850 ± 0.001) keV/pixel, respectively, for the high energy slit and spectrometer screens. Note that it is assumed that the energy spread remains constant during propagation from the slit to the spectrometer, which is reasonable if the RF deflector and laser modulator are turned off.

The fine tuning of the synchronisation between electron beam and CO_2-laser pulse was carried out by measuring the energy spread of the beam due to the inverse Free-Electron Laser interaction with the laser in the TEM_{00}-mode during a scan of the laser-electron beam delay, as described in Section 8.1. Figure 8.10 shows the results of the scan with the beam energy spread given as a function of laser-electron beam delay (top row) for two different measurement sets. A clear increase in spread is observed at delay settings between 7.25 and 7.75 mm which corresponds to the positioning of the delay stage producing the largest overlap between electron beam and laser in the undulator. As the bottom row of Fig. 8.10 shows, for this ideal delay setting (orange crosses), an increase in energy spread is observed with larger CO_2-laser energy, whereas for measurements away from the ideal delay (blue dots) the observed spread remains more or less constant and independent of the applied laser energy, as no interaction takes place.

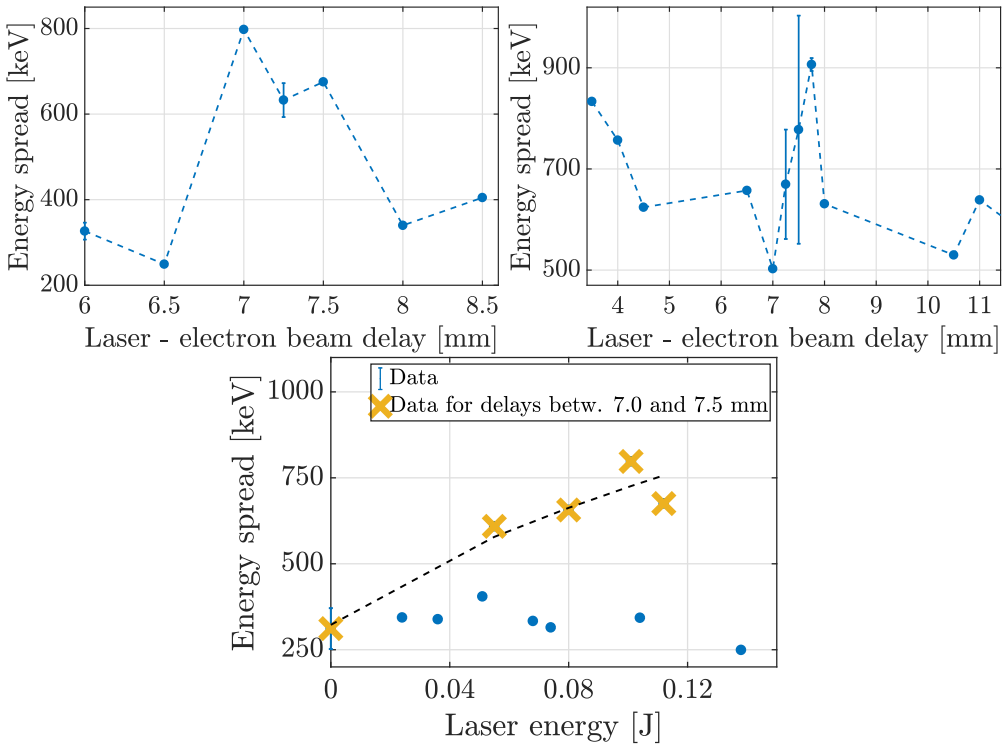

Figure 8.10: Fine-tuning of the laser-electron beam delay: the beam energy spread is measured at the spectrometer screen (IPOP8.5) for varying delay settings (top row) and laser energies (bottom row). The orange crosses in the bottom plot show the data points at delay settings with strong laser-beam interaction, whereas the blue dots depict all data points taken (with error bars, where possible).

The following measurements described in this section were thus taken at a delay setting of 7.25 to 7.5 mm. Note that the sub-picosecond scanning resolution used in these measurements was found to be sufficient for the setup, as both electron beam and laser pulse RMS lengths were on the order of picoseconds.

While the interaction with the TEM_{00}-mode induces an energy modulation in the electron beam, it does not lead to an angular spread of the beam. For the subsequent measurements, the TEM_{10}-mode was therefore employed in order to observe the actual streaking effect of the laser modulator. In Fig. 8.11 a few examples of how the laser modulator and RF-deflector influence the transverse beam distribution can be seen: in both rows the laser energy increases from left to right and an increase in the horizontal beam size is observed with two lobes forming in some cases. The difference in beam spread between the top and bottom row is caused by changes in the beam focusing through the transport line from undulator to imaging screen IPOP8, as the quadrupole strengths of the triplet behind the undulator were varied.

Figure 8.12 presents a more quantitative analysis of this effect. In all cases, the horizontal

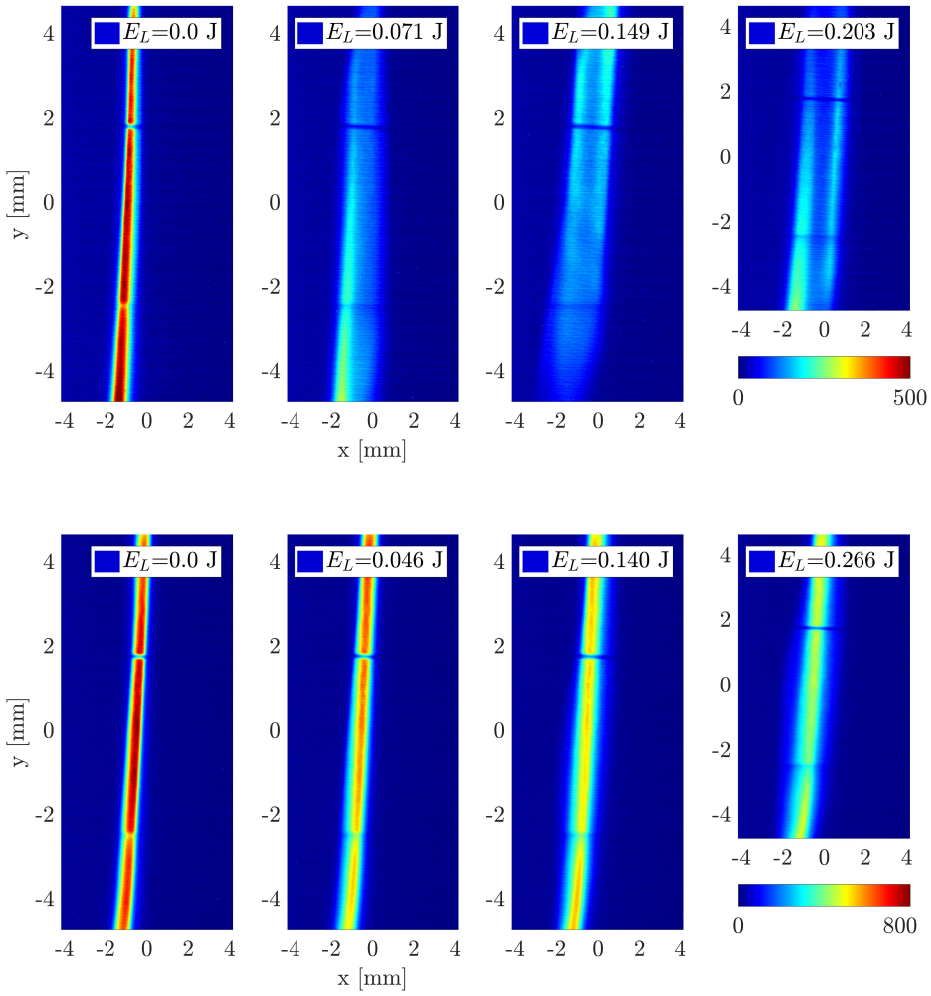

Figure 8.11: Streaked beam images at screen IPOP8 for different laser energies E_L (left to right) and varying focusing settings between the undulator and the imaging screen (top to bottom). Note that the focusing settings in the top and bottom row images correspond to quad settings 1 & 2, respectively, in Fig. 8.12. The colour bars describe the measured signal intensity in arbitrary units.

beam size is found to scale with the square-root of the laser energy in agreement with Eq. (7.16). Additionally, the gradient of the beam spread-laser energy relation can also be controlled via the quadrupole settings in the beamline between undulator and imaging screen. Based on a qualitative comparison with *elegant* simulations, as shown in Fig. 8.12c, this behaviour is directly related to the strength of the focusing of the electron beam after the undulator. With a strong focal point between the undulator and deflecting cavity (red lines), the modulation from the laser interaction is partially reversed and hence is not as clearly translated into the horizontal beam size as with a weaker focusing (blue lines). With a strong beam focus the

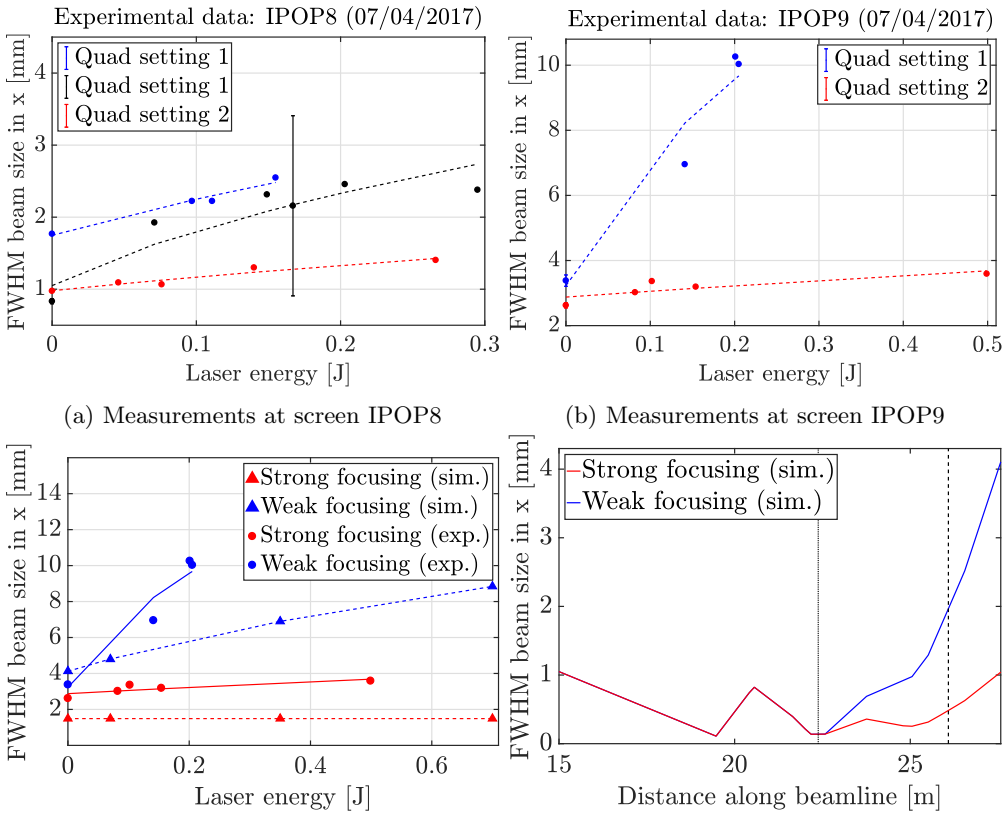

(a) Measurements at screen IPOP8

(b) Measurements at screen IPOP9

(c) Qualitative comparison with simulations

(d) Simulated beam size evolution in beamline

Figure 8.12: Horizontal beam size as a function of laser energy for different focusing settings between the undulator and imaging screen. Subplots (a) and (b) are measured at screens IPOP8 and IPOP9, respectively, whereas (c) is a qualitative comparison from simulations with *elegant* and measurements at IPOP9. (d) shows the respective evolution of the horizontal beam size in the simulations for the different focusing settings (without laser streaking). Note that in (d) the solid (dashed) line represents the position of the laser modulator (RF deflector) along the beamline.

effectiveness of the device is therefore reduced. Differences in the gradients shown for the simulation and measurement are caused by variations in the beamline and bunch properties considered in each case. Due to the length and complexity of the ATF beamline, the standard diagnostics installed are not sufficient to fully capture the experimental beam dynamics to reproduce in simulation. An approximate calculation of the beamline and beam development was thus used instead.

Despite the strong streaking effect in the horizontal direction, the characteristic sinusoidal streak pattern, as shown in Fig. 7.3 (bottom right-hand graph), cannot be clearly observed in these first measurements. There are oscillations in intensity observable in the transverse beam distribution (see Fig. 8.13a), but these may be caused by noise in the screen image measurement,

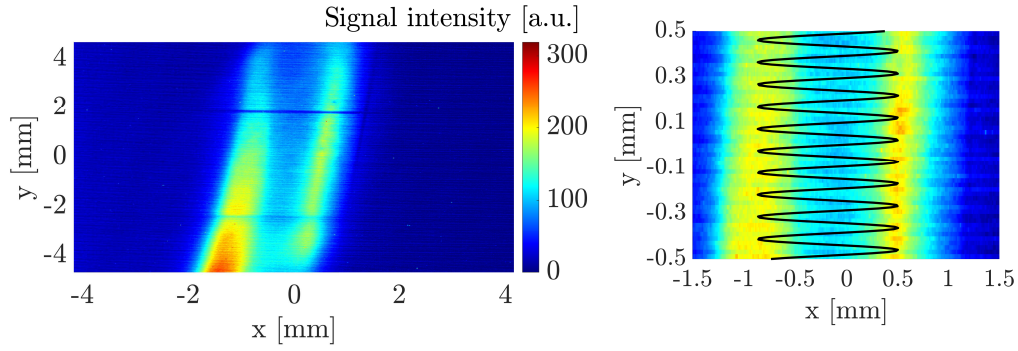

(a) Measured screen distribution (IPOP8)

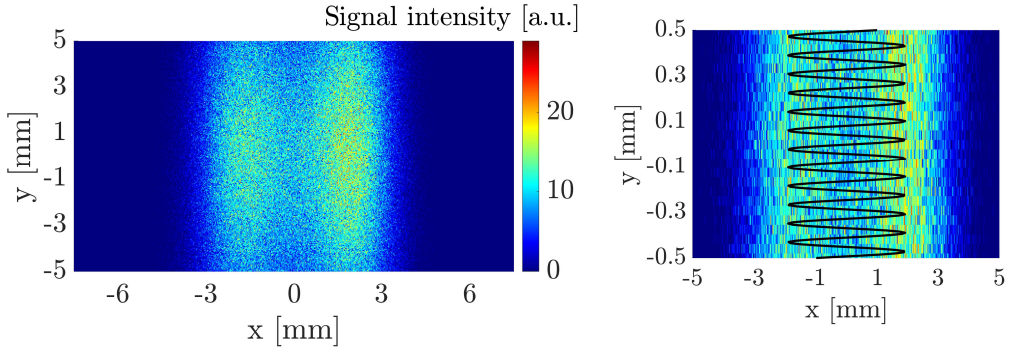

(b) Qualitatively comparable simulated screen distribution (IPOP8)

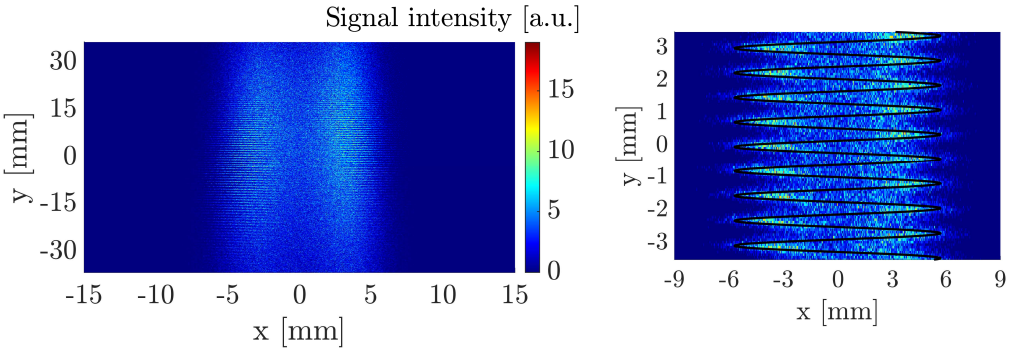

(c) Improved simulated screen distribution (IPOP9)

Figure 8.13: On-screen streaking pattern observed in (a) the experiment (at IPOP8), (b) a qualitatively comparable *elegant* simulation (at IPOP8), (c) an *elegant* simulation after improvement of deflector voltage and beam emittance (at IPOP9). For each case, the image on the right shows a zoom-in of the screen pattern with a sinusoidal curve overlaid.

as they are present also in the background signal and do not clearly coincide with the expected pattern period. Qualitative comparison simulations with *elegant* underpin this hypothesis, as they produce a similar pattern on the screen IPOP8, like depicted in Fig. 8.13b, with no distinguishable sinusoidal pattern in the vertical direction.

The lack of observable streaking pattern is found to be caused by two main factors: firstly, the resolution of the imaging screen is not sufficient to clearly resolve the intensity variations of the pattern. Assuming a deflecting voltage of (6 ± 3) MV - based on a measurement of the input power into the deflector klystron and a conservative error estimate of 50 %[1] - each period within the streaking pattern has a vertical size of (97.1 ± 48.5) µm. With a vertical screen resolution of 19.5 µm/pixel, this corresponds to approximately (4.98 ± 2.49) pixel across which each laser period is resolved. Taking into account that the pattern needs to pass between maximum and minimum intensity over this distance and that it has a finite width due to the intrinsic beam size, this resolution is likely not adequate and should be improved in the future. The second factor influencing the streaking pattern is the vertical intrinsic (i.e., unstreaked) beam size which is measured to be around 995 µm for the data set shown in Fig. 8.11 (top row). Unlike for a simple TDS setup, in this case this value needs to be smaller than the vertical streaked size of a single laser period, as it determines the spread in the vertical direction of the streak pattern. If this is not given, as in the measurement shown, the different turns of the sinusoidal signal partially overlap leading to a smearing out of the pattern.

Both of these issues can be mitigated by increasing the streaking voltage of the RF deflector, which is possible up to 15 MV for the ATF setup. Consequently, the full beam length would no longer be observable on the screen, however, the individual sinusoidal turns of the pattern would be streaked more strongly compared to the intrinsic beam size and spread over a larger number of pixels. Additional improvements can be achieved by decreasing the beam emittance and hence the intrinsic vertical beam size on-screen as well as by improving the measurement at the screen, e.g., through an increased camera zoom or use of a higher resolution screen. Figure 8.13c shows what effect such optimisations can have in the simulation scenario. While the image quality is artificially slightly limited by the number of simulation macroparticles used, the fine sinusoidal pattern can clearly be observed after the deflecting voltage has been doubled to 10 MV and the beam emittance has been reduced. A second upcoming experimental run at ATF is planned to test this strategy and fully resolve the streaking pattern of the diagnostic device.

Since the resolution of the diagnostic is determined by the effect of the laser modulator, an estimate for the experimentally measured images can be found in a similar way to that of the TDS as

$$\Delta t_{LM,exp} = \frac{\sigma_{x,D}}{S_{LM} c k R_{12}} \,. \tag{8.6}$$

[1] As the previous measurements with the X-band deflector had shown, it is difficult to determine the accuracy of the deflector voltage from power measurements due to unknown losses in the waveguides and possible amplitude jitter. Consequently, a large error is assumed here.

	measured (IPOP8)	**measured** (IPOP9)	**optimisation** 1 (IPOP9)	2	3
$\sigma_{x,D}$ [mm]	0.793	3.19	3.19	1.60	1.60
E_L (TEM_{00}) [J]	0.203	0.205	0.9	0.9	2.45
($S_{LM}\mathrm{R}_{12}$) [mm]	1.33	6.16	13.1	13.1	21.8
$\Delta t_{exp,LM}$ [fs]	3.27	2.83	1.34	0.668	0.401

Table 8.4: Measured experimental resolution in the horizontal direction at screens IPOP8 and IPOP9. Additionally, estimates of possible improved resolution values at IPOP9 through future optimisation of the beam line are listed using higher laser energy (opt. 1) and reduced electron beam spot sizes (opt. 2). Note that the last option (opt. 3) assumes that optical components with higher damage threshold than currently present are used in the mode conversion stage which allows for an even higher laser energy. The laser energy is given for the initial laser pulse before mode conversion; during conversion losses of about 50 % are expected.

While k as the laser wave number is known, $S_{LM}R_{12}$ and $\sigma_{x,D}$ can be measured from the horizontal signal spread with and without streaking, respectively.

Table 8.4 lists the estimated resolution for the data set discussed here both at screens IPOP8 and IPOP9 to be around 3 fs. With the on-screen beam size and laser energy varying throughout the full experimental run, these are just example values; they should, however, be quite representative for the entire measurement series. Considering that this first experiment was designed as a proof-of-concept without any efforts towards optimising the diagnostic device performance, the measured resolution is very promising and, as Table 8.4 also shows, leaves ample room for improvement. An increase of the laser energy to around 0.9 J (approximately 129 GW), for example, is expected to improve the temporal resolution to the single femtosecond level, while an additional reduction of the unstreaked beam size on the measurement screen through optimised beam transport will allow measurements down to the sub-femtosecond regime. The current setup at ATF is limited in laser energy at this point by the damage threshold of the beamsplitter in the mode conversion interferometer setup to below 1 J. If the setup could be improved, however, with more robust optical components, the terawatt-scale power of the CO_2-laser could be employed more effectively allowing to reach streaking resolutions on the order of 400 as with around 350 GW laser peak power.

8.3 Summary & Discussion

Part IV investigates two different longitudinal bunch profile diagnostic devices - an X-band deflecting cavity and a more complex sub-femtosecond diagnostic - theoretically as well as experimentally based on measurements at the Accelerator Test Facility (ATF) at Brookhaven National Laboratory. A reconstruction algorithm was developed to allow recovering the longi-

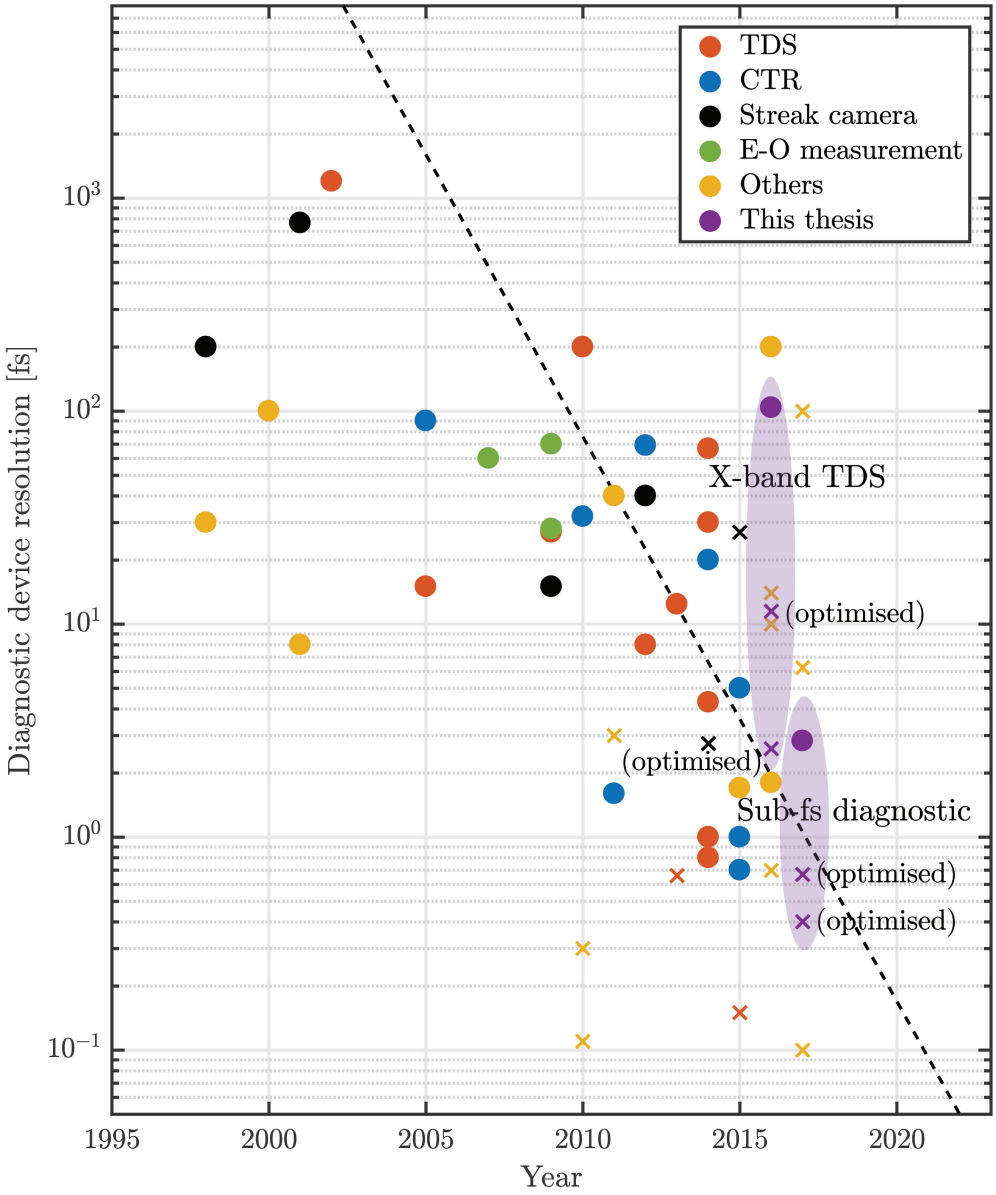

Figure 8.14: Comparison of measured and expected resolution from the two devices discussed in this part with measured (dots) and simulated (crosses) bunch length resolution values of different techniques described in the literature. A full list of the references used in the plot is given in Appendix D.

tudinal beam profile from a measurement, or as shown in example cases, from simulations of the diagnostic measurement with *elegant*. Applied in the following experiments, the X-band deflecting cavity was tested with regard to its diagnostic capability and stability with different example beams: the beam profile and duration were measured for a range of compressed electron bunches, microbunched beams and beams with a ramped longitudinal density profile, achieved

through interaction of the bunch with its wakefield inside a dielectric waveguide. While a resolution of, at best, (103.9 ± 55.9) fs was achieved, a main limitation in the measurement was found to be the large deflector jitter. It caused an uncertainty of almost 53 % in the deflecting voltage and leads to the requirement of a large number of measurements in order to reach statistically meaningful results. Nonetheless, an improvement in the resolution of the TDS is foreseen to the single femtosecond level assuming an increase in deflecting voltage, decrease in transverse beam size and longer transport beamline. For the experiment with the sub-fs diagnostic device the focus was on the observation of the horizontal laser streaking effect. Good control of the streaking strength through varying the laser energy and focusing settings between undulator and imaging screen was demonstrated. The full sinusoidal streaking pattern of the device was, however, not observed in the measurement. As comparisons with *elegant* simulations indicate, a limited screen resolution and large vertical beam size were the main causes and are planned to be improved in the next experimental run. The horizontal streaking resolution was estimated at around 3 fs; optimisations through an increase in laser energy, better beam focusing and improved beam transport promise possible resolutions down to 400 as in the future.

In theory both the RF deflector by itself and in combination with the laser modulator are capable of measuring bunch lengths with sub-femtosecond resolution, although the latter more complex device can provide superior resolution, among others, due to its reliance on micrometre-scale wavelengths instead of radio frequencies. In the experiment this enhanced resolution of the combined sub-femtosecond diagnostic was confirmed with an improvement in resolution by between one and three orders of magnitude, depending on the exact setup, compared to the RF deflector measurements. On the other hand, as this first run showed, the sub-femtosecond diagnostic setup is considerably more challenging to run due to its complexity. Its dependence on beam dynamics across a large propagation space, at least in a setup, such as at ATF, not specifically designed for the device, add to this. In both cases, the large jitter of the X-band TDS can play a significant role in the performance of the diagnostic, although this factor is considerably more important when using just the TDS for the measurement. Based on successful high-resolution experiments with X-band deflectors in the literature (e.g. [91]), however, it can be assumed that this jitter may generally be mitigated quite well.

Figure 8.14 places the results presented in this part in context with various experimental (dots) and simulation-based (crosses) reports found in the literature for alternative diagnostic techniques. A strong push towards single femtosecond resolution and below is observed from around 2010 onwards with first sub-femtosecond values experimentally achieved in 2014 and 2015 by use of an X-band deflecting cavity (TDS) and coherent transition radiation measure-

ment (CTR), respectively. It should be noted that the focus was placed on references with resolution in the range of hundreds of femtoseconds and below - hence the absence of picosecond techniques -, and the choice of references depicted here is not comprehensive due to the high number of publications on longitudinal bunch diagnostics in general.

Comparing the results from this thesis with other techniques, the reported measurement values cannot quite reach the current state-of-the-art in terms of temporal beam resolution yet. This is caused to a large extent by a lack of optimisation of the measurement setups presented here, an application of which could improve the experimental resolution considerably, as marked by the additional optimised data points for the X-band TDS and sub-fs diagnostic device. Further improvements are also expected if the beamline is designed more specifically for the diagnostic measurement, which at ATF is not the case, as seen, for example, by the long distances between the diagnostic components as well as the comparably large electron beams.

Nonetheless, the proposed optimised setups presented for the sub-femtosecond diagnostic do push at the boundary of what has currently been demonstrated experimentally. This is very promising, as most optimisation steps considered here are possible to implement into the existing ATF beamline and can thus likely be tested in the next experimental run. Unlike most other simulation results, they are also directly based on scaling the experimentally measured parameters through specific component improvements and hence still take into account many of the experimental limitations that may be neglected in pure simulations.

There are, however, a number of techniques promising equivalent or better resolution based on simulation results, such as [98, 99, 198, 199]. It should be noted that, besides [199] all of these proposed techniques have either larger space requirements (with e.g. [98] and [198] both requiring a chicane, TDS and transport line section) or more complex restrictions on its components (e.g. [99] requiring a short, terawatt-scale laser pulse in a specific transverse mode) than the sub-femtosecond diagnostic setup investigated here. Equally promising, novel techniques with attosecond-scale resolution also include streaking with plasma-based [93] or dielectric-based [94, 95] deflecting devices. While these are definitely more compact, they are also relatively complex techniques that have not been demonstrated experimentally at all yet and may come with additional restrictions regarding, for example, the acceptable charge and size of the electron beam.

In conclusion, the presented sub-femtosecond diagnostic is found to be particularly interesting for the measurement of electron beams of hundreds of attoseconds duration, as there are no experimentally proven techniques in this regime yet and the device can provide compact size based on conventional, well understood components. Additionally, if such beams are shorter in

full length than half of the laser wavelength, they may be streaked within a single laser period and hence do not require the second vertical streaking with the TDS - making the whole device smaller and more cost-efficient (see Section 9 for details). Another interesting application will be the study of long electron beams with fine sub-structures, such as microbunched beams [100]. Due to the beam trace being spread widely across the measurement screen, a large dynamic range can be provided superior to almost all other common bunch profile measurement techniques. In the regime of single femtosecond to sub-femtosecond bunch lengths, however, the diagnostic setup is found to be more complex than other better established techniques, among others due to the requirement of a high power CO_2-laser. For this regime the use of an X-band deflecting cavity by itself or a coherent transition radiation measurement setup are recommended instead. As shown in Chapter 8 as well as in the literature, these devices are definitely capable of reaching such a regime.

Chapter 9

Application to Ultrashort Beams

Both the previously published simulation-based studies [100, 200] and the experimental investigations of the sub-femtosecond longitudinal bunch profile diagnostic presented in Chapters 7 and 8 have so far focused on measuring comparably long electron beams of femtosecond to picosecond length, however, with a possibly fine intra-beam structure. In the following a first investigation of the application of the diagnostic device to ultrashort, sub-femtosecond beams is thus presented. To gain a better understanding of the experimental limitations of the measurement technique, a more general study into possible influences on the effective diagnostic resolution is included, before designs for a few example beams with ultrashort duration are discussed. In all cases the investigations are carried out by simulating the effect of the sub-femtosecond bunch length diagnostic on the electron beam with the particle-tracking code *elegant* from which a final transverse beam distribution, as would be measured in an experiment, is extracted and analysed using the reconstruction tool presented in Section 7.2. The beamline considered in *elegant* in this case is kept as simple and short as possible, containing, unless stated otherwise, only the laser modulator, a short drift space L_1, the RF deflecting cavity and a longer drift space L_2. The inclusion of further beamline components, such as focusing sections, may improve the presented results, yet goes beyond the scope of this thesis.

9.1 Factors Affecting Effective Resolution

The resolution estimate presented in Eq. (7.13) is based on the simple analytical theory of the sub-femtosecond diagnostic device discussed in Section 7.1. Yet in reality there are additional factors that influence the electron beam behaviour throughout the measurement device and hence the quality of the measured data. Three important factors to consider in this context

are discussed in the following: the initial electron beam emittance, energy spread and charge. This treatment hence still does not include factors, such as beam / instrument misalignments, device manufacturing errors and beam shape asymmetries, but allows for a more sophisticated estimation of the diagnostic suitability to realistic electron beams.

Laser power [GW]	50
Laser wavelength [μm]	10.3
Laser spot size [mm]	1.6
Undulator peak field [T]	0.67
Undulator period [cm], no. of periods	4.0, 10
RF deflector length [m]	0.46 (X-band)
RF deflecting voltage [MV]	12.0
Drift space lengths L_1, L_2 [m]	0.1, 1.4
Electron beam energy [MeV]	45.7
Beam β_{cs}-function in x,y [m]	9.77
Beam α_{cs}-function in x,y	0.0

Table 9.1: Parameters of the setup used in simulations to investigate the effect of electron beam emittance, energy spread and charge on the quality of the bunch profile reconstruction. Note that the properties of the RF deflecting cavity and the laser modulator are very similar to the actual device parameters at ATF (see Chapter 8).

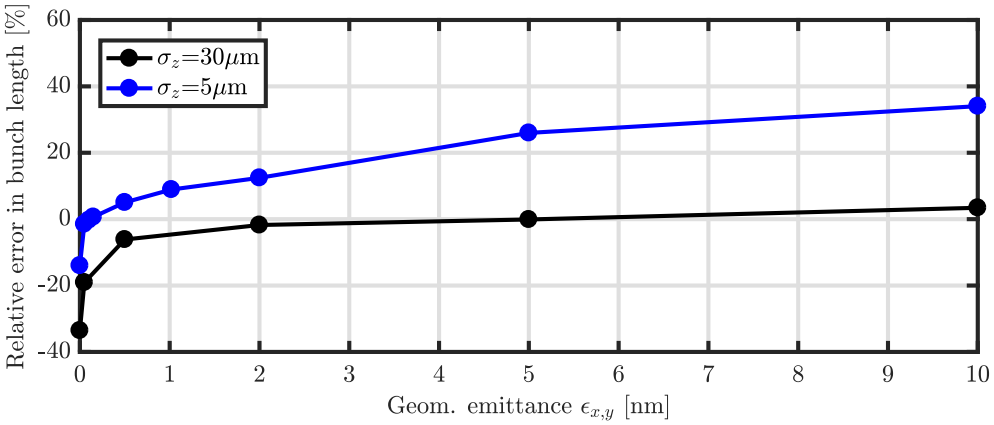

Figure 9.1: Dependence of the deviation of the reconstructed bunch length from the initial value on initial beam emittance for example bunches with relative energy spread of 0.1 % and RMS duration of 5 µm (blue) and 30 µm (black), respectively.

The effect of the beam emittance on the reconstructed bunch length accuracy is shown in Fig. 9.1 for test beams with mean energy 45.7 MeV, energy spread 0.1 %, $\alpha_{cs,x,y}$=0 and $\beta_{cs,x,y}$ of 9.77 m. The diagnostic setup parameters used in the simulation in this case are given in Table 9.1. It is found that generally a rise in emittance leads to a rise in error of the reconstructed electron bunch length, as would be expected also from the dependence of the theoretical resolution definition on the square-root of the emittance. The reason behind

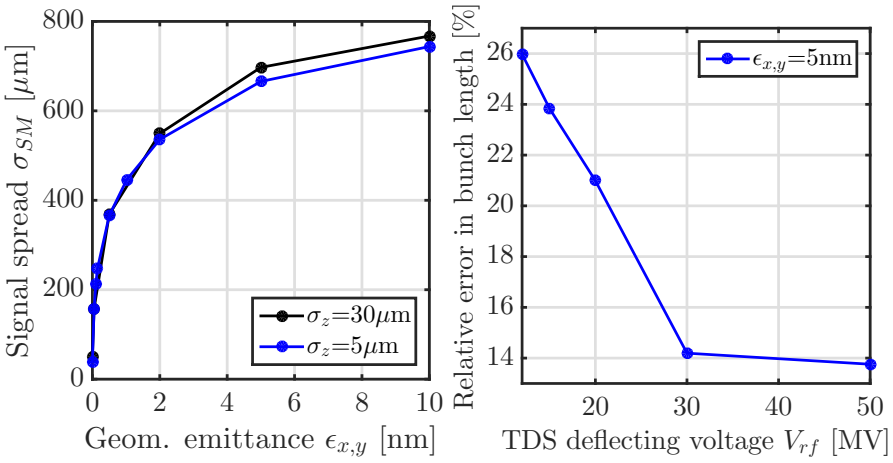

(a) Signal spread due to beam emittance (b) Reconstruction error vs. RF deflecting voltage

Figure 9.2: (a) Horizontal signal spread as a function of initial beam emittance: an increased spread in the signal due to a large emittance leads to the sinusoidal pattern being washed out and an increase in the error in reconstructed bunch length. (b) Dependence of reconstruction error on vertical streaking voltage for an example beam with 5 nm geometric emittance in x and y: this strategy can be used to compensate for the smearing of the screen signal due to a large emittance.

this is a washing-out effect of the sinusoidal screen profile the width of which depends on the intrinsic, i.e., unstreaked, electron beam size. If the latter becomes too large, due to an increased initial beam emittance and hence larger beam size and divergence, the different sections of the screen pattern start to overlap as the intrinsic transverse profile begins to dominate the screen signal over the translated longitudinal distribution; this makes the recovery of the longitudinal profile information more challenging. The effect can be quantified by investigating the average horizontal spread of the streaking signal along its most central turn, calculated as $\sigma_{SM} = \langle\sqrt{\frac{\sum_{i=1}^{M}(I_i(x_i-<x>)^2)}{\sum I_i - 1}}\rangle$ with I_i the signal intensity at each pixel. As the comparison in Fig. 9.2a shows, the beam spread follows a very similar trend to the bunch length error showing clearly its influence on the reconstruction quality. Note that the spread of the pattern in the vertical direction would behave equivalently, but is more difficult to calculate as soon as smearing out starts. For a very small emittance, an underestimation of the bunch length is observed which is particularly strong for the longer beam example. This is a consequence of the reconstruction algorithm fitting a perfect sinusoidal signal to the screen image which, however, can be slightly distorted due to higher order effects in the setup leading to mismatches between fit and screen signal. A larger emittance thus compensates for these mismatches which can be visible especially for longer beams where the misalignment adds cumulatively over multiple signal turns. The

overall higher error for shorter electron beams, which becomes even stronger than shown for bunch lengths below 1 µm, is likely not directly related to the emittance effect, as the signal spread is mostly independent of bunch length. Instead it may be a consequence of how the different beams are affected by the small, yet finite energy spread of the beam, which is discussed in more detail below.

Finally, an improvement in bunch length error by close to a factor of two is possible by increasing the streaking voltage, as seen in Fig. 9.2b, which separates the signal more clearly in the vertical direction to be distinguished better. At very large streaking voltages above 30 MV, however, the effect becomes less efficient as the beam starts to be distorted due to the strong forces in the TDS.

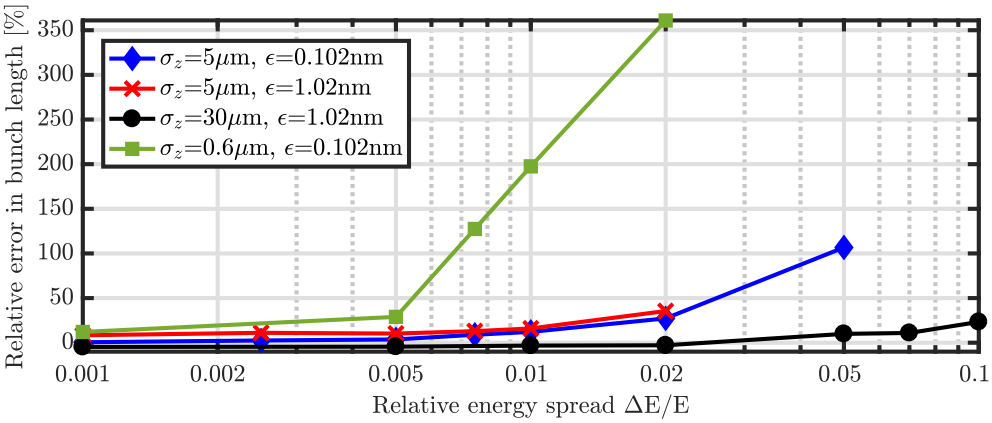

Figure 9.3: Dependence of the deviation of the reconstructed bunch length from the initial value on initial beam energy spread for example bunches with geometric emittance of 0.102 nm (blue, green) and 1.02 nm (black, red), respectively, as well as RMS duration of 0.6 µm (green), 5 µm (blue & red) and 30 µm (black).

With regard to the beam energy spread, the influence on the reconstruction accuracy is more bunch-length dependent, as Fig. 9.3 makes clear. The same parameters as for the emittance case were employed with a beam emittance defined as ϵ=0.102 nm or ϵ=1.02 nm, respectively. In this context two different effects play a role: on the one hand, the screen signal is washed out, similarly to the response to the transverse beam quality, as the streaking strength of both the laser modulator and the deflector depend on the beam energy and hence different parts of the beam are deflected slightly differently. This aspect can be seen again from the horizontal signal spread in Fig. 9.4a. It also shows clearly that the smearing due to energy spread becomes relevant only for $\Delta E/E \gtrsim 0.5\,\%$ and is generally not as strong as that due to beam emittance. The sudden drop in signal spread for the 30 µm beam above $\Delta E/E \sim 2\,\%$ is caused by increasing distortion of the streaking signal, likely due to the interaction of the high energy spread beam

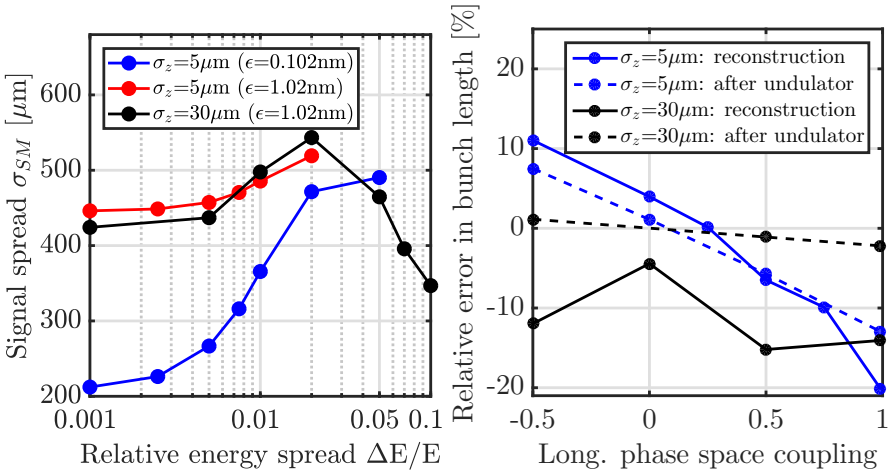

(a) Signal spread due to beam energy spread

(b) Reconstruction error vs. longitudinal phase-space coupling

Figure 9.4: (a) Horizontal signal spread as a function of initial beam energy spread: an increased spread in the signal due to a large energy spread leads to the sinusoidal pattern being washed out and an increase in the error in reconstructed bunch length. (b) Dependence of the reconstruction error on correlated energy spread: an error is observed for short beams due to bunch lengthening / compression in the undulator, while for long beams a mismatch in the signal wavelength is seen due to the strong variation in energy between beam head and tail.

with the laser modulator. The same occurs also for shorter beams, where the signal becomes so strongly changed that a reconstruction of the beam profile is no longer possible at all from energy spreads of 2 to 5 % upward.

Additionally to the signal smearing, the longitudinal bunch profile itself can also change during propagation through the diagnostic device, particularly through the laser modulator. This is a consequence of the energy dependence of the electron trajectories in the undulator leading to a correlation between bunch duration and energy spread as well as a change in bunch length described by [41]

$$\sigma_{zf} = \sqrt{(R_{56}\ \sigma_{\delta i,u})^2 + (1 - R_{56}\ C)^2 \sigma_{zi}^2}\,, \tag{9.1}$$

where σ_{zi}, σ_{zi} are the initial and final RMS bunch lengths, while $\sigma_{\delta i,u}$ and C are the initial uncorrelated energy spread and momentum chirp, respectively; $R_{56} = 2N_u\lambda$ is the momentum compaction factor of the undulator, i.e., the transfer matrix element describing the relation between the beam energy and longitudinal coordinate (more in Section 2.1). This effect is mostly relevant for short electron beams, as a significant bunch length change due to momentum compaction can already occur at low values of energy spread: for a beam of RMS length 0.6 µm, for example, an increase of the bunch length in the undulator by a factor $\sqrt{2}$ is expected at 0.3% uncorrelated energy spread, according to Eq. (9.1), whereas for a beam of RMS length

5 µm a similar stretching occurs for a spread of 2.4% with this example setup. A similar trend is also seen from simulations: for short beams on the order of a few micrometres, the error in reconstructed profile length increases much faster than for longer beams where the momentum compaction effect is negligible.

In Fig. 9.4b the effect of a momentum chirp or correlated energy spread - here described by the longitudinal phase-space coupling $\langle z\Delta E/E\rangle/(\sigma_z\sigma_{\Delta E/E})$ - on the bunch length reconstruction is shown: for the shorter beam example the error is closely matched by the change in bunch length measured just after the undulator, whereas for the longer beam the bunch length change is small, yet a comparably strong underestimation of the bunch length is observed for chirped beams. In the latter case, the energy chirp actually leads to a change in the screen signal shape and wavelength across the electron bunch, both due to their dependence on energy, such that a simple sinusoidal fit necessarily leads to a mismatch with the beam distribution in some parts of the screen image.

Finally, a less essential, but necessary point is the issue of the electron beam charge which has been studied here via the number of simulation macroparticles, as shown in Fig. 9.5 (same parameters as before, $\Delta E/E$=0.1 % and $\epsilon_{x,y}$=0.102 nm). A relatively large, wildly varying error on the order of a few percent was observed for small particle numbers, whereas at values above 1×10^6–2×10^6 the error stabilises close to zero. This is a consequence of noise arising and distorting the beam profile reconstruction if the screen signal is too weak. In an experiment the same would occur if the beam charge is small, especially since the bunch is streaked strongly across the entire measurement screen and hence small signal intensities may need to be measured at the monitors.

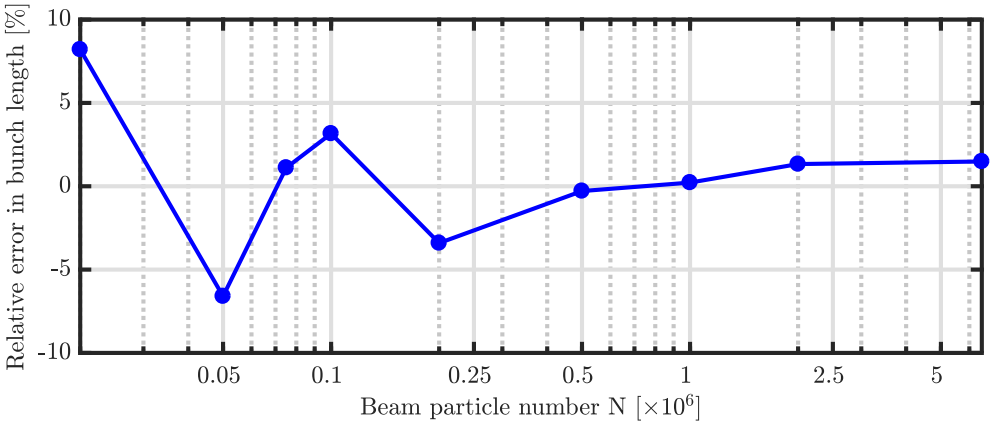

Figure 9.5: Dependence of the deviation of the reconstructed bunch length from the initial value on beam particle number for an example bunch with relative energy spread of 0.1 %, geometric emittance of 0.102 nm and RMS duration of 5 µm.

9.2 Ultrashort Beam Examples

In this section sub-femtosecond diagnostic setups for three example beams are tested and discussed. In each case the parameters for the laser modulator have been chosen to fulfill the resonance condition between the undulator, laser wavelength and electron energy (see Eq. (6.5)). Additionally, the required theoretical resolution for the beam application, based on Eq. (7.13) was a second criterion for the parameter choice. The use of an RF deflecting cavity is not necessary for electron beams with full duration of less than half the laser wavelength, as the entire bunch can be streaked within a single laser period; the inclusion of the X-band TDS with length 0.46 m and deflecting voltage 12 MV, as employed in the following cases for easier data processing, is thus optional.

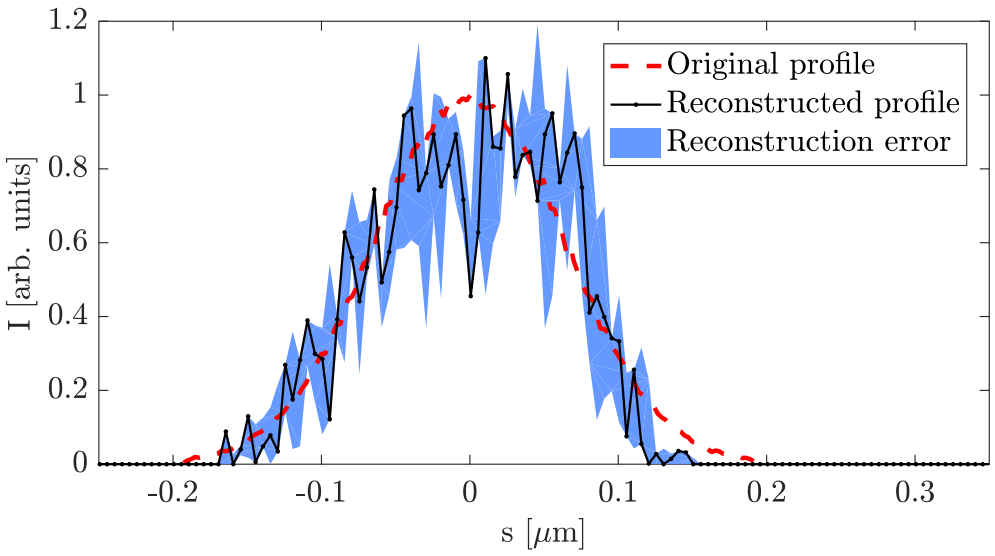

Figure 9.6: Reconstruction of an ultrashort electron beam as possibly achievable from the ARES linac at the SINBAD facility, based on simulation parameters by J. Zhu (see Table 9.2). The red dashed line shows the original longitudinal beam profile, while the black line depicts the reconstructed profile and the blue shaded area is the reconstruction error, estimated based on the uncertainty in the fitting coefficients of the reconstruction algorithm.

Table 9.2 shows the first example of an RF-accelerated and compressed electron beam with around 200 as RMS duration, as possibly achievable at the SINBAD facility at DESY (based on simulations by J. Zhu). Despite an expected resolution on the order of 1.48×10^{-8} m, it was found that the smearing of the screen signal due to energy spread and transverse beam properties leads to a significant error in the bunch reconstruction. By using a collimator (radius 50 µm) in front of the laser modulator, though, the transverse beam properties can be improved. The results of the bunch profile simulation with the collimator are shown in Fig. 9.6. The RMS

Laser power [GW]	350
Laser wavelength [μm]	10.3
Laser spot size [mm]	0.55
Undulator peak field [T]	1.354
Undulator period [cm], no. of periods	6.0, 3
Drift space lengths L_1, L_2 [m]	0.0, 1.0
Electron beam energy [MeV]	150.7 (0.25 % spread)
Momentum chirp [m^{-1}]	-19,165
Geom. emittance in x,y [nm]	0.72, 0.66
RMS duration [m]	6.32×10^{-8}
Theor. resolution [m]	1.48×10^{-8}
Recon. RMS duration [m]	6.03×10^{-8}
Recon. RMS duration (no collimator) [m]	1.08×10^{-7}
Recon. RMS duration (only TDS) [m]	1.22×10^{-7}

Table 9.2: Parameters of the setup, electron beam as well as reconstructed beam properties for the SINBAD example case.

beam length in this case can be recovered with an error of less than 4.6 % improving upon the error from reconstruction with the deflecting cavity alone by a factor of around 20. It should be noted, however, that due to the presence of the collimator slit a large fraction of the initial beam charge of 2.8 pC, in this specific case about 91 %, is lost. This leaves the remaining charge to be measured in the hundreds of femtocoulomb regime hence requiring a high sensitivity, high resolution imaging screen.

Laser power [GW]	50–100
Laser wavelength [μm]	10.3
Laser spot size [mm]	1.0
Undulator peak field [T]	0.43
Undulator period [cm], no. of periods	1.5, 3
Drift space lengths L_1, L_2 [m]	0.0, 1.0–1.5
Electron beam energy [MeV]	15.0 (1.63 % spread)
Momentum chirp [m^{-1}]	0
Geometric emittance in x,y [nm]	11, 11
RMS duration [m]	2.75×10^{-7}
Theor. resolution (P_L=50 GW, 100 GW) [m]	1.51×10^{-7}, 1.07×10^{-7}
Recon. RMS duration (50 µm-radius collimator, P_L=100 GW, L_2=1.5 m) [m]	3.38×10^{-7}
Recon. RMS duration (50 µm-radius collimator, P_L=50 GW, L_2=1.0 m) [m]	6.23×10^{-7}
Recon. RMS duration (100 µm-radius collimator, P_L=50 GW) [m]	8.91×10^{-7}
Recon. RMS duration (100 µm-radius collimator, only TDS, 15 MV) [m]	4.68×10^{-7}

Table 9.3: Parameters of the setup, electron beam as well as reconstructed beam properties for the AXSIS example case.

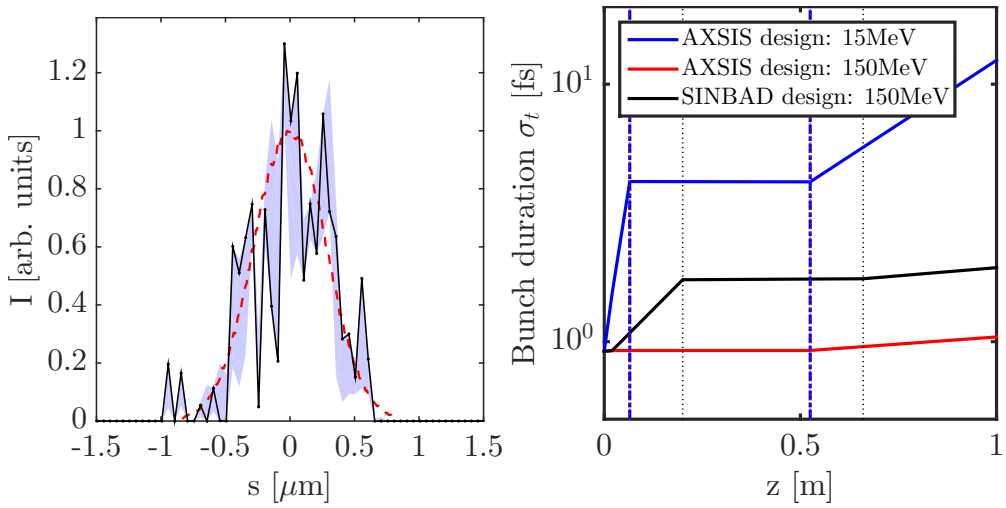

(a) Longitudinal profile reconstruction

(b) Change in beam duration during measurement

Figure 9.7: Reconstruction of a short electron beam as possibly achievable from the AXSIS project. Here, a particular working point by T. Vinatier has been tested based on Table 9.3. The red dashed line shows the original longitudinal beam profile, while the black line depicts the reconstructed profile and the lilac shaded area is the reconstruction error, estimated based on the uncertainty in the fitting coefficients of the reconstruction algorithm. In (b) the change in bunch length throughout the diagnostic line is compared with beams of higher energy where the red line denotes the same setup as the example case, but with higher energy, while for the black line the undulator and laser parameters have been taken from the SINBAD example beam design to allow for matching of the electron energy with the laser modulator, yet at equivalent theoretical streaking strength as for the blue line.

Another interesting case to investigate is that of an example beam expected from the AXSIS project, also based at DESY (see Section 1.3). The beam parameters, as shown in Table 9.3 together with a possible setup design, are based on simulations by T. Vinatier of a hybrid accelerator setup where a conventional S-band electron gun delivers a beam that is consequently accelerated in a THz-structure [201]. This setup, rather than an all-THz-based working point was chosen, as it predicts to-date particularly short electron beam lengths. The reconstruction in this case does not work quite as well as with the RF-accelerated beam, in large parts due to the comparably large energy spread and transverse size of the bunch. While a lower laser power of 100 GW can be employed due to the longer bunch length, the use of a 50 µm-radius collimator is essential here, as the comparison with the reconstruction with a 100 µm-radius collimator shows in Table 9.3. This, however, leaves a signal of only 1.9 % of the initial beam charge to reach the imaging screen likely making an experimental detection of the streaked beam challenging. In the reconstructed beam profile, shown in Fig. 9.7a, this is represented via the small remaining simulation macroparticle number by strong noise in the recovered signal.

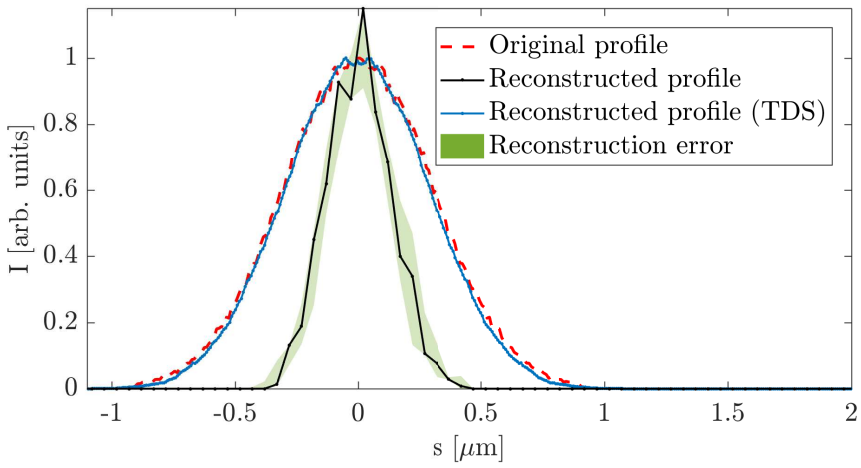

Figure 9.8: Reconstruction of a short electron beam as possibly achievable from laser wakefield accelerators. These beams are typically dominated by a correlated energy spread which is taken here to be 1 % (see Table 9.4). While the red dashed line shows the original longitudinal beam profile, the black and blue lines depict the reconstructed profile with the combined diagnostic device and just a TDS, respectively. The green shaded area shows the reconstruction error for the profile from the combined diagnostic, estimated based on the uncertainty in the fitting coefficients of the reconstruction algorithm.

The RMS bunch length can be reconstructed with an error of around 23 %; a significant factor leading to this comparatively large error in this context is the beam lengthening in the undulator, as can be observed in Fig. 9.7b. The low beam energy of only 15 MeV plays a significant role here, as the bunch length evolution can be controlled much better for higher energy beams, even e.g. with a setup with a longer undulator length and stronger undulator K-value, like the SINBAD example beam design, as shown in the plot. Nonetheless, the achievable result predicts an improvement over using a TDS alone with a reduction of the error by a factor of approximately three.

Finally, as a last example a plasma-accelerated electron beam is considered with characteristic parameters shown in Table 9.4 and the reconstructed profile given in Fig. 9.8. An energy chirp of approximately 1 % over the 1 fs RMS duration was assumed, yet, as can be seen by the reconstructed bunch length this already has a significant effect on the diagnostic capability. As described in more detail in the previous section, the momentum chirp leads to a compression of the electron beam in the undulator hence distorting the final result measured on the screen. Considering that the assumed energy chirp is comparatively small for plasma-accelerated electron beams, this constitutes a significant problem for their measurement. Possible solutions could be a further reduction of the undulator length to minimise the momentum compaction

Laser power [GW]	100
Laser wavelength [μm]	10.3
Laser spot size [mm]	0.55
Undulator peak field [T]	1.354
Undulator period [cm], no. of periods	6.0, 3
Drift space lengths L_1, L_2 [m]	0.0, 1.5
Electron beam energy [MeV]	150.7 (0.5 % spread)
Momentum chirp [m^{-1}]	-33,333 (1 % across bunch length)
Geometric emittance in x,y [nm]	3.4, 3.4
RMS duration [m]	3.0×10^{-7}
Theor. resolution [m]	1.31×10^{-7}
Recon. RMS duration [m]	1.31×10^{-7}
Recon. RMS duration (only TDS, 12 MV) [m]	2.88×10^{-7}

Table 9.4: Parameters of the setup, electron beam as well as reconstructed beam properties for the plasma-accelerated example case.

effect or a tapering of the undulator in order to compensate for the chirp. Both of these options, however, require further study going beyond the scope of the thesis. At the single femtosecond level, an RF deflecting cavity alone may provide a suitable alternative, which for the example provided e.g. can recover the beam RMS length with an error of around 4 % at a deflecting voltage of 12 MV. Note that in this case, too, a collimator was used to control the transverse beam properties. Based on a small assumed transverse beam size of 100 µm, which allows the transmission of 11.3 % of charge, and a typically large overall beam charge on the order of tens to hundreds of picocoulombs, the resolution of the beam signal on a final imaging screen should not be a major challenge in this case.

9.3 Discussion of Limitations

There is a number of effects and possibilities that have not been considered yet in this initial study. One option for such ultrashort electron beams could be the use of a modulation laser with shorter wavelength, as only half a laser period needs to be resolved and so the distance between laser periods - directly related to the distance between the pattern turns on the measured screen signal - is not relevant at the sub-femtosecond level. Employing for example a Ti-Sapphire laser with 800 nm wavelength could allow the use of considerably higher laser power at the terawatt level and hence better resolution, yet only for beams of less than 400 nm full length, as extremely strong RF deflecting strength is otherwise required to resolve multiple vertical screen signal turns.

In terms of the simulations presented, a few simplifications have been made: first of all space-

charge forces have not been taken into account in the simulations with *elegant*. Considering that in all examples the beam charge was significantly reduced due to beam collimation at the beginning of the diagnostic device, though, this should, while it will still need to be studied, not limit the validity of the presented results. Additionally, all simulations presented here assumed ideal theoretical parameters for the screen signal wavelength and amplitude in order to reconstruct the longitudinal profiles, as no clear sinusoidal signal is observable from the streaked ultrashort beam itself. In an experiment this would likely not be possible for two reasons: first, the laser and beamline parameters may not be measurable with every shot in enough detail to calculate ideal fitting parameters, and second, there may be additional factors, such as beam misalignments, that influence the effective signal shape and amplitude in unpredictable ways. Another point to consider in future studies will thus be a more realistic estimation of the signal fitting parameters which could be e.g. achieved experimentally by calibrating the streaking amplitude to laser power relation with a longer test electron beam that covers multiple laser periods and hence allows for a better sinusoidal fit.

Additionally, the experimental feasibility of the very compact setups assumed in this study, with no spacing between the collimator, undulator and deflecting cavity, needs to be assessed. Larger distances between the components may lead to the beam evolving hence building up errors in the measured profile with respect to the initial beam distribution, even for measurements with the TDS alone.

Finally, another challenge for the application of the diagnostic device to ultrashort beams is the phase dependence. For multi-femtosecond bunches, the exact laser phase that the beam experiences is irrelevant as it simply determines the start and end position of the beam along the sinusoidal signal with a fraction of the streaked beam always distributed over the linear, high-resolution section of the sine-signal. For beams that cover only a fraction of the laser wavelength, however, the phase position strongly influences the effective resolution of the measurement. Some level of phase control may be possible for schemes where the electron beam is generated with laser-based methods, like LWFA, such that synchronisation between this drive laser and the streaking laser can be achieved. A precise laser-electron beam synchronisation is nonetheless challenging and will need to be addressed in the future. Overall, the application of this sub-fs diagnostic device thus provides an interesting test bed for the bunch length measurement of ultrashort beams with both opportunities and challenges to be investigated further in the future.

Part V

Summary and Outlook

Theoretical and experimental studies on the generation, acceleration and measurement of attosecond electron beams are presented in this thesis. The generation and acceleration of ultrashort bunches is investigated for laser wakefield-accelerated beams with two specific methods examined and contrasted. First, employing a self-injection scheme where the wavebreaking and hence trapping point of electrons is controlled via a plasma density upramp, two- and three-dimensional particle-in-cell simulations predict a plasma injector generating electron beams with RMS duration of ∼200 attoseconds, charges on the order of sub-nanocoulombs and 5D beam brightness at the level of $1 \times 10^{18}\,\mathrm{A\,m^{-2}\,rad^{-2}}$. Due to the high density of both witness beam and background plasma, with the latter required to reach a few percent of the critical density, the dynamics in the plasma are extremely nonlinear and evolving quickly over tens of femtoseconds. Following depletion of the drive laser and electron beamloading, the witness beam acceleration is not stable after a few hundred micrometres propagation and deteriorates, yet beam extraction is possible and can preserve the short bunch duration despite charge and beam quality loss. The underlying mechanisms of the scheme are also found to be quite stable with regard to various factors, such as density fluctuations, density ramp shape and plasma temperature.

In the second scheme investigated in this thesis, an RF-accelerated, sub-femtosecond electron beam with charge at the picocoulomb level and high beam quality is externally injected into a low density plasma for energy boosting to hundreds of megaelectronvolts to gigaelectronvolts. Strategies to preserve the electron beam characteristics are investigated in the form of plasma density matching ramps for emittance conservation and controlled beamloading for energy spread minimisation. These successfully demonstrate the tunability of the scheme, but also show possible mitigation of emittance and energy spread growth to below 0.25 µm and 0.2 %, respectively, for a plasma target of length 4.75 cm as well as 1 µm and 0.45 %, respectively, for acceleration over 11.5 cm, with the latter limited by the computational methods employed. In all cases, the ultrashort bunch length is conserved within 11 % or less of its initial value hence allowing for 6D beam brightness values up to $6.5 \times 10^{15}\,\mathrm{A/m^2/rad^2/(0.1\%\ \Delta E/E)}$ comparable to current Free-Electron Laser facilities. Covering two very different, yet complementary regimes in terms of their properties, electron beams from both methods were, based on simple scaling laws, found to be not very suitable for application in Free-Electron Lasers, but interesting as potential sources for generating radiation from Thomson scattering in the X-ray to γ-ray range producing 1×10^4–5×10^8 photons per pulse. This direction may be investigated in more detail in the future.

In the context of high-resolution longitudinal beam profile measurements, a novel sub-

femtosecond resolution diagnostic device - working through combined streaking with a laser modulator and an RF deflecting cavity - as well as an X-band deflecting cavity (TDS) alone were studied theoretically and experimentally at Brookhaven National Laboratory. The TDS is characterised with a range of test beams demonstrating 104 fs resolution with possible optimisation to the single femtosecond level, while a considerable jitter in the deflection amplitude is identified as a main challenge and drawback. For the more complex and novel design, a first proof-of-concept experiment demonstrates the capability of the technique for streaking using a laser modulator achieving unoptimised resolution of 3 fs. Both estimations for the existing experimental setup and simulated designs for other sub-femtosecond example beams, using a bunch length reconstruction tool developed as part of this thesis, predict possibly improved resolutions to the few hundred attosecond level. In this case, electron beam emittance and energy spread are the biggest challenges to accurate measurements, which is found to be manageable for RF-accelerated beams, but becomes critical for electron bunches from novel accelerators, such as THz- and plasma-driven devices. The presented sub-femtosecond bunch length diagnostic could thus open up short bunch regimes not reachable with common techniques, like RF deflecting cavities, etc. For beams at the single femtosecond to sub-femtosecond level, however, the more conventional methods may yet be more suitable due to their reduced complexity.

Overall, the main problem of working with attosecond electron beams, with regard to their generation, acceleration as well as measurement, is determined to be beam stability and quality. On the one hand, this is caused, as is to be expected, by space-charge forces. In an external injection scheme, as the one discussed, these restrict the minimum achievable beam duration and place a strong limitation on the bunch current for beams from conventional accelerators, which are most suitable sources due to their reliable beam quality. At the same time, in the presented self-injection method they make beam transport inside and outside of the plasma challenging. In view of reaching towards the single attosecond and sub-attosecond level, this trend will be even more dominant with the stably transportable charge most likely the limiting factor for ultrashort electron beam acceleration. Radiation generation in this regime may thus become more viable based on other mechanisms than the direct generation from electron beams of equally small duration, as focused on in this thesis.

Yet, besides self-fields, the electron beam quality also plays an essential role in the handling of attosecond beams, in particular for plasma-based schemes where this characteristic is a well-known issue. This constitutes the largest challenge for the proposed sub-femtosecond longitudinal bunch diagnostic, but also for the presented self-injection scheme the intrinsic instability of the plasma setup is one of the main causes to compromise the beam. While for

the latter this issue may, among others, be improved by employing a different mechanism to control the wavebreaking process, that is not dependent on high plasma density, more generally miniaturisation is another strategy to mitigate this stability challenge. In the self-injection scenario this has been realised by keeping the plasma target short and extracting the electron beam already after a few hundred micrometres. Similarly, for the bunch length diagnostic a compact device with a short laser modulator section and little spacing between the different machine components is found to reduce the beam evolution during analysis, hence allowing for better control over the measurement.

A possible next step to better understand the acceleration and measurement techniques investigated in this thesis will be the design of first experiments. For upramp-assisted self-injection tests at SCAPA or other plasma acceleration facilities with similar short-pulse, multi-hundred-terawatt laser systems may be feasible. In contrast, for an external injection experiment with sub-femtosecond electron bunches the ARES linac at SINBAD is currently the only suitable machine to achieve the required small beam durations. Moreover, for both experiments, a major issue will also be the availability of a suitable, high-resolution bunch length diagnostic to detect the expected ultrashort beams; while a high-resolution deflecting cavity or coherent transition radiation measurements could be acceptable options, this will require further more detailed investigation.

For the sub-femtosecond longitudinal bunch profile measurement more experiments are planned to demonstrate the full diagnostic capabilities of the device. Due to the required deflecting cavity and high power CO_2-laser, however, ATF is one of the only facilities worldwide where this is possible. Alternatively, studies using streaking with just a laser modulator based on a more easily available Ti-Sapphire laser could also be interesting, yet this would require a stable source of accelerated sub-femtosecond electron pulses not yet existing. This close relation between generation and diagnostics hence also represents one of the main challenges for the study of attosecond electron pulses as a topic pushing the boundaries of currently achievable technology.

Appendix A

Derivation of the Weakly Nonlinear Wakefield Model Described in Section 3.2.3

The following describes the calculation steps taken to derive Eq. (3.27) from Eq. (3.26) with the Poincaré-Lindstedt perturbation method:

Normalising $k_p\xi$, the following expansions are made:

$$\phi = \epsilon\phi_1 + \epsilon^2\phi_2 + \epsilon^3\phi_3 + \epsilon^4\phi_4 \dots , \tag{A.1}$$

$$k = 1 + \epsilon k_1 + \epsilon^2 k_2 + \epsilon^3 k_3 \dots , \tag{A.2}$$

where k is defined via $\eta = k\xi$, $\partial/\partial\xi = k\partial/\partial\eta$ and $\partial^2/\partial\xi^2 = k^2\partial^2/\partial\eta^2$. Eq. (3.26) is rewritten in the following based on this expansion: the second partial derivative is expanded as

$$\begin{aligned}
\frac{\partial^2\phi}{\partial\xi^2} &= k^2\frac{\partial^2}{\partial\eta^2}\Big[\epsilon\phi_1 + \epsilon^2\phi_2 + \epsilon^3\phi_3 + \epsilon^4\phi_4\Big] \\
&= \epsilon\frac{\partial^2\phi_1}{\partial\eta^2} + \epsilon^2\Big(\frac{\partial^2\phi_2}{\partial\eta^2} + 2k_1\frac{\partial^2\phi_1}{\partial\eta^2}\Big) + \epsilon^3\Big(\frac{\partial^2\phi_3}{\partial\eta^2} + 2k_1\frac{\partial^2\phi_2}{\partial\eta^2} + 2k_2\frac{\partial^2\phi_1}{\partial\eta^2} + k_1^2\frac{\partial^2\phi_1}{\partial\eta^2}\Big) \\
&\quad \epsilon^4\Big(2k_1\frac{\partial^2\phi_3}{\partial\eta^2} + 2k_2\frac{\partial^2\phi_2}{\partial\eta^2} + k_1^2\frac{\partial^2\phi_2}{\partial\eta^2} + 2k_3\frac{\partial^2\phi_1}{\partial\eta^2} + 2k_1k_2\frac{\partial^2\phi_1}{\partial\eta^2} + \frac{\partial^2\phi_4}{\partial\eta^2}\Big) ,
\end{aligned} \tag{A.3}$$

where all terms with order higher than four for ϵ have been neglected. Equivalently, powers of

ϕ are re-written as

$$\begin{aligned}\phi^2 &= \epsilon^2\phi_1^2 + 2\epsilon^3\phi_1\phi_2 + \epsilon^4(2\phi_1\phi_3 + \phi_2^2)\,, &\text{(A.4)}\\ \phi^3 &= \epsilon^3\phi_1^3 + 3\epsilon^4\phi_1^2\phi_2\,, &\text{(A.5)}\\ \phi^4 &= \epsilon^4\phi_4\,, &\text{(A.6)}\end{aligned}$$

again with all ϵ-terms above fourth order ignored.

This re-defines Eq. (3.26) in the form

$$\begin{aligned}\epsilon\frac{\partial^2\phi_1}{\partial\eta^2}\epsilon^2\Big(\frac{\partial^2\phi_2}{\partial\eta^2} &+ 2k_1\frac{\partial^2\phi_1}{\partial\eta^2}\Big) + \epsilon^3\Big(\frac{\partial^2\phi_3}{\partial\eta^2} + 2k_1\frac{\partial^2\phi_2}{\partial\eta^2} + 2k_2\frac{\partial^2\phi_1}{\partial\eta^2} + k_1^2\frac{\partial^2\phi_1}{\partial\eta^2}\Big)\\ &+ \epsilon^4\Big(2k_1\frac{\partial^2\phi_3}{\partial\eta^2} + 2k_2\frac{\partial^2\phi_2}{\partial\eta^2} + k_1^2\frac{\partial^2\phi_2}{\partial\eta^2} + 2k_3\frac{\partial^2\phi_1}{\partial\eta^2} + 2k_1k_2\frac{\partial^2\phi_1}{\partial\eta^2} + \frac{\partial^2\phi_4}{\partial\eta^2}\Big)\\ &+ \epsilon\phi_1 + \epsilon^2\phi_2 + \epsilon^3\phi_3 + \epsilon^4\phi_4 - \frac{3}{2}\epsilon^2\phi_1^2 - 3\epsilon^3\phi_1\phi_2 - 3\epsilon^4\phi_1\phi_3 - \frac{3}{2}\epsilon^4\phi_2^2\\ &+ 2\epsilon^3\phi_1^3 + 6\epsilon^4\phi_1^2\phi_2 - \frac{5}{2}\epsilon^4\phi_4 = 0\,. \qquad\text{(A.7)}\end{aligned}$$

Sorting these terms with respect to $\epsilon, \epsilon^2, \epsilon^3$ and ϵ^4, the equation can be solved by setting each part of the sum to zero:

$$\begin{aligned}O(\epsilon) &: \frac{\partial^2\phi_1}{\partial\eta^2} + \phi_1 = 0\,, &\text{(A.8)}\\ O(\epsilon^2) &: \frac{\partial^2\phi_2}{\partial\eta^2} + 2k_1\frac{\partial^2\phi_1}{\partial\eta^2} + \phi_2 - \frac{3}{2}\phi_1^2 = 0\,, &\text{(A.9)}\\ O(\epsilon^3) &: \frac{\partial^2\phi_3}{\partial\eta^2} + 2k_1\frac{\partial^2\phi_2}{\partial\eta^2} + 2k_2\frac{\partial^2\phi_1}{\partial\eta^2} + k_1^2\frac{\partial^2\phi_1}{\partial\eta^2} + \phi_3 - 3\phi_1\phi_2 + 2\phi_1^3 = 0\,, &\text{(A.10)}\\ O(\epsilon^4) &: 2k_1\frac{\partial^2\phi_3}{\partial\eta^2} + 2k_2\frac{\partial^2\phi_2}{\partial\eta^2} + k_1^2\frac{\partial^2\phi_2}{\partial\eta^2} + 2k_3\frac{\partial^2\phi_1}{\partial\eta^2} + 2k_1k_2\frac{\partial^2\phi_1}{\partial\eta^2}\frac{\partial^2\phi_4}{\partial\eta^2} + \phi_4\\ &\quad -3\phi_1\phi_3 - \frac{3}{2}\phi_2^2 + 6\phi_1^2\phi_2 - \frac{5}{2}\phi_1^4 = 0\,. &\text{(A.11)}\end{aligned}$$

Eq. (A.8) can be solved as a simple harmonic oscillator equation:

$$\phi_1 = A_1\cos(\eta) + B_1\sin(\eta) = a_1 cos(\eta + \eta_0)\,. \qquad\text{(A.12)}$$

Eq. (A.9) can then be solved with the substitution $\frac{\partial^2\phi_1}{\partial\eta^2} = -\phi_1$ (Eq. (A.8)):

$$\begin{aligned}\frac{\partial^2\phi_2}{\partial\eta^2} + \phi_2 &= \frac{3}{2}\phi_1^2 + 2k_1\phi_1\\ &= \frac{3}{4}a_1^2 + \frac{3}{4}a_1^2 cos(2\eta + 2\eta_0) + 2k_1a_1\cos(\eta + \eta_0)\,, &\text{(A.13)}\end{aligned}$$

employing the trigonometric identity $\cos^2(\theta) = 1/2(1+\cos(2\theta))$. This is a second order, linear, nonhomogeneous differential equation with the solution

$$\phi_2 = a_2\cos(\eta+\eta_0) + \frac{3}{4}a_1^2 - \frac{1}{4}a_1^2\cos(2\eta+2\eta_0) \tag{A.14}$$

with $k_1 = 0$.

Similarly, Eq. (A.10) is re-written with the substitution $\frac{\partial^2\phi_1}{\partial\eta^2} = -\phi_1$ (Eq. (A.8)):

$$\begin{aligned}\frac{\partial^2\phi_3}{\partial\eta^2} + \phi_3 &= 2k_2\phi_1 + 3\phi_1\phi_2 - 2\phi_1^3 \\ &= \left[2k_2a_1 + \frac{3}{8}a_1^3\right]\cos(\eta+\eta_0) - \frac{7}{8}a_1^3\cos(3\eta+3\eta_0)\,,\end{aligned} \tag{A.15}$$

employing the trigonometric identities $\cos^3(\theta) = 1/4\cos(3\theta) + 3/4cos(\theta)$, $\cos(\theta)\cos(2\theta) = 2\cos^3(\theta) - \cos(\theta) = 1/2(\cos(3\theta)+\cos(\theta))$ and assuming $a_2 = 0$.

Taking $k_2 = -\frac{3}{16}a_1^2$ and $a_3 = 0$, the following solution is found

$$\phi_3 = \frac{7}{64}a_1^3\cos(3\eta+3\eta_0)\,. \tag{A.16}$$

Finally, Eq. (A.11) is re-written, with $\frac{\partial^2\phi_1}{\partial\eta^2} = -\phi_1$ (Eq. (A.8)) and $\frac{\partial^2\phi_2}{\partial\eta^2} = \frac{3}{2}\phi_1^2 - \phi_2$ ((Eq. (A.9)), as

$$\begin{aligned}\frac{\partial^2\phi_4}{\partial\eta^2} + \phi_4 &= -3k_2\phi_1^2 + 2k_2\phi_2 + 2k_3\phi_1 + 3\phi_1\phi_3 + \frac{3}{2}\phi_2^2 - 6\phi_1^2\phi_2 + \frac{5}{2}\phi_1^4 \\ &= \frac{1}{8}a_1^4 + 2k_3a_1\cos(\eta+\eta_0) - \frac{13}{128}a_1^4\cos(2\eta+2\eta_0) \\ &+ \frac{115}{128}a_1^4\cos(4\eta+4\eta_0)\,,\end{aligned} \tag{A.17}$$

employing the trigonometric identities listed above as well as $\cos^4(\theta) = 1/8\cos(4\theta) + 1/2\cos^2(\theta) - 1/8$ and $\cos(\theta)\cos(3\theta) = 1/2\cos(4\theta) - \cos^2(\theta) - 1/2$. This gives

$$\phi_4 = \frac{1}{8}a_1^4 + \frac{13}{512}a_1^4\cos(2\eta+2\eta_0) - \frac{23}{384}a_1^4\cos(4\eta+4\eta_0)\,, \tag{A.18}$$

where $k_3 = 0$.

The scalar potential and longitudinal electric field to order $\mathrm{O}(\epsilon^4)$ are hence given by (taking

$\epsilon = 1$):

$$\begin{aligned}
\phi &= a_1 \cos(\eta + \eta_0) + \frac{3}{4} a_1^2 - \frac{1}{4} a_1^2 \cos(2\eta + 2\eta_0) + \frac{7}{64} a_1^3 \cos(3\eta + 3\eta_0) \\
&+ \frac{1}{8} a_1^4 + \frac{13}{512} a_1^4 \cos(2\eta + 2\eta_0) - \frac{23}{384} a_1^4 \cos(4\eta + 4\eta_0)\,, \qquad \text{(A.19)} \\
\frac{E_z}{E_0} &= -\frac{\partial \phi}{\partial \xi} = -k \frac{\partial \phi}{\partial \eta} \\
&= k a_1 \sin(\eta + \eta_0) + (\frac{13}{256} a_1^4 - \frac{1}{2} a_1^2) k \sin(2\eta + 2\eta_0) \\
&+ \frac{21}{64} k a_1^3 \sin(3\eta + 3\eta_0) - \frac{23}{96} a_1^4 \sin(4\eta + 4\eta_0) \qquad \text{(A.20)}
\end{aligned}$$

with $k = b_1 = 1 - 3/16 a_1^2$ and $\eta = b_1 k_p \xi$. Note that k was renamed here for the main part of the thesis to avoid confusion with the laser wavenumber $k = 2\pi/\lambda$.

Appendix B

Realistic Density Ramp Profiles

For a more realistic estimate of the shape of a plasma density up- and downramp, a scalable ramp shape based on a piecewise polynomial fit to a hydrodynamically simulated plasma target was employed for many of the simulations presented in this thesis. Fig. B.1 depicts the original profile along the centre of the target simulated in OpenFOAM in 2D for a gas cell (courtesy of C. Thornton, Oxford University). Additionally, as red dashed lines the fitted ramps are shown based on the following models for the up- and downramp, respectively:

$$n_{upramp}(z) = \begin{cases} a_1 z + a_2, & \text{for } A_1 \leq z < A_2 \\ a_3 z + a_4, & \text{for } A_2 \leq z < A_3 \\ a_5 z^2 + a_6 z + a_7, & \text{for } A_3 \leq z < A_4 \\ a_8 z^2 + a_9 z + a_{10}, & \text{for } A_4 \leq z < A_5 \\ a_{11} z^3 + a_{12} z^2 + a_{13} z + a_{14}, & \text{for } A_5 \leq z < A_6 \\ a_{15} z + a_{16}, & \text{for } A_6 \leq z < A_7 \end{cases} \tag{B.1}$$

$$n_{downramp}(z) = \begin{cases} b_1 z^3 + b_2 z^2 + b_3 z + b_4, & \text{for } B_1 \leq z < B_2 \\ b_5 z^2 + b_6 z + b_7, & \text{for } B_2 \leq z < B_3 \\ b_8 z^3 + b_9 z^2 + b_{10} z + b_{11}, & \text{for } B_3 \leq z < B_4 \\ b_{12} z^2 + b_{13} z + b_{14}, & \text{for } B_4 \leq z < B_5 \end{cases} \tag{B.2}$$

The model is scalable to vary the plateau density as well as start and end of the ramps, so the size of the pieces of the functions ($A_1 - A_7$, $B_1 - B_5$) are defined through these values together with the relative size of the different profile sections based on the original data. The

co-efficients in the model, $a_1 - a_{16}$ and $b_1 - b_{14}$, on the other hand, are found from the fit. It should be noted that this simple scaling of the profile density and length is not as easy to achieve in an experimental setting where the exact plasma ramp shape depends strongly on the detailed plasma target design. However, this strategy does provide an improvement over employing a simple, idealised ramp shape and can thus be seen as a possible first step towards the design of an experiment.

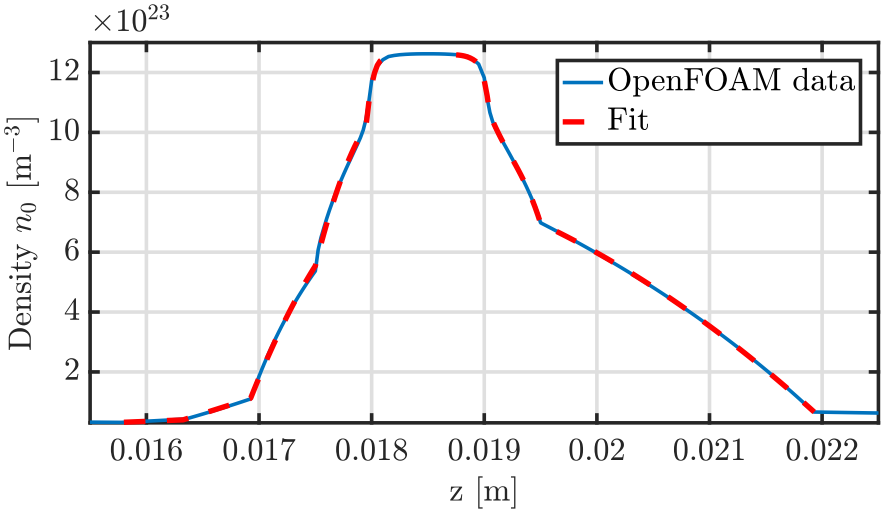

Figure B.1: Plasma target density profile simulated with OpenFOAM (C. Thornton) (solid line) together with a piecewise polynomial fit of the up- and downramp (dashed lines) to be used for particle-in-cell simulations of a realistic plasma ramp shape.

Appendix C

Details on Particle-in-Cell Simulations

Chapter 4: An Attosecond LWFA-Injector

Chapter 4.1 (3D)	
spatial resolution in z, x and y	15.2 nm×137 nm×137 nm
moving window size in z, x and y	30.4 µm×96.1 µm×96.1 µm
particle number per cell	1
Chapter 4.2 (1D)	
spatial resolution in z	5.0 nm
staionary window size in z	145 µm – 265 µm
particle number per cell	30
Chapter 4.2 (3D)	
spatial resolution in z, x and y	16.4 nm×157 nm×157 nm
moving window size in z, x and y	22.9 µm×110 µm×110 µm
particle number per cell	8
Chapter 4.3 (2D)	
spatial resolution in z and x	4.98 nm×49.8 nm
moving window size in z and x	14.7 µm×153 µm
particle number per cell	4
Chapter 4.4 (2D)	
spatial resolution in z and x	(9.1 nm – 9.3 nm) × (92 nm – 369 nm)
moving window size in z and x	(22.5 µm – 23.0 µm) × (137.5 µm – 184.3 µm)

particle number per cell	16

Table C.1: Input parameters for the OSIRIS simulations presented in Chapter 4.

Chapter 5: Energy Boosting of an Externally Injected Electron Bunch in LWFA

Chapter 5.1 (2D)	
upramp length R_{up}	100 µm
laser focal plane position z_{foc}	at the end of the upramp
spatial resolution in z and x	(23.7 nm – 25.7 nm) × (0.49 µm – 1.1 µm)
moving window size in z and x	(1 – 1.9)×λ_p in z, (425 µm – 690 µm) in x
particle number per cell	plasma: 1, beam: 1-2
field solver	Yee
Chapter 5.2 (2D)	
upramp length R_{up}	matched cases / space-charge studies: 0.0 m ramp length studies: (3.0 mm – 20 mm) ramp shape studies: 7.5 mm
laser focal plane position z_{foc}	guided cases: at the end of the upramp unguided cases: at the centre of the plasma stage
spatial resolution in z and x	(19.9 nm – 23.2 nm) × (0.10 µm – 0.96 µm)
moving window size in z and x	134.4 µm× (437 µm – 1008 µm)
particle number per cell	plasma: 1-4, beam: 2-32
field solver	Lehe (except where specified)
Chapter 5.3 (2D)	
upramp length R_{up}	100 µm
laser focal plane position z_{foc}	209 µm[1]
spatial resolution in z and x	(12.7 nm – 25.1 nm) × 1.1 µm
moving window size in z and x	109 µm× 504 µm
particle number per cell	plasma: 1-2, beam: 2
field solver	Yee
Chapter 5.4 (2D)	

[1] with the exception of the case with an optimised focal plane position, here z_{foc}=8.21 mm

upramp length R_{up}	0.0 m
laser focal plane position z_{foc}	134 µm
spatial resolution in z and x	19.9 nm × 0.98 µm
moving window size in z and x	134 µm× 504 µm
particle number per cell	plasma: 4-8, beam: 16-32
field solver	Lehe, Yee
Chapter 5.5 (2D)	
upramp length R_{up}	4.3 mm
laser focal plane position z_{foc}	7.6 mm
spatial resolution in z and x	25.0 nm × 0.99 µm
moving window size in z and x	134 µm× 504 µm
particle number per cell	plasma: 2, beam: 16
field solver	Lehe
Chapter 5.6 (2D)	
Working point WP1	
spatial resolution in z and x	19.9 nm × 0.96 µm
moving window size in z and x	134 µm × 504 µm
particle number per cell	plasma: 4, beam: 32
field solver	Lehe
Working point WP2	
spatial resolution in z and x	12.4 nm × 0.93 µm
moving window size in z and x	134 µm × 504 µm
particle number per cell	plasma: 2, beam: 64
field solver	Lehe
Working point WP3	
spatial resolution in z and x	19.5 nm × 0.99 µm
moving window size in z and x	134 µm × 756 µm
particle number per cell	plasma: 2, beam: 32-64
field solver	Lehe, Yee
Chapter 5.6 (3D)	
spatial resolution in z, x and y	22.9 nm × 1.43 µm × 1.43 µm
moving window size in z, x and y	126 µm × 504 µm × 504 µm
particle number per cell	plasma: 1, beam: distribution from ASTRA code

field solver	Lehe

Table C.2: Input parameters for the OSIRIS simulations in Chapter 5.

Appendix D

Reference List for Figures 6.1-6.3 and 8.14

Stupakov et al. (2001) [202]	Naumova et al. (2004) [63]
Ma et al. (2006) [60]	Kulagin et al. (2007) [62]
Sears et al. (2008) [55]	Liseykina et al. (2010) [59]
Buck et al. (2011) [73]	Lundh et al. (2011) [72]
Andreev et al. (2011) [78]	Floettmann et al. (2014) [188]
Di Lucchio et al. (2015) [58]	Heigoldt et al. (2015) [74]
Islam et al. (2015) [30]	Hu et al. (2015) [64]
Couperus et al. (2017) [203]	Daoud et al. (2017) [204]
Tooley et al. (2017) [32]	Zhu et al. (2017) [41]

Table D.1: Publications included in the comparison in Figs. 6.1, 6.2 and 6.3. The charge values refer to the full beam in the case of methods to produce single attosecond bunches, while for techniques for attosecond bunch train generation they describe the charge of the full bunch train. A Gaussian beam shape has been assumed to convert bunch lengths from FWHM (full width at half maximum) to RMS values. In cases where multiple values for similar conditions were provided the graphs show their average.

RF-TDS	**Streak camera**
Akre et al. (2002) [190]	Uesaka et al. (1998) [205]
Huening et al. (2005) [206]	Graves et al. (2001) [82]
Roehrs et al. (2009) [89]	Fruehling et al. (2009) [83]
Li et al. (2010) [207]	Grguras et al. (2012) [84]
Behrens et al. (2012) [88]	Fabianska et al. (2014) [86]
Craievich et al. (2013) [90]	Dehler et al. (2015) [85]
Dolgashev et al. (2014) [92]	**Other methods**
Behrens et al. (2014) [91]	Wang et al. (1998) (zero-phasing) [97]
Marchetti et al. (2015) [199]	Ricci et al. (2000) (zero-phasing) [208]
CTR measurement	Graves et al. (2001) (zero-phasing) [82]
Muggli et al. (2005) [209]	Huang et al. (2010) (zero-phasing) [98]
Lundh et al. (2011) [72]	Xiang et al. (2010) (phase-space mapping) [198]
Debus et al. (2010) [147]	Xiang et al. (2011) (phase-space mapping) [102]
Behrens et al. (2012) [88]	Ding et al. (2011) (phase-space mapping) [101]
Nozawa et al. (2014) [210]	Kotaki et al. (2015) (LWFA-based) [103]
Nozawa et al. (2015) [87]	Bettoni et al. (2016) (wakefield streaking) [96]
Heigoldt et al. (2015) [74]	Zhang et al. (2016) (LWFA-based) [104]
Islam et al. (2015) [30]	Dornmair et al. (2016) (plasma-TDS) [93]
E-0 detection	Jamison et al. (2016) (THz-TDS) [94]
Berden et al. (2007) [80]	Purwar et al. (2017) (three-phase method) [105]
Loos et al. (2009) [211]	Vinatier et al. (2017) (three-phase method) [106]
Steffen et al. (2009) [81]	Zhang et al. (2017) (phase-space mapping) [99]

Table D.2: Publications included in the comparison in Fig. 8.14. If provided, the device resolution value is included, otherwise the minimum measured bunch duration is used. Note that in cases where multiple values for different similar conditions were given the graph shows their average.

List of Figures

List of Tables

List of Frequently Used Acronyms

as	attosecond ($1\,\mathrm{as}=1\times10^{-18}\,\mathrm{s}$)
ATF	Accelerator Test Facility, located at Brookhaven National Laboratory (see Section 1.4)
AXSIS	Frontiers in Attosecond X-ray Science: Imaging and Spectroscopy; part of the SINBAD project at DESY (see Section 1.3)
CPR	chirped pulse amplification (see Section 3.1)
CTR	coherent transition radiation (see Section 2.4.2)
DESY	Deutsches Elektronensynchrotron, located in Hamburg, Germany
elegant	a 3D particle-tracking code [191]
EuXFEL	European X-ray Free-Electron Laser, located in Hamburg, Germany
FACET	Facility for Advanced Accelerator Experimental Tests, located at the SLAC National Accelerator Laboratory
FEL	Free-Electron Laser (see Sections 1.1 and 6.3)
fs	femtosecond ($1\,\mathrm{fs}=1\times10^{-15}\,\mathrm{s}$)
FWHM	full width at half maximum
GeV	gigaelectronvolt ($1\,\mathrm{GeV}\sim1.6\times10^{-10}\,\mathrm{J}$)
HHG	high-harmonic generation (see Part I)
ICS	inverse Compton scattering (see Sections 1.1 and 6.3)
LWFA	laser-wakefield acceleration
OSIRIS	a particle-in-cell simulation code [139]

pC	picocoulomb ($1\,\mathrm{pC}=1\times10^{-12}\,\mathrm{C}$)
PIC	particle-in-cell; a type of simulation code for plasma physics (see Section 3.5)
ps	picosecond ($1\,\mathrm{ps}=1\times10^{-12}\,\mathrm{s}$)
PWFA	plasma wakefield acceleration, referring to beam-driven wakefield acceleration
RF	radio-frequency
RMS	root mean square
SASE	self-amplified spontaneous emission; a specific FEL mode (see Section 1.1)
SCAPA	Scottish Centre for the Application of Plasma-based Accelerators, located in Glasgow, UK
SINBAD	Short INnovative Bunches and Accelerators at DESY; accelerator R&D facility located at DESY
TDS	transverse deflecting structure (see Section 2.4.2 and Part IV)
TEM-mode	transverse electromagnetic mode (see Section 3.1)
XUV	extreme ultraviolet

List of Frequently Used Symbols

$\mathbf{A}$	vector potential [$\mathrm{V\,s\,m^{-1}}$]
$\mathbf{a}$, a_0	normalised vector potential $\mathbf{a} = e\mathbf{A}/(mc^2)$ and its amplitude
$\mathbf{B}$	magnetic field [T]
c	speed of light in vacuum, c =299 792 458 $\mathrm{m\,s^{-1}}$
$\mathbf{E}$	electric field [$\mathrm{V\,m^{-1}}$]
$E,\ \sigma_E,\ \Delta E/E$	electron energy [eV], RMS energy spread [eV] and relative RMS energy spread [%]
e	absolute electron charge (unit charge), $e \sim\ 1.602 \times 10^{-19}\,\mathrm{C}$
E_0	cold, non-relativistic wavebreaking field, $E_0 = mc\omega_p/e$ [$\mathrm{V\,m^{-1}}$]
$\mathbf{F}$	force [N]
$I_b,\ I_{b,peak}$	full beam current, peak beam current [A]
K	focusing strength of a focusing channel [$\mathrm{m^{-2}}$] (see Section 2.3)
$K_{sc},\ K_{sc,L}$	generalised and longitudinal perveance (see Chapter 2)
$L_d,\ L_{pd}$	dephasing and depletion length [m] (see Section 3.4)
$L,\ L_{rms},\ L_{FWHM}$	laser full length, RMS length and FWHM length [m]
m	electron rest mass, $m \sim\ 9.11 \times 10^{-31}\,\mathrm{kg}$
$n,\ n_0$	plasma number density, plasma background number density [$\mathrm{m^{-3}}$]
n_c	critical plasma density [$\mathrm{m^{-3}}$] (see Section 3.2)
$\mathbf{p} = (p_z, p_x, p_y)$	particle momentum [eV/c]

$Q,\ \lambda_Q,\ \sigma_Q$	beam charge [C], 2D charge density [$\mathrm{C\,m^{-1}}$] and 1D charge density [$\mathrm{C\,m^{-2}}$]
R	plasma density ramp length [m]
$\mathbf{u}$	normalised particle momentum, $\mathbf{u} = \mathbf{p}/(mc)$
w, w_0	transverse laser spot size, spot size at the focus [m]
x', y'	particle divergence in the horizontal and vertical direction [rad]
$z,\ r,\ \theta$	position coordinates (in cylindrical coordinate system) [m,m,rad]
$z,\ x,\ y$	position coordinates (in Cartesian coordinate system) [m]
$\alpha_{cs},\ \beta_{cs},\ \gamma_{cs}$	Twiss (or Courant-Snyder) parameters [-,m,$\mathrm{m^{-1}}$]
$\boldsymbol{\beta}$	relative velocity (normalised by c)
$\beta_p,\ \beta_{gr},\ \beta_m$	relative phase velocity, group velocity and maximum electron velocity
$\beta_{cs,m},\ \sigma_m$	matched Twiss beta-function and matched transverse RMS beam size [m]
γ	Lorentz factor $\gamma = 1/\sqrt{1-(\boldsymbol{\beta})^2}$
ϵ_0	vacuum permittivity, $\epsilon_0 \sim\ 8.854 \times 10^{-12}\,\mathrm{F\,m^{-1}}$
$\epsilon_n,\ \epsilon$	normalised and geometric phase-space emittance [m rad]
$\epsilon_{tr,n},\ \epsilon_{tr}$	normalised and geometric trace-space emittance [m rad]
$\lambda,\ \lambda_p,\ \lambda_{rf}$	wavelength [m], in particular the laser, plasma and RF wavelength; related to the wave number through $k = 2\pi/\lambda$
ξ	co-moving variable, $\xi = z - ct$ [m]
Φ	scalar potential [V]
ϕ	normalised scalar potential, $\phi = e\Phi/(mc^2)$
$\omega,\ \omega_p,\ \omega_{rf}$	angular frequency [rad], in particular the laser, plasma wave and RF frequencies

Bibliography

1. Corde, S. *et al.* Femtosecond X Rays from Laser-Plasma Accelerators. *Rev. Mod. Phys.* **85,** 1–48 (2013).
2. Zewail, A. H. 4D Ultrafast Electron Diffraction, Crystallography, and Microscopy. *Annu. Rev. Phys. Chem.* **57,** 65–103 (2006).
3. Dunning, D. J., McNeil, B. W. & Thompson, N. R. Towards Zeptosecond-Scale Pulses from X-Ray Free-Electron Lasers. *Phys. Procedia* **52,** 62–67 (2014).
4. Krausz, F. & Ivanov, M. Attosecond Physics. *Rev. Mod. Phys.* **81,** 163–234 (2009).
5. Itatani, J. *et al.* Tomographic Imaging of Molecular Orbitals. *Nature* **432,** 867–871 (2004).
6. Uiberacker, M. *et al.* Attosecond Real-Time Observation of Electron Tunnelling in Atoms. *Nature* **446,** 627–632 (2007).
7. Kärtner, F. X. *et al.* AXSIS: Exploring the Frontiers in Attosecond X-Ray Science, Imaging and Spectroscopy. *Nucl. Instruments Methods Phys. Res. Sect. A Accel. Spectrometers, Detect. Assoc. Equip.* **829,** 24–29 (2016).
8. Wu, H. C., Meyer-ter Vehn, J., Fernández, J. & Hegelich, B. M. Uniform Laser-Driven Relativistic Electron Layer for Coherent Thomson Scattering. *Phys. Rev. Lett.* **104,** 234801 (2010).
9. Poulin, J. *Progress in the Generation of Attosecond Pulses and Coherent X-Rays* tech. rep. (Ecole Polytechnique de Montreal, Montreal, Canada, 2008).
10. Jochmann, A. *et al.* High Resolution Energy-Angle Correlation Measurement of Hard X Rays from Laser-Thomson Backscattering. *Phys. Rev. Lett.* **111,** 114803 (2013).
11. MacArthur, J. P., Duris, J., Huang, Z. & Marinelli, A. *High Power Sub-Femtosecond X-Ray Pulse Study for the LCLS* in *Proc. IPAC 2017* (Copenhagen, Denmark, 2017), 2848–2850 (WEPAB118).

12. Rosenzweig, J. B. *et al.* Generation of Ultra-Short, High Brightness Electron Beams for Single-Spike SASE FEL Operation. *Nucl. Instruments Methods Phys. Res. Sect. A Accel. Spectrometers, Detect. Assoc. Equip.* **593,** 39–44 (2008).

13. Zholents, A. A. & Zolotorev, M. S. Attosecond X-Ray Pulses Produced by Ultra Short Transverse Slicing via Laser Electron Beam Interaction. *New J. Phys.* **10,** 025005 (2008).

14. Saldin, E. L., Schneidmiller, E. A. & Yurkov, M. V. Self-Amplified Spontaneous Emission FEL with Energy-Chirped Electron Beam and its Application for Generation of Attosecond X-Ray Pulses. *Phys. Rev. Spec. Top. - Accel. Beams* **9,** 050702 (2006).

15. Emma, P. *Issues and Challenges for Short Pulse Radiation Production* in *Proc. EPAC 2004* (Lucerne, Switzerland, 2004), 225–229 (THYCH01).

16. Wheeler, J. A. *et al.* Attosecond Lighthouses from Plasma Mirrors. *Nat. Photonics* **6,** 829–833 (2012).

17. Ma, W. J. *et al.* Bright Subcycle Extreme Ultraviolet Bursts from a Single Dense Relativistic Electron Sheet. *Phys. Rev. Lett.* **113,** 235002 (2014).

18. Naumova, N. M., Nees, J. A., Sokolov, I. V., Hou, B. & Mourou, G. A. Relativistic Generation of Isolated Attosecond Pulses in a λ^3 Focal Volume. *Phys. Rev. Lett.* **92,** 063902 (2004).

19. Hentschel, M. *et al.* Attosecond Metrology. *Nature* **414,** 509–513 (2001).

20. Gaumnitz, T. *et al.* Streaking of 43-Attosecond Soft-X-Ray Pulses Generated by a Passively CEP-Stable Mid-Infrared Driver. *Opt. Express* **25,** 27506–27518 (2017).

21. Sansone, G., Poletto, L. & Nisoli, M. High-Energy Attosecond Light Sources. *Nat. Photonics* **5,** 655–663 (2011).

22. Corkum, P. & Krausz, F. Attosecond Science. *Nat. Phys.* **3,** 381–387 (2007).

23. McNeil, B. W. J. & Thompson, N. R. X-Ray Free-Electron Lasers. *Nat. Photonics* **4,** 814–821 (2010).

24. Huang, Z. & Kim, K. J. Review of X-Ray Free-Electron Laser Theory. *Phys. Rev. Spec. Top. - Accel. Beams* **10,** 034801 (2007).

25. Huang, Z. *Brightness and Coherence of Synchrotron Radiation and FELs* in *Proc. IPAC 2013* (Shanghai, China, 2013), 16–20 (MOYCB101).

26. HASYLAB. *PETRA III - Facility Information* (accessed on 24/10/2017). `http://photon-science.desy.de/facilities/petra_iii/facility_information/index_eng.html`; Kube, G. *et al. PETRA III Diagnostics Beamline for Emittance Measurements* in *Proc. IPAC 2010* (Kyoto, Japan, 2010), 909–911; Schlie, M. *Time-Resolved Studies at PETRA III with a Highly Repetitive Synchronized Laser System* PhD thesis (University of Hamburg, 2013).

27. Deutsches Elektronensychrotron - DESY. *FLASH* (accessed on 24/10/2017). `http://photon-science.desy.de/facilities/flash/index_eng.html` (2017); Deutsches Elektronensychrotron - DESY. *The Free-Electron Laser* (accessed on 24/10/2017). `http://photon-science.desy.de/facilities/flash/the_free_electron_laser/index_eng.html` (2017); Deutsches Elektronensychrotron - DESY. *FLASH - Accelerator* (accessed on 24/10/2017). `https://flash.desy.de/accelerator/` (2017).

28. Decking, W. in *Brill. Light Life Mater. Sci.* (eds Tsakanov, V. & Wiedemann, H.) 21–30 (2007); European XFEL. *European XFEL - Facts and Figures* (accessed on 24/10/2017). `https://www.xfel.eu/facility/overview/how_it_works/index_eng.html` (2017).

29. Jaroszynski, D. *et al.* Radiation sources based on laser-plasma interactions. *Philos. Trans. R. Soc. A Math. Phys. Eng. Sci.* **364,** 689–710 (2006).

30. Islam, M. R. *et al.* Near-Threshold Electron Injection in the Laser-Plasma Wakefield Accelerator Leading to Femtosecond Bunches. *New J. Phys.* **17,** 093033 (2015).

31. Cipiccia, S. *et al.* Gamma-Rays from Harmonically Resonant Betatron Oscillations in a Plasma Wake. *Nat. Phys.* **7,** 867–871 (2011).

32. Tooley, M. P. *et al.* Towards Attosecond High-Energy Electron Bunches : Controlling Self-Injection in Laser Wakefield Accelerators through Plasma Density Modulation. *Phys. Rev. Lett.* **119,** 044801 (2017).

33. Brunetti, E. *et al.* Low Emittance, High Brilliance Relativistic Electron Beams from a Laser-Plasma Accelerator. *Phys. Rev. Lett.* **105,** 215007 (2010).

34. Manahan, G. G. *et al.* Single-Stage Plasma-Based Correlated Energy Spread Compensation for Ultrahigh 6D Brightness Electron Beams. *Nat. Commun.* **8,** 15705 (2017).

35. Gonzalez-Izquierdo, B. *et al.* Towards Optical Polarization Control of Laser-Driven Proton Acceleration in Foils Undergoing Relativistic Transparency. *Nat. Commun.* **7,** 12891 (2016); Gonzalez-Izquierdo, B. *et al.* Optically Controlled Dense Current Structures Driven by Relativistic Plasma Aperture-Induced Diffraction. *Nat. Phys.* **12,** 505–512 (2016).

36. Manahan, G. G. *et al. High resolution, single shot emittance measurement of relativistic electrons from laser-driven accelerator* in *Proc. SPIE, Laser Accel. Electrons, Protons, Ions; Med. Appl. Laser-Generated Second. Sources Radiat. Part.* **8079** (2011), 807909. doi:10.1117/12.887175.

37. Deutsches Elektronensychrotron. *Innovative Accelerator Project Produces First Particle Beam* (accessed on 24/10/2017). http://www.desy.de/news/news_search/index_eng.html?openDirectAnchor=1063; Deutsches Elektronensychrotron. *Plasma Accelerator Produces First X-Rays* (accessed on 24/10/2017). http://www.desy.de/news/news_search/index_eng.html?openDirectAnchor=1261.

38. Mehrling, T. *The FLASHForward Project* (accessed on 24/10/2017). https://vi-pwfa.desy.de/e192843/ (2017).

39. Marchetti, B *et al. Status Update of the SINBAD-ARES Linac under Construction at DESY* in *Proc. IPAC 2017* (Copenhagen, Denmark, 2017), 1412–1414 (TUPAB040).

40. Dorda, U. *et al. The Dedicated Accelerator R&D Facility "SINBAD" at DESY* in *Proc. IPAC 2017* (Copenhagen, Denmark, 2017), 869–872 (MOPVA012).

41. Jun Zhu. *Design Study for Generating Sub-Femtosecond to Femtosecond Electron Bunches for Advanced Accelerator Development at SINBAD* PhD thesis (University of Hamburg, 2017).

42. Mayet, F *et al. A Concept for Phase-Synchronous Acceleration of Microbunch Trains in DLA Structures at SINBAD* in *Proc. IPAC 2017* (Copenhagen, Denmark, 2017), 3260–3263 (WEPVA006).

43. Mayet, F *et al. Simulations and Plans for a Dielectric Laser Acceleration Experiment at SINBAD* in *Proc. IPAC 2017* (Copenhagen, Denmark, 2017), 3264–3267 (WEPVA007).

44. Kuropka, W, Assmann, R, Dorda, U & Mayet, F. *Simulation of a Many Period Dielectric Grating-Based Electron Accelerator* in *Proc. IPAC 2017* (Copenhagen, Denmark, 2017), 3256–3259 (WEPVA005).

45. Marx, D. *et al.* Reconstruction of the 3D Charge Distribution of an Electron Bunch Using a Novel Variable-Polarization Transverse Deflecting Structure (TDS). *J. Phys. Conf. Ser.* **874,** 012077 (2017).

46. Zhu, J., Assmann, R. W., Dohlus, M., Dorda, U. & Marchetti, B. Sub-Fs Electron Bunch Generation with Sub-10-Fs Bunch Arrival-Time Jitter via Bunch Slicing in a Magnetic Chicane. *Phys. Rev. Accel. Beams* **19,** 054401 (2016).

47. CFEL. *AXSIS: Frontiers in Attosecond X-Ray Science: Imaging and Spectroscopy* (accessed on 26/10/2017). `https://axsis.desy.de/` (2017).

48. Brookhaven National Laboratory. *Accelerator Test Facility: CO_2 Laser* (accessed on 24/10/2017). `https://www.bnl.gov/atf/capabilities/CO2laser.php` (2017).

49. Reiser, M. *Theory and Design of Charged Particle Beams* 2nd edition (Wiley-VCh, Weinheim, 2008).

50. Floettmann, K. Some basic features of the beam emittance. *Phys. Rev. Spec. Top. - Accel. Beams* **6,** 034202 (2003).

51. Mehrling, T. *Theoretical and Numerical Studies on the Transport of Transverse Beam Quality in Plasma-Based Accelerators* PhD thesis (University of Hamburg, 2014).

52. Dornmair, I. *Advanced Beam Dynamics and Diagnostics Concepts for Laser-Plasma Accelerators* PhD thesis (University of Hamburg, 2017).

53. Courant, E. D. & Snyder, H. S. Theory of the Alternating-Gradient Synchrotron. *An. Phys.* **3** (1958).

54. Mehrling, T., Grebenyuk, J., Tsung, F. S., Floettmann, K. & Osterhoff, J. Transverse emittance growth in staged laser-wakefield acceleration. *Phys. Rev. Spec. Top. - Accel. Beams* **15,** 111303 (2012).

55. Sears, C. M. S. *et al.* Production and characterization of attosecond electron bunch trains. *Phys. Rev. Spec. Top. - Accel. Beams* **11,** 061301 (2008).

56. Dodin, I. Y. & Fisch, N. J. Stochastic extraction of periodic attosecond bunches from relativistic electron beams. *Phys. Rev. Lett.* **98,** 234801 (2007).

57. Lemos, N., Shaw, J. L., Marsh, K. A. & Joshi, C. *Sub-femtosecond electron bunches created by direct laser acceleration in a laser wakefield accelerator with ionization injection* in *AIP Conf. Proc.* **1777** (2016), 040009. doi:`10.1063/1.4965611`.

58. Di Lucchio, L. & Gibbon, P. Relativistic attosecond electron bunch emission from few-cycle laser irradiated nanoscale droplets. *Phys. Rev. Spec. Top. - Accel. Beams* **18,** 023402 (2015).

59. Liseykina, T. V., Pirner, S. & Bauer, D. Relativistic attosecond electron bunches from laser-illuminated droplets. *Phys. Rev. Lett.* **104,** 095002 (2010).

60. Ma, Y. Y. *et al.* Dense quasi-monoenergetic attosecond electron bunches from laser interaction with wire and slice targets. *Phys. Plasmas* **13,** 110702 (2006).

61. Yang, X. H. *et al.* Propagation of attosecond electron bunches along the cone-and-channel target. *Phys. Plasmas* **18,** 023109 (2011).

62. Kulagin, V. V., Cherepenin, V. A., Hur, M. S. & Suk, H. Theoretical Investigation of Controlled Generation of a Dense Attosecond Relativistic Electron Bunch from the Interaction of an Ultrashort Laser Pulse with a Nanofilm. *Phys. Rev. Lett.* **99,** 124801 (2007).

63. Naumova, N. *et al.* Attosecond electron bunches. *Phys. Rev. Lett.* **93,** 195003 (2004).

64. Hu, L.-X., Yu, T.-P., Shao, F.-Q., Zou, D.-B. & Yin, Y. Enhanced dense attosecond electron bunch generation by irradiating an intense laser on a cone target. *Phys. Plasmas* **22,** 033104 (2015).

65. Pan, K. Q., Zheng, C. Y., Cao, L. H., Liu, Z. J. & He, X. T. Stably propagating trains of attosecond electron bunches generated along the target back. *Phys. Plasmas* **23,** 093101 (2016).

66. Baton, S. D. *et al.* Evidence of Ultrashort Electron Bunches in Laser-Plasma Interactions at Relativistic Intensities. *Phys. Rev. Lett.* **91,** 105001 (2003).

67. Christie, F, Rönsch-Schulenburg, J., Schreiber, S. & Vogt, M. *Generation of Ultra-Short Electron Bunches and FEL Pulses and Characterization of Their Longitudinal Properties At FLASH2* in *Proc. IPAC 2017* (Copenhagen, Denmark, 2017), 2600–2603 (WEPAB017).

68. Zhu, J., Assmann, R., Dorda, U. & Marchetti, B. Matching sub-fs electron bunches for laser-driven plasma acceleration at SINBAD. *Nucl. Instruments Methods Phys. Res. Sect. A Accel. Spectrometers, Detect. Assoc. Equip.* **829,** 229–232 (2016).

69. Floettmann, K. Adiabatic matching section for plasma accelerated beams. *Phys. Rev. Spec. Top. - Accel. Beams* **17,** 054402 (2014).

70. Zeitler, B., Floettmann, K. & Grüner, F. Linearization of the Longitudinal Phase Space without Higher Harmonic Field. *Phys. Rev. Spec. Top. - Accel. Beams* **18,** 120102 (2015).

71. Sell, A. & Kaertner, F. X. Attosecond electron bunches accelerated and compressed by radially polarized laser pulses and soft-x-ray pulses from optical undulators. *J. Phys. B At. Mol. Opt. Phys.* **47,** 015601 (2014).

72. Lundh, O. *et al.* Few femtosecond, few kiloampere electron bunch produced by a laser-plasma accelerator. *Nat. Phys.* **7,** 219–222 (2011).

73. Buck, A. *et al.* Real-time observation of laser-driven electron acceleration. *Nat. Phys.* **7,** 543–548 (2011).

74. Heigoldt, M. *et al.* Temporal evolution of longitudinal bunch profile in a laser wakefield accelerator. *Phys. Rev. Spec. Top. - Accel. Beams* **18,** 121302 (2015).

75. Li, F. Y. *et al.* Dense attosecond electron sheets from laser wakefields using an up-ramp density transition. *Phys. Rev. Lett.* **110,** 135002 (2013).

76. Xu, X. L. *et al.* Nano-scale electron bunching in laser-triggered ionization injection in plasma accelerators. *Phys. Rev. Lett.* **117,** 034801 (2016).

77. Luttikhof, M. J. H., Khachatryan, a. G., van Goor, F. a. & Boller, K. J. Generating ultrarelativistic attosecond electron bunches with laser wakefield accelerators. *Phys. Rev. Lett.* **105,** 124801 (2010).

78. Andreev, N. E. *et al.* Electron bunch compression and acceleration in the laser wakefield. *Nucl. Instruments Methods Phys. Res. Sect. A Accel. Spectrometers, Detect. Assoc. Equip.* **653,** 66–71 (2011).

79. *Advanced Accelerator Physics* in *Cern Accel. Sch. (18 - 29 Aug 2013)* (ed W. Herr) (Trondheim, Norway, 2013).

80. Berden, G. *et al.* Benchmarking of Electro-Optic Monitors for Femtosecond Electron Bunches. *Phys. Rev. Lett.* **99,** 164801 (2007).

81. Steffen, B. *et al.* Electro-Optic Time Profile Monitors for Femtosecond Electron Bunches at the Soft X-Ray Free-Electron Laser FLASH. *Phys. Rev. Spec. Top. - Accel. Beams* **12,** 032802 (2009).

82. Graves, W. S. *et al. Ultrashort Electron Bunch Length Measurements at DUVFEL* tech. rep. (National Synchrotron Light Source, Brookhaven National Laboratory, 2001), BNL –68552.

83. Fruehling, U. *et al.* Single-shot terahertz-field-driven X-ray streak camera. *Nat. Photonics* **3,** 523–528 (2009).

84. Grguraš, I. *et al.* Ultrafast X-ray pulse characterization at free-electron lasers. *Nat. Photonics* **6,** 852–857 (2012).

85. Dehler, M *et al. Design Concept for a THz Driven Streak Camera with Ultra High Resolution* in *Proc. IBIC 2015* (Melbourne, Australia, 2015), 156–160 (MOPAB048).

86. Fabiańska, J., Kassier, G. & Feurer, T. Split Ring Resonator Based THz-Driven Electron Streak Camera Featuring Femtosecond Resolution. *Sci. Rep.* **4,** 5646 (2014).

87. Nozawa, I. *et al. Bunch Length Measurement of Femtosecond Electron Beam by Monitoring Coherent Transition Radiation* in *Proc. IPAC 2015* (Richmond, USA, 2015), 940–943 (MOPTY002).

88. Behrens, C. *et al.* Constraints on photon pulse duration from longitudinal electron beam diagnostics at a soft x-ray free-electron laser. *Phys. Rev. Spec. Top. - Accel. Beams* **15,** 030707 (2012).

89. Roehrs, M., Gerth, C., Schlarb, H., Schmidt, B. & Schmueser, P. Time-resolved electron beam phase space tomography at a soft x-ray free-electron laser. *Phys. Rev. Spec. Top. - Accel. Beams* **12,** 050704 (2009).

90. Craievich, P., Ischebeck, R., Loehl, F., Orlandi, G. & Prat, E. *Transverse deflecting structures for bunch length and slice emittance measurements on SwissFEL* in *Proc. FEL 2013* (New York, USA, 2013), 236–241 (TUPSO14).

91. Behrens, C. *et al.* Few-femtosecond time-resolved measurements of X-ray free-electron lasers. *Nat. Commun.* **5,** 3762 (2014).

92. Dolgashev, V. A. *et al.* Design and application of multimegawatt X-band deflectors for femtosecond electron beam diagnostics. *Phys. Rev. Spec. Top. - Accel. Beams* **17,** 102801 (2014).

93. Dornmair, I., Schroeder, C. B., Floettmann, K., Marchetti, B. & Maier, A. R. Plasma-driven ultrashort bunch diagnostics. *Phys. Rev. Accel. Beams* **19,** 062801 (2016).

94. Jamison, S. P. *et al. A THz Driven Transverse Deflector for Femtosecond Longitudinal Profile Diagnostics* in *Proc. IBIC 2016* (Barcelona, Spain, 2016), 748–751 (WEPG48).

95. Lemery, F, Floettmann, K, Vinatier, T. & Assmann, R. W. *A Transverse Deflection Structure with Dielectric-Lined Waveguides in the sub-THz Regime* in *Proc. IPAC 2017* (Copenhagen, Denmark, 2017), 215–218 (MOPAB052).

96. Bettoni, S., Craievich, P., Lutman, A. A. & Pedrozzi, M. Temporal profile measurements of relativistic electron bunch based on wakefield generation. *Phys. Rev. Accel. Beams* **19,** 021304 (2016).

97. Wang, D., Krafft, G. & Sinclair, C. Measurement of Femtosecond Electron Bunches Using a RF Zero-Phasing Method. *Phys. Rev. E* **57,** 2283–2286 (1998).

98. Huang, Z., Bane, K., Ding, Y. & Emma, P. Single-shot method for measuring femtosecond bunch length in linac-based free-electron lasers. *Phys. Rev. Spec. Top. - Accel. Beams* **13,** 092801 (2010).

99. Zhang, Z., Du, Y., Tang, C., Ding, Y. & Huang, Z. Optical Circular Deflector with Attosecond Resolution for Ultrashort Electron Beam. *Phys. Rev. Accel. Beams* **20,** 050702 (2017).

100. Andonian, G. *et al.* Longitudinal Profile Diagnostic Scheme with Subfemtosecond Resolution for High-Brightness Electron Beams. *Phys. Rev. Spec. Top. - Accel. Beams* **14,** 072802 (2011).

101. Ding, Y. *et al.* Femtosecond x-ray pulse temporal characterization in free-electron lasers using a transverse deflector. *Phys. Rev. Spec. Top. - Accel. Beams* **14,** 120701 (2011).

102. Xiang, D. *et al.* All-Optical Time-Resolved Measurement of Laser Energy Modulation in a Relativistic Electron Beam. *Phys. Rev. Spec. Top. - Accel. Beams* **14,** 112801 (2011).

103. Kotaki, H. *et al.* Direct Observation of the Pulse Width of an Ultrashort Electron Beam. *J. Phys. Soc. Japan* **84** (2015).

104. Zhang, C. J. *et al.* Temporal Characterization of Ultrashort Linearly Chirped Electron Bunches Generated from a Laser Wakefield Accelerator. *Phys. Rev. Accel. Beams* **19,** 062802 (2016).

105. Purwar, H, Bruni, C, Gonnin, A & Vinatier, T. *Estimation of Longitudinal Dimensions of Sub-Picosecond Electron Bunches with the 3-Phase Method* in *Proc. IPAC 2017* (Copenhagen, Denmark, 2017), 139–141 (MOPAB028).

106. Vinatier, T, Assmann, R. W., Dorda, U & Marchetti, B. *Simulation of Fs Bunch Length Determination with the 3-Phase Method and THz Dielectric-Loaded Waveguides* in *Proc. IPAC 2017* (Copenhagen, Denmark, 2017), 199–202 (MOPAB048).

107. Strickland, D & Mourou, G. Compression of amplified chirped optical pulses. *Opt. Commun.* **56,** 219–221 (1985).

108. Dabu, R. *High power femtosecond lasers at ELI-NP* in *AIP Conf. Proc.* **219** (2015), 219–227. doi:10.1063/1.4909578.

109. Papadopoulos, D. *et al.* The Apollon 10 PW laser: experimental and theoretical investigation of the temporal characteristics. *High Power Laser Sci. Eng.* **4,** e34 (2016).

110. Heyl, C. M., Arnold, C. L., Couairon, A & L'Huillier, A. Introduction to macroscopic power scaling principles for high-order harmonic generation. *J. Phys. B At. Mol. Opt. Phys.* **50,** 013001 (2017).

111. A. E. Siegman. *Lasers* (University Science Books, 1986); *Transverse Mode* (accessed on 26/10/2017). https://en.wikipedia.org/wiki/Transverse_mode (2017).

112. Saleh, B. E. A. & Teich, M. C. *Fundamentals of Photonics* 2nd edition (ed Bahaa E. A. Saleh) (John Wiley and Sons Inc., 2007).

113. Esarey, E., Schroeder, C. B. & Leemans, W. P. Physics of laser-driven plasma-based electron accelerators. *Rev. Mod. Phys.* **81,** 1229–1285 (2009).

114. Kruer, W. L. *The Physics of Laser Plasma Interactions* (Addison-Wesley, 1988).

115. Kibble, T. W. B. Mutual Reflection of Electrons and Photons. *Phys. Rev.* **150,** 1060–1069 (1966).

116. Cairns, R. A. *Plasma Physics* (Blackie, 1985).

117. Zeitler, B. *Phase Space Linearization and External Injection of Electron Bunches into Laser-Driven Plasma Wakefields at REGAE* PhD thesis (University of Hamburg, 2016).

118. Dawson, J. M. Nonlinear Electron Oscillations in a Cold Plasma. *Phys. Rev.* **113,** 383–387 (1959).

119. Esarey, E., Ting, A., Sprangle, P., Umstadter, D. & Liu, X. Nonlinear analysis of relativistic harmonic generation by intense lasers in plasmas. *IEEE Trans. Plasma Sci.* **21,** 95–104 (1993).

120. Sprangle, P., Esarey, E. & Ting, A. Nonlinear Theory of Intense Laser-Plasma Interactions. *Phys. Rev. Lett.* **64,** 2011–2014 (1990).

121. Ting, A., Esarey, E. & Sprangle, P. Nonlinear wake-field generation and relativistic focusing of intense laser pulses in plasmas. *Phys. Fluids B Plasma Phys.* **2,** 1390–1394 (1990).

122. Indiana University. *Making Complex Waves* (accessed on 26/10/2017). `http://hep.physics.indiana.edu/$\sim$rickv/Making_complex_waves.html` (2017).

123. Panofsky, W. K. H. & Wenzel, W. A. Some considerations concerning the transverse deflection of charged particles in radio-frequency fields [2]. *Rev. Sci. Instrum.* **27,** 967 (1956).

124. Lu, W., Huang, C., Zhou, M. M., Mori, W. B. & Katsouleas, T. Limits of linear plasma wakefield theory for electron or positron beams. *Phys. Plasmas* **12,** 063101 (2005).

125. Katsouleas, T., Wilks, S., Chen, P., Dawson, J. M. & Su, J. J. Beam loading in plasma waves. *IEEE Trans. Plasma Sci.* **15,** 210–217 (1987).

126. Hansson, M. *et al.* Down-ramp injection and independently controlled acceleration of electrons in a tailored laser wakefield accelerator. *Phys. Rev. Spec. Top. - Accel. Beams* **18,** 071303 (2015).

127. Swanson, K. K. *et al.* Control of tunable, monoenergetic laser-plasma-accelerated electron beams using a shock-induced density downramp injector. *Phys. Rev. Accel. Beams* **20,** 051301 (2017).

128. Audet, T. L. *et al.* Investigation of ionization-induced electron injection in a wakefield driven by laser inside a gas cell. *Phys. Plasmas* **23,** 023110 (2016).

129. Oz, E. *et al.* Ionization-Induced Electron Trapping in Ultrarelativistic Plasma Wakes. *Phys. Rev. Lett.* **98,** 084801 (2007).

130. Chen, M., Sheng, Z. M., Ma, Y. Y. & Zhang, J. Electron injection and trapping in a laser wakefield by field ionization to high-charge states of gases. *J. Appl. Phys.* **99,** 056109 (2006).

131. Hansson, M., Aurand, B., Ekerfelt, H., Persson, A. & Lundh, O. Injection of electrons by colliding laser pulses in a laser wakefield accelerator. *Nucl. Instruments Methods Phys. Res. Sect. A Accel. Spectrometers, Detect. Assoc. Equip.* **829,** 99–103 (2016).

132. Modena, A. *et al.* Electron acceleration from the breaking of relativistic plasma waves. *Nature* **377,** 606–608 (1995).

133. Geddes, C. G. R. *et al.* High-quality electron beams from a laser wakefield accelerator using plasma-channel guiding. *Nature* **431,** 538–541 (2004).

134. Mangles, S. P. D. *et al.* Monoenergetic beams of relativistic electrons from intense laser-plasma interactions. *Nature* **431,** 535–538 (2004).

135. Faure, J *et al.* A laser plasma accelerator producing monoenergetic electron beams. *Nature* **431,** 541–544 (2004).

136. Bulanov, S., Naumova, N., Pegoraro, F. & Sakai, J. Particle injection into the wave acceleration phase due to nonlinear wake wave breaking. *Phys. Rev. E* **58,** R5257–R5260 (1998).

137. Esarey, E., Sprangle, P., Krall, J. & Ting, A. Overview of plasma-based accelerator concepts. *IEEE Trans. Plasma Sci.* **24,** 252–288 (1996).

138. Chen, M., Sheng, Z., Zheng, J., Ma, Y. & Zhang, J. (in Chinese). *Chin. J. Comp. Phys.* **25** (2008); Wang, W.-M., Gibbon, P., Sheng, Z.-M. & Li, Y.-T. Integrated simulation approach for laser-driven fast ignition. *Phys. Rev. E* **91,** 013101 (2015).

139. Fonseca, R. A. *et al.* in *Lect. Notes Comput. Sci.* 342–351 (Springer, Berlin Heidelberg, 2002). doi:10.1007/3-540-47789-6_36.

140. Aschikhin, A. *et al.* The FLASHForward facility at DESY. *Nucl. Instruments Methods Phys. Res. Sect. A Accel. Spectrometers, Detect. Assoc. Equip.* **806,** 175–183 (2016).

141. Weikum, M. K., Li, F. Y., Assmann, R. W., Sheng, Z. M. & Jaroszynski, D. Generation of attosecond electron bunches in a laser-plasma accelerator using a plasma density upramp. *Nucl. Instruments Methods Phys. Res. Sect. A Accel. Spectrometers, Detect. Assoc. Equip.* **829,** 33–36 (2016).

142. Li, F. Y. *et al.* Radially Polarized, Half-Cycle, Attosecond Pulses from Laser Wakefields through Coherent Synchrotron Radiation. *Phys. Rev. E* **90,** 043104 (2014).

143. FACET. *Performance Metrics: User Time for FY16 Run* (accessed on 26/10/2017). `https://portal.slac.stanford.edu/sites/ard_public/facet/Pages/PerformanceMetricsFY16.aspx` (2017).

144. Rossi, A. R. *et al.* The External-Injection experiment at the SPARC_LAB facility. *Nucl. Instruments Methods Phys. Res. Sect. A Accel. Spectrometers, Detect. Assoc. Equip.* **740,** 60–66 (2014).

145. Feynman, R. *The Feynman Lectures on Physics, Volume II* (eds Gottlieb, M. A. & Pfeiffer, R.) `http://www.feynmanlectures.caltech.edu/II_toc.html` (2013).

146. Shadwick, B. A., Schroeder, C. B. & Esarey, E. Nonlinear laser energy depletion in laser-plasma accelerators. *Phys. Plasmas* **16,** 056704 (2009).

147. Debus, A. D. *et al.* Electron bunch length measurements from laser-accelerated electrons using single-shot THz time-domain interferometry. *Phys. Rev. Lett.* **104,** 84802 (2010).

148. Buck, A. *et al.* Shock-Front Injector for High-Quality Laser-Plasma Acceleration. *Phys. Rev. Lett.* **110,** 185006 (2013).

149. Goers, A. J. *et al.* Multi-MeV Electron Acceleration by Subterawatt Laser Pulses. *Phys. Rev. Lett.* **115,** 194802 (2015).

150. Guénot, D. *et al.* Relativistic electron beams driven by kHz single-cycle light pulses. *Nat. Photonics* **11,** 293–297 (2017).

151. Schmid, K. *et al.* Density-transition based electron injector for laser driven wakefield accelerators. *Phys. Rev. Spec. Top. - Accel. Beams* **13,** 091301 (2010).

152. Durfee, C. G., Lynch, J. & Milchberg, H. Development of a plasma waveguide for high intensity laser pulses. *Phys. Rev. E* **51,** 2368–2387 (1995).

153. Bottino, A. *Entropy evolution and dissipation in collisionless particle-in-cell gyrokinetic simulations* (at Numerical Methods for the Kinetic Equations of Plasma Physics (NumKin 2013)). `https://www.ipp.mpg.de/1525263/Bottino.pdf`. 2013.

154. Weikum, M. K. *et al. Improved Electron Beam Quality from External Injection in Laser-Driven Plasma Acceleration at SINBAD* in *Proc. IPAC 2017* (Copenhagen, Denmark, 2017), 1707–1710 (TUPIK013).

155. Floettmann, K. *ASTRA A Space Charge Tracking Algorithm* (accessed on 21/02/2018). `http://www.desy.de/~mpyflo/` (2018).

156. Xu, X. L. *et al.* Physics of Phase Space Matching for Staging Plasma and Traditional Accelerator Components Using Longitudinally Tailored Plasma Profiles. *Phys. Rev. Lett.* **116,** 124801 (2016).

157. Dornmair, I., Floettmann, K. & Maier, a. R. Emittance conservation by tailored focusing profiles in a plasma accelerator. *Phys. Rev. Spec. Top. - Accel. Beams* **18,** 041302 (2015).

158. Tomassini, P & Rossi, A. R. Matching strategies for a plasma booster. *Plasma Phys. Control. Fusion* **58,** 034001 (2016).

159. Michel, P, Schroeder, C. B., Shadwick, B. A., Esarey, E & Leemans, W. P. Radiative damping and electron beam dynamics in plasma-based accelerators. *Phys. Rev. E* **74,** 26501 (2006).

160. Lehe, R., Lifschitz, A., Thaury, C., Malka, V. & Davoine, X. Numerical growth of emittance in simulations of laser-wakefield acceleration. *Phys. Rev. Spec. Top. - Accel. Beams* **16,** 021301 (2013).

161. Godfrey, B. B. Numerical Cherenkov instabilities in electromagnetic particle codes. *J. Comput. Phys.* **15,** 504–521 (1974).

162. Cormier-Michel, E. *et al.* Unphysical kinetic effects in particle-in-cell modeling of laser wakefield accelerators. *Phys. Rev. E - Stat. Nonlinear, Soft Matter Phys.* **78,** 1–17 (2008).

163. *Laser-Plasma Interactions* (ed Jaroszynski, D.A., Bingham, R., Cairns, R.) (The Scottish Universities Summer School in Physics (CRC Press), 2009).

164. Esarey, E. & Leemans, W. P. Nonparaxial propagation of ultrashort laser pulses in plasma channels. *Phys. Rev. E* **59,** 1082–1095 (1999).

165. Paradkar, B. S., Cros, B., Mora, P. & Maynard, G. Numerical modeling of multi-GeV laser wakefield electron acceleration inside a dielectric capillary tube. *Phys. Plasmas* **20,** 083120 (2013).

166. Desforges, F. *et al.* Reproducibility of electron beams from laser wakefield acceleration in capillary tubes. *Nucl. Instruments Methods Phys. Res. Sect. A Accel. Spectrometers, Detect. Assoc. Equip.* **740,** 54–59 (2014).

167. The GSL Team. *Weighted Samples* (accessed on 26/10/2017). `http://www.gnu.org/software/gsl/doc/html/statistics.html#weighted-samples`.

168. Rossi, A. R. *et al.* Stability study for matching in laser driven plasma acceleration. *Nucl. Instruments Methods Phys. Res. Sect. A Accel. Spectrometers, Detect. Assoc. Equip.* **829,** 67–72 (2016).

169. Di Mitri, S. & Cornacchia, M. Electron beam brightness in linac drivers for free-electron-lasers. *Phys. Rep.* **539,** 1–48 (2014).

170. Schmid, K. & Veisz, L. Supersonic gas jets for laser-plasma experiments. *Rev. Sci. Instrum.* **83,** 053304 (2012).

171. Lin, M. W. *et al.* Programmable fabrication of spatial structures in a gas jet by laser machining with a spatial light modulator. *Phys. Plasmas* **13,** 110701 (2006).

172. Pai, C. H. *et al.* Fabrication of spatial transient-density structures as high-field plasma photonic devices. *Phys. Plasmas* **12,** 070707 (2005).

173. Burza, M. *et al.* Laser wakefield acceleration using wire produced double density ramps. *Phys. Rev. Spec. Top. - Accel. Beams* **16,** 3–7 (2013).

174. Schaper, L., Goldberg, L., Kleinwächter, T., Schwinkendorf, J. P. & Osterhoff, J. Longitudinal gas-density profilometry for plasma-wakefield acceleration targets. *Nucl. Instruments Methods Phys. Res. Sect. A Accel. Spectrometers, Detect. Assoc. Equip.* **740,** 208–211 (2014).

175. Zou, J. *et al.* Design and current progress of the Apollon 10 PW project. *High Power Laser Sci. Eng.* **3,** e2 (2015).

176. ELI Beamlines. *L2: 1 PW, 20 J, 10 Hz Beam Line* (accessed on 26/10/2017). `https://www.eli-beams.eu/en/facility/lasers/l2-pw-20-j-10-hz-beamline/` (2017).

177. Helmholtz Institute Jena. *JETI200 Laser* (accessed on 26/10/2017). `https://www.hi-jena.de/en/helmholtz_institute_jena/about-the-helmholtz-institute-jena/experimental_facilities/local/jeti200-laser-kopie/` (2017).

178. Leemans, W. P. *et al.* Multi-Gev electron beams from capillary-discharge-guided subpetawatt laser pulses in the self-trapping regime. *Phys. Rev. Lett.* **113,** 245002 (2014).

179. Lehe, R., Kirchen, M., Andriyash, I. A., Godfrey, B. B. & Vay, J. L. A spectral, quasi-cylindrical and dispersion-free Particle-In-Cell algorithm. *Comput. Phys. Commun.* **203,** 66–82 (2016).

180. Wiedemann, H. *Particle Accelerator Physics* 3rd. doi:10.1080/08940889408261288 (Springer, Berlin Heidelberg, 2007).

181. Bracewell, R. *The Fourier Transform and Its Applications* (McGraw-Hill, New York, 1965).

182. Maier, A. R. *et al.* Demonstration scheme for a laser-plasma-driven free-electron laser. *Phys. Rev. X* **2,** 031019 (2012).

183. Campbell, L. T. & McNeil, B. W. *Puffin: A Three Dimensional, Unaveraged Free Electron Laser Simulation Code* in *Proc. FEL 2012* (Nara, Japan, 2012), 73–76 (MOPD12). doi:10.1063/1.4752743.

184. Reiche, S. *Genesis 1.3* (accessed on 30/10/2017). http://genesis.web.psi.ch/index.html (2017).

185. Xie, M. Exact and variational solutions of 3D eigenmodes in high gain FELs. *Nucl. Instruments Methods Phys. Res. Sect. A Accel. Spectrometers, Detect. Assoc. Equip.* **445,** 59–66 (2000).

186. Weikum, M., Andonian, G., Assmann, R., Dorda, U. & Sheng, Z. Reconstruction of sub-femtosecond longitudinal bunch profile measurement data. *J. Phys. Conf. Ser.* **874,** 012079 (2017).

187. Andonian, G. *Sub-femtosecond Bunch Length Diagnostic* (at 18th ATF Users Meeting). https://indico.bnl.gov/conferenceDisplay.py?confId=1274. 2015.

188. Floettmann, K. & Paramonov, V. V. Beam dynamics in transverse deflecting rf structures. *Phys. Rev. Spec. Top. - Accel. Beams* **17,** 024001 (2014).

189. Akre, R., Bentson, L., Emma, P. & Krejcik, P. A transverse rf deflecting structure for bunch length and phase space diagnostics. *Proc. 2001 Part. Accel. Conf.* **3,** 3–6 (Cat. No.01CH37268) (2001).

190. Akre, R., Emma, P., Krejcik, P. & Bentson, L. *Bunch length measurements using a transverse RF deflecting structure in the SLAC linac* tech. rep. May (2002).

191. Borland, M. Elegant: A flexible SDDS-compliant code for accelerator simulation. *Adv. Phot. Source LS-287,* 1–11 (2000).

192. Andonian, G. *et al.* Generation of Ramped Current Profiles in Relativistic Electron Beams Using Wakefields in Dielectric Structures. *Phys. Rev. Lett.* **118.** doi:10.1103/PhysRevLett.118.054802 (2017).

193. Agustsson, R *et al. Normal Conducting Radio Frequency X-Band Deflecting Cavity Fabrication and Validation* in *Proc. IPAC 2012* (New Orleans, USA, 2012), 3389–3391 (THPPC046).

194. Corkum, P., Alcock, A. & Leopold, K. Electron-beam-controlled transmission of 10-micrometer radiation in semiconductors. *J. Appl. Phys.* **50,** 3079 (1979).

195. Shine, A. *Fitting Experimental Data to Straight Lines (Lecture Notes)* (University of Delaware). https://www.che.udel.edu/pdf/FittingData.pdf. 2006.

196. Huang, Z. & Kim, K. J. Formulas for coherent synchrotron radiation microbunching in a bunch compressor chicane. *Phys. Rev. Spec. Top. - Accel. Beams* **5,** 074401 (2002).

197. UCLA Particle Beam Physics Lab. *Magnetic Chicane Bunch Compressors* (accessed on 30/10/2017). http://pbpl.physics.ucla.edu/Research/Technologies/Magnets/Electromagnets/Dipoles/Chicane_Bunch_Compressors/ (2017).

198. Xiang, D. & Ding, Y. Longitudinal-to-transverse mapping for femtosecond electron bunch length measurement. *Phys. Rev. Spec. Top. - Accel. Beams* **13,** 094001 (2010).

199. Marchetti, B *et al. ARES : Accelerator Research Experiment At SINBAD* in *Proc. IPAC 2015* (Richmond, USA, 2015), 1469–1471 (TUPWA029).

200. Andonian, G *et al. Diagnostic concept for high-resolution temporal profile measurements* in *Proc. IPAC 2011* (San Sebastián, Spain, 2011), 1967–1969 (WEOBB02).

201. Vinatier, T., Assmann, R., Dorda, U., Lemery, F. & Marchetti, B. *Simulations of an Hybrid and Compact Attosecond X-Ray Source Based on RF and THz Technologies* (at European Advanced Accelerator Concepts (EAAC) Workshop 2017, Elba, Italy). https://agenda.infn.it/materialDisplay.py?contribId=169&sessionId=15&materialId=slides&confId=12611. 2017.

202. Stupakov, G. V. & Zolotorev, M. S. Ponderomotive laser acceleration and focusing in vacuum for generation of attosecond electron bunches. *Phys. Rev. Lett.* **86,** 5274–5277 (2001).

203. Couperus, J. P. *et al.* Demonstration of a beam loaded nanocoulomb-class laser wakefield accelerator. *Nat. Commun.* **8,** 487 (2017).

204. Daoud, H., Floettmann, K. & Miller, R. J. Compression of high-density 0.16 pC electron bunches through high field gradients for ultrafast single shot electron diffraction: The compact RF gun. *Struct. Dyn.* **4,** 044016 (2017).

205. Uesaka, M., Ueda, T., Kozawa, T. & Kobayashi, T. Precise measurement of a subpicosecond electron single bunch by the femtosecond streak camera. *Nucl. Instruments Methods Phys. Res. Sect. A Accel. Spectrometers, Detect. Assoc. Equip.* **406,** 371–379 (1998).

206. Huening, M. *et al. Observation of Femtosecond Bunch Length Using a Transverse Deflecting Structure* in *Proc. FEL 2005* (Stanford, USA, 2005), 538–540 (THPP035).

207. Li, R. *et al.* Note: Single-shot continuously time-resolved MeV ultrafast electron diffraction. *Rev. Sci. Instrum.* **81,** 036110 (2010).

208. Ricci, K. N. & Smith, T. I. Longitudinal electron beam and free electron laser microbunch measurements using off-phase rf acceleration. *Phys. Rev. Spec. Top. - Accel. Beams* **3,** 032801 (2000).

209. Muggli, P. *et al.* Coherent transition radiation to measure the SLAC electron bunch length. *Proc. IEEE Part. Accel. Conf.* **2005,** 4102–4104 (2005).

210. Nozawa, I. *et al.* Measurement of $<$ 20 fs Bunch Length Using Coherent Transition Radiation. *Phys. Rev. Spec. Top. - Accel. Beams* **17,** 072803 (2014).

211. Loos, H. *Longitudinal diagnostics for short electron beam bunches* in *Proc. PAC 2009* (Vancouver, Canada, 2009), 736–740 (TU3GRI01).